UNIVERSITY OF SOUTHAMPTON

Faculty of Physical Sciences and Engineering

Electronics and Computer Science

Dynamic Modulation of Plasmon Excitations in Monolayer Graphene

by

Nikolaos Matthaiakakis

A Thesis submitted for the acquisition of

PhD in Electronics and Computer Science

by examination and dissertation

UNIVERSITY OF SOUTHAMPTON
ABSTRACT
FACULTY OF PHYSICAL SCIENCES AND ENGINEERING
School of Electronics and Computer Science
Doctor of Philosophy
DYNAMIC MODULATION OF PLASMON EXCITATIONS IN MONOLAYER GRAPHENE
by Nikolaos Matthaiakakis

Abstract

Plasmonic devices based on noble metals have offered solutions in numerous scientific and commercial fields over the past decades. Nevertheless the optical properties of noble metals are hardly tuneable thus not allowing for dynamic control of device properties. Offering a solution for achieving efficient dynamically tuneable plasmonic devices is a crucial since it would significantly widen the range of plasmonic applications and open the way for on-chip photonic logic systems.

Graphene has demonstrated high quantum efficiency for light matter interactions, strong optical nonlinearity, high optical damage threshold, and plasmons with high confinement and long propagation distances. Having a linear dispersion, zero bandgap, as well as very few free electrons available under zero doping conditions, has made this material a strong candidate for realising dynamic and highly tuneable photonic and plasmonic devices.

The interest of graphene as a platform for photonic applications is enormous with numerous publications focusing on the realisation of electrostatically controlled optical devices utilizing novel properties offered by this material. Graphene plasmonics in particular have great promise in realising highly efficient on-chip modulators, optical interconnects, waveguides, sensors, and even photonic logic gates.

Naturally, several issues need to be overcome in order for such devices to reach commercialization. Obtaining strong coupling of light with plasmons in graphene while also providing efficient long range frequency and intensity modulation of the plasmon absorption is a crucial and highly anticipated goal for graphene based plasmonic devices.

This work overcomes these issues by utilizing a novel diffraction grating/gold-insulator-graphene combined structure to dynamically couple, enhance, and manipulate plasmons in a graphene monolayer. The proposed structure consists of a two-dimensional inverted pyramid grating on a Si wafer, which acts as a phase matching component, and utilizes a gold back reflector and a transparent spacer in order to enhance coupling of plasmons on the graphene layer that lies above. An extra ionic gel layer above the monolayer of graphene is used to achieve efficient electrostatic control of the plasmon frequency and absorption efficiency.

The pyramid grating structure properties were studied experimentally. Theoretical calculations as well as Rigorous Coupling Wave Analysis simulations of the final device setup provide evidence of extremely efficient plasmon modulation both in terms of frequency and absorption efficiency, reaching even total optical absorption under certain conditions. Furthermore the device configuration allows for dynamic switching of plasmon excitations thus providing a possible solution for photonic switching applications. Finally, alternative materials for achieving tuneable plasmonic devices are also discussed.

Table of Contents


To my dear friend Nikos
Love,

Acknowledgements

For their valuable contribution towards the completion of this thesis and the research results that are presented here I would like to acknowledge the effort and support of the following people.

I would like to thank my supervisor Professor Martin Charlton for his guidance, encouragement and overall input towards the completion of this work. Prof. Charlton is not only an excellent scientist but also a great person that is always supportive and offers solutions to any problem.

I would also like to thank Professor Hiroshi Mizuta for his significant contribution towards the realization of this work as well as for providing the opportunity for me to spend one year in beautiful Japan, a land with rich culture and history that resulted in an experience that I will never forget. I want to also thank all the members of Mizuta group and JAIST that provided their kind support and welcomed me there as a member of the University. Furthermore I would like to deeply thank my Kyudo sensei Kinoshita Kousuke, the members of the Sakuragi Kyudojo in Komatsu, as well as Mrs. Akiko Takizawa and Mrs. Kiki Watabe for welcoming me as part of their family during my stay in Japan.

For their efforts and contributions towards different aspects of this research I would like to acknowledge, Dr. Zakaria Moktadir and Dr. Harold Chong for the valuable conversations during the first months of my PhD, Dr. Stuart Boden for the assistance in acquiring high quality Helium Ion Microscopy images, Prof. Hideyuki Murata and Prof. Heisuke Sakai for providing the facilities for the development of the Ionic gel process, Prof. Euan Hendry, Dr. Xu Fang, and Dr. Benjamin Lowe for their valuable contribution towards the improvement of this thesis, Mr. Xinzhao Yan for the fabrication of wafers using the Southampton University clean room facilities while I was a visiting student in JAIST, Dr. Jamie Reynolds for the numerous graphene transfer attempts that we made together, and Mr. Peter Ayliffe for the assistance with the E-BEAM patterning of the devices. I would also like to thank University of Southampton as well as JAIST for providing the facilities as well as the funding for this project.

For their valuable guidance and continuous support during my first steps in academia as well as for inspiring me to follow a career in science I would like to thank Prof. Panagiotis Photopoulos and Prof. Cimon Anastasiadis.

For their never ending support and care I would like to thank my parents, Mr. Aristidis Matthaiakakis and Ms. Eleni Tsimekou, as well as my uncle Mr. George Matthaiakakis who is always ready to accompany me in my Journeys around the world. I would further like to thank my family and friends who have always been there for me in times of need. I would especially like to acknowledge Mr. Alexandros Pitsilis, Mr. Eustathios Kiriakopoulos, Mr. Lazaros Chanzoplakis, Mr. Manolis Demeneopoulos, Mr. Olsi Panto, Mr. Stelios S. as well as Dr. Benjamin Lowe, Mr. Christoph Riedel, Ms. Sahar Mirzaei, Mr. Zhongwang Wang, Mr. Jothiramalingam Kulothungan, Mr. Ahmed Hammam, and Mr. Mohit Dalal for their valuable friendship and for the great moments we always share together.

Finally, for being an important part of my life and for her loving care and support, I would like to express my deep appreciation and gratitude towards Ms. Yuko Fujimoto. Her beautiful and calming tea ceremony has been a great source of inspiration for me.

Academic Thesis: Declaration of Authorship

I, Nikolaos Matthaiakakis, declare that this thesis and the work presented in it are my own and has been generated by me as the result of my own original research.

Dynamic modulation of plasmon excitations in monolayer graphene

I confirm that:

1. This work was done wholly or mainly while in candidature for a research degree at this University;
2. Where any part of this thesis has previously been submitted for a degree or any other qualification at this University or any other institution, this has been clearly stated;
3. Where I have consulted the published work of others, this is always clearly attributed;
4. Where I have quoted from the work of others, the source is always given. With the exception of such quotations, this thesis is entirely my own work;
5. I have acknowledged all main sources of help;
6. Where the thesis is based on work done by myself jointly with others, I have made clear exactly what was done by others and what I have contributed myself;
7. Either none of this work has been published before submission, or parts of this work have been published as:

   N. Matthaiakakis, H. Mizuta, M. D. B. C. Strong modulation of plasmons in graphene with the use of an Inverted pyramid array diffraction grating. *Sci. Rep.* **6,** 1–11 (2016).

   Matthaiakakis, N., Y. Xingzhao, Mizuta, H. & Charlton, M. D. B. Tuneable strong optical absorption in a graphene-insulator-metal hybrid plasmonic device. *Sci. Rep. (2017).*

Signed: ……

Date: 30/07/2017

1. Introduction

Surface plasmons are electromagnetic waves propagating at the surface of a conductor in the form of collective electron oscillations that are in resonance with an incident electromagnetic wave [1–3]. These excitations allow coupling of light in sub-wavelength/sub-diffraction dimensions (spatial regions smaller than the wavelength of the incident light) and thus provide a method for light confinement in nanoscale devices. Providing an efficient method for not only confining but also dynamically controlling the properties of light in nanoscale systems is a significant step towards dynamically tuneable nano-photonic devices. However, traditional plasmonic materials like noble metals, do not allow for tuning of their optical properties due to their high free carrier density. It is thus important to investigate the properties of alternative materials as platforms for nanoscale light manipulation.

Graphene is a flat monolayer of carbon atoms that are tightly packed in a two-dimensional honeycomb lattice. Even though graphene has been well theoretically studied for sixty years and has provided a topic of debate for theoretical physics, it was initially presumed to be a material that cannot exist in the free state [4]. The reason for that is the assumption that during crystal growth thermal vibrations eventually lead to the formation of 3D systems thus not allowing stable 1D or 2D objects to be formed [4,5]. As a result, graphene used to be regarded only as a purely academic material. This changed when graphene in its free state was discovered by A. K. Geim and K. Novoselov in 2004, an achievement resulting in the award of a Nobel Prize, and opening the way for two-dimensional atomic crystals [6,7].

Novel and unprecedented properties of graphene attracted a huge interest from academia and industry resulting in a gold rush to unlock the potential of this newly discovered material [8]. Exhibiting unique electronic, photonic and mechanical properties, this one-atom thick crystal combines mechanical strength, thinness, high carrier mobility, and transparency, providing an excellent platform for replacing other materials in currently bottlenecked technologies or even to allow the creation of novel devices like flexible electronics and optoelectronics [4,5,9–12]. Furthermore, graphene is structurally malleable and the electronic, optical and phonon properties of graphene can be altered strongly by inducing strain and deformations [5] or with the use of electrostatic gating [11], allowing the creation of tuneable devices.

In terms of optical characteristics, graphene presents high quantum efficiency for light-matter interactions, strong optical nonlinearity, high optical damage threshold, and plasmons with high propagation distance and confinement as well as many other unique and unusual properties [13–15]. Combining these optical characteristics with the ability to dynamically tune the properties of the material is the key reason for the popularity of graphene in the field of photonics [14].

Furthermore, having no bandgap and very few available free carriers in zero doping conditions allows easy modulation of the carrier density in graphene. In terms of plasmon properties, this translates to the ability to strongly modulate and control the plasmon coupling frequency since this frequency directly depends on permittivity of the material. Plasmons in graphene can be controlled by electrostatic gating, doping, or even structural deformation of the layer. The promise of graphene in this area is undeniable and many papers and review articles focusing on graphene based

applications have been published during the last few years [16–35], with graphene photonics and plasmonics being amongst the most important market areas [13–15].

Several efforts have been made to couple and dynamically control plasmons in graphene [36–51]. In addition, a lot of effort has been placed on realizing devices that can achieve total optical absorption (absorption of all incident photons) in graphene [36,52–70]. Nevertheless, it is a crucial challenge to combine efficient wavelength modulation of plasmons with strong optical absorption in graphene. Even though research efforts towards achieving highly tuneable total optical absorption in graphene are numerous there is still huge difficulty in designing devices that provide such properties even individually. Thus the combination of these characteristics is a highly pursued goal for the field of graphene plasmonics and photonics in general.

This work aims to design and fabricate novel graphene-based tuneable devices capable of improved optical absorption and large frequency range of operation whilst improving fundamental understanding of the photonic and plasmonic properties of graphene.

In order to achieve this, a novel nanostructure setup is proposed, providing a dynamically and highly tuneable plasmonic device with a large frequency range of operation. The proposed device consists of a two-dimensional array of inverted pyramid pits forming a crossed diffraction grating and acting as a phase-matching component for coupling photons to graphene plasmons [36]. The graphene layer is placed above the diffraction grating. When incident photons diffract in the grating structure, their phase relations match those of the plasmons in the graphene and thus propagating plasmon modes are excited on the graphene monolayer. Introducing an ionic conducting liquid immobilized inside a polymer matrix ("ionic gel") to form a transparent gate above the graphene layer allows for dynamic and low voltage tuning of the phase matching frequency and thus the frequency of excitation of plasmons in graphene. The ionic gel allows for highly efficient modulation of the free carrier density of graphene which in turn defines the optical behaviour of the system and allows for a large range of control over the plasmon frequency.

An improvement over the original device, aiming to strongly enhance plasmon absorption in graphene, was also proposed. In order to achieve this, the device was modified to include a gold coating covering the pyramid structures which acts as a back reflector while also supporting plasmons. A transparent spacer was added separating graphene from the gold layer, also resulting in the formation of a low quality Salisbury screen cavity. This setup provides increased Electromagnetic field energy density at the vicinity of graphene layer due to the near field produced from the gold plasmons as well as better diffraction efficiency of the pyramid cavity. When phase matching conditions are met, and the graphene plasmon mode overlaps with the gold plasmon mode, strong enhancement of coupling efficiency of plasmons to the graphene layer is achieved.

Finally, Indium Tin Oxide based plasmonics devices are proposed as an alternative to graphene based devices. Overall the proposed methods in this work provide efficient plasmon modulation and tuneable strong optical absorption, thus providing valuable input and insight to the general field of Plasmonics.

2. Thesis Outline

The thesis is separated into 3 main chapters (excluding introduction and conclusion). Chapter 3 focuses on the necessary literature for understanding the theoretical background, the fabrication methods, the applications, and the current aims and issues faced by the graphene plasmonics community. This chapter begins by explaining the basic theory of plasmonics and then explains the band structure of graphene. A literature analysis on photonic and plasmonic properties of graphene is made, followed by a review of currently available photonic and plasmonic devices. Finally methods to grow, transfer, and characterize graphene are explained in detail.

Chapter 4 presents the design of a novel device and the development of a theoretical model that is used to predict the behaviour of graphene plasmons in the system. RCWA (Rigorous Coupled Wave Analysis) simulations accompanied by theoretical calculations are used to model the device, resulting in two publications [36,71]. The physical mechanisms behind the operation of the device are explained in detail and optimization methods are used to enhance the optical absorption in graphene. Using a combination of a diffraction grating with a Salisbury screen cavity, strong enhancement of absorption attributed to graphene plasmons was observed sufficient to achieving total optical absorption. With the introduction of an ion gel gate the wavelength of absorption can be dynamically controlled over a large spectral range thus providing a highly efficient total optical absorption tuneable device. The results of this chapter are used to provide a good understanding of the device operation and to predict optimal conditions for fabrication. Alternative materials to graphene for tuneable plasmonic devices are also discussed.

Chapter 5 focuses on the experimental methods used to fabricate and characterize the novel device that was theoretically studied in chapter 4. First the fabrication of the diffraction grating is presented in detail and the diffraction efficiency is studied with the use of reflectometry. An optimized method for transferring graphene is then presented and the results are analysed with the use of Raman spectroscopy, SEM (Scanning Electron Microscopy), and HIM (Helium Ion Microscopy) imaging. A method of providing strong modulation of free carrier density in graphene is presented. An Ion gel gate is prepared and studied with the use of a graphene microribbon transistor showing that the ion gel is ideal for chemical potential modulation in graphene. Finally, both a gold back reflector and a transparent spacer on the diffraction grating are introduced in order to achieve strong enhancement of plasmon excitations in graphene, as theoretically predicted in Chapter 4. Using a combination of the previously mentioned process steps, the final device can be fabricated.

3. Literature

3.1. General Background

In this section, fundamentals of plasmonics as well as graphene's band structure, photonic properties, plasmonic properties, and potential applications will be discussed. The goal of this chapter is to introduce the reader to the fundamental concepts of the field as well as to provide a general knowledge of existing techniques, designs, applications, current limitations and future targets set by the scientific community working on graphene plasmonics.

3.1.1. Plasmonics

Plasmonics is a rapidly growing field that has attracted a lot of attention due to the strong potential it demonstrates for overcoming a variety of bottlenecks currently limiting the rate of advancement in nanoscience [72]. As one of the leading fields in the advancement of nanophotonics it presents great promise in achieving commercialization in fields including biosensing, light generation, microscopy, and crucially in providing the missing link for integrating nanoelectronic with photonic devices [72].

Surface plasmons are electromagnetic waves that propagate along the surface of a conductor [1–3]. These waves propagate in the form of collective oscillations of electrons enabling confinement and control of electromagnetic energy at subwavelength scales. Excitation of such waves can be achieved either through photon probing or through high energy electron collisions [13,73]. Surface plasmon waves or SPPs (surface plasmon polaritons) are light waves trapped on the surface of a conductor due to electromagnetic energy being coupled to the movement of free electrons of the material [1]. When light of a certain frequency shines on the surface of the conductor, free electrons begin to oscillate collectively in resonance with the light wave. This interaction gives rise to a lot of unique physical properties.

Surface plasmons have the ability to concentrate light beyond the diffraction limit. This ability originates from the difference in the relative permittivity, ε, of the conductor and the surrounding insulating media [1]. In Figure 3.1.a the surface charge, as well as the electromagnetic wave character, of a surface plasmon wave traveling along a conductor/dielectric interface can be seen. This wave is transverse magnetic (magnetic field, H, in the y direction). Generation of charge on the surface of the conductor requires an electric field normal to it [1]. The nature of this electromagnetic wave results in the field component perpendicular to the surface to be maximum near the surface and exponentially decaying away from it (Figure 3.1.b). This Electromagnetic field is evanescent (a near field wave whose intensity exponentially decays independently of absorption as a function of distance from the formation boundary of the wave) meaning that it is non-radiative and thus the surface plasmon waves are bound to the surface of the conductor. The decay length, δ_d, of the field in the dielectric medium is of the order of half the wavelength of the incident light, while the decay length in the conductor, δ_m ,depends on the skin depth of the material [1].

Figure 3.1.c presents the dispersion curve of a surface plasmon mode. In order to couple light to surface plasmon modes, the wave vector mismatch between them has to be overcome. As seen in Figure 3.1.c, the surface plasmon mode line is lower than the light line, meaning that the wave vector ($\hbar k_{sp}$ where k_{sp} the surface plasmon wave vector) is higher than that of a free space photons ($\hbar k_o$ where $k_o=\omega/c$ the free space wave vector) for the same frequency [1].

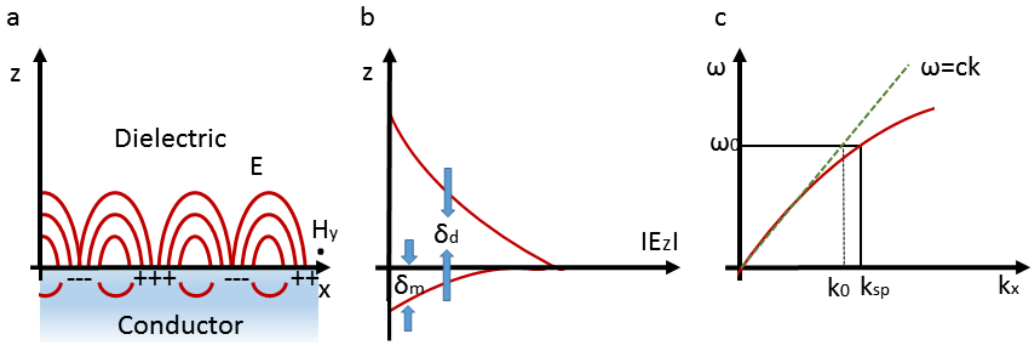

Figure 3.1 a. Surface plasmon wave propagating along a metal-dielectric interface. **b**. Evanescent field in the perpendicular direction, the power does not propagate far away from the surface. δ_m and δ_d are skin depth and decay length respectively. **c**. Dispersion curve of a surface plasmon mode – the green line represents the wave-vector of incident light and the red line represents the plasmon wave-vector. (reproduced from reference [1]).

Surface plasmon dispersion relation can be derived by solving Maxwell's equations with the appropriate boundary conditions, giving the frequency depended surface plasmon wave vector k_{sp} as

$$k_{sp} = k_o \sqrt{\frac{\varepsilon_d \varepsilon_m}{\varepsilon_d + \varepsilon_m}} \quad , (3\text{-}1)\ [1].$$

In order for surface plasmons to propagate in the conductor/dielectric interface, the permittivity of the conducting surface, ε_m, and the dielectric medium, ε_d, must have opposite signs (translating to a large plasmon wave vector). The wave-vector mismatch between incident light and the plasmon modes has to be overcome in order to induce surface plasmon waves on the conductor/dielectric interface [1]. This can be achieved with several methods. Typically a prism setup can be used to shift the wave-vector of incident light. Diffraction gratings can also be utilized, creating the appropriate phase relations for diffracted incident photons to couple with plasmons. Another method is introducing topological defects on the conductor's surface to generate localized surface plasmons. Periodic corrugations on the conductor's surface can also assist in the formation of plasmon waves.

Once excited, plasmon waves begin traveling along the conductor/dielectric interface and experiencing losses that depend on the absorption occurring in the conducting material [1], as well as on defects of the surface or due to unwanted radiative modes. Loses in the conductor are described by the dielectric function at the oscillation frequency of the surface plasmon waves [1]. From the dispersion equation, the propagation length, δ_{sp}, can be found. This can be achieved by solving the equation for the imaginary part of the complex wave vector $k_{sp}\left(k_{sp} = k_{sp}^{'} + ik_{sp}^{''}\right)$ giving

$$\delta_{sp} = \frac{1}{2k_{sp}^{"}} = \frac{c}{\omega}\left(\frac{\varepsilon_m^{'} + \varepsilon_d}{\varepsilon_m^{'}\varepsilon_d}\right)^{\frac{3}{2}} \frac{\left(\varepsilon_m^{'}\right)^2}{\varepsilon_m^{"}}, \quad (3\text{-}2)$$

where $\varepsilon_m^{'}$ and $\varepsilon_m^{"}$ are the real and imaginary parts of the conductors dielectric function $\left(\varepsilon_m = \varepsilon_m^{'} + i\varepsilon_m^{"}\right)$. Introducing periodic structures like hole arrays, apertures or nanoparticle formations (usually with a period half of the effective wavelength of the surface plasmon mode) on the conductor's surface can severely change the way surface plasmons waves propagate through it[1].

Plasmonics is a very promising field with new exciting physics that can lead and have already led to many novel applications. One of the biggest market areas for plasmonics is sensing and especially biosensing. The current 'gold standard' for label-free biosensing is SPR (Surface Plasmon Resonance) biosensors [74]. Several sensors based on localized surface plasmon resonance have been developed. This includes devices that can be used for measuring molecular concentrations, binding kinetics, dye absorbance spectra and conformational changes [2]. Surface Enhanced Raman spectroscopy can be used for biosensing and a current focus is upon its improvement to detect single molecules [2]. Other highly promising applications include plasmon nano-guiding (Figure 3.2), plasmon nano-focusing (concentrating light in a few nanometres regions), nanophotonic circuits (plasmon couplers, filters, nano-antennas), active components, and non-linear optics (modulation, amplification, generation and detection) [3,75]. Finally, plasmonic devices are highly promising for photovoltaic applications, catalytic applications, thermal management applications, and creation of metamaterials [76].

On the other hand, plasmonics implementing conventional metal conductors like gold or silver suffer from several significant limitations. The most important limitations of such conventional plasmonic conductors are the high amount of Ohmic losses [77] and the lack of active tuning in terms of plasmon frequency or absorption intensity [15,78].

Graphene is a promising candidate for overcoming these limitations. Plasmons in graphene have very large wave-vectors and can provide very efficient confinement of light [15,78]. At the same time, given that the quality of graphene is high, surface plasmon lifetimes of hundreds of optical cycles can be supported due to the very high mobility of carriers in graphene [15,78]. Furthermore, electronic and optical properties of graphene can be actively tuned by physical and chemical methods, also allowing electrostatic control of the plasmon properties [15,78]. Thus, graphene emerges as a promising alternative for further innovations in the field of plasmonics. More information about graphene plasmonics can be found in section 3.1.6.

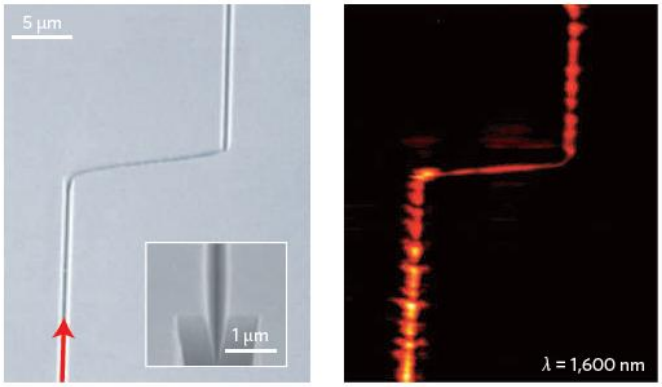

Figure 3.2 A V-groove shaped subwavelength waveguide plasmonic structure with a sharp bend (Reprinted by permission from Macmillan Publishers Ltd: Nature photonics ([75]), copyright (2010).

3.1.2. Diffraction and Wood-Rayleigh Anomalies

It was first observed by Wood in 1902 that there is a significant reduction of light reflected (or transmitted) by a diffraction grating for a range of wavelengths not greater than the pitch of the grating structure. This was observed as sharp drops in the measured reflection (or transmission) spectra with significant dependence on the angle of incidence of the light shining on the grating surface [79]. This effect was only found to occur when the electric field of the incident electromagnetic wave was perpendicular to the grating periodicity [79,80].

Rayleigh was first to propose a theoretical explanation for the existence of these anomalies [81]. The proposed explanation suggested that the observed anomalies occur for a specific wavelength when the diffracted wave propagates tangentially to the grating surface. Through this assumption, the grating equation, giving the diffraction angle of light interacting with a grating structure, was derived as

$$\sin(\theta_n) = \sin(\theta) + n_{or}\lambda/\alpha \text{ , (3-3)}$$

where θ the incidence angle measured from the normal of the grating, θ_n the angle of diffraction, λ the wavelength of the incident light, α the grating pitch, and n_{or} the diffraction order. When the light is diffracted at a 90° angle and is propagating in parallel to the grating structure $\sin(\theta_n) = \pm 1$, and thus the equation describing the wavelength and incidence angle dependence of the Wood-Rayleigh anomalies can be derived as

$$n_{or}\lambda/\alpha = -\sin(\theta) \pm 1, \text{ (3-4).}$$

Figure 3.3.a demonstrates a schematic of a diffraction grating and Figure 3.3.b shows the solutions of equation (3-4) for α=1500nm, α =1250nm, and α =1000nm (Matlab code in appendix 12.1.3). The plotted lines correspond to angular dispersion of the Wood-Rayleigh anomalies for a one dimensional grating structure. Understanding of the origin of such features is important as they appear in measurements later in the thesis.

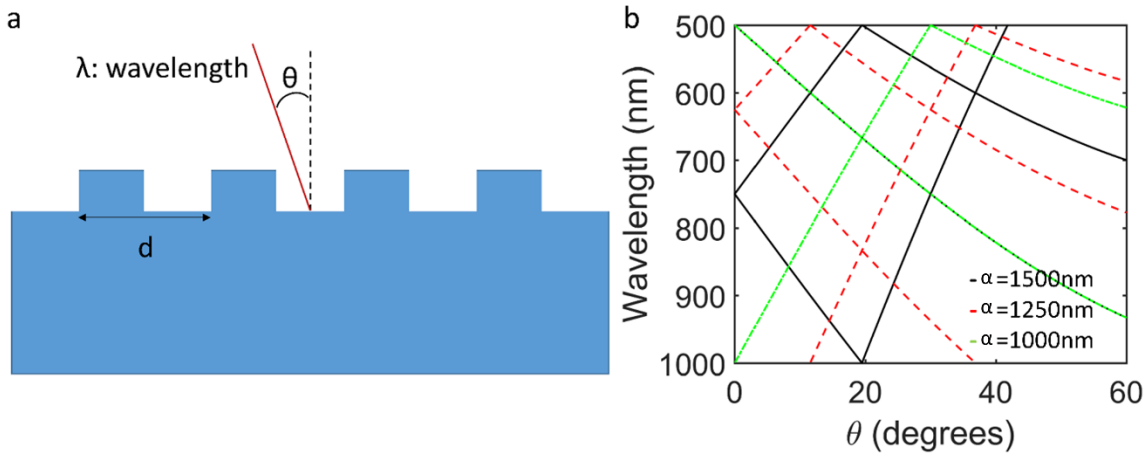

Figure 3.3 a. Schematic of diffraction grating **b.** Solution of equation (3-4) for α =1500nm, α =1250nm, and α =1000nm

3.1.3. Band Structure of Graphene

Graphene is an atomically thick layer of carbon atoms arranged in a honeycomb lattice formed by sp^2 hybridised orbitals [11]. For controlling and manipulating the properties of graphene, familiarity with its atomic and energy structure is necessary. It is important thus to describe how the energy band structure of graphene forms and why it is relevant to plasmonic applications.

In graphene, the p_z orbitals of neighbouring carbon atoms in the lattice overlap, forming bonding and antibonding states and the corresponding π-bands [11,12]. Bonding π-states form the valence band, while antibonding π* states form the conduction band [12]. These states are orthogonal and they cross each other forming the valance and conduction bands which touch at six points known as the Dirac points (Figure 3.4.a)[11,12]. The unit cell of graphene contains two carbon atoms and the lattice can be viewed as two separate sub-lattices (A and B) that are formed by those atoms (Figure 3.4.b)[12]. Because of the symmetry between the A and B sub-lattices the conduction and valence band are degenerate at the K and K' points, and as a result, the electronic bands have a linear dispersion [11]. For small energies (bellow ~1 eV – 1.5 eV) the band structure can be considered as two symmetric cones with the conduction and valence bands touching at the Dirac point [12]. Electrons located near the two inequivalent valleys in graphene have a linear relation between energy and momentum resulting in effectively massless Fermion behaviour [14]. The energy dispersion in this region can be written as $E_D = \pm v_f \hbar |k|$ where ħ the reduced Plank constant, $v_f = 10^6 \mathrm{m/s}$ is the Fermi electron group velocity in graphene (also known as Fermi velocity) k the 2D wave vector measured from the Dirac point, with the positive sign on the left of the equation corresponding to the conduction band and the minus sign to the valence band [82].

When moving away from the two K and K' points there is a saddle-point singularity in the electron bands (M point) [11]. There, electrons moving along the M-K points direction have negative band effective masses, while the electrons moving along the M-Γ direction possess positive effective masses [11]. The band gap at the Γ point is equal to 20eV [11]. The region of the band structure of particular interest for plasmonic applications can be fully described by the aforementioned cone

approximation of the band structure since low energy approximation is enough to accurately describe the behaviour of graphene almost up to the visible range of the electromagnetic spectrum. A very important characteristic of this band structure is that under zero doping conditions the chemical potential lies along the Dirac point and thus there are only few available free electrons. Any change in position of the chemical potential, μ, can have drastic consequences in the free carrier density of the system. The key reason why graphene is so heavily studied as a promising plasmonic material is the ability to dynamically change its carrier density and thus the frequency of plasmon oscillations, something long desired in the field and a significant limitation of conventional (noble metal) plasmonic materials.

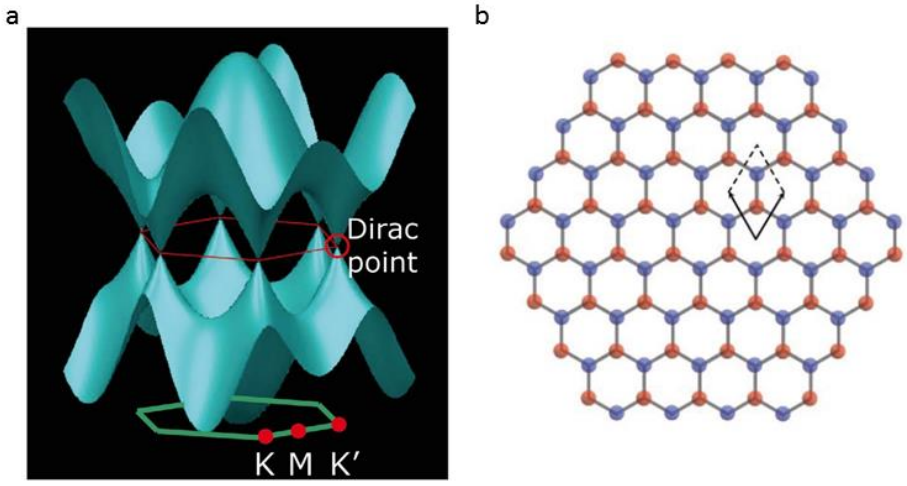

Figure 3.4 a. Band structure and Brillouin zone of graphene, for lower energies around the Dirac point a cone approximation can be used **b**. Graphene can be described as two sub-lattices A and B (shown in red and blue), and the unit cell is shown consisting of one atom from each sub-lattice. (with permission from reference [12] under a Creative Commons license).

3.1.4. Graphene Photonics

Before moving to a discussion of purely plasmonic properties of graphene a general understanding of the fundamental photonic properties of the material is necessary. Graphene has been proven to have high quantum efficiency for light-matter interactions and a strong nonlinear response in the THz regime [13,83]. Because of the peculiar electronic structure of graphene some unique optical characteristics occur.

One of the most important consequences of graphene's electronic structure in its optical properties is that its optical conductivity is independent of any material parameters. As a result, its optical conductivity can be described by a universal conductivity $\sigma_0 = \pi e^2 / 2h$ where h the Planck constant [13]. The transmittance, T_r, of graphene in vacuum is given by

$$T_r = \left(1 + \sigma_0 / 2c\varepsilon_0\right)^{-2}, \text{ (3-5)}$$

where ε_0 the permittivity of vacuum. Thus, $T_r = \left(1+e^2/8\hbar c\varepsilon_0\right)^{-2} = \left(1+\pi\alpha_g/2\right)^{-2} \approx 1-\pi\alpha_g$, where $\alpha_g = e^2/4\pi\varepsilon_0\hbar c$ is the fine structure constant [82]. This means that the optical absorption in graphene (which is remarkably high for an atomic monolayer, $\pi\alpha_g \approx 2.3\%$ depends only on its fine structure constant $\alpha_g = e^2/\hbar c \approx 1/137$ [9,11–15] (more information in appendix section 12.1). Naturally, increasing the number of layers of graphene results in a steady increase in absorption [14]. For energies approaching the upper limit of the visible spectrum there is a steady increase in absorption with a peak located at 4.6eV (Figure 3.5) [11,12]. The origin of this peak is due to trigonal warping effects. For higher energies, the cone approximation is no longer sufficient for describing the optical properties of graphene due to the exponential broadening of the band structure. More specifically, the M points of graphene's Brillouin zone lead to van Hove-like singularities (non-smooth point in the density of states of the crystal) (Figure 3.4.a) [13]. At this energy range is where π-π* interband transitions at the saddle point singularity near the M point are expected [12], causing the strong absorption peak observed in Figure 3.5. In theory this peak should be located at approximately 5.2eV but, because of many-body (excitonic) effects, the peak is observed at a lower energy [11–13].

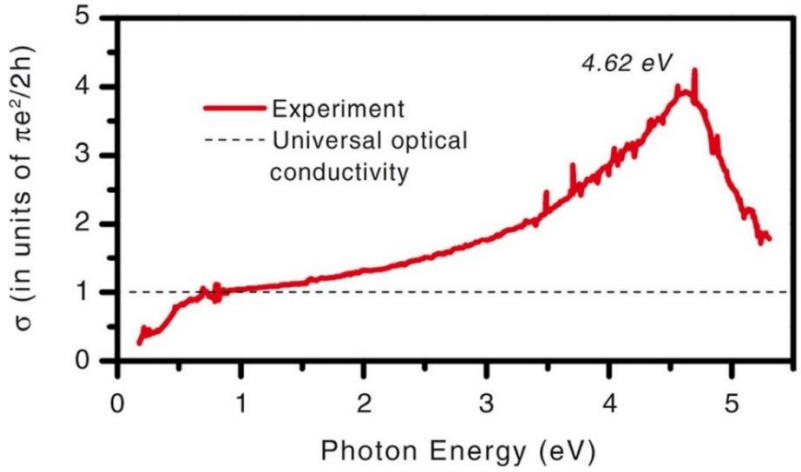

Figure 3.5 Solid line shows the optical conductivity of a graphene monolayer (experimental) in the spectral range of 0.2 - 5.5 eV (the dashed line is the universal optical conductivity of the monolayer). The energy peak in the experiment was found to be 4.62eV. (with permission from reference [12] under a Creative Commons license).

The absorption mechanism in the visible and near infrared spectrum, under zero doping conditions, is due to interband transitions between the valence and conduction bands [11]. In the far-infrared and terahertz regions the free carrier absorption (intraband) becomes the dominant contributing mechanism [11] and the frequency dependence of the carrier response can be described by Drude model with a dynamic conductivity of $\sigma(\omega) = iD/\left[\pi\left(\omega+i\Gamma\right)\right]$ where *D* is the Drude weight and Γ is the carrier scattering rate [12].

The optical behaviour of graphene has been extensively investigated using experimental methods such as absorption spectroscopy [84], optical reflectivity [85–87], surface plasmon resonance angle detection [87], and spectroscopic ellipsometry [88–93] to measure the optical conductivity or refractive index of the material. Theoretical as well as experimental studies have shown that optical conductiv-

ity of graphene changes significantly by application of gate voltage due to the shift in chemical potential [82,94–98]. Additionally, Pauli blocking (blocking of electron interband transitions due to already occupied states) in graphene does not allow photons with energy less than twice its chemical potential to be absorbed [13].

By introducing doping to the system, either chemically or electrostatically, and taking advantage of Pauli blocking, the interband transitions can be effectively shut down and the intraband contribution can become dominant for shorter wavelengths approaching the visible spectrum. Thus, by doping graphene, or by inducing electrical gating, the optical properties of the material can be dynamically controlled [15]. The complex refractive index of graphene can be well predicted by theoretical models based on the Kubo formula as a function of gate voltage [86]. Figure 3.6 presents the complex refractive index of graphene as reported by several different groups for both exfoliated and CVD (Chemical Vapour Deposition) graphene.

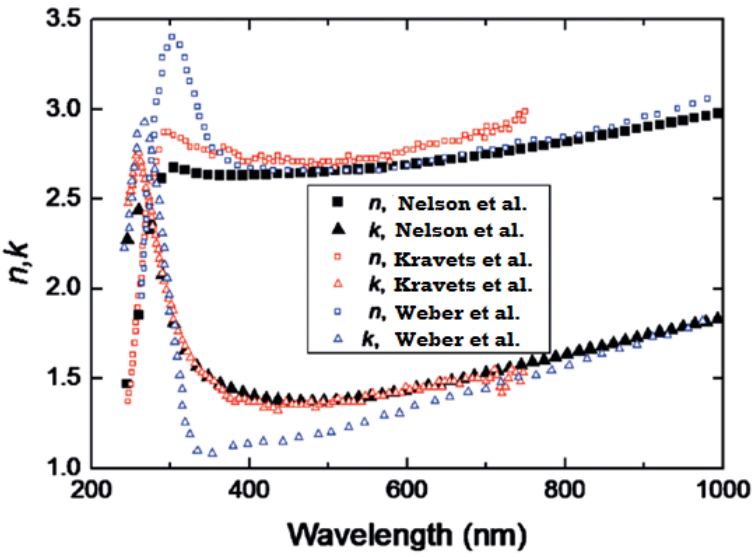

Figure 3.6 Comparison of the real (n) and imaginary (k) parts of the refractive index values of graphene as obtained from different groups. The values of Nelson et al. Group were obtained from CVD graphene while the other two were obtained from exfoliated graphene [99–101].

Luminescence in graphene can be induced. Non-equilibrium carriers in graphene can result in hot photoluminescence with a wide spectral range [11,14]. Graphene can also be made luminescent by introducing a bandgap [102]. This can be achieved by chemical and physical treatments (doping, graphene oxide) or by altering the geometry of the layer (nanoribbons and quantum dots) to reduce the available routes for the π-electrons[14]. Finally, if an electromagnetic field gradient is present, photoexcitation of graphene produces a photocurrent allowing for photovoltaic applications [12]. Given the great variety and quality of optical characteristics, graphene can play a fundamental role in the field of photonics, with significant opportunities for commercialization as will be discussed in the next section.

3.1.5. Photonic Devices Based on Graphene

In this section a short review of currently available graphene-based devices in literature is made. Optical properties of graphene make it a suitable candidate for a variety of photonic devices. A

popular device concept are graphene photodetectors [19–22]. Graphene, has a very broad absorption range covering the Terahertz and infrared regions of the spectrum which are typically unexplored regions for commercial devices to-date. Devices have demonstrated wide spectral range of operation from ultraviolet to the infrared and additionally very high operating bandwidth (>500GHz per wavelength) [9,19].

Graphene has also been studied as a material for lasing applications, most commonly used as a saturable absorber. Wide spectral range mode-locked lasers have been realized, taking advantage of the saturable absorption in graphene (caused due to Pauli blocking after intense illumination) and can be used to mode-lock fibre lasers [16,18] or semiconductor lasers [9]. Terahertz generators have also been investigated, demonstrating several advantages over semiconductor lasers achieving terahertz spectral range operation at room temperature [17]. Compact terahertz lasers and amplifiers of only a few microns size, based on graphene, have been proposed [30]. Population inversion in graphene has been achieved experimentally both via optical and electrical pumping [30]. Stimulated emission in the near-infrared and terahertz frequencies has been experimentally observed for such devices [17,103–107]. Nevertheless, graphene based lasers currently exhibit a much lower intensity than III-V semiconductor devices and further research is required if they are to become competitive [9].

Photodetectors based on graphene/Si junctions have been experimentally studied, presenting excellent detection of weak signals with a photovoltage responsivity exceeding 10^7 V/W and with a noise-equivalent power reaching ~1 pW/Hz$^{1/2}$ with a linear response of over six decades of incident power in the photocurrent mode and with a tuneable responsivity of up to 435mA/W [108]. The time response of the reported device is in the order of milliseconds with ON/OFF ratios exceeding 10^4 thus allowing the fabrication of highly scalable and tuneable photodetectors.

Optical modulation is another promising field for commercializing graphene-based devices. Graphene provides excellent optical modulation efficiency by exploiting its ability to absorb small amounts of incident light over an extremely large spectral range while providing ultrafast response [9]. Graphene optical modulators providing compact footprint, low operation voltages, ultrafast modulation, and large optical bandwidth at a device volume amongst the smallest to-date have been reported [25].

Optical polarization controllers can also be created using graphene[26]. It has been demonstrated that broadband polarizing effect in graphene can provide an all-in one solution for ultra-broadband modulation at a lower cost than metal-clad polarizers while having the advantage of being easily and dynamically tuneable [26]. Compact hybrid isolators can also be constructed by combining graphene faraday rotators with graphene based polarizers [9]. The efficiency of such structures could be further improved by introducing multilayer stacks of graphene.

Hybrid graphene-Si optical cavities for chip-scale optoelectronics have been reported opening the way for commercialization of graphene devices in the field of on-chip photonics [27]. Those devices demonstrate third order nonlinear optical responses ranging from resonant optical bistability for optical signal processing at femtojoule-level switching per bit, to temporal regenerative oscillations at record femtojoule levels for optically driven and controlled reference oscillators. Four-wave mixing at femtojoule energies on the chip has also been reported [27].

Efforts have also been made to use graphene as a current generating, or distributed electrode material in solar cells [9,28]. Finally, transparent flexible conductive electrodes or coatings, with applications in touch screen displays, roll-able e-paper Organic Light Emitting Diodes (OLED) and several other optoelectronic products which are taking advantage of graphene's electrical, optical and mechanical properties have been investigated [9].

3.1.6. Graphene Plasmonics

As mentioned in chapter 3.1.1, plasmons are high frequency collective oscillations of electrons that enable confinement and control of electromagnetic energy at subwavelength scales and can be excited from incident photons or electron collisions [13,73]. Noble metals have been long regarded as the best materials for plasmonic devices. Nevertheless, noble metals have large Ohmic losses translating to poor propagating distances for plasmon oscillations. Crucially, conventional plasmonic materials are hardly tuneable in terms of frequency or absorption intensity operation [15,78].

Graphene, as a material whose effectively massless carriers exhibit large propagation distances without scattering and whose electronic and optical properties can be easily tuned by physical and chemical treatments, or even by controlling them with an electrostatic gate, emerges as a promising alternative for further innovations in the field of plasmonics. Providing efficient tuning and control of the plasmon absorption, extreme confinement of light (in the order of 10^6 smaller than the diffraction limit for doped graphene) and surface plasmon lifetimes of hundreds of optical cycles, graphene could revolutionize the field of plasmonics [15,78]. Plasmons in graphene demonstrate different behaviours not only from noble metals, but also from their counterparts in conventional 2DEG (2-Dimentional Electron Gas) systems [11]. In dot structures of doped graphene there is an increased degree of electromagnetic field enhancement and interaction strength with reduced dimensionality leading to decay rates exceeding the natural decay rate by six orders of magnitude [78]. Graphene opens up the way for quantum plasmonics and could also assist in fundamentally new types of plasmonic interactions [78]. Nevertheless, there are multiple challenges both in terms of fabrication as well as in exciting plasmons and avoiding losses over a large spectral range of operation. Devices heavily depend on the quality of the graphene layer and also on the interaction of graphene with the surrounding environment, resulting in big limitations in operation, especially when moving to shorter wavelengths. Currently there is a necessary trade-off between the range of frequency tuning and losses in graphene.

Pristine graphene, or graphene with a very low Fermi energy level, has a negative imaginary part for its dynamic conductivity over a large frequency range. This means that graphene, in theory, could be capable of guiding transverse-electric electromagnetic SPP surface waves (Figure 3.7.a) [15]. For graphene with a large chemical potential ($|\mu| > \hbar\omega/2$) the imaginary part of the conductivity will be positive and thus graphene will act as a thin metal film that can support transverse-magnetic electromagnetic SPP surface waves (Figure 3.7.b) [15].

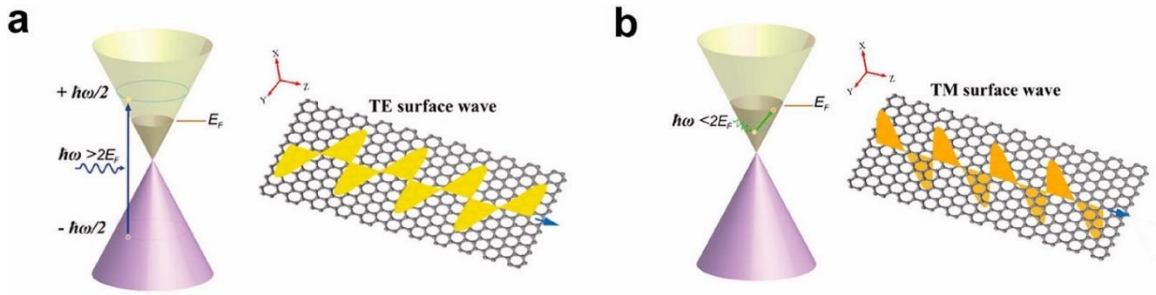

Figure 3.7 a. TE (Transverse electric) wave propagating in graphene. **b**. TM (Transverse magnetic) wave propagating in graphene with high chemical potential. Reprinted (adapted) with permission from (reference [15]). Copyright (2012) American Chemical Society.

In practice direct absorption of light by plasmon excitations on an undoped graphene film is not possible (although interesting collective modes have been predicted for undoped bulk graphene [13,109]) due to interband interactions governing the optical response of the material. This issue can be overcome by increasing the chemical potential of graphene, either chemically or through electrostatic gating [78]. This leads to Pauli blocking disallowing interband transitions for certain photon energies (bellow twice the chemical potential of graphene) and also introduces more free carriers in the system resulting in a more metallic behaviour.

In order to excite plasmons a phase matching method is further required to match the wave-vector of incident photons with that of the plasmons in graphene. This can be achieved by introducing a grating geometry on the substrate bellow or the layer above the graphene [37,38]. Graphene, being extremely sensitive to the surrounding environment can allow control over the plasmon frequency simply by altering the geometry or material of surrounding structures. Varying the periodicity of the grating [37,38] as well as designing the thickness and topology of a dielectric cladding on graphene [110], and altering the permittivity of the substrate, can all result in different responses from plasmon excitations [111].

Graphene plasmons also strongly interact with polarisable insulator substrates like commonly used SiO_2 wafers. Those substrates have surface polar phonons that generate fluctuating electric fields extending above the substrate surface and coupling with plasmons in graphene [112]. These hybrid plasmon/phonon modes have longer lifetimes than those of pure plasmons because of longer phonon lifetimes that are typically ranging in the picosecond range [112–114].

Coupling can also be achieved by taking advantage of scattering from nearby plasmonic structures like nanoantennas [48,49], bowties [115], and nanorods [50] above or below the graphene monolayer. Alternatively, exciting plasmons and achieving control over the plasmon frequency in graphene can be achieved by altering the geometry of the graphene layer itself. In this case excited plasmons are localized in nature instead of propagating. This can be achieved by fabricating graphene structures like nanoribbons [33,113], nanodisks [41,42,116], and rings [116,117] and adjusting their size, doping as well as in-between spacing [113]. In the following chapter a more detailed discussion is made regarding the physics of plasmon oscillations and how excitation of plasmons and electrostatic tuning can be achieved in graphene.

3.1.7. Excitation and Tuning of Graphene Plasmons

Graphene, unlike metals whose plasmon resonance frequency mostly depends on the geometry of the structure, offers the capability of plasmon tuneability, both in terms of wavelength and amplitude of absorption, through altering its free carrier density [112]. It is possible to electrostatically tune plasmon oscillations in graphene both by applying an electric field through a gate contact [33,112,118–120] or through a driving direct current (DC) electric field (applied through source/drain contacts) [116]. Applying stronger electric fields has been suggested to allow binary on/off switching of plasmon excitations [73].

The basic concept behind plasmon oscillations is that when electrons are screened by an electromagnetic field they travel a certain distance away from the lowest energy position. As a result, they are pulled back towards the charge disturbance, overshooting again and creating a damped oscillation with a restoring force proportional to the gradient of the electric field generated by the electrons [13]. When doping of the graphene layer is sufficiently high $(|\mu| > \hbar\omega/2)$ TM surface plasmons can be sustained propagating with a wave vector $k_{sp} \approx i(\varepsilon_d + 1)\omega / 4\pi\sigma$, where σ the conductivity of graphene, and an electric profile $\mathrm{E}_z \sim \exp\left[k_{sp}\left(ix - |z|\right)\right]$ [78]. These electrostatic expressions which are valid for $\hbar\omega << \mu$ reduce to the following form with the insertion of Drude formula showing a quadratic dependence of k_{sp} on ω [78].

$$k_{sp} \approx \left(\frac{\hbar^2\omega}{4e^2\mu}\right)(\varepsilon_d + 1)\omega(\omega + i\Gamma), \text{ (3-6)}$$

Plasmon frequency in doped graphene bellow the interband transition threshold is given by

$$\omega_{pl}(q) = \sqrt{\frac{8\mu\sigma_0 q}{\hbar\varepsilon_d}}, \text{ (3-7)}$$

where μ is the chemical potential, σ_0 the universal conductivity, q the plasmon momentum and ε_d the dielectric constant of the substrate [13].

The in-plane plasmon propagation distance in graphene can be larger than 100 plasmon wavelengths [78]. At higher frequencies this distance drops rapidly because of the generation of electron-hole pairs and the resulting interband transitions [13,78]. Since the chemical potential of graphene is proportional to the square root of its charge carrier density $\mu \propto n_c^{1/2}$ the plasmon frequency is also proportional to the charge density as follows $\omega_{pl} \propto n_c^{1/4}$, where the charge carrier density n_c is given by

$$n_c = \frac{V_g \varepsilon_0 \varepsilon_d}{ed}, \text{ (3-8)}$$

where V_g the applied gate voltage through an external electrode, separated from graphene by an insulator, *e* is the electron charge, *d* the substrate thickness, ε_0 the permittivity of air and ε_d the

relative permittivity of the substrate [8,120]. As a result, graphene allows the modification of the chemical potential and corresponding carrier density by electrostatic gating. The optical conductivity (and thus the permittivity and refractive index) of a material heavily depends on the carrier density of the system hence the plasmonic properties of graphene can be directly and dynamically controlled through the application of gate voltage [119].

There are several methods already available in the literature that allow for excitation and tuning of plasmons in graphene [36]. Silicon diffraction gratings below the graphene layer can serve the role of a wave vector matching component in order to excite plasmonic waves in the system [37,38]. By altering grating period the device can operate in different resonant frequencies due to the formation of different phase relations of the diffracted electromagnetic waves. When the periodicity of the grating becomes denser, the resonant frequency blue shifts. Electrostatic tuning of the plasmon frequency in such devices can be achieved by using the grating as a backgate (gate electrode connected to the back side of the device) electrode capable of altering the chemical potential in graphene [37,38].

Excitation and dynamic control of plasmons has been achieved through several types of hybrid graphene/metal structures, typically metamaterials [46,47], nanoantennas [48,49], nanorods [50], and bowties [51]. Hybrid graphene-gold nanorod configurations have accomplished efficient control of plasmon resonances ranging in the near infrared spectrum [50]. Modulation of both the resonance frequency and quality factor of localized plasmons excited in a gold nanorod has been achieved through electrostatic gating of graphene. Even a single extra electron in graphene at the plasmonic hotspot (location where the near field is strong) has been reported to have an observable effect on the plasmon scattering intensity [50]. A similar device consisting of an array of gold bowtie antennas fabricated on top of a large continuous graphene monolayer has been reported [51]. This device provides dynamic control over plasmon frequency in Au structures at mid-infrared spectral range [51]. Similarly a device where graphene is used as an electrically tuneable load between the nanoscale gap of two (or an array of) metallic nanoantenas has been shown to provide efficient frequency control over a wavelength range of 650nm in the mid infrared region, with an increased tuning range when coupling multiple antennas end to end [48].

Designing sub-wavelength sized patterns of graphene can also enable excitation and dynamic control of plasmons in the material. Literature reports of such devices include graphene patterned into ribbon [33,38–40], disk [41–44,121], and ring structures [43–45]. Micro-ribbon arrays are the simplest form of micro- and nano- scale metamaterials. Plasmon excitations in these structures correspond to collective localized oscillations of electrons across the width of the ribbon [33]. The frequency of these excitations can be controlled by altering the micro-ribbon width [33,38] or array periodicity [38].

Graphene nanodisks operate under a similar principle as graphene nanoribbons with the advantage that excitation of plasmons is independent of incident light polarization due to the symmetry of the structure [42]. Altering dimensions of the disks results in a shift of the plasmon frequency [121]. Furthermore, control over the resonance frequency can be achieved by altering the distance between adjacent disks [41]. Stacking graphene/insulator disks has been reported to increase plasmon absorption since multilayer stacks add up to single layer absorption [41,116]. In this kind of stacked device the resonance frequency upshifts with an increasing number of graphene layers, due to coupled plasmon modes that form between adjacent layers [42].

Ring structures follow the same principle of operation as disk structures. In more detail, plasmons in such structures can be treated as plasmon hybridization (coupling between plasmons generated in a disk and a hole structure) from a graphene disk and a smaller anti-dot (hole) [116,121]. The interaction of dipole resonances occurring from the hybrid structure take the form of a symmetric (bonding) and an anti-symmetric (anti-bonding) mode. The symmetric mode has an in-phase dipole oscillation and lower resonance energy while the anti-symmetric mode has an out-of-phase dipole oscillation and higher resonance energy. Non-concentric graphene structures give rise to further multipolar plasmon modes [117]. Finally, ring structures can be electrostatically tuned in a similar way as disk structures. In general, interactions of complex graphene structures lead to a shift and a broadening of the plasmon resonance frequency [112].

All of the mentioned methods provide an effective way for coupling light to and tuning plasmons in graphene. Diffraction gratings have the advantage of simpler fabrication and are suitable for coupling light to propagating surface plasmon polaritons. Localized modes can also be excited by allowing graphene to follow the surface morphology of an underlying structure. Investigating different diffraction grating shapes and materials could potentially lead to much stronger coupling of the incident photons in such devices. On the other hand, graphene/metal hybrid structures only enable the excitation of localized plasmon modes. A great advantage of such structures is that even though they are still tuneable through electrostatic control of the chemical potential in graphene, they can operate in the visible spectrum. This is because plasmon oscillations actually occur in the metal structure and not in graphene. On the other hand, the frequency range tuning of such devices is limited. Finally, graphene nanostructures have localized plasmons that are highly tuneable since, in contrast to the metal/graphene hybrid devices, modulation occurs directly in graphene through direct increase or decrease of the free electron population. These types of structures along with diffraction grating based devices could allow dynamic switch off of the plasmon oscillations by reducing the amount of free carriers and also by screening plasmon excitations via allowing interband transitions to occur.

The general disadvantage of all graphene plasmonic devices is the difficulty in terms of fabrication compared to conventional metals, but the promise of enabling highly tuneable devices is a strong driving force for overcoming such issues. The field of graphene plasmonics is currently limited in terms of the frequency tuning range which has been achieved, and also in terms of the very low amount of absorption occurring in the graphene layer. Finding ways to improve coupling efficiency and electrostatic control of plasmon oscillations in graphene is crucial in order to provide real world applications.

3.1.8. Optimising the Plasmon Absorption of Graphene

The text presented in this section is published as part of a Scientific Reports paper [71]. It is a crucial challenge to enhance light absorption in graphene while maintaining strong frequency modulation. A lot of effort has been placed on realizing devices that can achieve total optical absorption in graphene [36]. Perfect graphene absorbers have been proposed based on graphene disks [52], and ribbons [53] positioned a small distance from a metallic ground plate. Additionally, patterned graphene has been used as a light trapping component that can enhance optical absorption in surrounding ab-

sorptive mediums [54]. Attenuation total reflection multilayer structure configurations (prism/graphene/Quartz) [55], and Hetero-structure devices have also been used to significantly enhance light absorption in graphene at optical frequencies [56,57].

Devices implementing a Salisbury screen [58] have been proposed to enhance optical absorption in graphene since they can provide strong field enhancement in the vicinity of the monolayer when carefully optimized. Such devices have effectively been used to enhance interband absorptions in graphene by a factor of 5.5 in the mid-infrared spectral region, also providing a very strong modulation efficiency of 3.3% of absorption change per Volt but provide limited amount of absorption enhancement and wavelength modulation [59]. It has been theoretically predicted that under grazing angle for s polarized incident light such Salisbury screen/graphene setups can provide nearly total optical absorption, also achievable when using multiple stacked graphene films but wavelength tuning remains weak [60]. Absorption due to plasmon excitations in graphene nano-resonators have also been suggested to be enhanced when utilizing Salisbury screen setups, also allowing for absorption tuning by electrostatic gating but the absorption efficiency remains low (24.5%).[61]

Hybrid metal-graphene structures have been studied by several independent groups demonstrating strong optical absorption enhancement. Theoretical studies have shown that ribbon [62] or cross-shaped [63,64] metallic resonators positioned above a graphene layer can, at certain resonant conditions, be used as light trapping components for increasing the interaction of light with graphene, thus achieving total optical absorption. Similarly, cross- and ribbon-shaped metallic resonators combined with double layer graphene wires have been theoretically studied, achieving similar results [65]. Furthermore, metamaterial resonators like split rings [66] and interdigitated structures [67] have been combined with single or multilayer graphene stacks providing high-speed modulation capabilities as well as strong absorption modulation. Theoretical and experimental studies where graphene is used to fill several periodic metallic apertures of subwavelength sizes have also demonstrated very high optical absorption [68,69]. Finally critical coupling with photonic crystal slab guide mode resonances has been predicted to achieve total absorption [70].

Even though a lot of effort has been directed towards achieving total optical absorption in monolayer graphene, combining strong optical absorption with efficient dynamic electrostatic tuning has been proven to be highly challenging. It is thus necessary for further research efforts to be directed into combining these properties in a single device for the realization of highly efficient academic or commercial devices.

3.1.9. Plasmonic Devices Based on Graphene

Several plasmonic devices based on graphene have been reported, taking advantage of graphene's high tuneability, broad operational spectrum, strong confinement of light, high surface-to-volume ratio, and high surface plasmon lifetime. The wavelength region where graphene plasmonic applications have attracted most attention is the terahertz to mid-infrared spectral range which, even though has a strong technological significance, has been relatively unexplored in the past in terms of commercial devices [122]. Graphene plasmonics have been proved to be promising in a wide range of commercial fields including computing, telecommunications, and a range of devices such as Terahertz oscillators [30], nano-transceivers [29,123], lasers [103,124,125], waveguides [23,24], polarizers [126,127118], filters [120,128], modulators [119], plasmonic switches [119,129,130], plasmonic logic gates [131], photodetectors

[108,113,132], absorbers [35,133,134], SERS [135–139] and SPR [32,140–145] sensing platforms. In the following, important classes of plasmonic graphene devices are introduced in more detail:

Graphene lasers and oscillators: Lasers are important part of a broad range of applications in modern society and scientific laboratories. There is interest in improved tuneable terahertz lasers, and graphene proves to be a promising material for this application. It has been theoretically and experimentally observed that excitation of plasmons in population inverted graphene by terahertz photons result in propagating plasmons with very high gain in a wide terahertz range [124]. With the use of heterostructures like graphene microribbon arrays, amplification of plasmons can be achieved providing super-radiant plasmonic lasing in the terahertz frequency range (between 2 and 10 THz) at room temperature while allowing for dynamic voltage tuning of the emitted spectrum [124,103].

Graphene plasmonic photodetectors: Photodetectors are used to quantify electromagnetic energy, and are important in a range of application both in everyday life and in laboratories. Providing wide range and tuneable photodetection is highly desired especially in the terahertz and Infrared frequencies and thus tuneable graphene plasmonic devices are perfect candidates for fulfilling this role. Gate tuneable plasmonic-enhanced photodetection at room temperature at mid infrared frequencies has been achieved with the use of graphene nanoribbons, providing a photo-response enhancement of one order of magnitude at ambient conditions [113]. A strong enhancement of the overall quantum efficiency and spectral selectivity enabling multicolour detection in graphene by coupling it with plasmonic nanostructures has also been reported [146]. In more detail, it was demonstrated that metallic nanostructures in combination with graphene can enhance photocurrent and external quantum efficiency by up to 1500%. Furthermore, by using nanostructures for various resonant frequencies the photo-response was amplified over a range of different wavelengths allowing multicolour detection. Finally, a planar-type graphene-based plasmonic photodetector that includes a waveguide has been demonstrated, creating an all-in-one structure and detecting horizontally incident light (Figure 3.8) [132]. Graphene-based photodetectors hold a strong promise for imaging devices, spectroscopy, switching, and especially all graphene-based photonic integrated circuits.

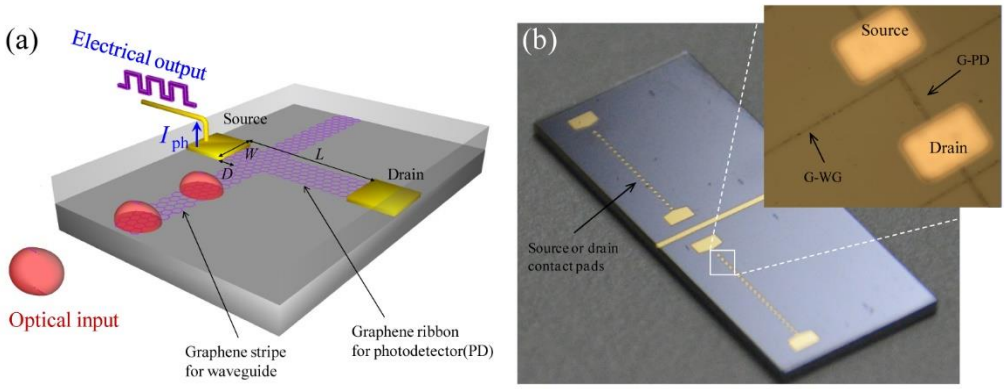

Figure 3.8 a. Schematic of a graphene-based photodetector for horizontal detection of light **b**. Fabricated device incorporating a graphene waveguide and a graphene ribbon for photodetection. (with permission from reference [132] under a Creative Commons license)

Graphene plasmonic filters: Plasmonic filters can cut off unwanted Electromagnetic radiation and provide selectivity over the properties of light that is allowed to pass through. Allowing the fabrication of easily and dynamically tuneable filters is another example where the tuneable optical properties of graphene can be useful. Graphene micro- and nano- ribbons have been used to achieve linear polarization control within the terahertz and mid infrared frequency spectrum, with extinction ratios up to 90% [33,127]. It has been theoretically predicted that with the use of a total reflection structure containing a graphene layer, tuneable polarizers can be achieved [118]. Another way of achieving this is by using two orthogonal periodic arrays of graphene ribbons with different widths supported on a dielectric film which is in turn placed on a thick piece of metal (Figure 3.9) [126] Far infrared notch filers with 8.2dB rejection ratios and with a shielding capability of 97.5% of the incoming terahertz radiation with relative transparency over the rest of the frequency regimes have been demonstrated [42]. In addition, gate tuneable band-pass filters in the terahertz and infrared frequency range have also been theoretically demonstrated [120,128]. Finally, a gate tuneable Bragg reflector formed in a graphene waveguide has been numerically presented [147].

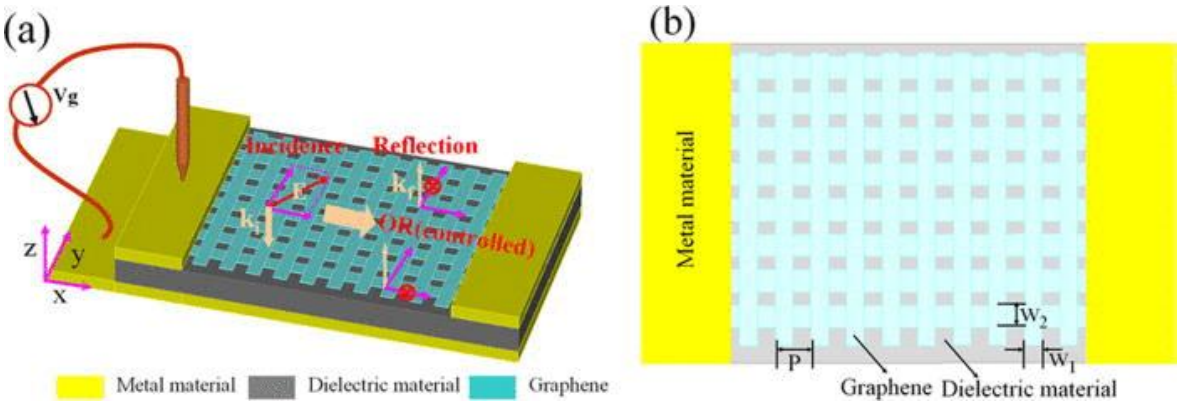

Figure 3.9 **a**. Schematic of polarizer with electrically controllable polarization direction **b**. Top view of the device. Reprinted from[126], with the permission of AIP Publishing.

Graphene plasmonic waveguides: Waveguides are structures which guide electromagnetic radiation with minimal loss of energy, and have broad range applications in the field of telecommunications. Experimental as well as theoretical investigations studying the characteristics of graphene-based plasmonic waveguides for the development of photonic integrated circuits and quantum information systems have been made [23,24]. It has been reported that doped graphene ribbons can allow propagation of plasmons along large distances thus being suitable for fabrication of plasmonic waveguides. The reported waveguides can support high-speed optical data transmission with low extinction rates [24]. Transport of information between neighbouring waveguides is also possible due to the high electromagnetic field intensity near the ribbon edges [23]. These waveguides not only support longer propagation distances compared to conventional plasmonic waveguides (lower Ohmic loses), but the plasmon wavelength, dispersion characteristics and even propagation distance can be controlled by applying an external field [23]. Optical signals of 2.5Gbps have been successfully transmitted via 6mm long graphene plasmonic waveguides with an extinction ratio of 19 dB at a wavelength of 1.31µm [24]. Figure 3.10 presents a graphene ribbon based plasmonic waveguide.

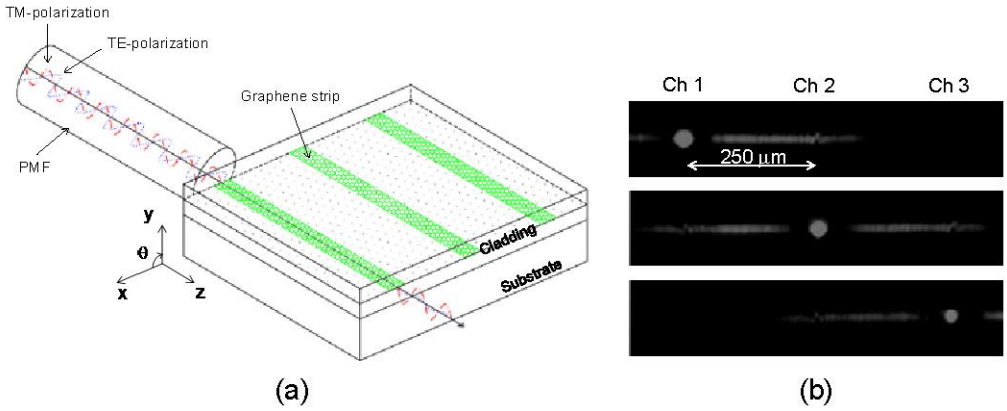

Figure 3.10 a. Schematic of a graphene ribbon based plasmonic waveguide. **b**. Infrared images of the intensity of the guided mode measured at the output of the fabricated graphene plasmonic waveguide. (with permission from reference [24] under a Creative Commons license).

Graphene plasmonic switches, modulators and logic gates: Switches, modulators and logic gates are important in the field of telecommunications. Being able to fabricate such devices in nanoscale dimensions could revolutionize computing by allowing the creation of nanophotonic logic circuits. Graphene plasmonics can potentially provide a solution for achieving such devices since it allows for confinement and manipulation of light in nanoscale dimensions. Novel graphene-incorporating plasmonic switching devices have been reported through theoretical [129,130] and experimental [119] studies. A hybrid metal-insulator-metal waveguide in combination with a graphene ring resonator structure has been theoretically modelled, demonstrating the possibility to achieve switching through the application of a gate voltage on the graphene sheet [129]. The structure achieved a perfect on/off switching effect by applying different bias voltages at different locations of the device. The on/off switching can be observed in Figure 3.11. By integrating graphene with an array of metal atoms and metallic wire gate induced switching and linear modulation of terahertz waves has been experimentally demonstrated [119]. With this method both the amplitude and the phase of the transmitted wave were modulated by a 47% and a 32.2° respectively at room temperature. Furthermore, for the same device hysteresis was observed in the transmission of terahertz waves, indicating persistent photonic memory effects. Finally, electro-optical graphene plasmonic logic gates have been reported, something that could potentially lead to building blocks for nanoscale mid-infrared to THz photonic integrated circuits [131]. Those logic gates were reported to not only achieve ultra-compact lengths of 28 times less than the operating wavelength of 10μm, but also a minimum extinction ratio of 15dB.

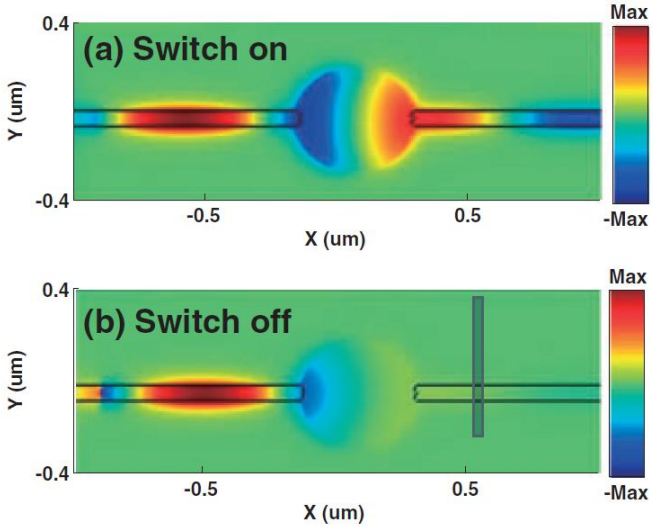

Figure 3.11 Plasmonic switch based on graphene. Surface plasmon polaritons propagating through the graphene ring resonator can be controlled by applying an electric field. **a**. Switch on **b**. Switch off. Reprinted from [129]. Copyright (2014) The Japan Society of Applied Physics

Graphene plasmonic biosensors: Biosensing represents a huge commercial field of plasmonic devices with applications as broad as point-of-care healthcare diagnostics, food safety, and explosives detection. As introduced in Section 3.1.1, SPR biosensors are currently the leading technology in this field. By placing a graphene sheet above a bi-dimensional grating of subwavelength size with holes, drilled in a gold thin film, enhancement over the surface plasmon resonant absorption was observed [144]. An SPR biosensor using silicon and graphene layers coated over the base of a high index prism sputtered with gold has also been presented [141]. The graphene layer increases the amount of molecular adsorption while the addition of the silicon layer between the gold and graphene causes an increase in the sensitivity. It has been numerically demonstrated that by placing a graphene layer on top of silver substrates, high sensitivity can be achieved while prohibiting the oxidation of silver [140]. Using a graphene ribbon array on top of a quartz substrate and taking advantage of graphene's dynamic tuneability can lead to the detection of refractive index changes over a broad spectral range allowing the fabrication of sensors that can be used for sensing both gas and low-refractive index materials in an aqueous environments [142]. Furthermore, a high sensitivity and selectivity sensor able to read molecular vibrations and molecular electrostatic potentials, implementing graphene nanoribbons has been proposed [31]. The operation is based on the extreme sensitivity of plasmons to any moiety approach (causing a big change in the optical signal that passes through the graphene ribbons) [31]. Finally, graphene-based surface plasmon resonance fibre optic sensors have been investigated, based on the principle that the SPR signal changes according to the refractive index of the substance under investigation [32].

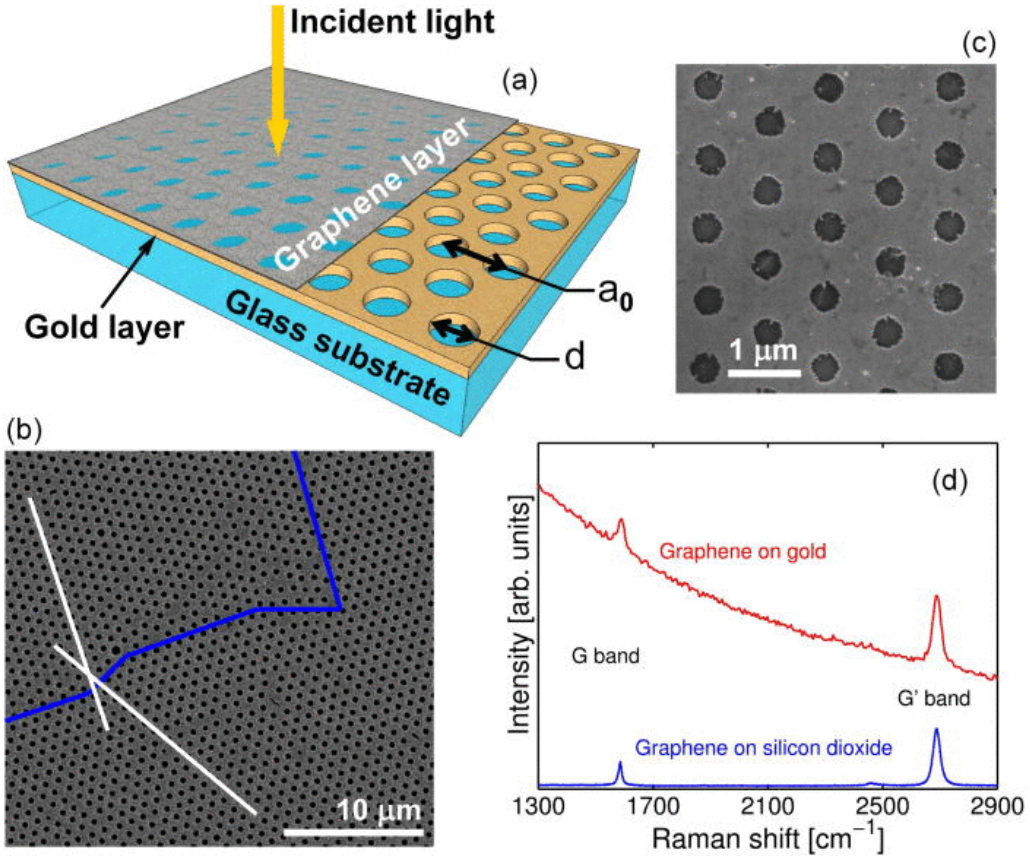

Figure 3.12 a. Schematic of the device **b**. SEM image of the device (the blue line depicts the graphene edge) **c.** SEM image of the hole structures **d.** Transmission through graphene-coated gold and bare gold. The area with graphene presents a wavelength shift enhancement of 33% compared to the area without graphene. Reprinted from [144], with the permission of AIP Publishing.

Graphene has found its way into a wide variety of biosensing schemes [148]. Graphene plasmons occur in the near infrared to far infrared regime and the ability to tune plasmon resonance by modulating carrier density, the possibility of using graphene as a structure for mid-infrared vibrational spectroscopy techniques has arisen [122]. Several efforts have been made towards fabricating SERS (Surface Enhanced Raman Spectroscopy) devices implementing graphene in order to introduce signal enhancement or to avoid photo-induced damage [135–139]. It has been reported that combining gold nanoparticles with few-layers graphene is highly beneficial for SERS detection [139]. Furthermore, by placing a graphene monolayer underneath or on top of Rhodamine 6G molecules, higher stability and reproducibility of SERS is achieved [137]. When graphene is placed above organic molecules it isolates them from ambient oxygen and greatly enhances their photo-stability [137]. Graphene/metal hybrid structures have shown significant advantages over traditional SERS devices including cleaner vibrational information which is free of metal-molecule interactions and reduced photo-induced damage, while still maintaining a good enhancement factor [136]. Combining graphene with conventional metallic SERS substrates can lead to up to three to nine times higher signal enhancement when compared with bare nanohole or nanoparticle structures thus including graphene in existing SERS structures could provide an effective way of improving their sensitivity (Figure 3.13) [136]. Finally, graphene-Au nano-pyramid hybrid structures capable of single molecule detection have been demonstrated. It was observed that the graphene layer can improve detection sensitivity leading to an enhancement factor over 10^{10} for rhodamine 6G and lysozyme molecules [138]. Electrostatically

tuneable SERS and SPR sensors can offer a highly selective and sensitive environment for biosensing and further research is required to provide functional devices with high enhancement values and tuneability.

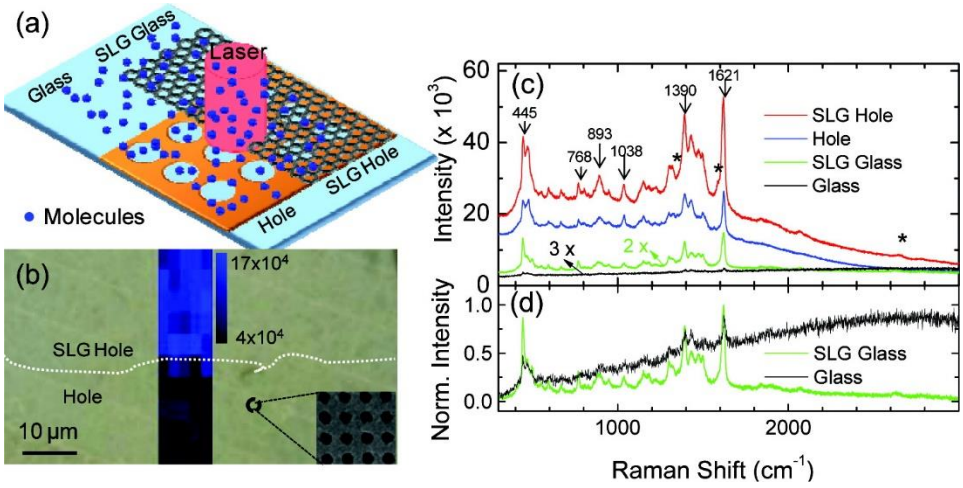

Figure 3.13 **a**. Schematic of a graphene nanohole structure **b**. Raman mapping of 121 cm^{-1} methylene blue peak at the graphene edge on the nanohole array overlaying an optical image of the sample. The dotted lines demonstrate the graphene border. **c**. Raman spectra of methylene blue on four different substrate areas (glass, graphene on glass, Au nanoholes, graphene on Au nanoholes). **d**. Raman spectra for glass and graphene-glass areas. Reprinted (adapted) with permission from ([135]). Copyright (2012) American Chemical Society.)

Other graphene plasmonic devices: Several other graphene based plasmonic devices have been investigated. Graphene based tuneable nano-patch antennas for terahertz radiation have been proposed and studied theoretically [29,123]. These antennas could possibly enable wireless communications at the nanoscale [29,123]. A broadband subwavelength imaging device using a tuneable graphene lens has also been theoretically reported [149] as well as transformation optical devices [34,35]. A good example of transformation optic devices based on graphene plasmonics is the recently reported planar electromagnetic "black hole" [35] as well as other terahertz absorbers based on graphene [133,134] that take advantage of the ability to electrostatically tune losses in the material [35]. Other potential transformation optics applications are beam shifters, invisibility cloaks and lenses [35].

The large amount of plasmonic applications based on graphene demonstrate the importance of the material in the field. This underlines the significance of establishing valid theoretical models, understanding underlying physical mechanisms behind the optical characteristics of graphene, and further investigating different types of structures and devices in order to create novel applications operating from the THz to the visible spectrum. Most of graphene based plasmonic devices operate below the optical frequencies and as such the visible range still offers an interesting and fairly unexplored region for graphene plasmonics. Higher chemical potential in combination with smaller graphene nanostructures or carefully designed diffraction gratings should be investigated in order to shift the plasmon frequency into the visible region. Improving optical coupling to graphene plasmons is also crucial in order to increase the efficiency of the devices.

3.2. Growth and Transfer Process of Graphene

In this chapter a general introduction to methods for obtaining and transferring graphene will be provided. As a newly discovered material this is a crucial and challenging aspect for scientists working with graphene. Understanding of the different growth or transfer methods is of great importance for successfully fabricating devices based on graphene, yet many challenges are still to be overcome.

3.2.1. Graphene Growth

Graphite is a naturally occurring allotrope of carbon which is composed of layers of graphene, and therefore it is not surprising that the first method ever used to produce graphene is based on micromechanical exfoliation of graphite which is able to produce high purity graphene with very good optoelectronic properties and extremely high carrier mobility. This method is still considered as the one that provides the highest quality samples of graphene [7]. On the other hand, this process is not suitable for mass production and thus several approaches have been made to find an appropriate fabrication method that provides mass-producible high-quality graphene [9,14]. These methods include liquid phase and thermal exfoliation of graphite [150,151], CVD [152] and synthesis on SiC [153]. In just a few years, these methods have managed to provide large area controlled growth of graphene, bringing graphene devices closer to mass production.

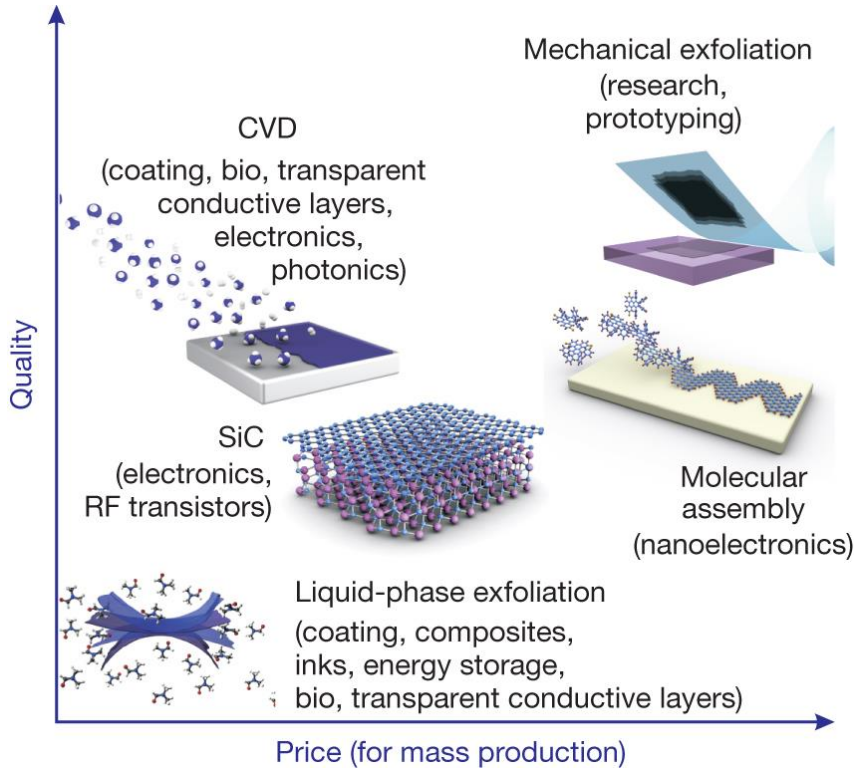

Figure 3.14 Graph showing the Quality versus price factor for different graphene fabrication methods. This graph also states which fabrication method is more suitable for different applications. Reprinted by permission from Macmillan Publishers Ltd: Nature ([9]), copyright (2012).

3.2.2. Chemical Vapour Deposition of Graphene

Amongst the various available fabrication methods, CVD of graphene on transition metal surfaces (especially on copper foils that are used as a catalyst for graphene growth) has gained a lot of attention and is believed to be one of the most suitable candidates for mass-producible graphene electronics and photonics [9,12,154]. The reason for that is that CVD is a cost effective method of producing large area, high quality graphene as shown in Figure 3.14. Additionally, when graphene is grown on a copper substrate the process is self-limiting, stopping at one monolayer [12].

Since CVD on copper has become such an important process for the future of graphene as a commercial product, it is important to describe it in more detail. In general the growth of graphene on copper is straightforward and is a highly efficient method that produces quality large area graphene. Additionally, copper is a fairly inexpensive material that can be etched away with chemicals that are easily attainable even outside of laboratories. Graphene can be grown not just on copper but also on other transition metals like Ru, Ir, Co, Re, Ni, Pt and Pd through simple thermal decomposition of hydrocarbons on their surface or through surface segregation of carbon upon cooling from a metastable carbon-metal solid solution [154]. Parameters like the carbon solubility in the metal, as well as other growth conditions, are crucial for defining the mechanism of the deposition itself. The mechanism is also defined by the number of layers and morphology of graphene. Using the previously mentioned methods, high quality uniform single-layer graphene has been grown over large areas on copper foils with even 30-inches of uniform graphene layers reported [154]. Graphene grown on copper foils is mostly a monolayer with some small areas having two or three layers of graphene (this is usually independent of growth method) [154].

The reason copper (as well as other transition metals) can be used as a catalyst for graphene growth is that it has partially filled orbitals and provides the possibility for formation of intermediate compounds that adsorb to reacting substances [154]. As a catalyst, copper can lower the required energy for reactions to occur, thus assisting the formation of graphene. The advantage of copper for growing graphene over other transition metals is not only cost. Amongst these metals copper has the lowest affinity to carbon and it also has very low carbon solubility [154]. This means that copper can only form weak bonds with graphene through charge transfer from the π electrons in the sp^2 hybridized carbon network with empty 4s states in copper [154]. Combining the ability to form soft bonds with carbon as well as the low affinity to it, makes copper the ideal catalyst material for the growth of any carbon related material.

The most common way of growing graphene on copper is through the decomposition of methane gas over a copper substrate at 1000 °C. Most commonly the substrate used for growing graphene is a 25μm to 50μm thick copper foil but Si wafers with evaporated thin copper films on their surface (typically thicker than 500nm) can also be used. The growth process can be carried out in a low pressure environment typically around 0.5 and 50 Torr or even at atmospheric pressure in a methane and hydrogen atmosphere. [154]

The deposition parameters during graphene growth play only a small role on the quality of the final graphene layer. It is crucial though that the copper substrate has been carefully prepared before the actual deposition. In order to achieve high quality uniform graphene, any native oxide on the

surface of the copper substrate needs to be removed since it can reduce catalytic properties. Annealing the catalytic substrate in a hydrogen reducing atmosphere at 1000 °C can remove any unwanted oxide from the surface. Additionally, due to this process the copper grain boundaries increase in size and the defects on the surface are significantly reduced providing a more suitable area for growing a uniform graphene layer [154]. Since bonds between graphene and the copper catalyst are relatively weak, the graphene flakes can overcome any grain boundaries on the copper surface with none or minimum amount of defects. During the deposition process and after the nucleation, growth, and the final formation of the graphene monolayer, the process stops and no further layers of graphene are formed for even up to 60 minutes. This happens because the catalytic properties of copper can no longer assist graphene growth, thus this process is self-limiting, always stopping at one monolayer. Unfortunately some wrinkles and other defects cannot be avoided since they originate from the difference in thermal expansion of graphene and that of the copper substrate. Ridges and swells can also be formed because of the poor adhesion of graphene with the copper substrate [154]. Table 3-1 presents some typical parameters used to grow graphene on copper substrates as obtained from several literature sources.

The results of the growth process in the literature are in general very good, leading to excellent quality monolayer graphene as evidenced by only few wrinkles and grain boundaries thus providing high quality properties for electronic or photonic applications. The resulting graphene layer retains its high quality during transfer from the copper substrate to an insulating substrate (although any wet process during the transfer could possibly result in doping the graphene layer and cracks could be formed during some of the transfer process steps), which is a performed in order to fabricate practical devices. [154]

There are also methods to directly obtain a graphene monolayer on dielectric surfaces without the need of a transfer process. It has been suggested that evaporating the thin copper film precursor during or immediately after the graphene growth leads to graphene being directly positioned on the dielectric substrate below [155]. This can be achieved by taking advantage of the high temperature during the growth process and the low pressure in the chamber leading to well controlled metal evaporation. This could allow direct growth on many dielectric substrates like single crystal quartz, sapphire, fused silica, and silicon oxide wafers.

Direct growth on germanium has also been reported [156]. This was the first approach to deposit a graphene monolayer directly on a desired non-metal wafer. Germanium is both a semiconductor and a semi-metal and, as a result, has similarities to transition metals allowing CVD graphene to be grown onto it. It has been reported that under optimal conditions a homogeneous monolayer of graphene of superior quality can be produced on a germanium wafer [156]. APCVD (Atmospheric Pressure Chemical Vapour Deposition) was the method that was used to achieve that and it generated high quality large-scale graphene monolayers with a self-limiting mechanism analogous to the one on copper foils. Germanium is a very promising material and will play an important role in the future of high performance MOSFET (metal–oxide–semiconductor field-effect transistor) generations and thus this is a very important milestone for graphene fabrication [157]. Furthermore, this method has been reported to be compatible with modern nanoelectronic technology hence allowing for high volume production and CMOS integration.

Table 3-1: Literature obtained process parameters for growing graphene on copper substrates. Reproduced ("Adapted" or "in part") with permission of The Royal Society of Chemistry from ref [154]

Method	Pressure during growth (Torr)	Pre-annealing	H_2/CH_4 flow ratio (sscm), growth time, cooling rate	Temperature (°C)	Copper thickness	Number of graphene layers
1	0.560	1000°C H_2 (2 sccm, 0.04 Torr) 30min	0.06 (1min-60min, cooling rate 40-300°C/min)	1000	25µm	1
2	11	900°C, 30min, H_2, 10 Torr	0.23 (10-20min, cooling rate 20°C/min+gas flow)	1000	500nm, 25µm	1
3	50	Acetic Acid+ 1000°C H_2 (50-200 sccm, 2 Torr, 40°C/min)	10Torr/40Torr (10min, cooling rate 10 °C/s) CH_4 (99.999%)	850-900	50µm	Few layers
4	760	1000°C in ambient pressure. 1000°C He (1000sccm) + H_2 (50sccm)	15:50:1000 sccm ($H2:CH_4$:He)(5min, cooling rate in He 10°C/s)	1000	700nm	1 and 2
5	0.39	Ar (20 sccm, 0.41 Torr, 12 min). H_2 (20sccm, 0.3 Torr, 1.25min), 766°C	5 (10min) cooling in Ar 80 sccm 1 Torr	800	206nm	1, 2 and 3
6	0.1-0.5	(pre-vacuum) heating in H_2 up to 950°C	0.06 (from 15min up to 420min) CH_4 (99.99%)	1000	100-450nm	1
8	0.3	(pre-vacuum) heating in H_2 up to 1000°C, H_2 (13sccm, 0.1 Torr) 30min	0.5 (30 s-30min) cooling rate 9°C/min	1000	25µm,125µm	1 and 2
9	1.6	1000°C H_2 (8sccm, 0.18 Torr) 30min	0.33 (30min)(cooling rate 10°C/s, H_2 0.18 Torr)	1000	25µm	1

For most photonic and plasmonic applications copper catalytic graphene growth provides sufficient quality results, providing a monolayer with very few wrinkles and cracks and in a very simple way

compared to other more advanced growth methods even after transfer. Thus, CVD grown graphene on copper substrates was the growth process of choice for the work within this project.

3.2.3. Transfer Process of Graphene

Until a direct method of growing graphene on dielectric substrates has been perfected, CVD graphene grown on a copper precursor remains the most popular method of obtaining large monolayers of graphene. In order to create functional devices, graphene grown on a copper catalyst should be able to be transferred to a wafer of choice (like SiO_2). This can be achieved with the use of a transfer process [9,12]. The transfer process itself is extremely important as it heavily affects the final properties and quality of the graphene layer and, as a result, defines the final performance of the fabricated devices. Electronic and optoelectronic applications require graphene layers to be transferred on insulating substrates like polymer foils, glass, Si or SiO_2 wafers or even to substrates that have holes, are perforated, or pre-patterned. The transfer must be achieved in way that damage on the graphene monolayer can be avoided, so that the properties and quality of the material are preserved. This process can be as complicated as the fabrication of graphene itself and can often be the most crucial fabrication step of a graphene based device, several methods to transfer graphene without damage have been proposed [9,12,152,154,158–168].

The most common methods of transferring graphene are based on the idea of applying a type of polymer support on the surface of a copper foil where the graphene was grown on. The copper layer is then etched in order to obtain a free standing bilayer of graphene/polymer which can then be picked up with the use of a substrate of choice. Other methods include dry transfer or direct transfer that do not require any kind of secondary supporting membrane.

The most popular method for transferring graphene is the PMMA (polymethylmethacrylate) assisted wet transfer process [158,159]. In this method, a thin PMMA layer is spin coated (typically around 1000rpm for 20-60 seconds) on top of a graphene layer. After that the sample is baked for several minutes or is left to dry overnight in order to remove residual PMMA solvent. Then, the sample is placed in an etching solution in order to remove the copper. The most commonly used etchant is ferric chloride ($FeCl_3$) typically in a 0.5 to 1 M concentration. Other etching solutions that can be used include HCl, HNO_3, $Fe(NO_3)_3$ in H_2O, $(NH_4)_2SO_8$ and $CuCl_2$ [154]. The most important reason that $FeCl_3$ is the most commonly used etchant is that it successfully etches copper without forming any gaseous products or precipitates. Nitric acid leads to formation of bubbles that can damage the graphene monolayer and HNO_3 can have negative effects on the carbon sp^2 network. HCl releases corrosive vapour and is also much slower. In the case of $CuCl_2$, even though it has the advantage of being regenerated from waste, it is much more toxic than other solutions [154]. After copper is etched away, the PMMA/graphene bilayer is placed in DI (deionized) water to remove any contamination from the $FeCl_3$. The bilayer is then lifted up using a substrate of choice and is let to dry. Finally, the sample is placed in an acetone bath in order to remove the PMMA layer [159]. The diagram of Figure 3.15 presents all the required steps of the process. In general, this method can be carried out on hard substrates like glass, silicon, boron nitride or commodity plastic foils [166].

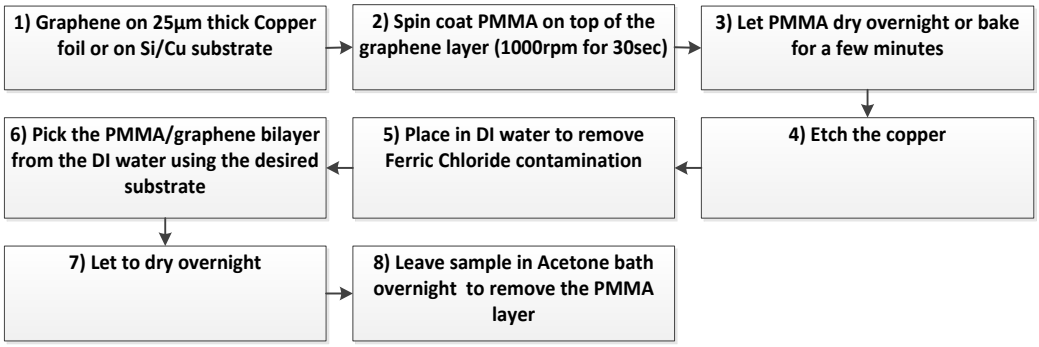

Figure 3.15 Simple PMMA assisted wet transfer process.[166]

A negative effect of this process is that PMMA is hard to remove since it forms strong dipole interactions with graphene [160]. Even after extensive rinsing with organic solvents like acetone, thin layers of residual long chain molecules remain on the graphene layer. Furthermore, even after annealing at 200-250°C in forming gas, part of the contamination still remains. Prolonged annealing in hydrogen or oxygen atmosphere is more effective but is also time consuming. High temperature annealing in H_2/Ar atmosphere has been suggested as a method to remove most of remaining PMMA contamination [158,169]. A solution to this problem could be the use of a different polymer support. Poly(bisphenol A carbonate) or 'PC' has been suggested as an alternative supporting layer [160]. Unlike PMMA, PC can be easily removed with the use of organic solvents (like chloroform) without the need of annealing, thus providing a large area of clean graphene.

Another problem that can occur is that graphene maintains the copper substrates morphology which in general tends to be rough because of the significant surface reconstruction that occurs during the high temperature growth process [161]. This means that when graphene is moved to a new substrate along with the PMMA supporting layer, contact with it is not perfect. Because of the gaps between the graphene layer and the new substrate, when the PMMA layer is removed, cracks are formed at the regions of poor contact. This can be avoided by introducing a second PMMA coating step after the graphene/PMMA bilayer has been moved to the new substrate [161]. When PMMA is dropped on the transferred PMMA/graphene bilayer, the old PMMA layer gets dissolved leading to mechanical relaxation of the underlying graphene layer. As a result contact with the new substrate is highly improved. The process including the second PMMA coating step is presented in Figure 3.16.

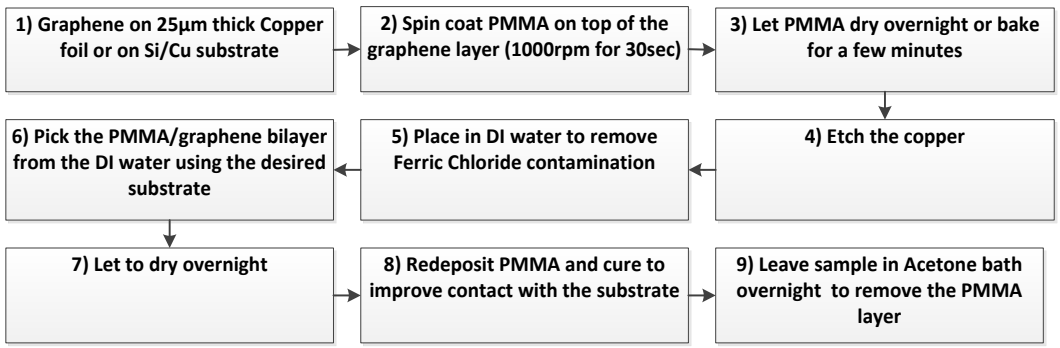

Figure 3.16 Simple PMMA assisted wet transfer process with second PMMA step to improve contact with the new substrate. [161]

It has also been observed that some chemicals used to etch copper (iron nitrate, iron chloride, ammonium persulfate) during the transfer process can contaminate the graphene layer with oxidized metal particles that cannot be cleaned away by simply rinsing the sample with DI water. After the transfer process is complete, these contaminants are trapped between the substrate and the graphene layer. A method of improving the PMMA transfer process by including RCA (Radio Corporation of America) cleaning steps to remove any metal particle contamination from the graphene layer has been suggested [162]. Additionally, in the same work, a method to reduce the amount of defects like cracks and folds that form during the transfer process was suggested [162]. The proposed solution was to introduce two extra bake steps after the graphene and PMMA layer have been transferred on the new substrate. Furthermore, it was proposed that by making the target substrate hydrophilic the amount of fold like defects is highly reduced.

In more detail, this process introduces a SC-2 ($H_2O/H_2O_2/HCl$) cleaning step after the etching of copper in order to remove any ionic and heavy metal contamination followed by a SC-1 ($H_2O/H_2O_2/NH_4OH$) cleaning step to remove any organic contamination. Both cleaning steps should be performed at room temperature to avoid the generation of bubbles that could damage the graphene layer; additionally they should be composed of 20:1:1 stoichiometry in order to reduce their reactivity. After each cleaning step the sample has to be cleaned with DI water.

Introducing a second PMMA coating step can reduce the amount of cracks on the graphene layer, a simple bake at 150°C for 15min can greatly improve the contact with the new substrate and provide even better results [162]. Another bake at 200°C for 10min after removing the PMMA layer can also improve the adhesion of the graphene layer to the new substrate. Finally, making the target substrate hydrophilic (for example by briefly dipping a SiO_2 wafer in HF or by performing an oxygen plasma treatment) improves the smoothness of the graphene layer, thus reducing the amounts of folds and cracks that form during transfer process [162]. A rough substrate surface can also improve adhesion since it provides a bigger contact area for the graphene layer [154]. This process was reported to produce very high quality results. The several steps required can be seen in Figure 3.17.

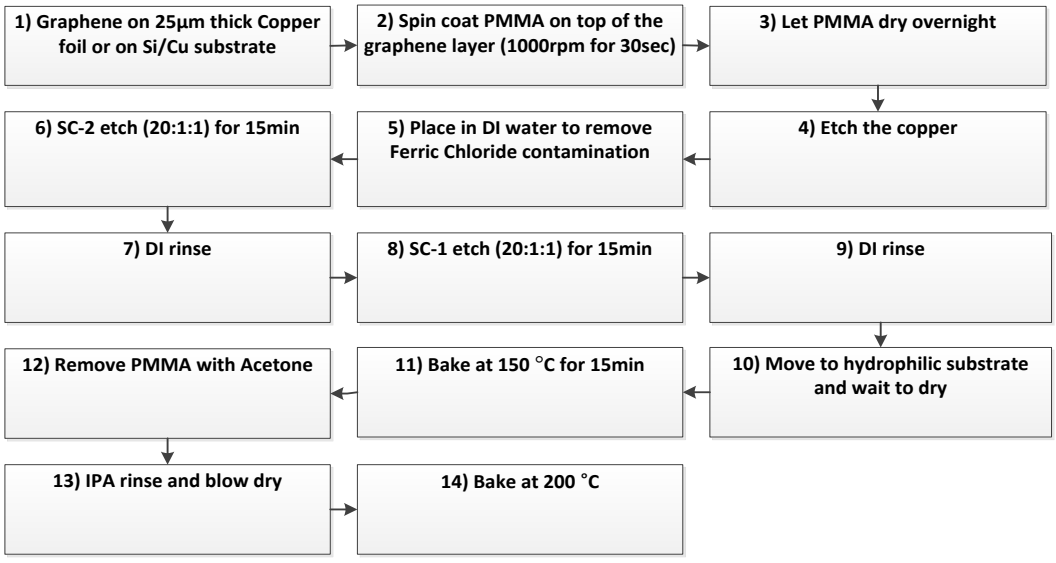

Figure 3.17 Modified RCA clean PMMA assisted wet transfer process that removes any metal contamination and includes further bake steps to improve the contact of graphene with the new substrate [162].

Another very popular method of transferring graphene is by using an elastomer stamp. This way graphene can be placed on the target substrate by stamping with an easy pick and place capability [166]. Additionally, this method has the advantage that it does not leave any contamination, unlike the PMMA method that usually leads to n-type doping of the monolayer [158]. An example of the stamp method can be considered by starting with a PDMS layer is bonded on the graphene surface. Afterwards, the copper substrate is etched away and the PDMS stamp along with the graphene layer is washed with DI water and positioned on top of the desired wafer. Subsequently, the wafer is heated while pressure is applied in order for the graphene layer to get attached to the new substrate (80°C for 30min). Finally, the PDMS layer is delaminated, leaving only the graphene layer behind [152,158]. This method also provides a way of patterning graphene layers without requiring the use of any lithographic processes after the transfer process. By using a copper substrate or a PDMS stamp with a predefined geometry, the shape of the transferred graphene layer can be effectively controlled [163]. The PDMS-assisted transfer method tends to provide lower quality graphene since the amount of cracks and defects that form during the transfer process is higher than in the PMMA assisted method [154,166]. This method also requires a stronger adhesion between the graphene layer and the target substrate than between graphene and the PDMS support layer. This means that it can only be used on hard hydrophilic surfaces [166]. Finally, method of an etching free transfer process where the graphene layer was transferred by a facile peel off process of graphene from copper surfaces has also been suggested using a stamp-based process [164].

If the graphene layer needs to be transferred on perforated substrates or to substrates that are patterned with shallow wells, then the transfer processes mentioned above are not always suitable. The reason for that is that when the substrate has shallow wells, liquid can be trapped in them. Furthermore, transferring graphene on perforated substrates can cause the layer to be broken by the surface tension during the drying process [165].

In order to overcome the problem of transferring graphene on substrates with shallow wells, a dry transfer method where a PDMS frame is used to support the graphene/PMMA bilayer has been introduced [165]. This way the film can easily be removed from the etching solution and then dried. As a result, no liquid is trapped when the graphene layer is finally moved to the target substrate. This method also includes a heat treatment after transferring graphene in order to increase its adhesion with the substrate. After the heat treatment, the adhesion is very strong and the PDMS frame can be peeled off without delaminating the graphene/PMMA layers. The PMMA layer can then be removed by placing the sample in a furnace at 350 °C in an Ar and H_2 atmosphere for two hours. Another recently suggested method for overcoming the problem of PMMA residue is replacing the acetone cleaning step with an acetic acid bath followed by ethanol cleaning process [170]. This method has been reported to eliminate most of the residual PMMA but introduces a slight disorder in graphene [171].

A method for transferring graphene on perforated substrates while avoiding any cracking during the drying process has also been reported [165]. After cleaning the PMMA/graphene bilayer in DI water, instead of lifting the film with the target substrate, the water level is lowered until the layer comes in contact with it. Rupturing of the graphene layer during the drying process can be avoided by inducing rapid evaporation and minimizing surface tension. This can be achieved by using critical-point drying or by using hexamethyldisilazane as a dehydrating solution [165].

It is important to mention some of the transfer processes that do not fall in any of the previous categories but still produce very high quality results or very large areas of transferred graphene. Recently a method was demonstrated that combines the advantages of the PMMA and elastomer stamp methods and has the ability of transferring graphene with high-quality results on almost any kind of surface (including hydrophobic and soft surfaces like thin molecular and polymeric films, or even on substrates with prefabricated structures) where other methods usually fail [166]. This method is basically a modification of the elastomeric stamp method and the basic idea behind it is introducing a self-releasing polymer layer between the PDMS stamp and the graphene monolayer. This sacrificial layer (usually polystyrene which can easily be dissolved with toluene) reduces the adhesion of the stamp to the graphene layer and as a result the stamp can be easily removed when the graphene layer has been placed on the target substrate. This method supports both dry and wet transfer and also protects the graphene layer from the low molecular weight siloxane oligomers that are present in PDMS.

A direct method of transferring graphene on PET (Polyethylene terephthalate) flexible substrates with the use of hot press lamination process has also been reported [167]. Copper foils where graphene is grown are hot press rolled with a PET film. Copper is etched away and after that only the PET film supports the graphene layer. The sample is then washed with DI water and dried. In such a simple way, a very adherent graphene layer on a flexible transparent film can be acquired on a relatively large area. Additionally, deforming the film barely damages the graphene layer, allowing for flexible devices to be fabricated.

Another way of direct transfer of graphene is referred to as a face-to-face transfer [172]. This method relies on capillary bridges forming between the graphene film and the underlying substrate during the etching of the metal precursor. In more detail, the capillary bridges hold the graphene monolayer above the wafer while the copper layer is etched away. As the wafer is removed from the liquid the graphene layer attaches directly to the surface of the wafer below. This method has the advantage of reduced defects and the possibility of batch processing in a production line.

Finally, using thermal adhesive tapes has been proposed as a very useful method of transferring very large areas of graphene on plastic substrates with excellent uniformity [154]. A method of producing high quality large area (30-inch) graphene by roll-to-roll production on flexible substrates has been reported [168]. Unfortunately this method has the disadvantage of contaminating the transferred graphene surface with residues from the thermal release tape, thus negatively affecting the performance of fabricated devices [154,162].

In general the simple PMMA transfer method when including a ferric chloride etching solution, the RCA clean steps for removing contamination, and the post drying bake for improving the adhesion and reducing wrinkles and cracks of the graphene monolayer, presents quality results in a relatively simple and straightforward way and thus is the method of choice for this project.

3.2.4. Chemical Doping of Graphene

Chemical doping is a very effective way of tuning material properties. Tailoring graphene's properties in a stable and efficient way is both highly longed for and challenging to achieve. Chemical doping can shift the plasmon frequency in graphene devices thus allowing for devices to operate

closer to the visible spectral range. Due to its very high surface to volume ratio graphene is very sensitive to atmospheric conditions. Thus even though pristine graphene FET (field effect transistor) devices have very clear ambipolar I_D-Vg characteristics, this behaviour is not stable under normal atmospheric conditions due to adsorption from the surrounding environment or even from residues that occur during the fabrication process [173]. In order to avoid this type of surface transfer doping, annealing treatments are used as well as vacuum, nitrogen or Argon chambers when taking measurements. There are two ways to chemically dope graphene, surface transfer doping, and substitutional doping [174]. Surface transfer doping is achieved through charge transfer from adsorption of dopants on graphene. This type of doping does not damage the graphene lattice structure and is easily reversible. Substrate, atmosphere and fabrication induced contaminants can also induce such kind of doping on graphene. Substitutional doping happens when carbon atoms in the graphene lattice are replaced by different atoms (donors or acceptors) such us nitrogen or boron. This type of doping results in the disruption of sp^2 hybridization of carbon atoms.

Surface transfer doping can occur when charge is transferred from adsorbed dopants to graphene. This charge transfer depends on the density of states of the highest occupied molecular orbital and the lowest unoccupied molecular orbital of the adsorbing material, in relation with the chemical potential of graphene [174]. Techniques to reduce the effect from atmospheric and substrate doping due to surface transfer interactions have been demonstrated typically involving high temperature annealing [175]. For example, the commonly used SiO_2 substrate can introduce p-type doping which can be overcome by a simple hydrogen intercalation process [175].

For substitutional doping, electron donor or acceptor atoms are introduced directly into the material of interest. For this to be achieved, some of the atoms of the host material are removed and are then replaced by donor atoms. When compared to carbon, nitrogen atoms have an additional electron and boron lacks one, this means that by incorporating nitrogen atoms in the basal plane of graphene, n-type doping is achieved [174]. Nitrogen doping of graphene is a very popular method for achieving n-type doping and many different methods including directly growing nitrogen doped graphene, or later introducing nitrogen donors to repair intentionally occurring vacancies (post treatment) have been reported [174,176,177]. Substitutional doping has also been reported to introduce a bandgap in graphene due to suppressed density of states near the chemical potential [176]. Unlike surface transfer methods that can be very sensitive to atmosphere and difficult to maintain, substitutional methods provide a more reliable and stable method for doping graphene.

3.3. Characterization of Graphene

In this section several methods used for characterizing graphene are briefly discussed. In general these characterization methods are used to accurately identify the number of the graphene layers, as well as the uniformity and the quality (number of defects like cracks and wrinkles) of graphene. The most popular methods for achieving this are Raman spectroscopy [178,179], SEM [180–183] and AFM (Atomic Force Microscopy) [184–187], but other methods like optical microscopy [188,189], STM (Scanning Tunnelling Microscopy), TEM (Transmission Electron microscopy), Fluorescence quenching microscopy [188], and Auger electron spectroscopy are also common [190].

3.3.1. Raman Spectroscopy of Graphene

Raman spectroscopy is a powerful high-throughput, non-destructive tool for capturing graphene's unique electronic and atomic structure [178,179]. In general Raman spectroscopy can be used to investigate many parameters of graphene like the number of layers [152,178,179,184], the amount of defects [160,178,179], doping, and strain [165]. Distinguishing between monolayer, bilayer and multilayer graphene is easily achievable by observing the ratio of the 'G' (~1580cm^{-1}) and '2D' (~2680cm^{-1}) peaks intensity (I_G/I_{2D}) and the band morphology of the 2D peak [184]. The D peak provides information about the quality of the graphene layer since it arises from defects [178].

Phonons are compressional waves or vibrations of the crystal lattice. Since the 2D peak originates from the two phonon double resonance process (second order of zone-boundary phonons) it is very closely related to the band structure of graphene which in turn highly depends on the number of graphene layers [178,179]. Thus, the 2D peak provides a high amount of information for determining the number of graphene layers [164]. Single layer graphene presents a 2D peak with much higher intensity than the G peak. Additionally, it exhibits a very symmetric (Lorentzian shaped) 2D peak unlike bilayer graphene, multilayer graphene, and graphite, where the 2D peak is no longer symmetric and the intensity of the G peak becomes almost equal or bigger than that of the 2D peak (Figure 3.18.a) [184]. Typical values of the I_G/I_{2D} ratio for single layer graphene are around 0.1 to 0.5 with a symmetric 2D peak centred at ~2680 cm^{-1} with a FWHM (full width at half maximum) of around 22 to 33 cm^{-1} [152,165]. In more detail, unlike single layer graphene that has a sharp and symmetric 2D band, bilayer graphene presents a much broader and up-shifted 2D band [179]. This band splits into four components ($2D_{1B}$, $2D_{1A}$, $2D_{2A}$, $2D_{2B,}$ with $2D_{1A}$ and $2D_{2A}$ having higher relative intensities than the other two). By increasing the number of graphene layers, the $2D_1$ peaks are further reduced in terms of relative intensity and after five layers the spectrum cannot be easily distinguished from that of bulk graphite (2D peak in graphite consists of two components, $2D_1$ and $2D_2$ with about ¼ and ½ the height of the G peak respectively).

The G peak originates from the doubly degenerate E_{2g} in-plane optical vibrational mode at the centre of the Brillouin zone (Figure 3.18.b) [160,179]. The position of this peak provides a good estimate of the charge density in graphene. The FWHM of this peak (usually around 15-16 cm^{-1}) provides an estimate of electron-phonon coupling strength [160,165]. By taking intensity maps of the G peak in graphene, the uniformity of the layer can be investigated since wrinkles or graphene grain boundaries can alter the otherwise stable intensity of this peak [154]. In general, wrinkled regions cause peak

height variations for both the G and 2D bands (the 2D band can also become broadened) [152]. Both the 2D and G peaks are sensitive to doping, strain and temperature [165].

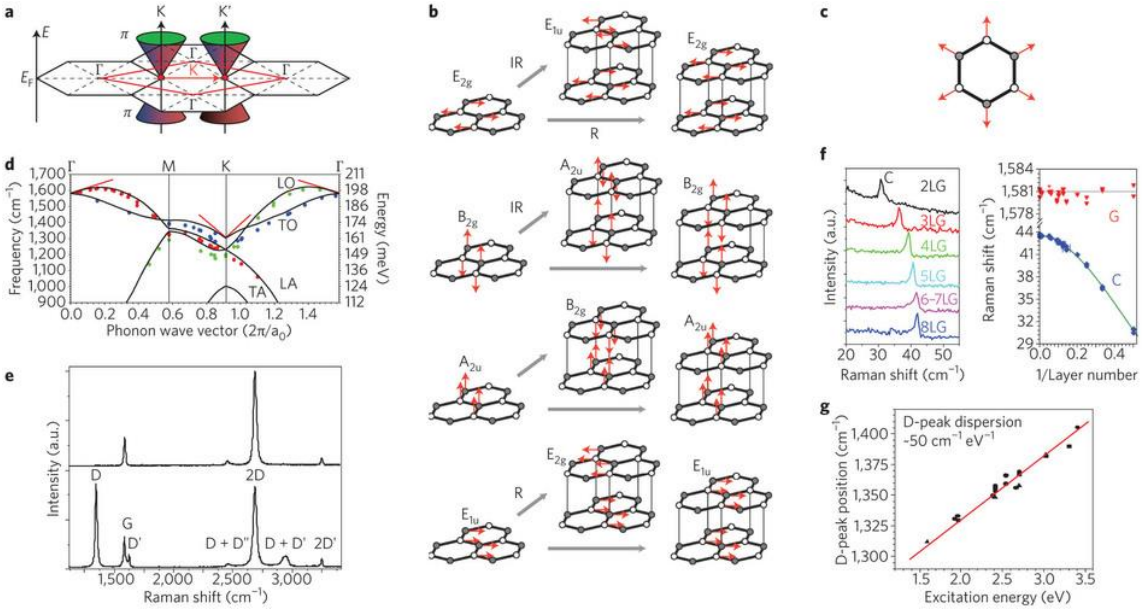

Figure 3.18 a. Electronic Brillouin zones of graphene and electronic dispersion. Phonon wave vectors connecting electronic states in different valleys labelled in red. **b**. Γ- point phonon-displacement pattern for graphene and graphite. Red arrows show atom displacements. Grey arrows show how each phonon mode in graphene gives rise to two phonon modes of graphite. Their labelling shows Raman-active (R), infrared-active (IR) and inactive (unlabelled) modes. **c**. Atom displacements (red arrows) for the A1g mode at K. d, black curves represent the dispersion of in-plane phonon modes in graphene in the energy and frequency range relevant for Raman scattering. Red lines represent Kohn anomalies. **e.** Raman spectra of pristine (top) and defected (bottom) graphene. The main peaks are labelled. F**.** C peak as a function of number of layers (left). Fitted C- and G-peak position as a function of inverse number of layers (right). Flakes with N layers are indicated by NLG. G**.** D-peak position as a function of excitation energy. Reprinted by permission from Macmillan Publishers Ltd: Nature Nanotechnology([178]), copyright (2013).

The D peak (~1350 cm^{-1}) originates from TO (transverse optical) phonons around the K point of the Brillouin zone and is activated by defect-induced double resonance scattering [160]. This means that this peak is an obvious measure of defects in the graphene layer since it does not exist on pristine graphene (it is induced by disorder) and its intensity increases as the defects increase (Figure 3.18.e). By analysing the intensity ratio of the D and G peaks (I_D/I_G) the amount of defects in graphene can be compared with other samples (it is important to mention that this ratio has been found to be highly affected by the laser excitation energy [191]). Higher I_D/I_G ratios indicate more defects in the graphene layer (if this ratio is below or around 0.3, the quality of single layer graphene is considered appropriate) [162]. Probing the edge of the graphene layer can also cause the observation of a D peak [179]. Finally, the D band in graphene consists of a single sharp peak, while for graphite it consists of two peaks (D_1 and D_2). A set of empirical relations can be used to quantify point like defects in graphene samples with inter-defect distances (L_D) bigger than 10nm for any excitation wavelength in the visible range [191]. The interdefect distance can be calculated as

$$L_D{}^2\left(\mathrm{nm}^2\right)=\left(1.8\pm0.5\right)\times10^{-9}\lambda_L{}^4\left(\frac{I_D}{I_G}\right)^{-1} \quad \text{, (3-9)}$$

where λ_L the excitation wavelength in nanometers (nm). In terms of defect density n_D it can be expressed as

$$n_D\left(\mathrm{cm}^{-2}\right)=\frac{(1.8\pm0.5)\times10^{22}}{{\lambda_L}^4}\left(\frac{I_D}{I_G}\right), \text{(3-10).}$$

The doping and the strain of the sample can also be evaluated from the 2D and G bands. The FWHM as well as the position of the 2D and G peaks are sensitive to temperature, strain and doping [165]. At low laser power, the temperature parameter can be ignored since it has a very low effect. This way the 2D band position, which is not very sensitive to doping compared to strain, can be used to identify the amount of strain on the graphene layer. With both temperature and strain effects eliminated the G peak can be used to identify the amount of doping since both its position and FWHM are a function of doping. Higher doping concentrations (electron or hole) cause an upward shift in the G peak position and a decrease in the G bands width[165].

One disadvantage of Raman spectroscopy is that it is limited to low fluorescence substrates since otherwise interference will overwhelm the Raman signal of graphene. Furthermore, care has to be taken when choosing the power of the laser (no more than a few mW should be used) since it can lead to heating of the graphene layer which, in turn, can result in graphene being damaged by going through local decomposition [188].

Since the Raman spectrum of graphene provides so much useful information, a basic understanding of physical mechanisms is required. There are three optical and three acoustic phonon dispersion (where dispersion the phase velocity dependence of the wave on wavelength) modes in single layer graphene[178]. The out-of-plane modes (Z direction) are much weaker than the in-plane longitudinal and transverse modes. Graphene has two atoms in its unit cell, giving rise to six normal modes at the centre of the Brillouin zone (A_{2u}+B_{2g}+E_{1u}+E_{2g}), out of which two are degenerate (Figure 3.18.b). The E_{2g} mode is a degenerate in-plane optical mode and its phonons are both Raman and infrared active. The B_{2g} is an out-of-plane optical mode but its phonons are neither Raman nor infrared active.

As mentioned before, the G peak arises from the high frequency E_{2g} phonon at Γ point of the Brillouin zone. The D peak originates from the A_{g1} breathing modes of the six-atom graphene rings and requires the existence of defects in order to be activated. This arises from the TO phonons around the Brillouin zone corner K and is activated by double resonance. Furthermore it is heavily dispersive with excitation energy [178]. Another way for double resonance to occur is by an intravalley process, where two points belonging to the same cone around K or K' are connected giving rise to a D' peak. The 2D peak is the D-peak's overtone and the 2D' peak is D'-peak's overtone. Those two peaks do not require any defects in order to be activated. They originate from a momentum conservation process that is satisfied by two phonons with opposite wave vectors and they are always present [178].

The 2D peak in single layer graphene originates from two phonons with opposite momentum in the highest optical branch near K (A'_1 symmetry at K) [178]. Because of the double resonance process that links the phonon wave vectors to the electronic band structure of graphene, altering the excitation

energy also alters the peak's position. Within the double resonance the Raman scattering is a fourth order process that involves four virtual transitions. First the laser excites an electron-hole pair. Then an electron-phonon scattering of an exchanged momentum, q, occurs close to the K region. This is followed by another electron-phonon interaction with the opposite exchanged momentum and finally an electron-hole recombination [178]. The double resonance condition is satisfied when the energy is conserved through all these transitions. The frequency of the 2D peak is twice that of the scattering phonon with its momentum being determined by the double resonance condition. Equivalent processes happen for the hole-phonon scattering. As the number of graphene layers increases, the electronic band structure also changes. For bilayer graphene the interaction between the two layers causes the π and π* bands to split in four, with different splitting degrees for electrons and holes. While the incident light only couples two pairs out of the four bands the almost degenerate TO phonons can couple all of them [178]. This means that four phonons are involved with momentum q_{1B}, q_{1A}, q_{2A} and q_{2B}. Different frequencies correspond to each phonon due to the phonon dispersion in K giving four distinct peaks that comprise the components of the 2D peak of bilayer graphene [178].

3.3.2. Scanning Electron Microscopy Imaging of Graphene

Scanning Electron Microscopy is a very popular method of imaging graphene since it provides large area identification and is very fast to perform [180]. The electron beam used to probe the material generates backscattered electrons, secondary electrons (through interaction with the materials atoms), auger electrons, and X-rays [188]. For imaging graphene, most commonly, secondary electron detection is used [180–183]. In general, SEM can be used to examine nanostructures of graphene, such as folds, wrinkles, ruptures, and impurities, as well as the existence of multilayer regions [180–183]. Quantitative identification of the number of graphene layers is possible because it is possible to distinguish the thickness variation in graphene through low energy primary electron acceleration probing, in which the intensity values of the captured secondary electrons are analysed [181,182].

In order to successfully image graphene, several requirements need to be met. First of all, low beam energy is required to detect the atomically thin layer of graphene. Because of its thickness, graphene is transparent to high energy electrons and almost no secondary electrons are generated from the graphene layer. Additionally, using low energy primary electrons has the advantage of not causing any damage on the graphene layer and reducing charging that occurs on substrates with low conductivity, thus allowing easier imaging [180]. Since a low energy beam is used, a high performance detector should also be utilized in order to obtain high quality images with good contrast and topological sensitivity. The SEM should also have a high spatial resolution if observation of any nanoscale features in graphene's structure is necessary. This means that a small beam spot is required [180]. Figure 3.19 shows some SEM images of graphene on a SiO_2 and a copper substrate.

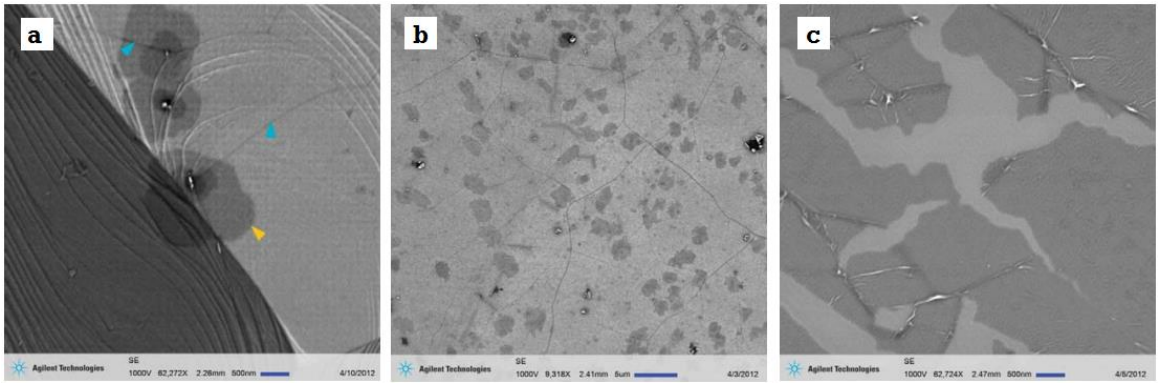

Figure 3.19 a. SEM image of CVD graphene on the copper foil that it was grown (scale bar 500nm). **b**. SEM image of graphene on a SiO_2 wafer after transfer (scale bar 5μm). **c**. SEM of cracked graphene on a SiO_2 wafer after transfer (scale bar 500nm). (with permission from reference [180])

Unfortunately, imaging graphene on insulating substrates is difficult and the charging effect usually distorts the quality of the image. Using electron energies around 1kV have been reported to overcome this problem [180]. In this project Helium Ion microscopy has been used to provide higher quality images than possible with an SEM.

3.3.3. Atomic Force Microscopy Imaging of Graphene

Atomic Force Microscopy has been used extensively in order to image graphene and identify the number of layers and thickness of a single graphene layer [184–187]. Usually tapping mode is used to avoid damaging the graphene layer [187]. AFM is an excellent tool for identifying defects like cracks, wrinkles and folds on graphene. It is important to mention though that during thickness measurements, and especially for single layer graphene, several deviations from the theoretical thickness based on the molecular structure have been observed with values varying from 0.3nm to 1nm [184,187]. This phenomenon highly depends on how the tip-sample interaction changes when the tip moves from the substrate to the graphene layer [184]. When the tip moves from one layer of graphene to a second the thickness is always found to be ~0.35nm since the local force gradient on the tip is not different like it would be if moving from a non-graphene material to graphene [184]. This can be observed in Figure 3.20.

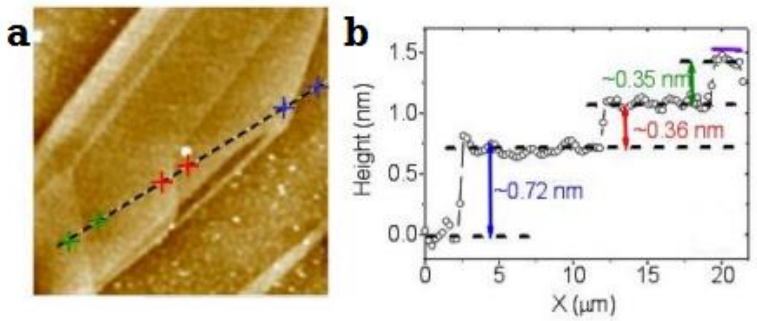

Figure 3.20 a. AFM image of few layer graphene. **b**. Thickness of graphene layers obtained on a SiO_2 wafer, it is clear that when the tip moves from the SiO_2 wafer surface to the first layer of graphene a big thickness offset occurs because of the change in the force gradient experienced on the tip. (with permission from reference [184] under creative commons licence)

AFM can also be used to study the frictional properties of graphene [185]. It has also been reported that with the use of carefully chosen AFM tips contrast of atomic periodicity is observable (Figure 3.21) [186].

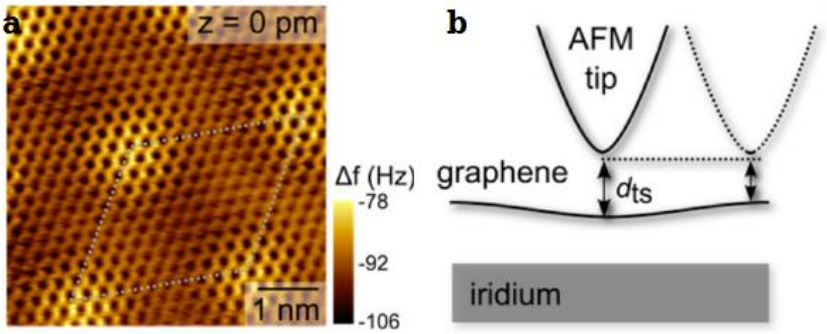

Figure 3.21 **a**. Image acquired with constant height measurement using an iridium-terminated tip, the periodicity of the carbon atoms can be observed **b**. Schematic of the tip-sample distance. Reprinted (adapted) with permission from ([186]). Copyright (2012) American Chemical Society.

Finally, substrate topology as well as tip-sample interaction must be carefully considered in order to image the graphene surface. Isolation from any source of vibration is mandatory. AFM is a very useful but very low throughput technique since it cannot investigate large areas of the sample.

3.3.4. Optical, Scanning Tunnelling and Transmission Electron Microscopy of Graphene

Optical microscopy has been used to characterize larger areas of graphene than the aforementioned techniques. It can be used to observe the existence, position and size of graphene layers [188]. Furthermore, it has been reported that by analysing the contrast difference of the obtained image, the number of layers can be identified, with lower contrast being associated with fewer layers of graphene [184,189]. Even though suspended graphene layers can be seen while using bright-field microscopy, when it is placed on substrates observation becomes much more difficult [188]. Typically in order to be able to observe a graphene monolayer a SiO_2/Si substrate with 100-300nm thick oxide has to be used [183,184]. This way the optical contrast between the substrate and the graphene layer is maximized in the visible range due to constructive interference from the optical cavity that is formed [184,188]. It has also been reported that graphene can be observed with the use of optical microscopy on a copper substrate that it is grown on by following a certain oxidizing process of the underlying copper [189].

Scanning Tunnelling Microscopy imaging has been used to image graphene, especially when information of its atomic structure is required. STM has the disadvantage of requiring special preparation for the sample to provide information on the graphene's grain boundaries. Additionally STM shares some disadvantages of AFM, meaning that it is time consuming, low throughput and impossible to use for examining large areas of graphene [188].

Transmission Electron Microscopy imaging can also offer information with atomic scale resolution (like STM) but it is also a very slow technique that requires substrates transparent to electrons. Low energy electrons need to be used like in the case of SEM to avoid damaging graphene. Additionally it usually requires special substrates in order to observe graphene's grain boundaries[188].

3.3.5. Comparison of Characterization Methods

All these techniques offer different advantages and disadvantages. Raman spectroscopy is a fast and reliable method of identifying the number of graphene layers as well as structural and electronic information but care must be taken to avoid damaging the graphene layer by the heat that the laser generates (low power should be used). Currently Raman spectroscopy is the most common method for characterizing graphene due to its high throughput and the variety of information it can provide.

SEM is a rapid non-invasive imaging technique that is complementary to Raman spectroscopy or other techniques. With the use of SEM, large areas of the graphene layer can be investigated in terms of uniformity and defects. Furthermore, it can even provide information on the number of graphene layers. On the other hand, it has the disadvantage of requiring conductive substrates and vacuum for operation.

AFM can also be used to identify the number of graphene layers and material thickness, as well as defects on the graphene film but it is a very slow technique and requires smooth substrate surfaces as well as requiring very good isolation from vibrations to be able to observe graphene. Because of the low throughput of AFM, it can only be a complementary technique, especially in industrial environments.

Optical microscopy is a fast method that can provide some limited structural information or even a qualitative analysis on the number of layers of graphene. On the other hand, it requires special conditions in order for graphene to even be observable. This method must be complemented by others as it only provides a quick estimation on the quality of the graphene sample.

STM and TEM are very useful when information on the atomic structure of graphene is required. On the other hand, both techniques are limited to studying very small areas of the sample and also require special substrates for graphene to be visible (low electron absorbance substrates for TEM, conductive and very smooth substrates for STM). Both techniques are also relatively slow and require a vacuum chamber for operation.

Table 3-2: Comparison of the most popular techniques used for characterizing graphene (reproduced from reference [188])

Method	Mechanism	Speed	Substrate requirement	Other requirement
Raman Spectroscopy	Inelastic photon scattering	Fast	Low fluorescence and effective heat dissipation	Carefully choosing laser power to avoid damage
SEM	Secondary/back scattered Electrons	Medium (scan)	Conductive	Vacuum
AFM	Force between sample and tip	Low (scan)	Smooth surface	Vibration isolation
Optical	Interference	Fast	Si with dielectric coating	Well defined dielectric thickness and wavelength
STM	Electron tunnelling	Low (scan)	Conductive and atomically smooth	Vacuum
TEM	Absorption of electrons	Slow	Transparent to Electrons	Vacuum

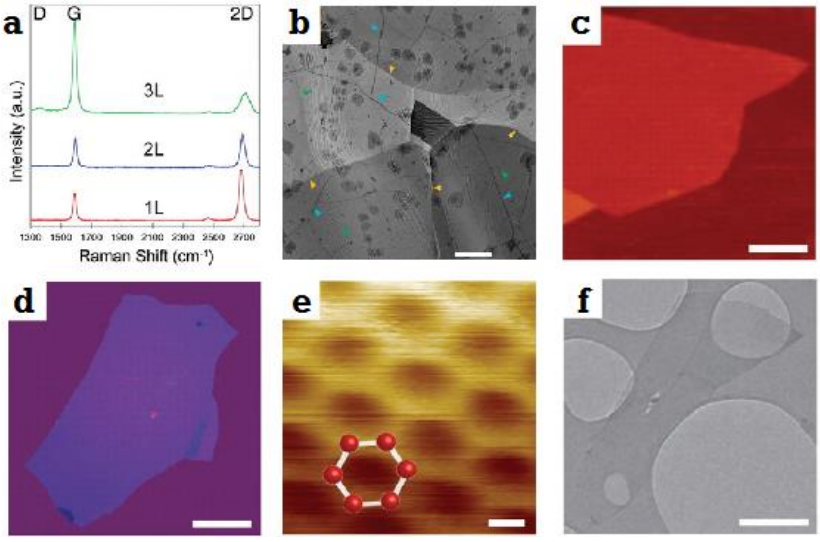

Figure 3.22 a. Raman spectrum of graphene for one, two and three layers[152]. **b.** SEM image of single layer graphene after transfer on a SiO_2/Si substrate[180]. **c.** AFM imaging of graphene (1µm scale bar)[188]. **d.** Optical interference image of graphene (20µm scale bar)[188]. **e.** STM image of graphene (0.1nm scale bar), the atomic structure can be seen[188]. **f.** TEM image of graphene (500nm scale bar) [188].

4. Theoretical Modelling and Simulations

4.1. Tuneable Graphene Plasmonics Device Based on a 2D Grating

In this chapter a theoretical model describing the behaviour of excited propagating plasmons in graphene for an original device geometry is presented. In this device geometry, a diffraction grating is used as a phase matching component, and the carrier concentration of graphene can be modulated with the use of an ionic gel gate. This novel device setup that allows excitation and manipulation of plasmons in graphene is developed and studied via analytical modelling and through Rigorous Coupling wave Analysis simulations. The theoretical work presented in this chapter has resulted in a publication offering valuable information for advancing the field of graphene plasmonics [36]. The text presented in this section has been published as part of a Scientific Reports paper [36].

4.1.1. Theory for Electrostatic Tuning of Optical Properties of Graphene

Obtaining strong coupling and highly tuneable plasmons in graphene up to near infrared and visible frequencies is a difficult but highly anticipated task. In order to achieve this goal, in this work an inverted pyramid array diffraction grating with an ionic gel [192,193] gate setup is proposed as an efficient coupling method for plasmons in graphene. A two-dimensional array of inverted pyramid pits forms a crossed diffraction grating functioning as a phase-matching component coupling incident photons to plasmons in the graphene layer positioned above the diffraction grating as the active plasmonic medium. Ionic gel is chosen as the gate dielectric due to its transparent nature and high capacitance values when compared to conventional high-k gate dielectrics. Modulation of graphene chemical potential is then achieved by applying a small voltage across the ion gel / Silicon substrate. The configuration is shown in Figure 4.1.

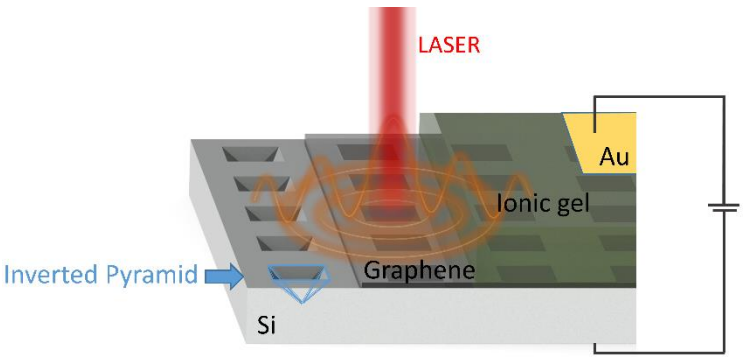

Figure 4.1 Schematic of the device setup showing the graphene layer sandwiched between the diffraction grating and the ionic gel that is used as the gate dielectric. When the device is illuminated by a laser beam, photons are diffracted in the inverted pyramid pits and then couple with plasmons in graphene.

In this thesis a device capable of supporting propagating plasmons on a continuous graphene layer is desired instead of device supporting localized plasmons in nano-patterned graphene. Thus a diffraction grating is utilized to couple light to surface plasmons in the atomic monolayer. There are several types of nanostructures that can be used for an efficient two-dimensional diffraction grating. Some examples include nano-gaps [194], nano-voids [195], nano-triangular holes [196,197], circular na-

noholes [197,198], and inverted nano-pyramids [195,199–201]. Such structures have been extensively investigated in literature for different plasmonic applications and especially for SERS where excellent reviews are already available [202,203] and thus more details about them will not be included in this thesis. Nevertheless, the reasons behind the choice for utilizing the inverted pyramid structure in this thesis over other possible structures will be discussed in detail.

There are several reasons behind selecting the inverted pyramid structures for fabricating the diffraction gratings in this thesis. One of the most important reasons is the fact that inverted pyramid arrays are very easy to fabricate (see section 5.1.1 for details on the fabrication process), and also allow for perfect control over structural parameters such as width, depth, sidewall angle, and inter-structure distance (also providing control over the optical properties of the device). Since the pyramid structures are patterned through KOH etching of <100> silicon, the sidewalls of the resulting structures are atomically smooth and highly reproducible [204]. Furthermore, inverted pyramid arrays can very easily be patterned and mass produced on flexible polymer substrates through a roll-to-roll ultraviolet embossing method providing a very low cost method for the fabrication of highly efficient diffraction gratings [205]. Since fabrication of the alternative structures typically involves complicated bottom-up techniques that are hardly reproducible or very high cost top-down techniques that are also limited in terms of the smallest possible feature size [194], these advantages of the inverted pyramid structure make it ideal for the realization of commercial applications. Furthermore, since graphene is also a mechanically flexible material, low cost bendable plasmonic devices could be fabricated by transferring graphene layers on flexible polymer substrates incorporating the inverted pyramid structures.

Finally, it has been proven that inverted pyramid structures when coated with gold, due to the excitation of plasmons, produce very strong near fields that are projected upwards from the edges of the sidewalls even up to 200nm above the surface of the grating structure (due to the adiabatic taper of the pits, the plasmon absorption is also very broad) [205]. This is very useful for enhancing plasmon excitations in monolayer graphene as will be discussed in section 4.2. In general, due to their very strong near field enhancement gold coated inverted pyramid structures have been used in SERS applications providing very high enhancement factors [199–201]. For example, when inverted pyramids are compared with nano-void structures for SERS applications, they provide very slightly weaker enhancement, but at the same time they allow for a much easier, more cost effective, and more highly reproducible fabrication process [195]. For these reasons SERS devices based on inverted pyramid structures have also become commercially successful products under the name of Klarite [195].

Before providing more details regarding the operation of the device, a solid theoretical model describing the electrostatically controlled optical properties and plasmon dispersion of graphene needs to be developed. By providing such a model, the behaviour of a device can be described both theoretically and through simulations. A Matlab code of the model used for the theoretical calculations in this project is available in the Appendix section 12.1.1.

Carbon atoms have a total of six electrons out of which only four valence electrons can participate in bonds. The remaining two core electrons are strongly bound to the nucleus. In graphene carbon atoms are arranged in a honeycomb lattice formed by the sp^2 bonds [11]. The p_z orbitals of the neighbouring carbon atoms overlap, forming bonding and antibonding states and thus the π-bands of

graphene [11,12]. The low energy band structure of graphene involves the π electrons. The bonding π states form the valence band, and the antibonding π* states form the conduction band [12]. These states are orthogonal and as a result cross each other. Valance and conduction bands touch at six points known as the Dirac points [11,12]. Two of these points (known as the K and K' points) are independent [12]. The unit cell of graphene contains two carbon atoms and its lattice can be viewed as two separate sub-lattices (A and B) that are formed by those atoms [12]. Because of the symmetry between the A and B sub-lattices the conduction and valence bands are degenerate at the K and K' points and as a result the electronic bands have a linear dispersion [11]. For small energies (below ~1.5eV) the band structure can be considered as two symmetric cones with the conduction and valence bands touching at the Dirac point [12], which is where the chemical potential of graphene is located for undoped samples.

The position of the chemical potential can easily be shifted above or below the Dirac point, (thus altering the carrier concentration in the material) by applying a voltage. The carrier concentration in graphene in relation with the applied voltage can be calculated as

$$n_c = \frac{V_g \varepsilon_0 \varepsilon_d}{ed}, \text{ (4-1)}$$

where V_g is the applied voltage, ε_0 and ε_d the permittivity of vacuum and the relative permittivity of the substrate respectively, e the electron charge, and d the substrate thickness [8,120]. Having obtained the carrier concentration of the system the chemical potential can be calculated as

$$\mu = \hbar v_f \sqrt{\pi n_c}, \text{ (4-2)}$$

where $\hbar$ is the reduced Planck constant and, v_f Fermi velocity [206]. To observe the change in optical behaviour of graphene, conductivity is calculated as a function of wavelength taking into account the intraband and interband transitions. The complex conductivity of graphene for varying chemical potential values is obtained with use of the Kubo formula as

$$\sigma_{real}(\omega) = \frac{\sigma_0 \mathrm{H}}{2}\left[\tanh\left(\frac{\hbar\omega + 2\mu}{4k_B T}\right) + \tanh\left(\frac{\hbar\omega - 2\mu}{4k_B T}\right)\right], \text{ (4-3)}$$

$$\sigma_{imag}(\omega) = \frac{4\mu\sigma_0}{\hbar\omega\pi}\left(1 - \frac{2\mu^2}{9t^2}\right) - \frac{H\sigma_0}{\pi}\log\frac{|\hbar\omega + 2\mu|}{|\hbar\omega - 2\mu|}, \text{ (4-4)}$$

$$\sigma_{total}(\omega) = \sigma_{real}(\omega) + i\sigma_{imag}(\omega), \text{ (4-5)}$$

where $\sigma_0 = e^2/4\hbar$, $\mathrm{H} = \left[1 + (\hbar\omega)^2/(36t^2)\right]$, T the temperature, t the hopping parameter, and ω the angular frequency [94]. By including a cubic term in the density of states this equation goes beyond the Dirac-cone approximation thus providing highly accurate results for high photon energies. In this case scattering losses are assumed to be negligible. In section 4.1.6, the results of the ideal case discussed here are compared with results obtained for different values of the phenomenological scattering rate Γ.

Even though the response of the permittivity is essentially determined by valence and conduction electrons, the highly polarized environment originating from core electrons shouldn't be ignored. The dielectric function including the contribution of the core electrons (background permittivity) can be expressed as

$$\varepsilon_m(\omega) = \varepsilon_\infty + i\frac{\sigma_{total}}{\omega d_g} \quad , (4\text{-}6)$$

where $\varepsilon_\infty = 5.5\varepsilon_0$ is the background permittivity [82,207–209], and d_g graphene's thickness (taken as 0.34nm).

It should be mentioned that for wavelengths shorter than 410nm (3.02eV) an exciton-dominated peak with a maximum at 270nm (4.6 eV) begins to appear [88,91] and thus this model is no longer valid. Complex permittivity of graphene is plotted as a function of photon energy and chemical potential in Figure 4.2.a (*real*) and Figure 4.2.b (*imaginary*) parts at a temperature *T* of 300K and a hoping parameter *t* of 2.7eV for photon energies between 0.4eV and 3eV and chemical potential μ in the range 0eV to 1.5eV.

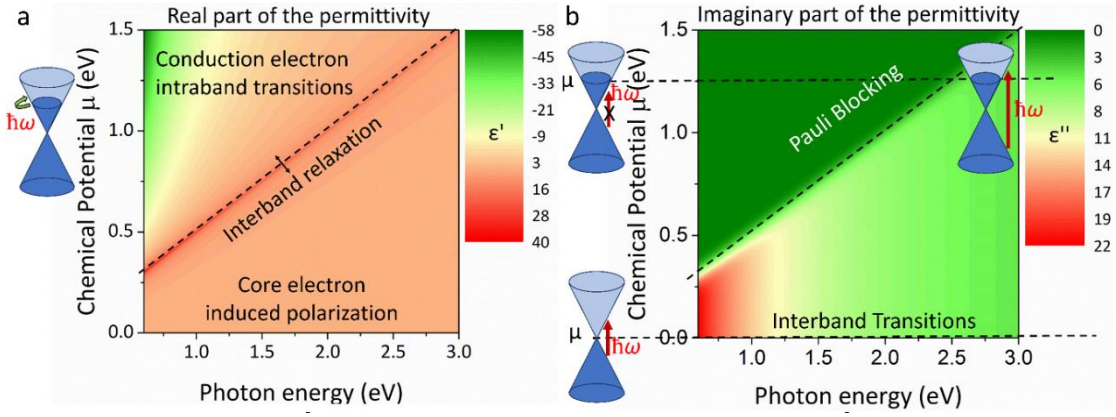

Figure 4.2 a. Contour plot of the real part of the permittivity of graphene at visible and near infrared (NIR) wavelengths for a range of chemical potentials. Dirac cone diagrams are used to demonstrate the interactions responsible for the observed optical response and the dominant contributing mechanisms are labelled. The green arrows correspond to intraband transitions. **b.** Contour plot of the imaginary part of the permittivity of graphene at visible and NIR wavelengths for a range of chemical potentials. The red arrows correspond to interband transitions.

For photon energies $\hbar\omega > 2\mu$ *imaginary* permittivity is positive, corresponding to energy loss for photons propagating through the material. This loss is due to absorption of photons by valence electrons participating in vertical interband transitions. In the same spectral region, *real* permittivity has a stable value of 5.5 due to the polarization originating from the core electrons as seen in Figure 4.2.a. A sudden and severe change occurs in both *real* and *imaginary* permittivity at the limit where photon energy equals twice the chemical potential in graphene ($\hbar\omega = 2\mu$). As conduction band states become occupied with electrons they become unavailable for transitions (Pauli blocking). As a result photons with energy less than twice the chemical potential ($\hbar\omega < 2\mu$) cannot contribute to interband transitions and so losses experienced by light propagating through the material become low giving an almost zero value for *imaginary* permittivity.

Finally, for increasingly high chemical potential and when $\hbar\omega < 2\mu$, *real* permittivity becomes negative and thus graphene demonstrates plasma behaviour. Due to the high chemical potential value, the conduction band has enough filled states, such that a large quantity of free electrons are provided which can flow in a similar way as in metals. In this spectral range Transverse Magnetic Surface plasmon polaritons can be supported due to the metallic behaviour of graphene.

In multilayer systems of alternating dielectric/ conducting materials each individual interface with a conducting layer can support Transverse Magnetic (TM) modes of bound surface plasmon polaritons [72,210]. When the separation distance (here d_g) between the interfaces is smaller than the decay length $\hat{z}$ of individual TM modes (as is the case for very thin metal films) they begin to interact with each other resulting in coupled modes. Even though such modes should be possible in bi-layer/multi-layer graphene structures, they shouldn't be allowed in single layer graphene. This is because graphene is a two dimensional sheet of carbon atoms and thus the charge distribution in monolayer graphene is more accurately described by a purely two dimensional surface.

It is important to also mention that in the simulations in this thesis graphene is treated as a layer with a finite thickness of 0.34nm. This means that even though hybrid-coupled modes as the ones described previously are not allowed in real graphene samples, they are not forbidden in the simulation. This of course means that the simulations have a certain limitation when it comes to the degree of accuracy that they can describe the behaviour of the plasmons in graphene. Nevertheless, as will be shown later this limitation does not lead in any significant inaccuracy and the volumetric model for graphene simulations can still be considered to provide highly accurate predictions for the behaviour of the device presented here.

Since graphene in this work is modelled as a very thin conducting layer (instead of a 2D surface) and the device under study in this work has dielectric materials both above (ionic gel) and below (air) the graphene layer (Figure 4.3.a), a multilayer assumption is used to obtain the plasmon dispersion that most accurately matches the results obtained by the simulation. Taking into account only lowest order bound modes and TM modes that are non-oscillatory in the z-direction normal to the interfaces (see axis in Figure 4.3.a), plasmon wave-vector k_{sp} is implicitly related to frequency ω by the equation

$$\exp(-4k_1 d_g / 2) = \left(\frac{k_1/\varepsilon_1 + k_2/\varepsilon_2}{k_1/\varepsilon_1 - k_2/\varepsilon_2}\right)\left(\frac{k_1/\varepsilon_1 + k_3/\varepsilon_3}{k_1/\varepsilon_1 - k_3/\varepsilon_3}\right), \quad (4\text{-}7)$$

where $k_i = \sqrt{k_{sp}^2 - k_0^2 \varepsilon_i}$ is the component of the wave vector perpendicular to the interfaces for each distinct region (in this case i=1,2,3 where i=1 corresponds to the graphene layer) and $k_0 = \frac{\omega}{c}$ the wave-vector of the incident photons [72]. For simplicity both dielectric materials will be assumed as infinitely thick and described by the permittivity of air (Figure 4.3.b). Since dielectrics above and below the graphene layer have equal permittivity values, equation (4-7) can be further reduced and the dispersion relation split as

$$\tanh k_1 d_g / 2 = -\frac{k_2 \varepsilon_1}{k_1 \varepsilon_2}, \quad (4\text{-}8)$$

and

$$\tanh k_1 d_g / 2 = -\frac{k_1 \varepsilon_2}{k_2 \varepsilon_1}, \text{ (4-9).}$$

Equation (4-8) describes modes of odd vector parity ($E_x(z)$ component of electric field is odd, $H_y(z)$ component of magnetic field and $E_z(z)$ component of electric field are even functions) and equation (4-9) describes modes of even vector parity ($E_x(z)$ is even, $H_y(z)$ and $E_z(z)$ are odd functions)[72].

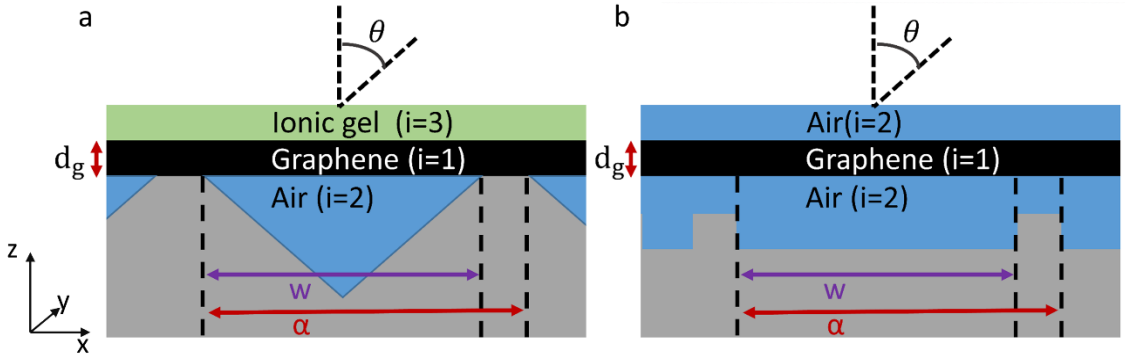

Figure 4.3 a. Schematic of the multilayer setup and cross-section of the diffraction grating structure. **b.** simplified device schematic used for theoretical calculations, the thickness of the two air layers is assumed as infinite when calculating the plasmon dispersion.

The odd mode described by equation (4-8) supports excitations at frequencies slightly higher than a simple non-hybrid mode whose plasmon dispersion is described by $k_{sp} = k_o \sqrt{(\varepsilon_d \varepsilon_m)/(\varepsilon_d + \varepsilon_m)}$. This can be seen from Figure 4.4.a and b. where the dispersion of the odd mode is compared to that of a normal non-hybrid plasmon mode for the same chemical potential (0.6eV). It can be seen that the odd mode allows coupling for slightly higher photon energies for the same wave-vector. The frequency difference between the two modes is small and stable especially for gratings with shorter lattice constants like the ones used for the simulations in this thesis.

Figure 4.4.c shows the dispersion of the odd mode obtained from equation (4-8), for a graphene layer with a chemical potential of 0.55eV and 0.6eV. Strong modulation of plasmon mode is observed with an increase of 0.05eV in plasmon energy for just 0.04eV increase in graphene chemical potential.

As will be shown later in this chapter, the simulation results have a better agreement with the odd plasmon mode dispersion than with that of the non-hybrid mode (the even mode can be ignored as its corresponding dispersion is very far red-shifted when compared to that of the odd and non-hybrid plasmon mode). This means that indeed simulating graphene with an assigned finite volume (instead of as a 2D surface) can introduce a small inaccuracy in the results. It can be seen from Figure 4.4.d (reference [210]) that odd plasmon modes are (weakly) sensitive to the thickness of the conductive layer, with the dispersion of the plasmon mode for the thicker layers converging faster to the surface plasmon frequency for the same wave-vector values. Thus a small thickness dependence can be also expected in the simulation results. The expected inaccuracy from the volumetric simulation of graphene is too small to be considered significant and thus the model can be used to accurately predict the behaviour of the device proposed in this chapter. Recently simulation tools

like the software suite offered by Lumerical have started offering the ability to simulate graphene as a purely 2D surface described by a surface conductivity thus overcoming such limitations that simulation tools had in the previous years.

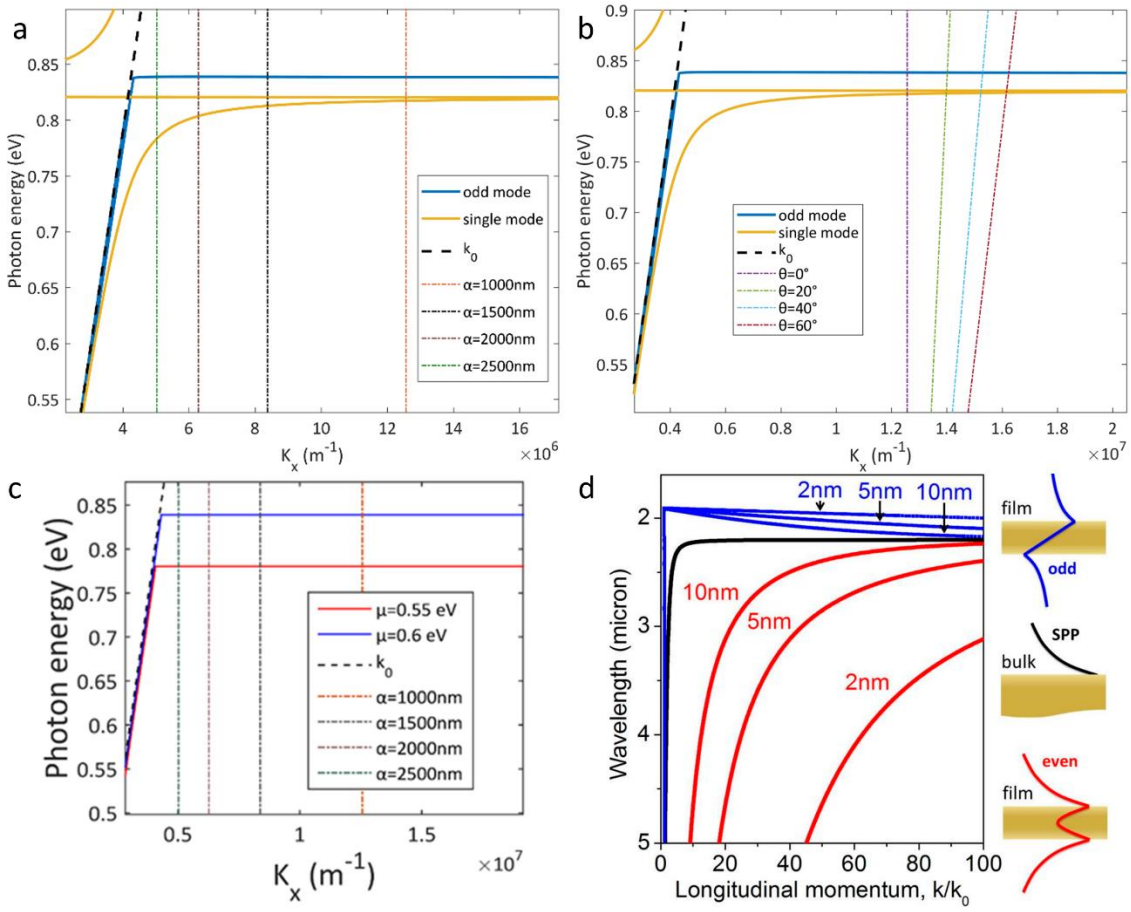

Figure 4.4 In **a.** and **b.** a comparison is made between the dispersion of the odd and non-hybrid (single) plasmon modes (μ=0.6eV). Phase matching conditions are also presented for **a.** various grating lattice constants α under a 60 degree angle of incident light **b.** different angles of incidence on a 1000nm pitch grating. It can be seen that regardless of angle of incidence or pitch length (especially for shorter pitch length as used in this thesis) there is a stable but small offset between the bulk and odd plasmon modes. **c.** Odd mode of the graphene plasmon dispersion is plotted as solid lines for a chemical potentials μ of 0.55eV (red) and 0.6eV (blue). The light line (k_0) is plotted as a black dashed line. **d.** SPP modes dispersion for a metal air interface. The black curve corresponds to a bulk system with a single interface with air. The Red and blue lines correspond to even and odd modes respectively for different thicknesses of a metal film that has two interfaces with air. The modal profiles are demonstrated on the right side (d. of this graph has been included from reference [210] under a Creative Commons license).

4.1.2. Phase Matching

Interaction between free carriers and the incident electromagnetic field, results in the wave vector of surface plasmon modes ($\hbar k_{sp}$) being greater than that of incident photons ($\hbar k_0$) for the same frequency. Because of the mismatch in wave-vectors, surface plasmons cannot normally be generated and thus phase matching is required. In this device, phase change is achieved by the introduction of a 2-dimensional grating below the graphene in the form of an inverted pyramid array (Figure 4.3.a). A simple one-dimensional groove approximation (Figure 4.3.b) can be used to calculate the

required lattice constants (or pitch), α, of the diffraction grating. Phase matching between surface plasmons and incident photons takes place due to the increased wave-vector of the diffracted photons whenever

$$k_{sp} = k_x \pm v2\pi / \alpha \text{ , (4-10)}$$

where grating order v is an integer (1,2, 3,…) and $k_x = ksin\theta$ the in plane wave vector of impinging photons [72].

Dispersion of the odd mode is plotted in Figure 4.5.a together with the diffracted photon wave-vector lines (solutions of equation 4-10) for diffraction grating lattice constants varying between 1000nm and 2500nm and a graphene chemical potential of 0.55eV and 0.6eV in graphene, with $v = 2$. The dashed lines show the wave vector of directly diffracted photons. Points where the lines cross correspond to perfect phase matching conditions under which incident light couples to surface plasmon polaritons in graphene, *via* diffractive scattering from the underlying pyramid structure. Hence Figure 4.5 visually displays phase matching conditions under electrical bias conditions for graphene.

Taking a closer look at the spectral region close to the plasmon excitation energy, Figure 4.5.b (which shows the same information as Figure 4.5.a but with highly zoomed y-scale) it can be seen that the excitation frequency experiences a weak blue-shift (photon energy increases) as the diffraction grating lattice constant becomes longer. This blue-shift is expected for the odd mode [210], and in this case is weak due to the extreme thinness of graphene and strong coupling between the top and bottom interface plasmon modes. As seen in Figure 4.4.a, especially for the shorter grating lattice constant values the phase match frequency is only weekly affected for the non-hybrid mode, in general having only a small shift in photon energy when compared to the results for the odd plasmon mode.

Figure 4.5.c / .d show phase matching conditions for various angles of incidence for impinging photons. As expected larger angles of incidence result in an increase in diffracted photon wave vector. However since the plasmon dispersion is almost flat, coupling can occur for a wide range of angles even up to 60° with no change of plasmon excitation frequency. This is extremely unusual for a grating coupler, and highly important because it means coupling is essentially non-directional. In practice, the structure will collect and couple incident light over a very wide range of angles of incidence, as is the case when light is tightly focused by a short focal lens. This is investigated in more depth in the next section. The same holds true for the non-hybrid (single) plasmon mode as can be seen in Figure 4.4.b. As was the case for the phase matching conditions for different lattice constants, once again there only difference that can be observed between the phase matching conditions for the odd and non-hybrid plasmon mode is a small shift in the phase match frequency.

In general the shift between the odd and the non-hybrid plasmon mode is small and remains constant in terms of phase match frequency under all the different structural conditions. It can be seen in the following section that (due to the limitation of having to assign a finite thickness to the graphene layer) there is a better agreement of the simulation results with theoretical results for the odd plasmon mode. As mentioned before such a mode is not allowed in single layer graphene (but is possible to exist in bi-layer/multi-layer graphene or graphene layers separated by atomically thin

dielectrics like hexagonal boron nitride), but since the difference between the two modes is very small the model and simulations described in this chapter can be expected to accurately predict the behaviour of a real experimental device.

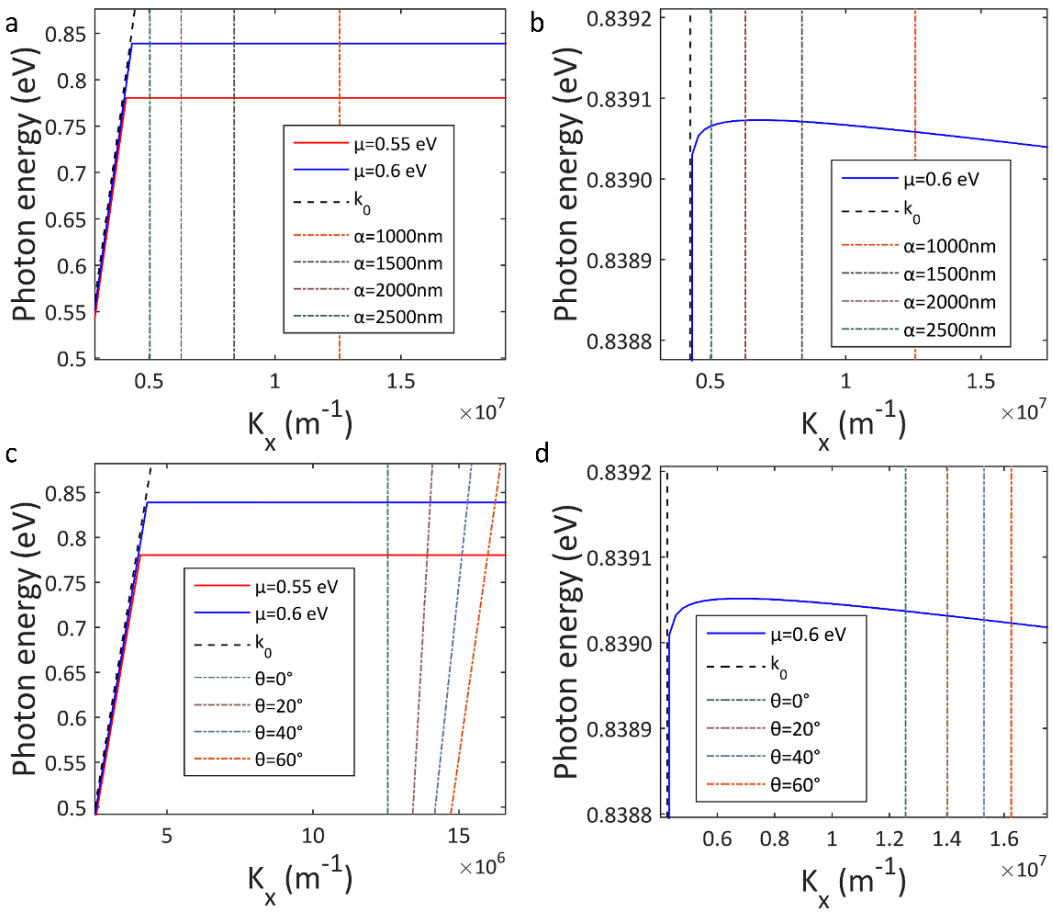

Figure 4.5 Odd mode of the graphene plasmon dispersion is plotted as solid lines for a chemical potentials μ of 0.55eV (red) and 0.6eV (blue). The light line (k_0) is plotted as a black dashed line and the dash-dot lines represent the diffracted photon wave-vector due to the diffraction grating. In **a.** the diffracted photon lines are plotted for varying lattice constants α of the diffraction grating between 1000nm and 2500nm, **b.** a zoomed in scale of photon energy axis showing the negative slope of the dispersion line for increasing wave-vectors. In **c.** the diffracted photon lines are plotted for varying angles of incidence θ from 0 to 60 degrees, **d.** a zoomed in scale of photon energy axis showing the negative slope of the dispersion line for increasing wave-vectors.

4.1.3. Rigorous Coupled Wave Analysis of the Device

The properties of the phase matched solutions (points of intersection of the lines on Figure 4.5) are studied more carefully, by cross comparing to other methods of simulation.

RCWA (Rigorous coupled wave-analysis) is a highly efficient semi-analytical method for simulating electromagnetic behaviour of periodic structures. Electromagnetic fields and device geometries are represented by a sum of harmonic functions in Fourier space, and fields are solved in the form of a transmission line problem. RCWA simulations are particularly useful for graphene devices because (in contrast to FDTD (Finite-Difference Time-Domain) methods or FEM (Finite Element Methods)) they do not require solution of Maxwell's equations over dense grids. Instead, structure is divided

into uniform layers in the z direction and electromagnetic modes calculated by applying a layer by layer analytical solution.

Unlike RCWA, FDTD is a grid based time domain differential numerical analysis technique. In this method the time-dependent Maxwell's equations are discretized by using central-difference approximations to the space and time partial derivatives resulting in finite-difference equations that can then be repeatedly solved at given instant times with the use of a computer to provide the electric and magnetic field vector components until a steady-state electromagnetic field is fully evolved.

In this thesis the RSoft software provided by Synopsis was used for the simulations. Both RCWA and FDTD simulations have been used to provide cross-verification of the results.

In this section, the relationship between geometrical parameters associated with the underlying inverted pyramid array diffraction grating (as indicated in Figure 4.6.a) and the behaviour of coupled surface plasmons are investigated using RCWA simulations, for the purpose of optimising the geometry. The effect of geometry on plasmon energy, excitation efficiency (plasmon peak strength), and electrical modulation of plasmon frequency are investigated. Substrate permittivity is taken as that of Si.

A 50nm thick ionic gel layer positioned above of graphene provides an alternative to high-k gate dielectrics, and provides a practical method to apply strong electrical modulation of graphene chemical potential. Parameters for the underlying diffractive pyramid structure correspond to those achieved by KOH etching of <100> silicon wafers. Graphene is then suspended above the inverted pyramid by (wet / dry) transfer process. Graphene is sufficiently accurately modelled as a 0.34nm thick layer (since skin depth is significantly thicker in the spectral range of interest) with permittivity given by equation (4-6). Realistic thickness is chosen over thicker effective layers or a 2D sheet in order to have an accurate separation distance for the two interfaces.

Figure 4.6.b shows RCWA simulated plasmon absorption for underlying 1000nm pitch (α) / 500nm side width (w) pyramid structure and a chemical potential in range of 0.3eV to 0.6eV. Solutions of the matched wave vectors coupled by the underlying structure calculated by the analytical method are superimposed as dashed lines for the odd mode (black) and the single interface mode (cyan) for $v = 2$.

An absorption peak is observed away from the interband transition region and at the location of the phase match frequency appearing as a sharp (white) line. As graphene chemical potential increases, the real part of permittivity becomes increasingly negative due to higher quantity of free carriers. Thus a blue-shift in plasmon excitation frequency is observed (dispersion line moves to larger energy), thereby confirming electrically tuneable plasmon absorption.

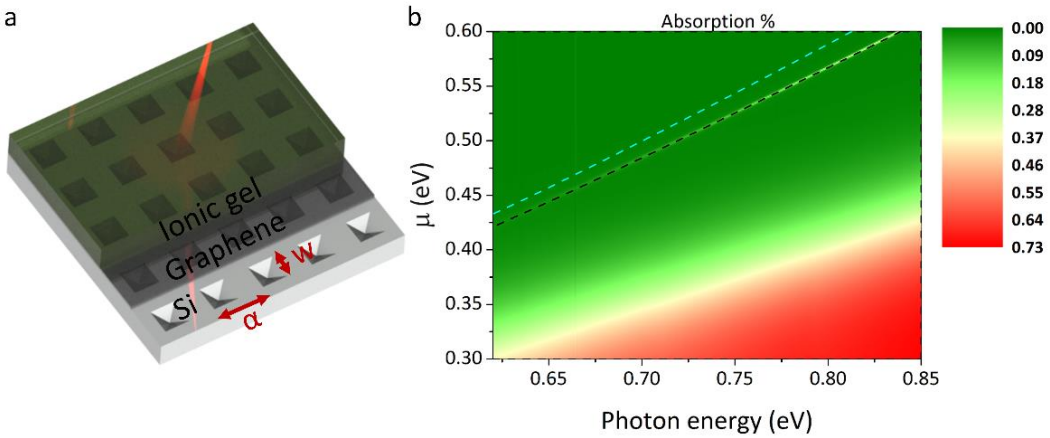

Figure 4.6 a. 3D schematic of the simulated device under laser illumination demonstrating the pyramid structures, the graphene layer placed above them, and above the monolayer an ionic gel layer which is typically used to electrostatically modulate the chemical potential in graphene. Pitch (α) and pyramid side width (w) is also shown **b.** RCWA simulation result showing the chemical potential versus photon energy, demonstrating the large tuning range for plasmon excitations. Theoretical calculation results for the odd mode (black dashed lined) and single interface (non-hybrid) mode (cyan dashed line) can also be seen with the odd frequency mode having an excellent overlap with the plasmon absorption peak obtained from the simulation (white sharp line). On the lower part of the figure the onset of interband transitions can be seen.

Looking more closely at the superimposed lines for the analytical model, for the single interface mode (cyan line) it predicts plasmon excitations at lower frequencies compared to the RCWA method, whereas they are in excellent agreement to RCWA solutions for odd vector parity mode (black line). This provides proof that the excited mode in the simulations is indeed better described by the odd mode theory. As mentioned earlier, even though such a mode is not supported by a single real graphene monolayer, this model can still be very highly accurate as the difference with the single plasmon mode is expected to be only a small shift in phase match frequency. In both cases strong modulation of plasmon excitation energy can be clearly observed with 0.04eV shift in chemical potential resulting in ~0.05eV shift in plasmon energy. Intensity of the absorption peak heavily depends on optical loss in graphene, mainly characterized by the imaginary part of permittivity, with higher losses corresponding to broader and lower peaks [38]. Plasmon excitation peaks become larger and narrower with increasing graphene chemical potential as a result of moving further away from the interband absorption region (observed as a broad absorption region at the lower part of the graph). It was found that plasmon excitation can effectively be shut down by lowering graphene chemical potential. This is due to a change from interband to interband transition region of operation, and can occur over a broad wavelength range. This result is of great importance for applications as it provides a dynamic means of photonic switching which can be exploited for high density optical interconnects.

Figure 4.7 demonstrates how the absorption spectra in the simulation changes for a. increasingly thick graphene layers with effective permittivity values and b. without changing the value of the permittivity. In both cases only small changes in terms of plasmon frequency and absorption can be observed. It is important to mention that Figure 4.7.b (where the thickness of the graphene layer is increased while maintaining the same permittivity value for the layer) agrees well with what would be expected for an odd plasmon mode when the conductor layer thickness is increased (as

seen in Figure 4.4.d). In both cases having an increasingly thick layer results in a very small red-shift of the phase-match frequency due to the faster convergence of the odd plasmon mode dispersion to the surface plasmon frequency for the same wave-vector. It is clear from this result, as well as the fact that the simulation better agrees with the odd plasmon mode theory, that the simulation is not perfect at reproducing the behaviour of a real 2D graphene layer. Nevertheless, since the difference between the odd mode that is observed in the simulations and the non-hybrid mode that is expected in reality is pretty much negligible, and also the fact that the results hardly change for increasingly thick graphene layers, it can be assumed that the simulation results are highly accurate at predicting the behaviour of a real experimental device. At the point of time that this research was performed utilizing 2D surfaces in simulation environments was not easily available. Nowadays several software packages include 2D rectangles as options to simulate 2D materials like graphene. It is thus now recommended that these simulations are performed on such 2D rectangles instead of assuming a graphene layer with a finite thickness since they can provide more highly accurate results.

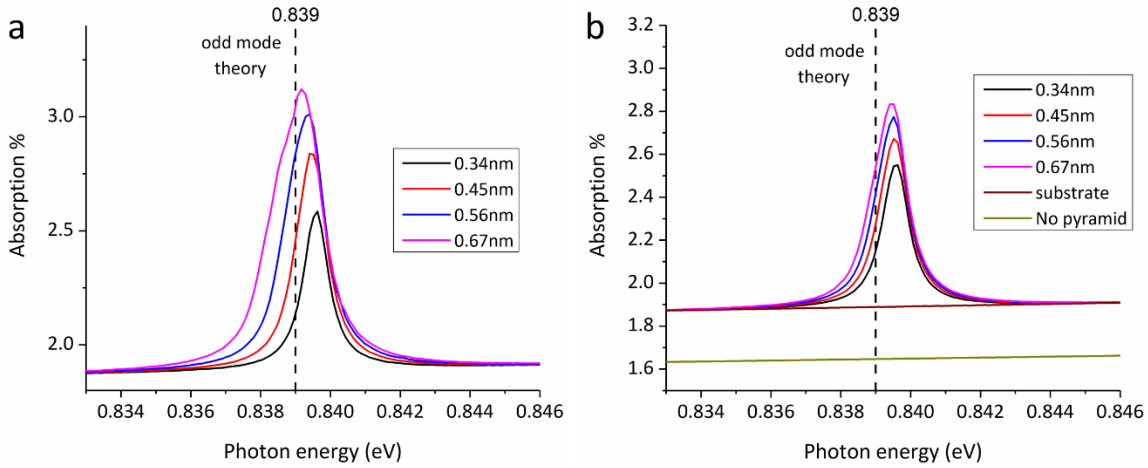

Figure 4.7 a. RCWA simulation of plasmon absorption for a graphene layer modelled as a 0.34nm thick layer and increasingly thicker effective graphene layers (thickness change taken into account for permittivity calculations). **b.** RCWA simulations demonstrating the plasmon absorption for different thicknesses of the graphene layer. The permittivity of the thicker layers has not been adjusted and thus they are not effective graphene layers. Also demonstrated is the absorption spectra when the diffraction structure is removed (No pyramid). Without the pyramid there is no longer phase matching and the plasmon is not excited thus there is no absorption. Finally the substrate absorption without the graphene layer is demonstrated.

4.1.4. Optimisation of Structure Geometry

The underlying 2D grating geometry can be scaled to shift the coupled graphene plasmon frequency to match a broad range of incoming wavelengths and incidence angles, and also improve coupling efficiency. Plasmon absorption strength depends heavily on diffraction efficiency of the underlying grating structure used for phase matching. Improved diffraction efficiency increases coupling between incident light and graphene plasmons, resulting in higher intensity plasmon absorption peaks.

Diffraction efficiency is related to density and size of diffractive structures. Optimization of size and spacing between inverted pyramids results in significantly improved diffraction efficiency. Effect of

pyramid width (w) is investigated in Figure 4.8.a which shows RCWA simulations for fixed diffraction grating pitch of 1000nm and chemical potential of 0.6eV.

Plasmon absorption becomes stronger with increasing pyramid width, until the pyramid becomes approximately ¾ the size of the pitch where it begins decreasing again. Investigating this further, Figure 4.8.b reveals a linear relationship between pyramid size and grating pitch allowing prediction of maximum plasmon absorption. This is helpful when scaling the device for different applications. Plasmon energy (frequency) is found to be unaffected by pyramid size.

Diffracted photon k-vector is related to grating pitch (α) and so provides control of phase match frequency between incident photons and graphene plasmons. This is investigated in Figure 4.8.c, for pyramid width (w=500nm), graphene chemical potential of 0.6eV. A very small blue-shift of plasmon energy is observed with increasing pitch length (α), which is in agreement with theoretical expectations for the odd mode (but once again the difference with the non-hybrid mode is small). The analytical calculations are found to be highly accurate agreeing with RCWA simulations within 0.001eV (1nm).

Virtually no shift in excitation energy is observed as a function of incidence angle (Figure 4.8.d) for a 1000nm pitch/ 500nm pyramid width grating structure, and 0.6eV graphene chemical potential. This is also predicted by the analytical calculation (showing similar results of the odd and non-hybrid plasmon modes). Wide angle wavelength independent absorption of incident light is very unusual and useful in practice. High efficiency coupling of incident light by short focal length high numerical aperture lens is predicted.

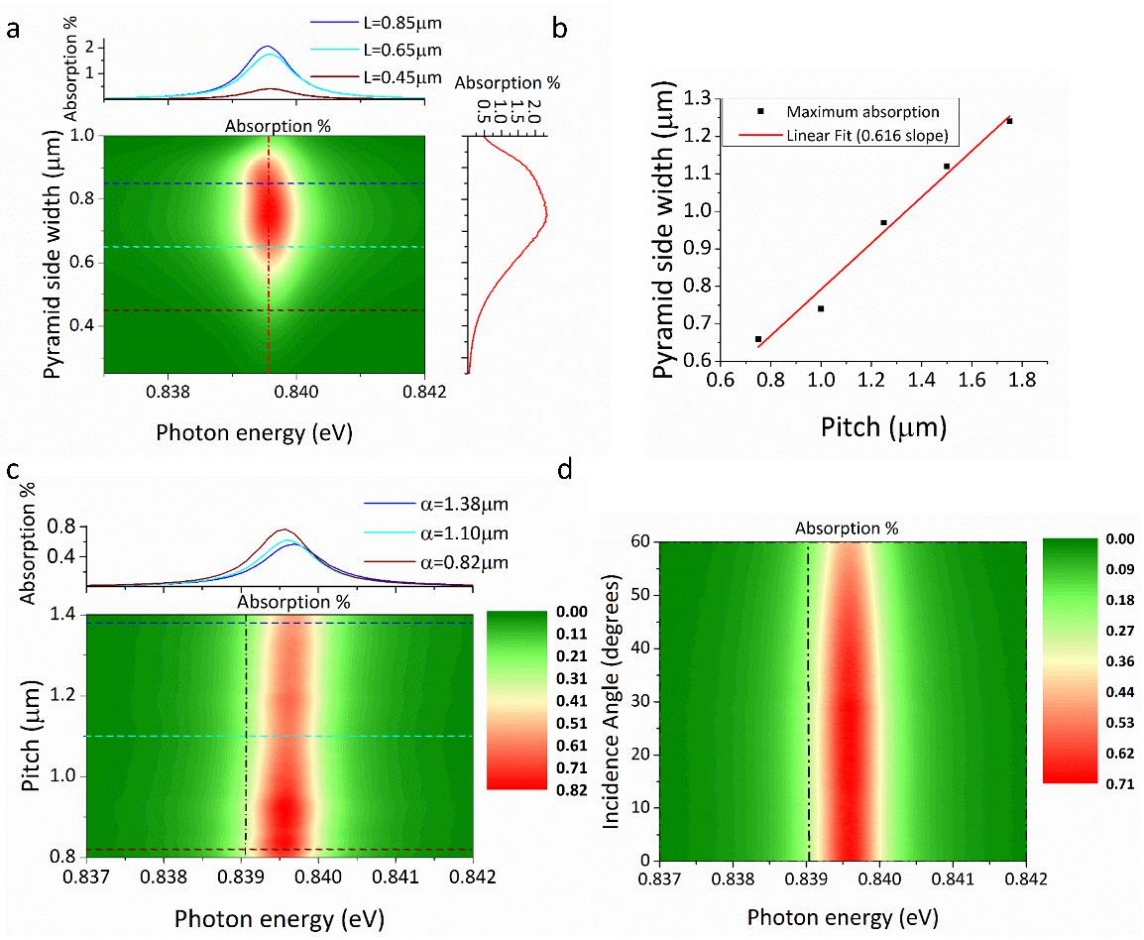

Figure 4.8 a.The effect of pyramid size on plasmon absorption strength is demonstrated for pyramid side width ranging from 0.25μm to 1μm while maintaining an aspect ratio of 1.0. **b.** The linear relation for pyramid size and pitch length is demonstrated for achieving highest plasmon excitation efficiency when scaling the device. **c.** The effect of pitch length on plasmon energy and absorption strength is demonstrated, the brown, cyan and blue dashed lines over the contour plot correspond to the three plasmon peaks on the profile plot above. Theoretical calculation results are overlaid as the black dash-dot line. **d.** The effect of incidence angle on plasmon energy and absorption strength is demonstrated. Theoretical calculation results are overlaid as the black dash-dot line.

4.1.5. Incident Light Polarization

Phase matching can only occur for surface plasmon polaritons propagating perpendicular to the diffraction features when incident photons are polarized in the same direction [211]. Unlike 1-Dimensional trench based gratings [37,38], the symmetric pyramid structure diffracts both s and p polarizations with equal efficiency as seen in Figure 4.9.a and b.

Finally it is interesting to see what happens when the aspect ratio of the system changes and how this affects plasmon excitations for different incident photon polarizations. Increasing the width (w) of only one side of the pyramid (moving from square to rectangular structures) breaks the symmetry, thus an increase of coupling efficiency for the polarization satisfying excitations perpendicular to the direction of the extended feature is expected. At the same time a decrease of efficiency is expected for the other polarization. This can be observed in Figure 4.9.b, c and d where for the 1.0 aspect ratio there is no difference between s and p polarisations and the excited plasmons have

the same absorption strength. Figure 4.9.c and d reveal that when moving towards the 2.0 ratio, coupling due to s polarized light begins to decrease until it becomes 0 when the structure becomes a continues trench, while coupling due to p polarized light becomes significantly stronger due to the extended diffraction structure in the direction favouring this polarization.

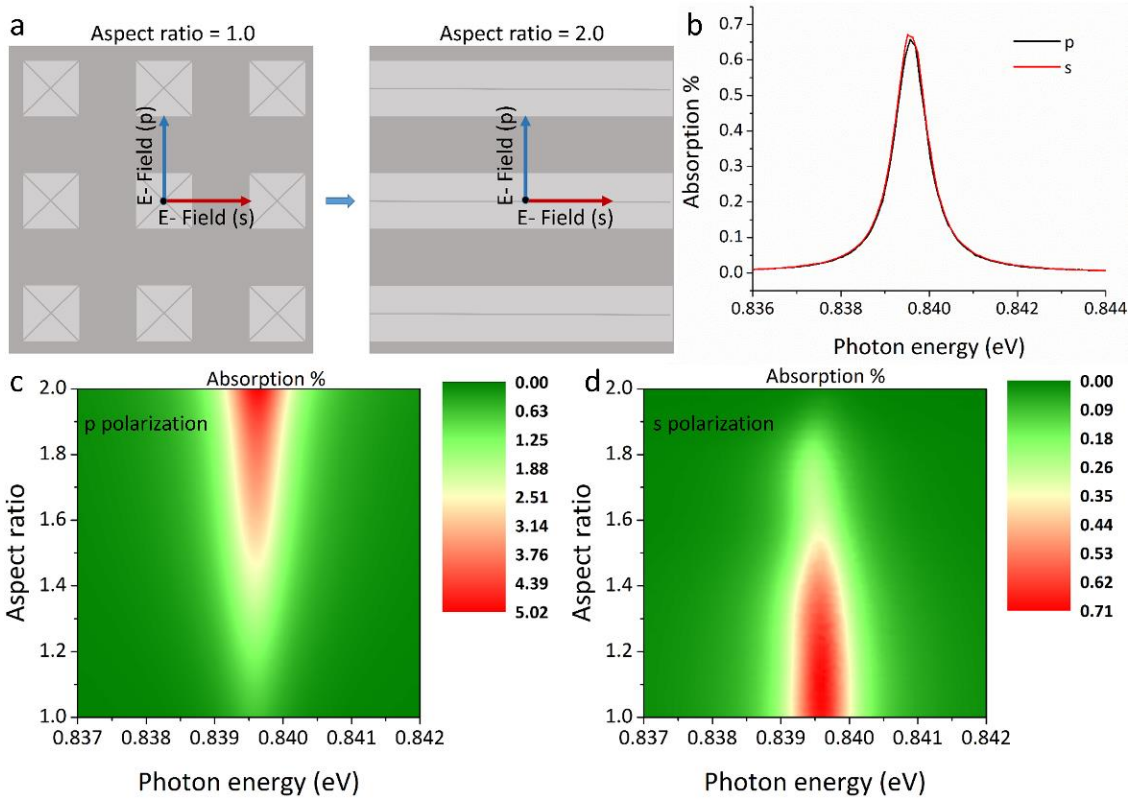

Figure 4.9 a. Demonstration of the E field direction in respect to the diffraction grating for s and p polarization for gratings of 1.0 and 2.0 aspect ratio. In **b.** plasmon excitation for a structure with an aspect ratio of 1.0 is compared for p and s polarization revealing identical absorption peaks. In **c.** and **d.** the effect of aspect ratio of the pyramid sides on plasmon excitation for s and p polarization can be seen where **c.** corresponds to p polarization and **d.** to s polarization.

4.1.6. Dissipative Losses in Graphene

It has been reported that dissipative losses in graphene in the Terahertz [212] and also in the Infrared and Optical frequencies [213] can be significant thus hindering the potential of graphene as a plasmonic material. Even though for suspended graphene layers carrier mobility in excess of 200.000 $cm^2 V^{-1} s^{-1}$ has been demonstrated (by employing current induced heating in order to reduce impurities), these high mobility values are limited over a small range of carrier concentrations [214]. For unsuspended devices recently high mobility values have been demonstrated for CVD graphene by introducing hBN/graphene/hBN heterostructures on Si/O2, achieving mobility values comparable to exfoliated graphene (as high as 350.000 $cm^2 V^{-1} s^{-1}$ at low temperatures and above 50.000 $cm^2 V^{-1} s^{-1}$ at room temperature) but once again for larger carrier concentrations the scattering loss increases [215]. Ionic gels can achieve very high electrostatic doping levels in graphene at the expense of introducing strong carrier scattering. Typical carrier mobility for graphene devices with ionic gel gates ranges between 500 $cm^2 V^{-1} s^{-1}$ and 1200 $cm^2 V^{-1} s^{-1}$ for unsuspended graphene layers [44,193,216,217].

Even though this study is a purely theoretical approach, it is important to investigate how the device performs when including experimentally obtained mobility values in the calculations. In this case simplified equations for the conductivity of graphene are used instead of equations (4-3) and (4-4) as

$$\sigma_{inter}(\omega) = i\frac{e^2}{4\pi\hbar} ln\left[\frac{2|\mu| - \hbar\omega - i\Gamma}{2|\mu| + \hbar\omega + i\Gamma}\right], \text{(4-11)}$$

$$\sigma_{intra}(\omega) = i\frac{e^2}{\pi\hbar(\hbar\omega + i\Gamma)}\left[\mu + 2k_B T \ln\left(\exp(-\mu / k_B T) + 1\right)\right], \text{(4-12)}$$

where the mobility is included through the phenomenological scattering rate Γ [218]. Unlike in equations (4-3) and (4-4) where a cubic term is included in the density of states, equations (4-11) and (4-12) do not go beyond the limitations of the Dirac cone approximation. A further simplification is the exclusion of thermal broadening for interband transitions. Nevertheless these simpler equations can accurately demonstrate the effect of dissipative losses in the absorption spectra when included in RCWA calculations by choosing different mobility rates. The resulting complex permittivity of the graphene layer for different mobility values μ_g is demonstrated in Figure 4.10.a in comparison with the result obtained through the use of equations (4-3) and (4-4).

By including the permittivity values for different mobility rates when modelling the graphene layer for the RCWA simulations the effect of dissipative loss can be observed in the absorption spectra as seen in Figure 4.10.b. Due to the linear Dirac cone assumption and thus the exclusion of the cubic term in the density of states the position of the absorption peak is slightly blue shifted when compared to the result obtained through equations (4-3) and (4-4). Since equations (4-3) and (4-4) go beyond the limitations of the Dirac cone approximation, the position of the absorption spectra obtained from them is expected to be more accurate, nevertheless the difference is very small. As seen in the simulation results, absorption spectra is largely depended on losses in graphene and the peaks become significantly shallower and broader with decreasing mobility. Dissipative losses can thus have a very negative effect on plasmon absorption and can be a very significant issue when designing real world applications. Therefore, it is crucial that care is taken to improve the mobility in the graphene layer by reducing layer damage, impurities, and substrate interactions, while maintaining strong electrostatic control over the chemical potential. Further research is required for providing easily transferred CVD graphene samples with high mobility values as well as effective gating methods that do not introduce strong scattering in the graphene layer.

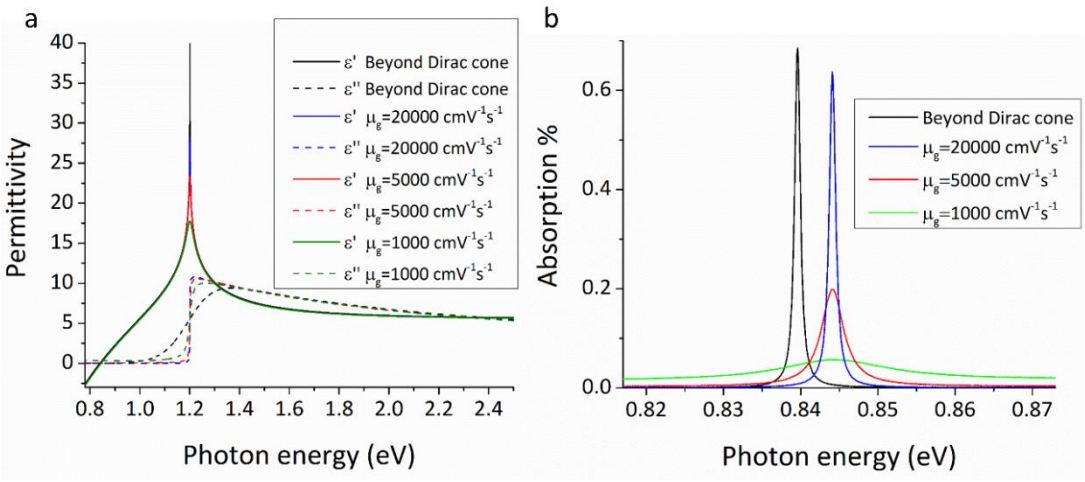

Figure 4.10 a. Complex permittivity of graphene for different mobility rates at 0.6eV chemical potential. The black lines represent results obtained when including a cubic term in the density of states (thus departing from the linear Dirac cone approximation) and the thermal broadening for interband transitions. **b.** RCWA simulation results for different mobility values for a chemical potential of 0.6eV. Decreasing carrier mobility results in shallower and broader absorption peaks. Black line corresponds to absorption spectra as obtained when modelling the graphene layer when including thermal broadening for interband transitions and the cubic term in the density of states.

4.1.7. Conclusion

In conclusion this simulation and modelling work of the reported optical device configuration shows strong electrical modulation of surface plasmon energy and absorption intensity. The underlying 2-dimensional array of inverted pyramids is highly efficient for coupling photons to the graphene film supporting excitation of plasmons equally for both s and p polarizations due to the structure symmetry. By optimizing the diffraction efficiency of the underlying structure, significant increase in plasmon absorption intensity was observed. The device provides highly efficient dynamic modulation of the plasmon energy operating over a very large spectral range and up to the near infrared for currently easily achievable graphene chemical potentials. Assuming higher chemical potentials, operation of the device can be extended to the visible spectrum as is. Furthermore, plasmon excitation can be effectively shut down by lowering the chemical potential, providing dynamic means of photonic switching which can be exploited for high density optical interconnects. Plasmon absorption was also found to be highly unaffected by angle of incidence thus providing the possibility of exciting plasmons on the monolayer with the use of high numerical aperture lenses. Finally, an analytical model assuming a multilayer setup was presented with excellent agreement to the RCWA simulation results for the odd plasmon mode. In reality this mode cannot be excited in monolayer graphene but since the difference between the odd mode and a non-hybrid plasmon mode is small the results off this model can be expected to be highly accurate in predicting the behaviour of a real experimental device. Overall the device can be utilized in a large number of possible applications including sensors, photonic logic gates, optical interconnects and modulators. Nevertheless, the absorption due to plasmon excitations in graphene remains low even after optimising the structure and thus improvements over this basic setup are necessary to produce high efficiency devices.

4.2. Tuneable Total Optical Absorption Device Based on Graphene

Modelling of the novel device design presented in chapter 4.1 predicted that the device design would be successful at efficiently exciting and controlling the frequency of plasmons in graphene over a very large spectral range. Nevertheless, the results demonstrated very low coupling efficiency between incident photons and graphene plasmons thus resulting in a very small percentage of light absorbed in the graphene layer. In order to overcome this issue, a new and improved device structure based on the previously mentioned concept was designed with the aim of providing efficient plasmon coupling over a large spectral range. The results in this chapter are published in Scientific Reports [71].

In more detail, an optical device configuration allowing efficient electrical tuning of near total optical absorption in monolayer graphene is reported. This is achieved by combining a two-dimensional gold coated diffraction grating with a transparent spacer and a suspended graphene layer to form a doubly resonant plasmonic structure. Electrical tuneability is achieved with the inclusion of an ionic gel layer which plays the role of the gate dielectric. The underlying grating comprises a 2-dimensional array of inverted pyramids with a triple layer coating consisting of a reflective gold layer and two transparent dielectric spacers, also forming a vertical micro-cavity known as a Salisbury screen [58]. Resonant coupling of plasmons between the gold grating and graphene result in strong enhancement of plasmon excitations in the atomic monolayer. Plasmon excitations can be dynamically switched off by lowering the chemical potential of graphene. Very high absorption values for an atomic monolayer and large tuning range, extremely large electrostatically induced changes in absorption over very small shifts in chemical potential are possible thus allowing for very sharp transitions in the optical behaviour of the device. Overall this leads to the possibility of making electrically tuneable plasmonic switches and optical memory elements by exploiting slow modes.

4.2.1. Limitations of Basic Device

Figure 4.11.a shows the basic pyramid structure studied in the previous chapter and Figure 4.11.b shows spectra generated by RCWA analysis for a single graphene layer positioned above a silicon 2-D inverted pyramid diffraction grating with 1.165µm pitch, pyramid base width of 0.65µm, ionic gel refractive index of 1.42 and thickness of 150nm, as a function of chemical potential for an angle of incidence of θ=0°. It can be seen that plasmon absorption can be tuned over a large wavelength range by adjusting chemical potential. Solutions to equation 4-10 are superimposed as a white dashed line overlaying perfectly with the RCWA data. Inter-band absorption can be observed as a broad absorption region when moving to higher frequencies and lower chemical potentials since the Pauli blocking effect is no longer evident (region below the black dash-dot line). Nevertheless, from Figure 4.11.c it is clear that the absorption efficiency for this structure is very poor with only about 3% of incident light absorbed by the graphene layer.

Figure 4.11.d shows an example FDTD simulation plotting the electric field (E-field) energy density through the diffraction structures for a wavelength/chemical potential combination corresponding to the black circle marker of Figure 4.11.b. It can be seen that a large part of the incident electromagnetic field is lost in the bulk silicon material due to its transparency in the infrared, and so does not assist the generation of graphene plasmons.

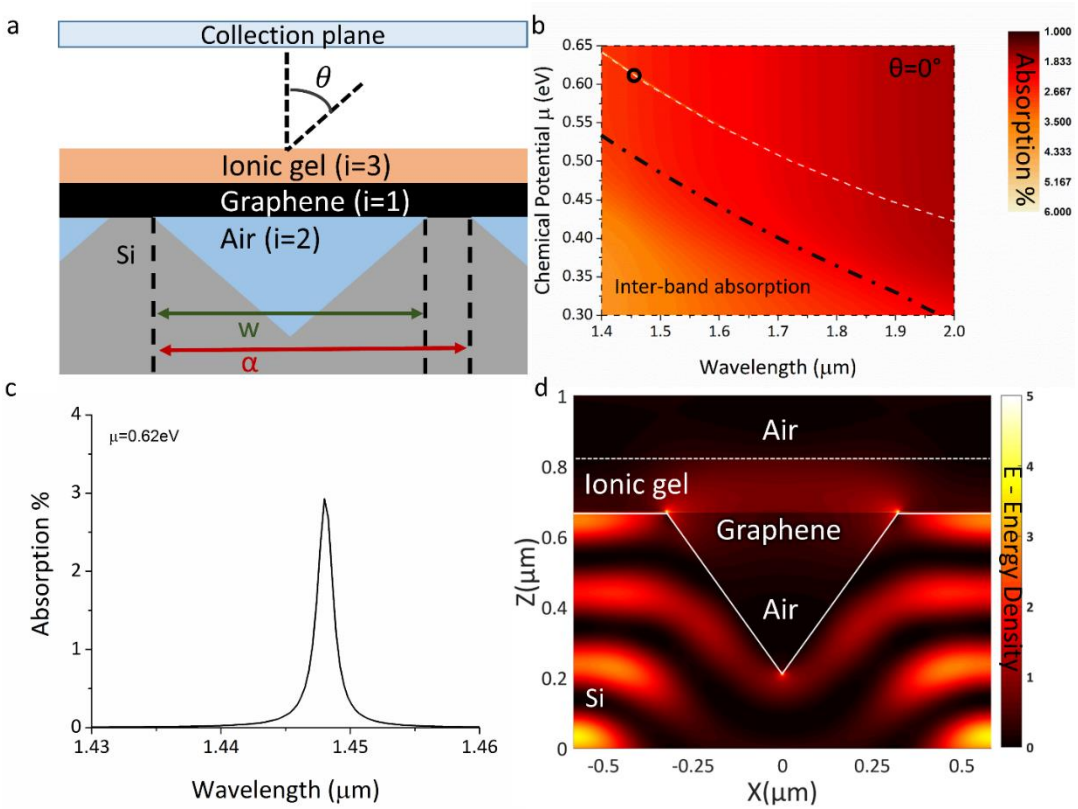

Figure 4.11. a. Slice schematic of the 2-D inverted pyramid diffraction grating **b.** RCWA simulation results of the same device demonstrating excitation and electrostatic control over plasmons in graphene. **c.** Plasmon absorption for a chemical potential of 0.62eV. **d.** FDTD simulation at a wavelength of 1.448μm and P polarization demonstrating the E field energy density resulting from the interaction of incident radiation with the diffraction grating, chemical potential/wavelength combination corresponds to the black circle of b.

4.2.2. Improved Device Concept

Despite advances in the field as discussed in section 3.1.8, achieving strong optical absorption in monolayer graphene in combination with the ability to dynamically tune the wavelength of absorption over a large spectral range remains a difficult but highly anticipated task. Especially so for achieving absorption away from mid infrared and THz frequencies. In this work a device capable of overcoming these limitations by providing efficient electrical modulation of nearly total optical absorption over a large range of wavelengths while allowing operation even at mid-infrared and almost visible light frequencies is presented.

Figure 4.12.a shows a schematic of the device. A two-dimensional array of inverted pyramid pits forms a crossed diffraction grating, which functions as a phase-matching component that couples incident photons to plasmons in a continuous graphene layer [36]. In contrast to previous works, a continuous graphene layer instead of micro/nano patterned graphene allows excitation of propagating modes instead of localized modes. Such propagating modes typically have higher electric field confinement in the surface normal [38].

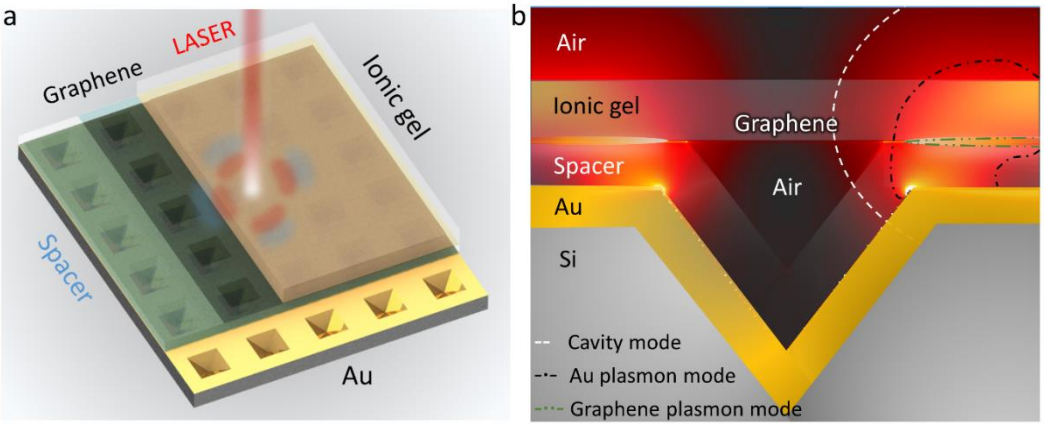

Figure 4.12 a. Schematic of the device setup. **b.** Schematic representation of the device operation, showing the individual mode components.

Optical absorption by the monolayer is further enhanced by positioning Graphene in close vicinity to a gold layer that also allows propagation of plasmons. The structure consists of a conformal two-layer metal-dielectric coating deposited over the underlying diffraction grating. The role of the dielectric spacer is to separate the graphene layer from the gold back reflector but can also be used as a back-gate in order to modulate the chemical potential of graphene. An ionic gel layer is further placed on top of graphene in order to provide a highly efficient gating method for achieving strong electrostatic doping of the atomic monolayer (there is a large variety of ionic gel types that can be used [192]). Using an ionic gel as the top dielectric overcoat material in a gate setup [192,193] enables strong modulation of the chemical potential at low voltage operation (from 0eV up to 0.8eV within 3V of applied voltage) [44] thus providing a wide wavelength tuning range for plasmon excitations in the graphene layer. The inclusion of the spacer and ion gel layers also results in the formation of a weak 1-dimensional micro-cavity transverse to the grating surface that is also known as a Salisbury screen [58].

When phase matching conditions are met, incident light couples by diffraction to slowly propagating surface plasmon modes (traveling across the micro-structured surface), associated with the periodic gold coated pyramid structure. Similarly, surface plasmon modes are excited on the suspended graphene layer. Due to the geometry of the structure and the excitation of the gold plasmon mode, at the edges of the pyramid groove a strong near field is produced that is extended upwards and strongly interacts with the plasmon mode in graphene (Figure 4.12.b). This results in a doubly resonant mode and in the transfer of energy from the gold plasmon mode to the free carriers in graphene thus indirectly increasing coupling of light to the atomic monolayer. Stationary modes of the vertical Salisbury screen cavity do not directly transfer energy to the plasmon modes but independently increase the total amount of absorption in the device. This two-step energy transfer process is explained and validated in full detail later. Overall this arrangement results in strong enhancement of light absorption in the monolayer, greatly increasing coupling efficiency between incident light and graphene.

Most importantly the resonance frequency can be adjusted by changing the chemical potential of the graphene layer. Using realistic chemical potentials for the graphene layer it is demonstrated that optical absorption can be tuned from mid infrared frequencies to near-infrared wavelengths

(up to 1.4μm for a chemical potential of 0.65eV). The rate of wavelength tuning for plasmon absorption was found to be 100nm/0.05eV of change in graphene chemical potential (estimated 1μm/0.5V at the near infrared region).

4.2.3. Strong Enhancement of Optical Absorption in Graphene

In this device, optical absorption of the graphene layer can be enhanced by coating the grating with a conformal reflective gold layer and a transparent dielectric (SiO_2, or ITO) spacer layer, with the absorbing graphene mono-layer placed on top. This setup allows for transfer of energy from the excited gold plasmon mode to the graphene plasmon mode, thus increasing the efficiency for coupling light in the atomic monolayer. Once again an ionic gel layer serves the role of the transparent gate dielectric for controlling the chemical potential of graphene. The inclusion of the spacer and ITO layers also forms a flexible vertical Salisbury screen micro-cavity.

The Salisbury screen [58] was invented in the 1940s as a selective wavelength anti-reflection radar material. Its original implementation consisted of a metal reflector and a graphite absorber layer separated by a transparent dielectric spacer. Similar to a quarter-wave antireflective coating, reflections at the material interfaces destructively interfere to give zero reflection at a specific incident wavelength. Nearly total absorption is achieved when waves reflected from the back reflector and the surface of the absorptive layer have equal amplitude and a phase difference of 180°. In order to achieve strong destructive interference the transparent spacer separating the back reflector from the top absorptive layer must have a thickness

$$d_s = m\lambda / 4n_s \text{ , (4-13)}$$

where d_s the thickness of the spacer and n_s the value of the spacer refractive index, and m is an integer cavity mode number. For the device discussed in this chapter the quality of the Salisbury screen that is formed is poor. This is due to the spatial modulation of the formed vertical micro cavity from the inverted pyramid structures.

4.2.4. Simulation Results

Identical parameters for the diffraction grating and ionic gel as used for the non-hybrid structure in Figure 4.11 are now used for FDTD and RCWA simulations of the multilayer structure *(stack layers: 75nm Gold, 120nm SiO2, graphene, 150nm ion gel)* (Figure 4.13.a).

As seen in Figure 4.13.b the gold back reflector no longer allows the radiation to leak through the silicon substrate, significantly enhancing the diffraction efficiency of the pyramid structures. It is clear from Figure 4.13.b that the graphene layer can be moved across the vertical cavity by adjusting the spacer / ion gel thickness ratio. *(Detailed discussion of* Figure 4.13.b *is given later.)*

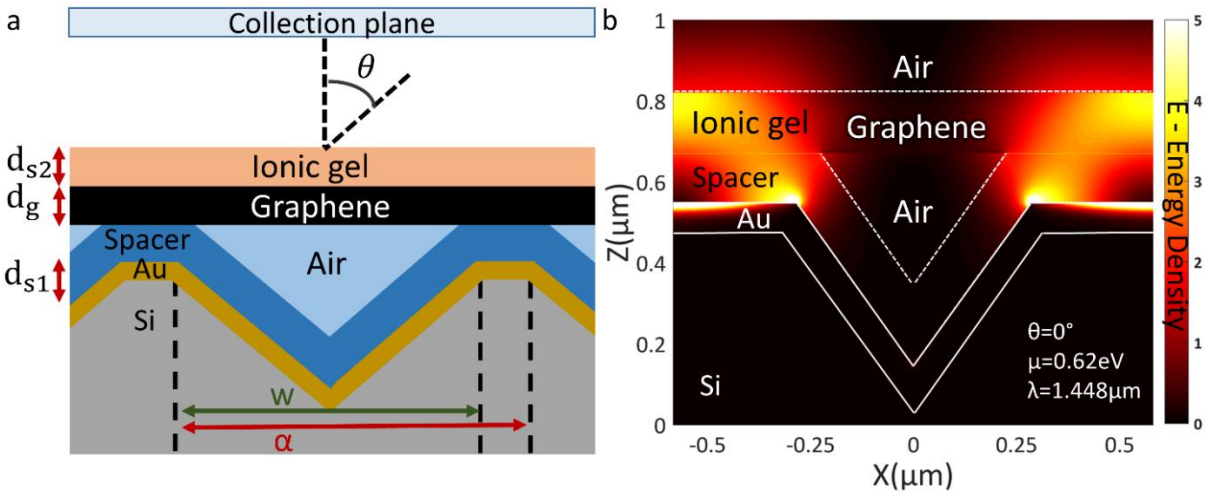

Figure 4.13. a. Schematic setup and **b.** E field density plot for the hybrid gold-insulator-graphene plasmonic device.

Figure 4.14.a shows simulated spectra (plotted as a colour map) for a range of chemical potentials. The broad absorption peak centred at 1.5 μm is independent of chemical potential and is due to the excitation of a gold plasmon mode. The sharp diagonal curved line which has a strong dependence on the chemical potential of the graphene layer is due a plasmon mode excited in graphene.

From the contour plot in Figure 4.14.a, it is clear that when the graphene and gold plasmon modes overlap there is a transfer of energy to the graphene plasmon mode and the absorption in the atomic monolayer is significantly increased. This is verified by the FDTD simulation result in Figure 4.14.b where it can be observed that there is a strong near field originating from the gold plasmon mode that is projected upwards from the edges of the pyramid structure and strongly interacts with the graphene layer. Near 100% tuneable absorption occurs at wavelengths where the graphene plasmon peak is in close vicinity to the gold plasmon peak while strong absorption *(60%-100%)* occurs over a bandwidth of a few hundred nm when the graphene plasmon peak is tuned further away. It is thus clear that is doubly resonant process provides strong dynamically tuneable optical absorption.

It is important to mention that in this case the Salisbury screen cavity mode has been tuned to overlap with the gold plasmon mode. Due to the inclusion of the pyramid structures and the limited amount of flat area on the surface of the device the vertical Salisbury screen cavity only contributes to a few percent of the total optical absorption from the device and thus it is difficult to observe from this graph. The absorption of the Salisbury screen has been identified as an isolated absorption mechanism in the device and does not contribute in energy transfer towards the graphene layer. More information about the absorption due to the Salisbury screen cavity is provided later on.

Absorption attributed solely to the graphene layer can be de-convolved from the data by subtracting equivalent results for the multilayer structure without the graphene layer. This is plotted in Figure 4.14.b and reveals an impressive 50% transfer of power to a single graphene monolayer. For shorter wavelengths and lower chemical potentials, the inter-band absorption in graphene is still visible over a broad spectral range. By selecting the data for a specific chemical potential value from

Figure 4.14.b and comparing the resulting spectra with those of the non-hybrid device, a boost in graphene layer absorption of 1650% can be observed (Figure 4.14.c).

The enhancement wavelength range can be tuned by changing the thickness or refractive index of either of the transparent layers (spacer/ionic gel). An example of this can be seen in Figure 4.14.d where increasing the thickness of the ion gel layer to 750nm shifts the enhancement range by almost 0.2μm.

It is important to mention that the modulation of plasmon frequency is very strong, demonstrating a wavelength shift of about 100nm per 0.05eV of chemical potential change in graphene (estimated 1μm/0.5V at the near infrared region - more details can be found in section 5.3) allowing for extremely low voltage tuning of absorption over a broad spectral range. Combining strong absorption and effective dynamic tuning over a large spectral range is ideal for fabrication of highly efficient modulators. Additionally the plasmon excitation can be effectively shut down by lowering the chemical potential (voltage) in graphene thus providing capability for dynamic electro-optical switching.

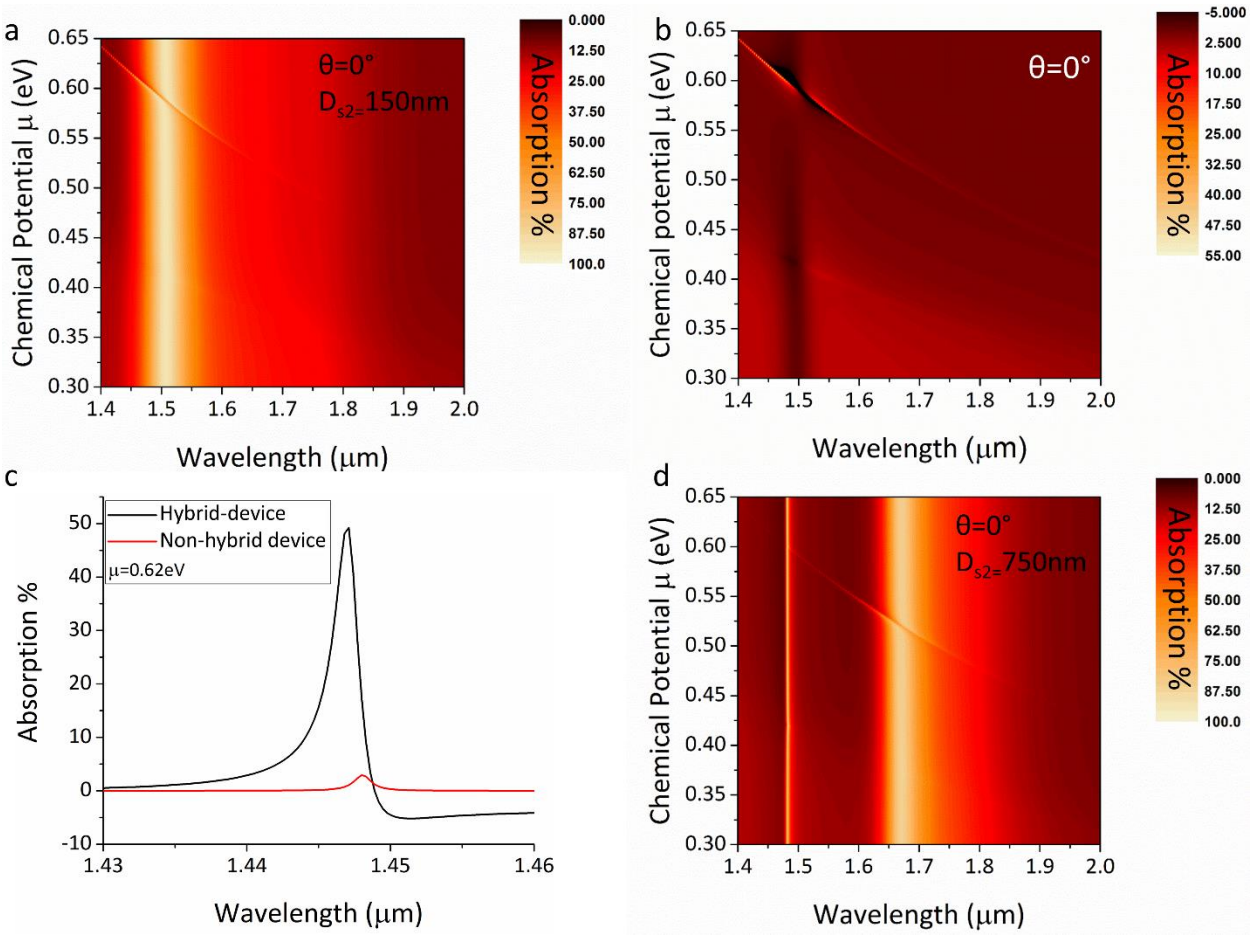

Figure 4.14. RCWA simulation spectra for the hybrid device setup where large tuneable optical absorption approaching 100% can be observed. **a.** Resulting spectra for a device with 150nm ionic gel thickness. **b.** Absorption attributed only to the graphene layer for the same setup by subtracting absorption due to the grating structure and other layers. **c.** Comparison of absorption between non-hybrid and hybrid device. **d.** Resulting spectra for a device with an ionic gel thickness of 750nm.

4.2.5. Deconvolution and Explanation of Plasmon Coupling Mechanisms

The physical processes underway are now deconvolved on a step by step basis. Figure 4.15.a plots total reflection of normally incident light as a function of ion gel thickness for a simplified structure consisting of the underlying grating coated with the 2-layer dielectric stack, but without the gold back reflector or graphene layer. This is equivalent to a fully dielectric structure supporting photonic crystal / diffraction modes associated with the lateral grating, (propagating across the surface of the device), as well as slow / static modes in the vertical direction associated with the cavity formed by the dielectric bi-layer coating. In contrast to Figure 4.11.b and Figure 4.14, total reflection is plotted instead of absorption in order to enhance visibility of key features which are much weaker due to the exclusion of the gold layer.

The set of sharp (but very feint) curved lines (labelled with red dashed lines) correspond to dispersion modes associated with the underlying dielectric pyramid grating structure. These relate to phase matching conditions coupling vertically incident light from free space to lateral propagating modes in the dielectric structure via a scattering / diffraction mechanism [81].

The dark fringes result from destructive interference in the dielectric bi-layer stack, whereas the broad light fringes are associated with weakly resonant modes of the vertical micro-cavity resulting from constructive interference. Modifying equation 4-13 to adjust it for a multilayer setup gives the following conditions for destructive interference in the vertical cavity

$$\lambda = 4(n_{s1}d_{s1} + n_{s2}d_{s2})/m, \quad (4\text{-}14)$$

where d_{s1} the thickness of the spacer and n_{s1} the value of the spacer refractive index, d_{s2} the thickness of the ion gel and n_{s2} the refractive index of the ionic gel, and m is an integer cavity mode number.

Figure 4.15.b plots data for the full structure now including the gold back reflector and graphene layers, for a fixed graphene chemical potential of 0.6eV. Solutions of equation 4-14 are overlaid for a range of values of d_{s2} as black dashed lines revealing perfect agreement with the diagonal bright fringes seen in the RCWA simulation. Hence Figure 4.15.b reveals how variation in ionic gel layer thickness affects wavelength conditions for destructive interference in the vertical dielectric cavity and its interaction with diffraction conditions associated with the pyramid grating. As the vertical micro-cavity becomes wider (d_{s2} becomes larger) destructive interference conditions shift to longer wavelengths. Eventually the cavity becomes multi-moded and destructive interference conditions become satisfied for more than one value of *m*, hence the fringes become periodic with cavity width.

With the inclusion of the gold back reflector the diffraction lines previously associated with the dielectric grating (marked with red crosses in Figure 4.15.b) become very sharp and visible. More significantly, an extra set of dispersion lines appears in-between them. These correspond to surface plasmon mode dispersion associated with the periodic gold coating (marked with blue x symbols) [205].

Introduction of the graphene layer gives rise to a sharp vertical line at 1.478μm corresponding to plasmon modes supported by the graphene monolayer. Points where the graphene resonance line crosses the gold plasmon mode dispersion features (curved lines marked with x) correspond to resonant coupling conditions (perfect phase matching) between plasmons supported by the underlying periodic gold pyramid structure, and surface plasmons supported by the graphene film (green dashed circle marker). Energy transfer to the graphene layer, and thus higher absorption in the monolayer, was found to occur only when the graphene plasmon peak overlaps or is in close vicinity to the gold plasmon peaks.

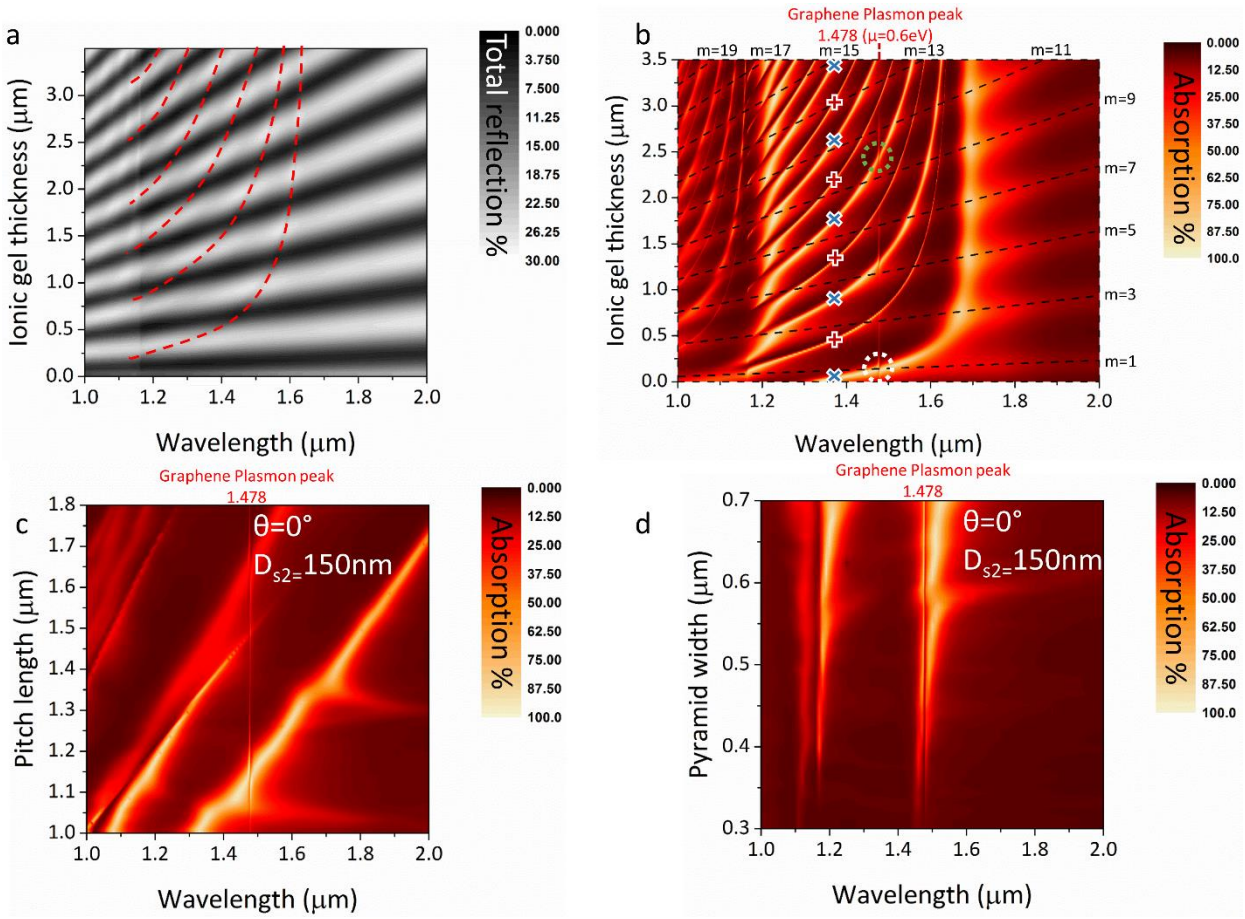

Figure 4.15. RCWA simulation of the device showing **a.** Total reflection spectra for varying ionic gel thickness when not including the gold back reflector and graphene layer, red dashed lines correspond to dispersion modes of the pyramid grating structure **b.** Absorption spectra now including the graphene and Au layers, vertical absorption line corresponds to plasmon excitations labelled at 1.478μm, the black dashed lines correspond to destructive interference originating from the micro-cavity, curved lines marked with blue "x" markers to Au plasmon modes and curved lines marked with red "+" markers to modes of the pyramid grating structure. Green and white dashed circles are examples of doubly resonant modes. **c.** and **d.** correspond to RCWA simulation results for varying pitch lengths and pyramid structure size respectively.

On the contrary, when the graphene peak overlaps with diffraction features (marked with red crosses), or features originating from the Salisbury screen vertical cavity (marked by black dashed lines), the amount of absorption attributed to the graphene monolayer is not increased. When features overlap with the Salisbury screen peak the overall absorption from the device increases (as marked by the white dashed circle marker). It is important to mention though that this increase is

a simple additive effect and there is not transfer of energy between the individual effects and the vertical micro-cavity mode (more details later on). For transfer of energy to occur, not only the intensity but also the gradient of the electromagnetic field is important.

The wavelength of dispersion features associated with the underlying grating structure (curved lines labelled with + and x markers in figure 5.b) depend on the pitch and size of the pyramid structures, providing a simple means to change the operational range of the device to shorter or longer wavelengths. Figure 4.15.c shows that diffraction and Au plasmon features shift towards longer wavelengths as the pitch becomes longer, (as would be the case for a dielectric photonic crystal with the same geometry). Figure 4.15.d shows that pyramid size provides control over the intensity and spectral width of the dispersive features. Smaller pyramids result in shallower and sharper peaks. Changing the thickness/refractive index of either the ion gel or spacer layer also induces a shift in the wavelength of the Salisbury screen cavity mode, as well as to phase matching and diffraction modes associated with the pyramid structures.

As shown in Figure 4.11.b and Figure 4.14.b the wavelength of the graphene plasmon resonance is dependent on chemical potential and can be tuned. This in combination with the ability to have complete control over all of the device's optical properties through optimizing the geometric parameters of the grating structure or the thickness of the spacer or ionic gel layers allows for a flexible range of applications that operate in different spectral ranges.

4.2.6. Contribution of the Salisbury Screen to the Absorption Spectra

It can be seen from Figure 4.16 that the absorption due to the Salisbury screen (peak marked by an S and a white dotted) is spectrally wide and quite low in terms of intensity when compared to the gold and graphene plasmon peaks. The absorption from the Salisbury screen is low because of the existence of the pyramid structures resulting in the majority of the surface not being flat thus providing only a few percent of extra absorption. From the contour profile inset of Figure 4.15. (top) it can be seen that the Salisbury screen does not actually result in increased absorption in the graphene or gold layers, instead it is an isolated effect that increases the absorption additively but independently from the other absorption features that appear in the spectrum. This is easy to see as the absorption is increased for the overall spectral region and the peaks originating from other physical mechanisms are simply shifted upwards but are not increased in intensity. Only when the graphene plasmon excitation has at least some overlap with the gold plasmon peak, enhanced absorption in the monolayer can be observed.

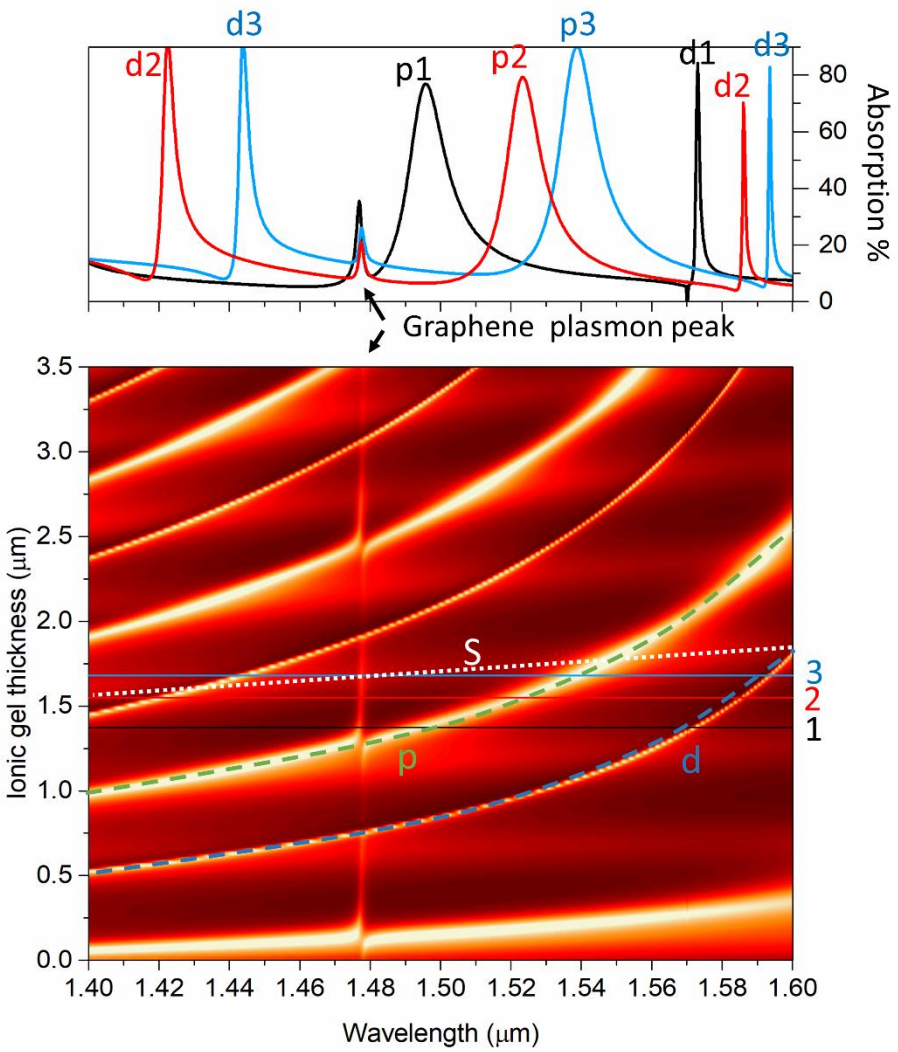

Figure 4.16. Contour plot and corresponding contour profiles inset (top) of absorption spectra for increasingly thick ionic gel layers. The white dashed line in the contour plot corresponds to the Salisbury screen peak (labelled as S), the green dashed curve line to the gold plasmon peak (labelled as p), and the blue dashed curved line to the diffraction line (labelled as d). The solid black, red, and blue lines labelled as 1,2, and 3 respectively correspond to the contour profiles presented in the inset on top. The graphene peak has been marked with black arrows.

4.2.7. Angle of Incidence and Polarization

So far only the behaviour for waves incident exactly perpendicular to the surface of the device have been examined. The analysis is now extended to look at what happens for any angle of incidence to the surface, again on a step by step basis to aid clarity and show proof of physical processes at play. The angular analysis will focus only on s polarization as its purpose is to further elaborate the physical mechanisms behind the absorption enhancement in graphene. The angular dependence of the absorption spectra of the device for both s and p polarization can be seen in Figure 4.17 but will not be further discussed.

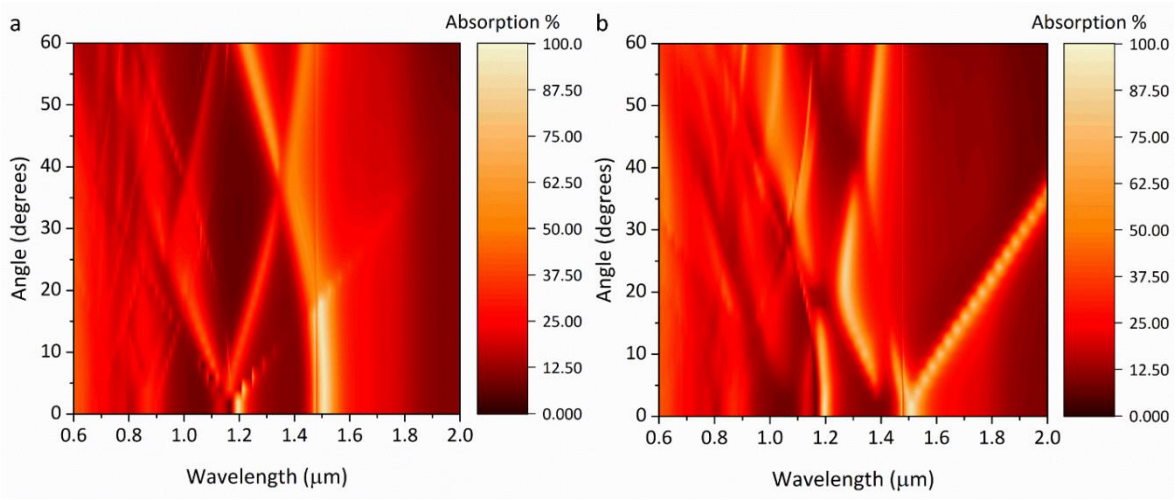

Figure 4.17. Absorption spectra versus angle of incidence for **a.** s polarization and **b.** p polarization.

Figure 4.18.a shows a greyscale RCWA simulation mapping spectra for a purely dielectric device without the gold back reflector or graphene layer (*as was the case for* Figure 4.15.*a*). X-axis relates to angle of incidence and y-axis scales as λ/α (wavelength/pitch). Putting the analysis in the context of photonic crystals, Figure 4.18.a effectively plots the 'photonic band structure' of the lattice along one symmetry direction (ΓX). In this case the y-axis is proportionate to normalised frequency, and the x-axis relates to k-vector component resolved in the plane of the lattice.

A set of straight and curved diagonal lines with multiple crossing points are observed. Straight lines (*white dashed overlay lines*) correspond to zero and 1st order diffraction [81], whereas curved lines (*black dashed overlay lines*) correspond to dispersive modes associated with the 2-dimensional grating geometry. Points along these lines correspond to conditions whereby incident light becomes coupled to the lattice resulting in propagating waves in the lateral direction (in the plane of the lattice). Simple crossing points between bands are observed rather than points of inflection (which would indicate presence of mini stop-bands). This is because the lattice pitch of the underlying structure is relatively large hence photonic band gaps are not observed, just continuous dispersive and diffractive modes. One point to note, no features associated specifically with the Salisbury screen micro-cavity are observed in this situation because without the gold back reflector light mainly passes through the substrate (as shown previously in Figure 4.11.d), and interaction with the micro-cavity is extremely weak.

Figure 4.18.b shows the equivalent data with the gold reflector and graphene reinstated with the same guide-lines overlaid. As was the case in Figure 4.15.b a new set of gold plasmon resonances become introduced (green and blue dashed overlay lines), as well as the graphene plasmon band (*purple dash-dot overlay line*) which can be wavelength tuned by adjusting chemical potential. The plasmon bands are much broader than the dielectric dispersion lines (black and white dashed overlay lines). Points of intersection between the graphene and gold plasmon bands correspond to perfect phase matching conditions (*x-axis of this diagram relates to in-plane phase*) allowing efficient transfer of energy between the structures.

Figure 4.18.c, d, and e, show the resulting E-field density for different combinations of wavelength and incidence angle. These correspond to the white, green, and purple circle markers on Figure

4.18.b respectively and are chosen to illustrate conditions for different spectral features of interest and further verify the mechanism behind the increased absorption in the graphene monolayer. (Incidentally the E-field energy density plot in Figure 4.13.b corresponds to the black coloured circle on Figure 4.18.b)

Figure 4.18.c corresponds to the white circle in Figure 4.18.b, which lies on a diffractive mode associated with the underlying periodic dielectric structure (diagonal straight white dashed line), and is present irrespective of the gold coating (as it shows up identically on Figure 4.18.a). Looking at the E-field distribution in Figure 4.18.c a strong optical field present in the internal volume of the pit can be seen. No field is present above the top surface between the pits, hence showing that the periodic array of pyramidal pits interacts strongly with incident light via a diffraction process.

Figure 4.18.d corresponds to the green circle in Figure 4.18.b, which lies on the fundamental gold plasmon band (green dashed line in Figure 4.18.b), but away from the diffraction band (white dashed diagonal line) and vertical cavity resonance (broad peak marked but the green arrow). The excitation of a surface plasmon located at the top surface of the gold in the spatial regions between the pits can be clearly seen. It is also noted that a significant part of the plasmon field is thrown vertically upwards into the z direction and some of it is located inside the pyramidal pit. The graphene layer is also weakly visible in the E-field energy density plot showing that a small portion of the field is coupled to the atomic monolayer. It is noted that the graphene layer is not visible in Figure 4.18.c confirming that a gold surface plasmon mode is required to feed power into the graphene layer.

Inspecting Figure 4.18.b more closely one can observe that between 0^0 - 18^0 the fundamental (lowest order) plasmon band (dashed green line) does not change wavelength with angle of incidence, has zero gradient, and therefore corresponds to a zero group velocity (stationary) plasmon mode which is localised to the top surface of the gold between the pits. This results in strong single step coupling of incident light over a wide range of surface incidence angles, and allows efficient coupling of light directly to the fundamental plasmon mode from a high NA focussing lens.

By adjusting the chemical potential, the graphene plasmon resonance (purple dash-dot line Figure 4.18.b) can be tuned to overlay the stationary plasmon mode (dashed green line in Figure 4.18.b) over the wide angular range where it is flat, resulting in optimal coupling to the graphene layer itself. It is also noted that the vertical cavity (Salisbury screen) mode overlaps directly and independently provides increased absorption over this region resulting in the wide horizontal white feature of the plot marked by the green arrow.

Figure 4.18.e shows the E-field distribution corresponding to this point where the diffracted mode (diagonal white line) overlaps with both the graphene plasmon (dash-dot purple line), as well as the fundamental plasmon mode (dashed green line), and the vertical cavity mode (white horizontal feature). Features of the plot are very similar to Figure 4.13.b (black circle marker in Figure 4.18.b), Figure 4.18.f is a zoomed in version of 6.e clearly showing coupling between the gold plasmon mode and the graphene plasmon mode. Overall this energy transfer process between the gold and graphene plasmon mode results in very efficient coupling of incident light to excited plasmons in the atomic monolayer.

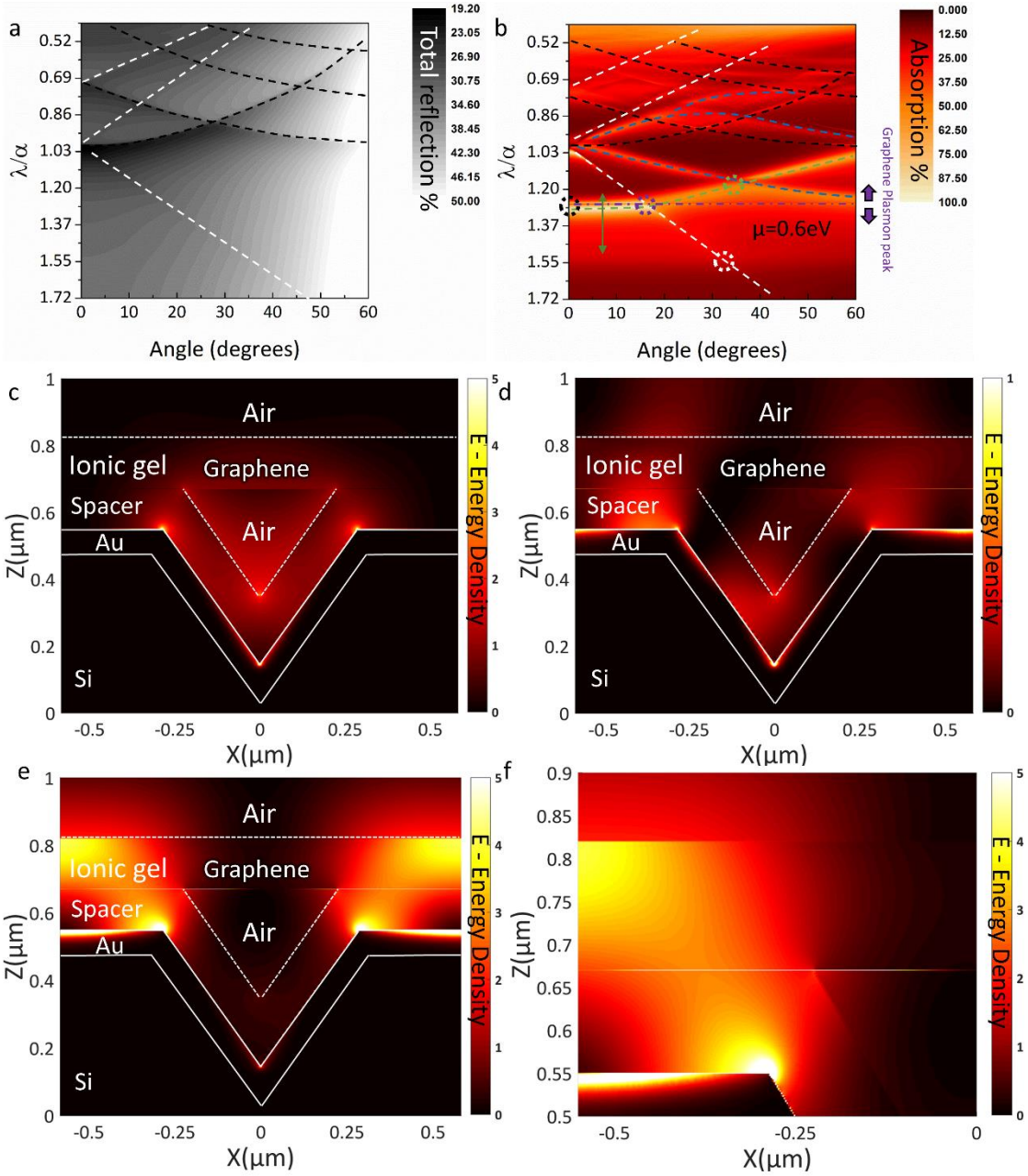

Figure 4.18. RCWA simulation of the device showing **a.** total reflection data for a range of photon incident angles plotted versus normalized frequency (wavelength/pitch) when not including the gold back reflector and graphene layer. White dashed lines correspond to 1st order diffractive modes and black dashed lines to dispersive modes associated with the 2-dimensional grating geometry**. b.** absorption spectra now including the graphene and Au layers. The extra green (fundamental mode) blue and purple lines appearing correspond to Au and Graphene plasmon modes respectively. **c.**, **d., and e.,** show FDTD simulation results from the white, green, and purple circle markers in b. respectively. **f.** Zoomed in version of figure 6.e showing that the coupling that occurs between the gold and graphene plasmon modes.

4.2.8. Rapid Optical Switching

Most significantly, since incident light couples to a doubly-resonant static (non-travelling) wave, it can be predicted that a very small change in chemical potential would rapidly detune the coupling conditions blocking optical energy transfer to the graphene, hence this design provides basis for

fast electro-optical switching which could be exploited in as an optical modulator, or as an optical memory element.

4.2.9. Tuneable Sensors and Couplers

Referring back to Figure 4.18.b, it is noted that all other surface plasmon bands (dashed blue lines in Figure 4.18.b) are curved. This means that coupling wavelength would change with either applied gate voltage (chemical potential) or angle of incidence, hence under these circumstances plasmon coupling wavelength can be electrically or mechanically tuned. Electrical wavelength tuning of surface plasmons in a practical configuration would be extremely important for chemical sensing methods such as SPR and SERS, and would introduce the possibility of a host of new integrated optical plasmonic devices.

4.2.10. Effect of losses on the Graphene Layer

Intensity of the plasmon absorption peak strongly depends on optical losses in graphene. As lower mobility values introduce broader and shallower absorption peaks it is important to investigate at what point the device approaches maximum efficiency. Figure 4.19 demonstrates the effect of dissipative losses through running RCWA simulations where different mobility values have been used to model the graphene layer. For the ideal case of 30,000$cm^2\ V^{-1}\ s^{-1}$ the device operates at over 80% optical absorption even though the plasmon peak is located tens of nm away from the central wavelength of enhancement. At mobility values down to 10,000 $cm^2\ V^{-1}\ s^{-1}$, the device maintains an almost ideal performance with absorption values close to 70%. Nevertheless, when the losses in the graphene layer are significant and the mobility becomes lower than 5000 $cm^2\ V^{-1}\ s^{-1}$ the device operation becomes significantly hindered while maintaining a shallow but still notable absorption even at 1500 $cm^2\ V^{-1}\ s^{-1}$.

The design suggested is this study is extremely flexible and gate setups implementing different types of transparent dielectrics can be used for different applications without much change in design given that their refractive index is of a similar value. Applications that require broad-band modulation but not extremely high optical absorption, can use an ion gel as the gate dielectric. In contrast, devices that require short-range modulation and strong absorption can simply use a SiO_2 back gate (which also acts as the spacer for the vertical cavity) in combination with chemical doping to define a central region for the chemical potential in graphene to electrically tune around. Progress in the field of graphene is moving at extremely rapid rates and thus higher mobility rates in combination with effective gating methods should be achievable in the future, lifting this limitation of the suggested device.

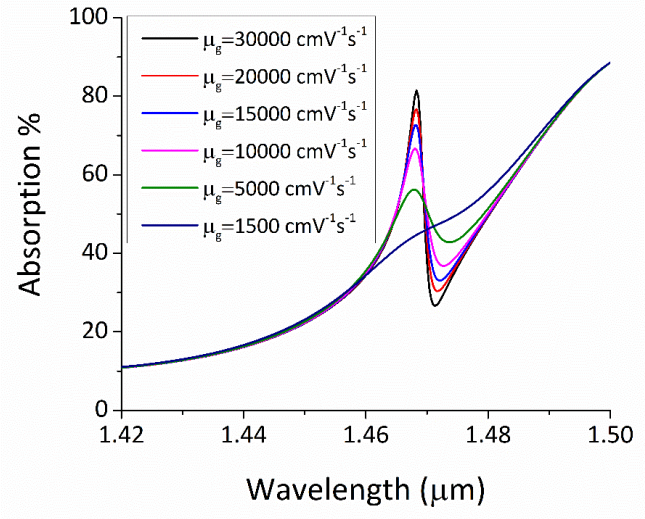

Figure 4.19. RCWA simulation spectra for different values of mobility for the graphene layer. As the mobility decreases the absorption also becomes much lower and broader

4.2.11. Conclusion

In conclusion efficient electrically tuneable near total optical absorption in a device implementing monolayer graphene is reported. The combination of a two-dimensional diffraction grating with a hybrid gold-insulator-graphene multilayer setup forms a doubly resonant plasmonic structure providing strong absorption enhancement in the graphene film. This enhancement can even provide a 1650% percent of absorption increase in the graphene layer when compared with a device not implementing the proposed hybrid setup. The physical mechanism behind this enhancement is a combination of increased diffraction efficiency for the grating structure, and resonant coupling between plasmons generated in the gold layer to the ones generated in graphene. The frequency of plasmon excitations in the graphene layer can be controlled electrostatically with the use of an ionic gel layer used in a gate configuration. Tuning is highly efficient allowing for an estimated 1μm/0.5V shift of plasmon absorption wavelength and allowing the device to operate at near-infrared frequencies. Furthermore, the absorption peak that is due to graphene plasmons is spectrally narrow and in combination with the efficient electrostatic control can potentially allow for rapid dynamic switching between high and low absorption values. Most importantly, plasmon excitations can be switched off completely by lowering the chemical potential and moving to the inter-band transition region. Finally, a near zero group velocity plasmon mode was found to be excited in the Au layer over a large range of angles thus allowing optimal coupling over a wide range of incidence angles as would for a large NA focusing lens. Crucially, this configuration allows for probing a static non- travelling wave thus potentially providing the basis for fast electro-optical switching to an optical memory element. The device presented in this work has potential in enabling a variety of tuneable nano-photonic devices including sensors, photonic logic gates, optical interconnects, and electro-optical memories.

4.3. Epsilon-Near-Zero Tuneable Plasmonic Device

Graphene is not the only material allowing for electrostatically tuneable plasmonic devices. Electrical tuneability can be achieved in any conductor with relatively low carrier concentration. Changes in the amount of free carriers in such conductors can have a significant effect on their permittivity thus allowing for electrical tuning of their optical properties. Since there is a direct and positive correlation between the plasma frequency of a conductor and the carrier concentration in the material, carrier accumulation or depletion with the use of a gate structure can result in a shift of plasmon excitation frequency. This becomes possible if the plasmonic structures enabling resonant coupling with light are designed to operate in a spectral region in proximity with this plasma frequency. This can be easily demonstrated by modelling the free electron behaviour of a material as a free electron gas system by utilizing a voltage-dependent Drude model under different carrier concentrations. Highly doped semiconductors [219–223], transition metal nitrides [224–226], and transparent conducting oxides [224,226–235] are ideal candidates for this type of devices. In this chapter an ITO ENZ (Epsilon-Near-Zero) device based on a modified version of the structure suggested in chapter 4.2 is demonstrated. Simulations show efficient modulation of plasmon excitations under low applied voltage with potential of further improvement. The ENZ tuneable device presented in this chapter was conceptualized in collaboration with Mr. Christoph Riedel.

4.3.1. Triply Resonant MIM/Salisbury Screen Device

Before demonstrating the electrostatically tuneable ITO ENZ device, an introduction to a simple triply resonant plasmonic device based on a 2D-inverted pyramid grating structure and a MIM (Metal-Insulator-Metal) tri-layer is necessary. Exciting a MIM mode instead of having a single layer mode can significantly enhance coupling of incident light in the structure thus transferring more energy to the device. As seen in Figure 4.20.a, the structure can be prepared by coating a basic 2D-inverted pyramid array grating with a tri-layer structure consisting of an optically thick Au layer (in this case d_{Au1}=74nm) that plays the role of the back reflector, a transparent spacer (refractive index of 1.8) and finally an optically thin Au layer to allow for MIM modes to be excited (d_{Au2} between 5nm-40nm). The default value for the spacer thickness used in the simulations of this chapter is d_s=20nm and for the top Au layer d_{Au2}=20nm unless mentioned otherwise. The pitch of the grating is set at α=700nm and the pyramid side width w=600nm.

Figure 4.20.b shows RCWA simulation results when varying the thickness of the top Au layer (d_{Au2}) from 0nm to 150nm. It can be seen that when the top Au layer is not included the absorption in the structure is not as strong and the peak is narrower. For the range where the thickness d_{Au2} is between 5nm and approximately 40nm the top Au layer remains optically thin allowing for MIM plasmon excitations in the multilayer structure. This results in a significant increase in plasmon absorption as well as a broadening of the absorption peak due to the higher amount of energy coupled in the system. For higher values of d_{Au2} the top Au layer is no longer optically thin and thus excitation of the MIM mode is no longer possible. Instead excitations are allowed only on the top Au layer and thus the absorption is once again reduced and the peak becomes narrower.

In Figure 4.20.c the E-field energy density in the structure when the top Au layer is not included can be seen. A relatively weak propagating single layer plasmon mode is excited, traveling in the

Gold/Air interface. Additionally localized plasmons can be observed at the tip of the pyramid pit resulting in very high E-field energy density in the pyramid cavity. When including the top Au layer a MIM plasmon mode, which is a result of the top Au layer (Au2) electron oscillations coupling to these of the bottom Au layer (Au1), is excited. It can been seen that the excited propagating MIM mode produces a significantly higher E-field energy density in the structure in comparison to the single layer plasmon mode. It is important to mention that due to coupling occurring between the top and the bottom layer plasmon modes, there is a very high E-field energy density within the spacer cavity. If an active layer whose optical properties can be electrostatically controlled is included inside the spacer region, tuning of the MIM mode properties becomes possible (this will be discussed in more detail later). Localized plasmons can once again be observed at the tip of the pyramid cavity, this time excited on the top Au layer (Au2). This localized mode once again results in very strong E-field energy density in the pyramid cavity as was the case for Figure 4.20.c.

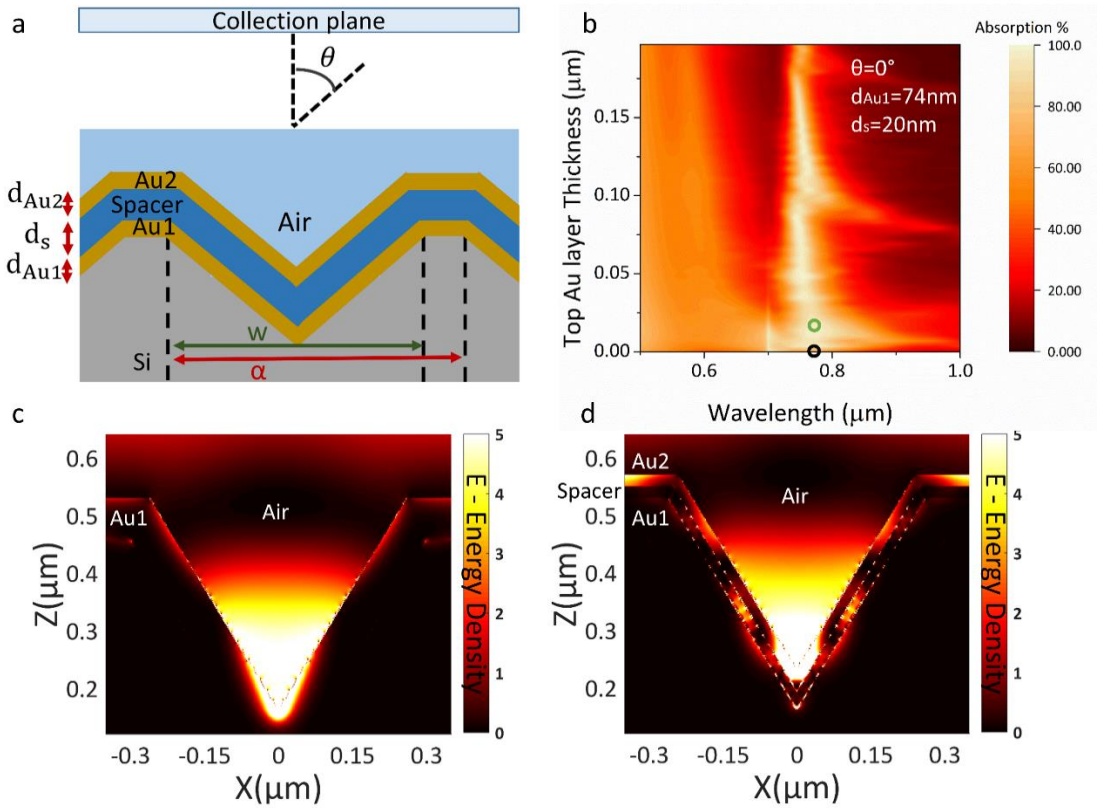

Figure 4.20 a. Schematic of the Metal-Insulator-Metal structure. **b.** RCWA Absorption spectra for a range of thicknesses for the top *Au* layer. **c.** E-Field energy density in the device corresponding to black circle marker of b. **d.** E-Field energy density corresponding to green circle marker of b.

The properties of the excited MIM mode heavily depend on the distance between the two metallic layers, thus changing the thickness of the spacer can have a strong effect on plasmon excitations in the device. Figure 4.21.a shows the absorption spectra of the device when varying spacer thickness. The black circle marker corresponds to the FDTD simulation E-field energy density graph of Figure 4.20.d and lies on top of the excited MIM mode with a central wavelength at λ=0.785μm. It is clear that for thinner spacer layers the coupling between plasmons on the two metallic layers is stronger and thus the absorption due to the MIM mode is higher. For increasing spacer thicknesses, the MIM becomes weaker and is no longer significant after d_s=150nm.

As the spacer becomes thicker, modes excited due to the vertical cavity that is formed appear (diagonal absorption lines) as previously seen in chapter 4.2. The green circle marker corresponds to an interesting point where the MIM mode overlaps with the first order vertical cavity mode. The resulting E-field energy density can be seen in Figure 4.21.b. In this case the MIM mode is still visible since there is obvious coupling between the individual plasmon modes excited on the top and bottom Au layers. At the same time there is very strong E-field energy density at the vicinity of the top Au layer (Au2) which is due to the interaction of a vertical cavity mode (in this case, the first order cavity mode) with the secondary pyramid structure formed by the Au2 layer. The inclusion of the vertical cavity mode in the system, results in a triply resonant plasmonic excitation since it couples with the MIM mode thus providing very high E-field energy density at the vicinity of the top Au layer.

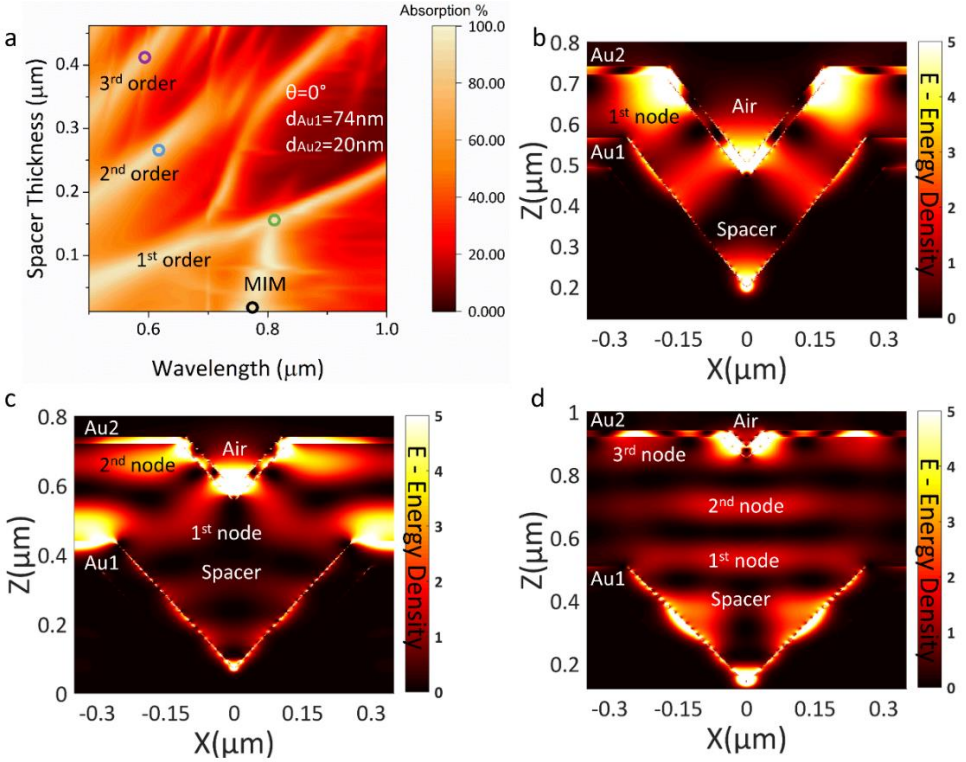

Figure 4.21 a. RCWA absorption spectra for a range of Spacer thicknesses. **b.** FDTD simulation showing E-field energy density in the device for the green circle marker of a. **c.** For the blue circle marker of a. and **d.** For the purple circle marker of a.

For very thick spacers the MIM is decoupled and plasmon excitations on the top and bottom Au layers no longer interact. The blue marker of Figure 4.21.a lies on the second order cavity mode. The resulting E-field energy density can be seen in Figure 4.21.c and it becomes obvious that there is no longer coupling between the plasmons excited at the top and bottom Au layers. Since the FDTD simulation is run on the second order cavity mode, two constructive interference nodes are seen originating from the Salisbury screen vertical cavity (while another two can be seen within the pyramid since there is a periodic modulation of the vertical cavity in the x-direction). The first cavity node strongly interacts with the Au1 layer of the main pyramid thus assisting the generation of plasmons and resulting in high E-field energy density at the vicinity of the structure. Similarly the second node of the vertical cavity mode overlaps with the Au layer (Au2) in the second pyramid

structure significantly assisting the generation of plasmons. Interaction between the E-field in the top and bottom pyramid structures is still visible but is not due to the MIM mode.

Finally the purple marker of Figure 4.21.a is lying on top of the third order cavity mode and corresponds to the E-field energy density plot that can be seen in Figure 4.21.d, where three nodes can now be observed. Similarly as in Figure 4.21.c, there is no longer a MIM mode excited and there is an overlap of the third node of the vertical cavity mode with the top pyramid structure, thus assisting the generation of plasmons on the top Au layer (Au2 layer). It is important to mention that, in every case, the extra nodes appearing inside the main pyramid due to the extension of the vertical cavity in the structure seem to couple with plasmon modes generated in the bottom Au layer (Au1).

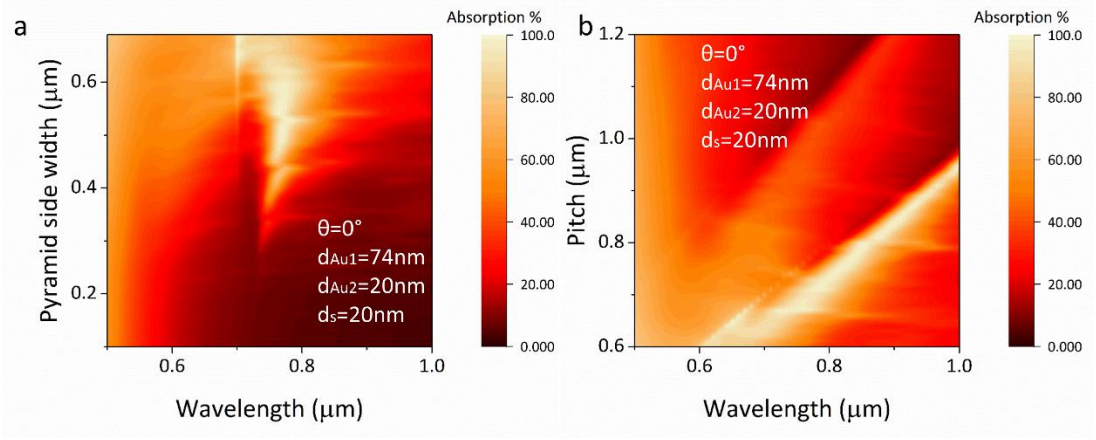

Figure 4.22 RCWA absorption spectra for **a.** a variety of pyramid side widths and **b. F**or a range of pitch length values.

Returning to the simple layer structure corresponding to a 20nm thick spacer and 20nm top Au layer, the effect of pitch and pyramid size on the MIM plasmon mode can be investigated. From Figure 4.22.a it can be seen that as the pyramid size increases the absorption becomes higher and the peak becomes wider. Thus it is better to use larger pyramid structures for better grating efficiency. Figure 4.22.b shows that, as expected from grating theory [81], when the pitch becomes longer there is a redshift in the diffraction features as well as in the resulting plasmon excitations.

It is also interesting to observe the resulting absorption spectra under different angles of incidence as can be used to evidence the underlying mechanisms of resonance. In Figure 4.23.a RCWA simulations showing the angular dependence of the device can be seen. The absorption due to the MIM mode is found to be maximum from 0° and up to 10° of incident angle. For larger angles, initially the MIM mode blue-shifts and after reaching 30° it begins to red-shift. The black circle marker in the graph is for normal incidence and corresponds to the E-field energy density graph of Figure 4.20.d. The green circle marker corresponds to 6° degrees of incident angle and the resulting E-field energy density can be seen in Figure 4.23.b. Due to the change in angle of incidence there is a shift in the location of the near-field hotspot in the device. Figure 4.23.c corresponds to the blue circle marker of Figure 4.23.a. Due to the significantly larger angle there is a massive change in the near field hotspot. Furthermore, additional hotspots appear periodically above the surface of the device. The near-field hotspots extend far in the z-direction over a large area of the device surface, which is ideal for sensing applications since the hotspots can strongly interact with analytes in the vicinity of the device surface.

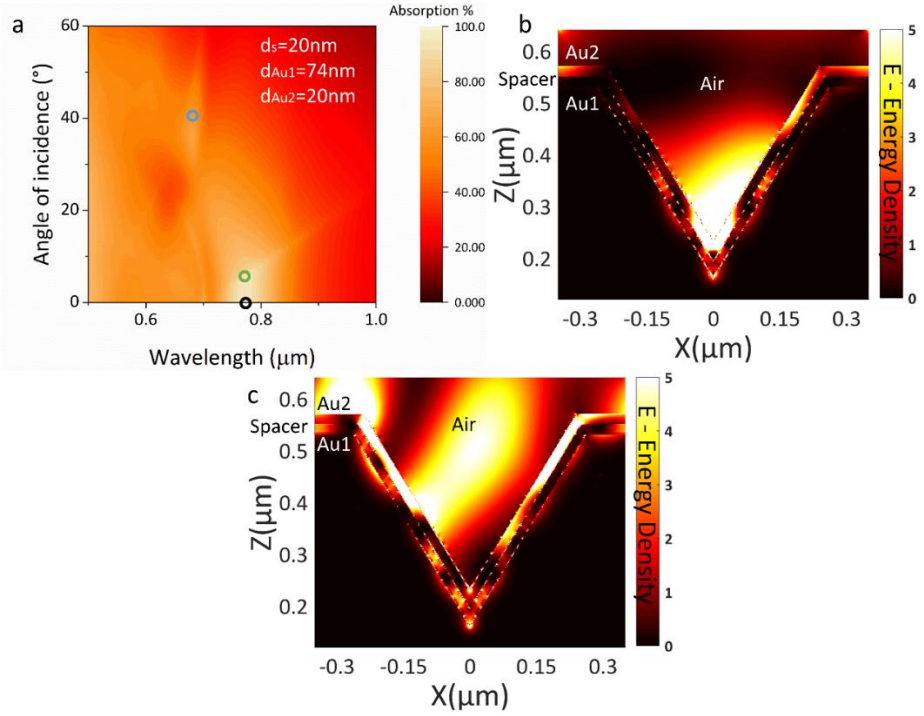

Figure 4.23 a. RCWA absorption spectra for various angles of incidence. **b.** FDTD simulation spectra for green circle marker of a. and **c. F**or blue circle marker of a.

4.3.2. Background for Epsilon-Near-Zero ITO devices

Taking advantage of the fact that there is high electromagnetic field energy density located in the spacer separating the two metallic layers of the device presented in chapter 4.3.1, an active layer can be included in order to provide control over the optical properties of the device. In more detail, the previously mentioned spacer can be replaced by a high-k/ENZ-material double layer (in this case HfO_2 and ITO) to form a capacitor structure as seen in Figure 4.24. Voltage can easily be applied through the surrounding metallic layers. When a voltage is applied, there is either a depletion or accumulation region forming in the HfO_2/ITO interface inside the ITO layer, where the carrier concentration can be electrostatically controlled through a gate voltage.

A simple equation can provide an estimate of the carrier concentration in the ITO interface under an applied voltage,

$$n_{c_i} = n_{c_0} + \frac{\varepsilon_0 \varepsilon_d}{e} \frac{V_g}{d_d^2}, \quad (4\text{-}15)$$

where n_{c_0} the free carrier density in ITO, and ε_d and d_d the permittivity and thickness of the dielectric respectively [231]. n_{c_0} can be effectively controlled through carefully defining the deposition parameters for the ITO layer. Since the voltage depended carrier concentration is known, the plasma frequency can be calculated in rad/s by using the equation

$$\omega_p^{\,2} = n_{ci} e^2 / (m_{eff} \varepsilon_0), \quad (4\text{-}16)$$

where m_{eff}=0.45m_e the effective mass of electrons in ITO [233]. The permittivity of the bulk ITO layer and that of the accumulation/depletion region can be calculated with the use of the Drude model (see appendix section 12.1.2 for Matlab code) where the voltage dependent plasma frequency is included from equation 4-16 (in case of the bulk ITO layer V_g=0) as

$$\varepsilon_I = \varepsilon_\infty - \omega_p^2 / (\omega^2 + \Gamma\omega), \text{ (4-17).}$$

The thickness of the accumulation region that is formed in the ITO due to the application of voltage through the gate structure can be approximated by calculating the Thomas-Fermi screening length as

$$\lambda_{TF} = \left[\frac{\varepsilon_{ITO}\varepsilon_0 h^2}{4\pi^2 m_{eff} e^2}\right]^{1/2}\left[\frac{\pi^4}{3n_{c_0}}\right]^{1/6}, \text{ (4-18)}$$

where ε_{ITO} the dielectric constant of ITO [231].

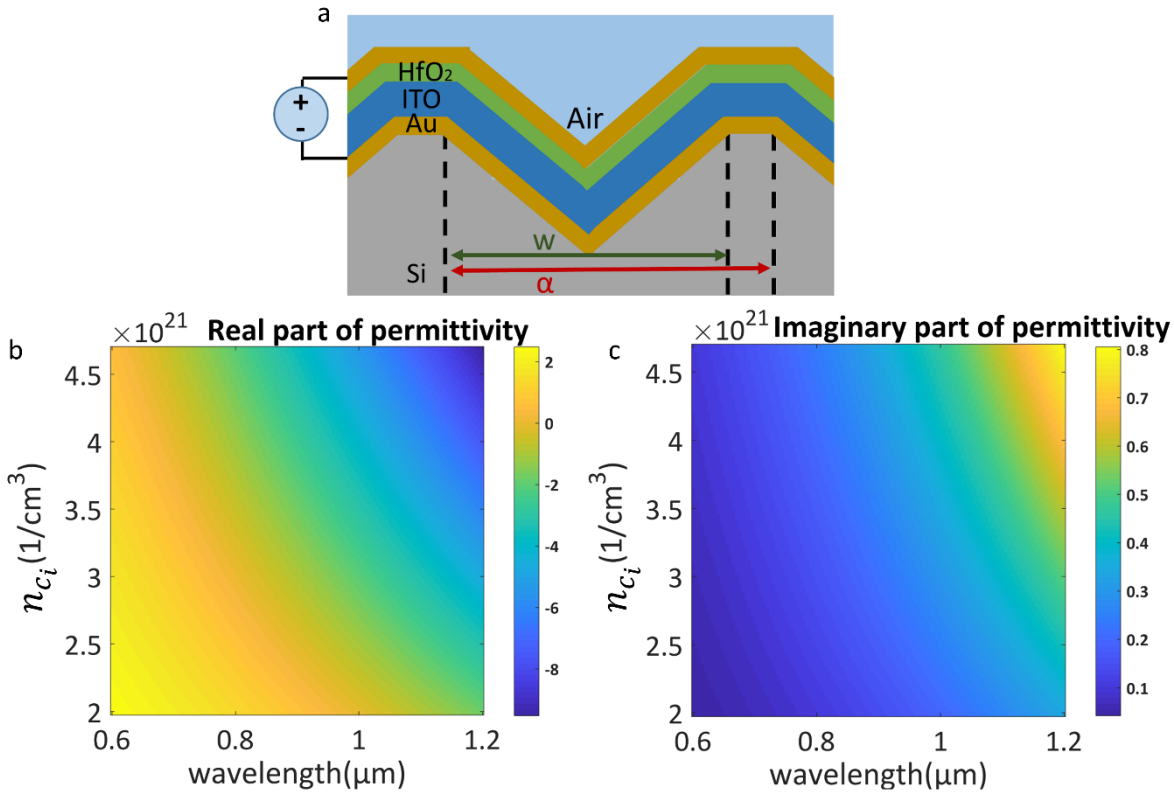

Figure 4.24 .a Schematic of the device. **b.** and **c.** are the carrier concentration dependant real and imaginary parts of the permittivity of the active region respectively. For d_d=10nm, ε_d=25 (HfO_2), ε_{ITO}=3.34, and n_{c_0} =2x10^{21} cm^{-3}, the screening length λ_{TF} is found to be approximately 0.3nm. Nevertheless, the accumulation region thickness has been experimentally found to be approximately 1nm thick [233] which is the value that is going to be used for the simulations in this chapter.

Using the same values, and by taking into account a scattering rate Γ=1x10^{14}rad/s, the carrier concentration dependant real and imaginary parts of the permittivity of the ITO layer can be calculated, as seen in Figure 4.24.c and Figure 4.24.d. Having n_{c_0} =2x10^{21} cm^{-3} gives an ENZ wavelength for the bulk ITO in the visible spectrum, at approximately 1μm. When a voltage is applied the ENZ point of

the accumulation region can be tuned to shorter wavelengths than that of the bulk ITO due to the introduction of extra carriers (in case of depletion the ENZ point red-shifts). Operating near the ENZ point is crucial since it lies exactly at the cross-point between metallic and non-metallic behaviour for the material. When operating near this point any change in the amount of free carriers in the ITO layer has a strong effect on the permittivity and thus electrostatic modulation of the carrier concentration results in significant changes in optical behaviour.

4.3.3. Tuneable Metal-ENZ-Insulator-Metal device

In order for electrostatic tuning to work in the device shown in Figure 4.24.a, the ENZ wavelength of bulk ITO must be in proximity with the wavelength of the MIM plasmon mode excitations. In order to achieve that, the n_{c_0} of ITO can be shifted by changing deposition parameters. Alternatively the pitch of the diffraction grating can be adjusted to have plasmon excitations match the ENZ point of the bulk ITO layer. Having n_{c_0} =2x10^{21} cm^{-3} and setting the pitch as α=700nm and a pyramid width as w=600nm results in the effects being in proximity, with the MIM mode at λ=0.78μm and the bulk ITO ENZ at λ=1μm. The accumulation region carrier concentration dependant reflection spectra of the device can be calculated through RCWA simulations (code file in appendix section 12.2.1) as seen in Figure 4.25.a.

The effect of tuning the carrier concentration of the accumulation region can be more clearly seen in Figure 4.25.b where normalized reflection ($\frac{\Delta R}{R}$) is plotted, which is the reflectance (R) before and after a voltage has been applied, divided by the initial reflectance. The normalized reflectance in Figure 4.25.b showed a relative shift of 94%. The highest amount of reflection modulation occurs at λ=0.775μm which as seen in Figure 4.25.a is where the MIM mode is excited. This proves that the modulation occurs due to the interaction of the ITO accumulation region with the metal-insulator-metal plasmon mode that is excited in the two metallic layers. Another point where reflection modulation occurs is at λ=0.7μm, when the ENZ wavelength of the accumulation layer is shifted to be in proximity with the sharp diffraction line visible in Figure 4.25.a. The modulation is much weaker than for the MIM mode spectral region and could be attributed solely to the ITO accumulation region crossing over to metallic behaviour (thanks to the high carrier concentration) and allowing excitation of plasmons at this specific wavelength.

FDTD simulations (code file in appendix section 12.2.2) are used to observe how the electric field energy density in the device changes for different applied carrier concentrations in the accumulation region. It is especially interesting to compare the E-field energy density for n_{c_i} =2x10^{21} cm^{-3} at the MIM mode wavelength, to the points where the modulation effect is strongest as seen in Figure 4.25.b. This can help identify the mechanism behind the modulation that occurs at these points. At n_{c_i} =2x10^{21} cm^{-3} (Figure 4.25.c black circle marker) the basic MIM mode can be observed similarly to chapter 4.3.1 with the only difference being that the E-field energy density in the spacer region is not uniform and is more prominent in the ITO region. Moving to higher carrier concentrations and to the green circle marker of Figure 4.25.b, a plasmon mode appears at the ITO/HfO_2 interface (since the accumulation layer in the ITO now has a metallic behaviour), coupling with the pre-exist-

ing MIM mode, as evident by the strong field interaction between the three conductive layers (Figure 4.25.d). This gives rise to a triply resonant mode (Metal-ENZ-Insulator-Metal mode) which explains the deepening in the reflection spectra of Figure 4.25.b.

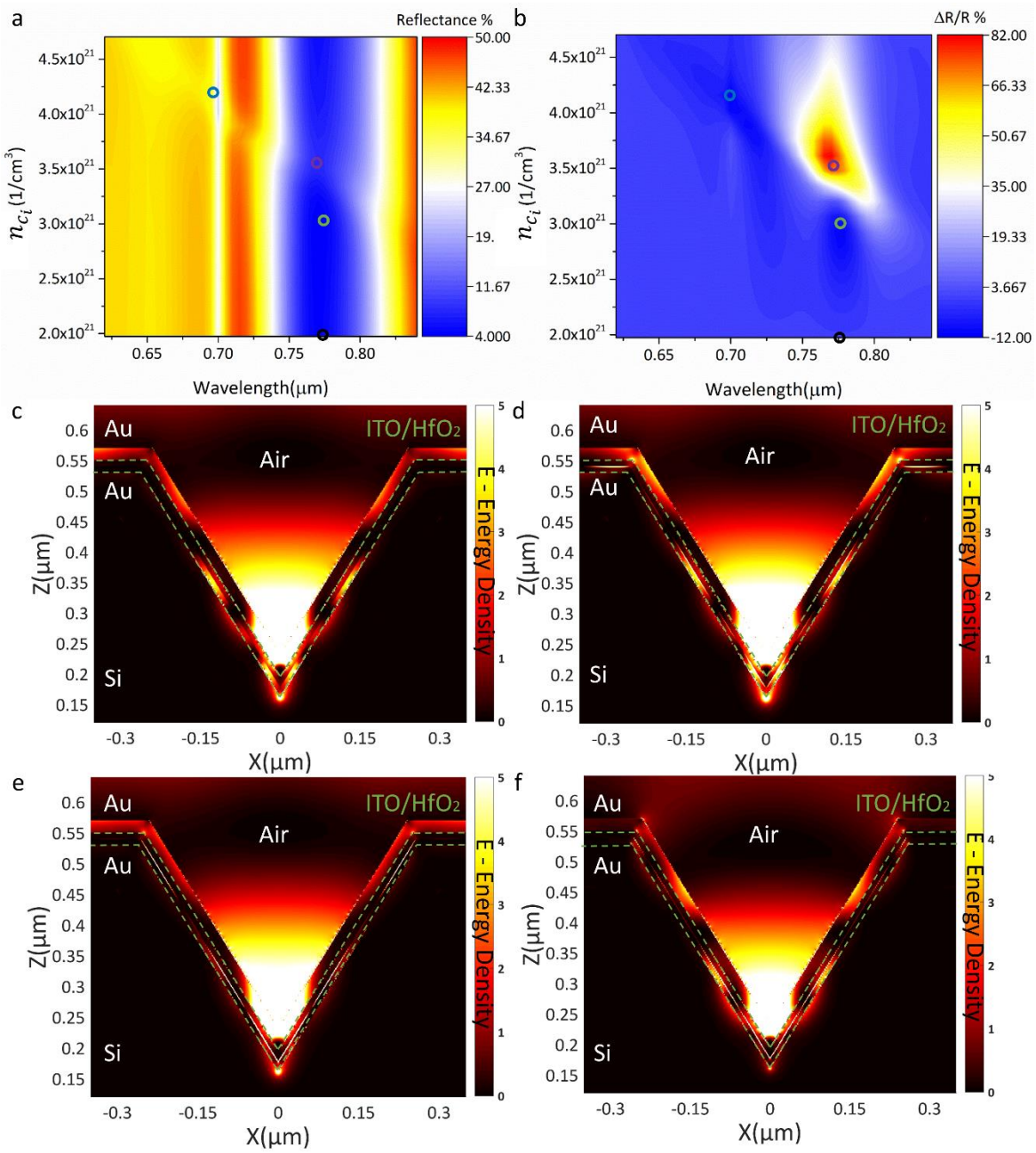

Figure 4.25 .a RCWA simulation results showing tuneable reflection spectra. **b.** Normalized Reflection spectra. **c. d. e.** and **f.** show the E-field energy density in the structure for the black, green, purple, and green circle markers of a. and b respectively. The ITO/HfO_2 bilayer lies within the dashed green lines.

Moving to even higher carrier concentrations and to the purple circle marker of Figure 4.25.b, it can be seen that the plasmon mode in the active region of the ITO becomes more prominent but is mostly localized within the pyramid region (Figure 4.25.e). In this case there is no evidence of significant electromagnetic field interaction between the plasmon modes in the two surrounding Au layers and the ITO plasmon mode and hence there is no coupling between them. It can thus be

assumed that the screening effect from the plasmons excited within active ITO region decouples the MIM resonance, resulting in reduced absorption.

Finally, it is interesting to observe the E-field energy density in the structure when the effect of the active ITO region overlaps with the diffraction peak at λ=0.7μm (Figure 4.25.b blue circle marker). As seen from (Figure 4.25.f) there are no longer propagating plasmon modes on either of the Au layers outside of the pyramid structure. On the other hand there are still plasmon modes excited within the pyramid cavity. Similarly, there is an excited plasmon mode in the ITO accumulation region only inside the pyramid pit. Strong electromagnetic field interaction can be observed between the plasmon modes excited in the three conductive layers in the pyramid pit and thus the reduction of reflectivity in this spectral region can again be attributed to triply resonant coupling.

4.3.4. Tuneable ENZ/ Salisbury Screen Device

It is also interesting to observe what happens when the thickness of the ITO layer (and thus the thickness of the vertical cavity) is increased. Figure 4.26.a shows the reflection spectra of the device for increasingly thick ITO layers. As the spacer becomes thicker, the MIM mode decouples and weakens while cavity modes and higher order plasmon modes begin to appear. Figure 4.26.b shows the accumulation region carrier concentration dependant normalized reflection spectra of the device for an ITO layer with a thickness of 0.155μm (dashed line in figure Figure 4.26.a).

In Figure 4.26.b, it can be seen that as the accumulation region carrier concentration becomes higher and the ENZ wavelength approaches the wavelength of the 1st order cavity mode, tuning becomes possible even though the MIM mode is no longer excited. In this case, the tuning occurs due to the interaction of plasmons in the ITO accumulation region with the vertical cavity mode and the top Au layer plasmon excitations. This can be seen in Figure 4.26.c-f which show the resulting E-field energy density FDTD simulation results for the black, green, blue, and white circle markers respectively.

Figure 4.26.c and d. show the E-field energy density for the black and green circle markers which correspond to the same wavelength (0.7μm) for n_{c_i} =2x10^{21} cm^{-3} and n_{c_i} =4.7x10^{21} cm^{-3} respectively. It can be seen that for n_{c_i} =2x10^{21} cm^{-3} there are no plasmon excitations in the ITO/HfO_2 interface since no accumulation region is formed. In the same graph it can be seen that there are plasmon modes excited in both the top and bottom Au layers. The resulting electromagnetic field due to the plasmons excited in the two Au layers seems to weakly interact. Nevertheless, the field that appears within the cavity could be attributed to the vertical cavity mode, or to diffraction that occurs from the bottom pyramid structure (since at this specific wavelength a strong diffraction peak is observed in Figure 4.26.a), or an overlap of the effects. For n_{c_i} =4.7x10^{21} cm^{-3} a weak propagating mode is excited in the ITO accumulation region but is out-of-phase with the top layer Au plasmon mode, thus resulting in screening of the absorption.

Similarly, Figure 4.26.e and f. show the E-field energy density for the blue and yellow markers which correspond to the same wavelength (0.66μm) for n_{c_i} =2x10^{21} cm^{-3} and n_{c_i} =4.3x10^{21} cm^{-3} respectively. For n_{c_i} =2x10^{21} cm^{-3} there are no plasmon excitations in the ITO/HfO_2 interface. In this case

only the top Au layer supports plasmon excitations and there is no significant electromagnetic field interaction between the bottom and top Au layers (although the interaction with the vertical cavity mode is still visible but faint). The lack of the strong electromagnetic field extending in the z direction, as was evident in Figure 4.26.c, can be attributed to the fact that there is no diffraction peak in this spectral region. Thus, having an overlapping effect with the diffraction peak can improve the coupling between the two Au layers. For n_{c_i} =4.3x10^{21} cm^{-3} plasmons are once again excited in the ITO accumulation region, this time with a much stronger intensity. In this case the plasmons in the top Au layer and within the ITO accumulation region appear to be in phase, thus justifying the reduction of reflectivity in the device.

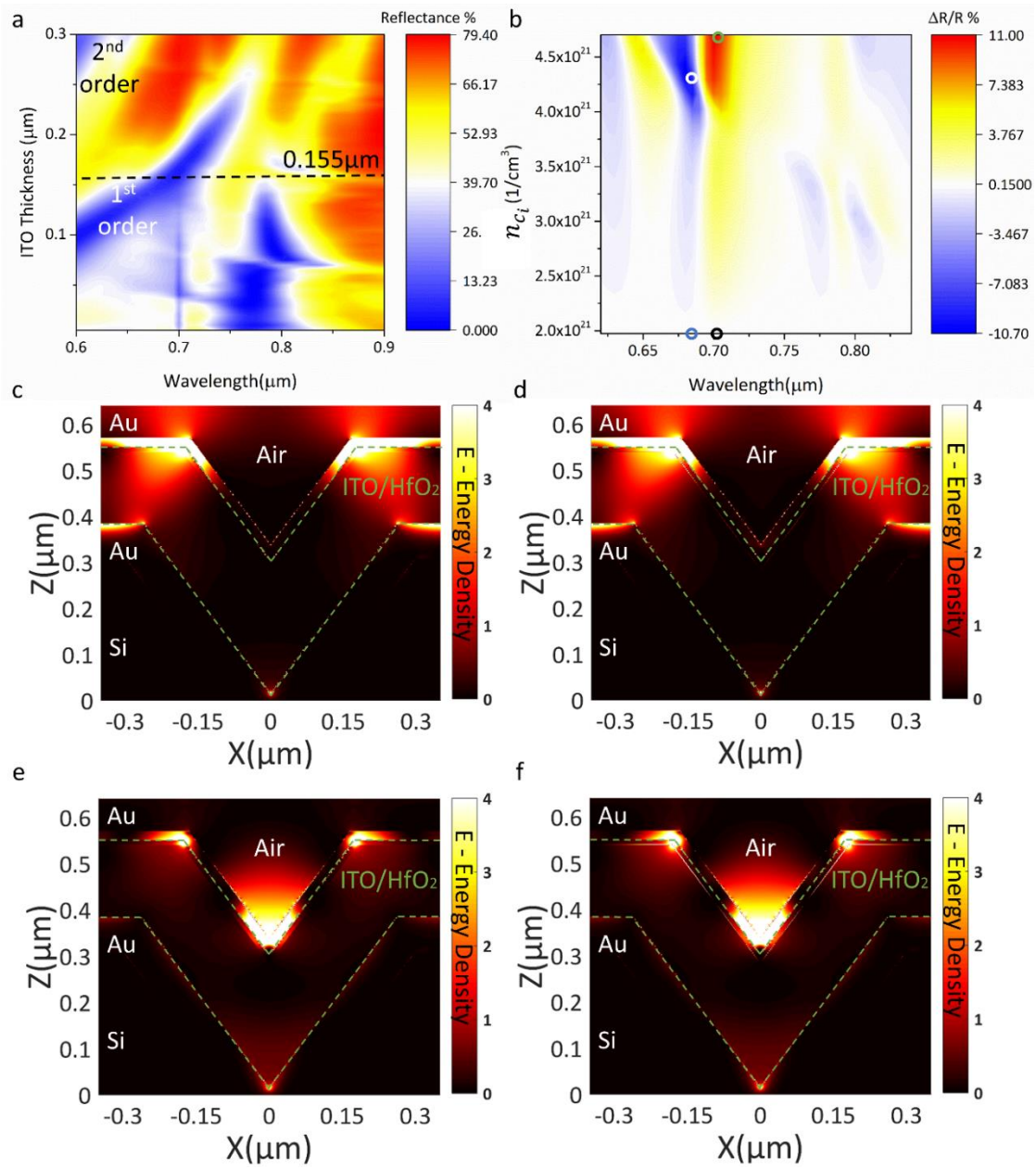

Figure 4.26 .a ITO Thickness dependence of reflection spectra **b.** Normalized reflection spectra for an ITO thickness of 0.155µm under different accumulation region carrier concentrations. **c. d. e**. and **f.** correspond to E field energy density FDTD simulation results of the black, green, blue, and white circle markers of b. respectively.

This ENZ/Salisbury screen hybrid device is significantly less efficient than the M-ENZ-IM device of section 4.3.3. Nevertheless if the device parameters are optimised to provide a better overlap between the individual excited modes then more efficient modulation is expected. For future work it would be interesting to investigate if the device could operate without the top Au layer, thus only having plasmon excitations within the ITO accumulation region.

4.3.5. Conclusion

In this chapter an alternative tuneable plasmonic device implementing an ENZ ITO layer instead of graphene was presented. The suggested device combines a 2D inverted pyramid diffraction grating with a M-ENZ-IM (Metal-Epsilon-Near-Zero-Insulator-Metal) structure in order to enable dynamic electrostatic tuning of reflection. A Salisbury screen cavity hybrid device was also presented. The device operates by applying a voltage through the metallic layers which then in turn forms an accumulation (or depletion) active region in the ITO layer at the location of the interface with the insulator.

FDTD and RCWA simulations were used to investigate the properties of the proposed device, showing that reflectivity can be dynamically controlled. It was found that any change in free carrier density in the ITO accumulation region has a significant effect on the refractive index when operating near the ENZ wavelength. Since the active ITO region is located at an electromagnetic field energy density hotspot of the MIM plasmon mode that forms between the two metallic layers, changes in the refractive index of this layer can effectively modulate the reflection spectra. This is achieved by either screening the coupling between the two layers to reduce the absorption of the MIM mode or by allowing triply resonance plasmon coupling thus enhancing the absorption of the structure.

Even though this device is much less efficient than the one proposed in chapter 4.2 it has the advantage of being much easier to fabricate since it does not require any complicated transfer process or special gating methods. The Au and ITO layers can be simply deposited through electron-beam evaporation and the HfO_2 through atomic layer deposition.

It is important to mention that the ENZ point of the bulk ITO in this chapter was set at λ=1μm which is far from the MIM plasmon mode located at λ=0.78μm. The ENZ point of the bulk ITO layer can thus be shifted closer to the wavelength of the plasmon excitations in order to reduce the necessary modulation range of the carrier concentration of the accumulation region. This can allow for more effective electrostatic gating and tuning of the reflection spectra. Modulation of the permittivity of the ITO accumulation (or depletion) region is expected to be much more efficient (allowing for lower voltage operation) for longer wavelengths since there is an inverse exponential dependence of the ENZ wavelength on carrier concentration, as seen in figures Figure 4.24.b and c.

Finally, it should be noted that the results of this chapter are preliminary and improved methods of simulating the behaviour of the structures presented in sections 4.3.3 and 4.3.4 are currently being prepared, but will not be included in this thesis due to time constraints. In more detail, an improved electro-optical model, that takes into account the charge distribution in the accumulation region and the effect it has in the refractive index, is developed to replace the simplistic approach presented in sections 4.3.3 and 4.3.4 (which instead used a step function in the index profile of the ITO layer).

5. Fabrication

5.1. Inverted Pyramid Diffraction Grating

This section focuses on the several steps required for fabricating the novel devices presented in chapters 4.1 and 4.2. In this section, the reasoning behind each of the design choices is clearly explained including the methodology followed for the fabrication. An analysis of each step is also presented. Several inverted pyramid-based diffraction gratings were fabricated and characterized with the use of reflectometry in order to obtain the optimum device parameters for efficient light diffraction. A graphene transfer technique was also optimised in order to successfully transfer graphene monolayers on top of the diffraction grating. Ionic gel was prepared as a way of providing control over the chemical potential in graphene, demonstrating much higher efficiency in controlling the chemical potential than the usage of high-k dielectrics.

5.1.1. Fabrication Steps

The diffraction gratings used in this project consist of an array of inverted pyramid structures that are fabricated on Si substrates through chemical etching methods. The process used to prepare the pyramid structures can be seen step-by-step in Figure 5.1.

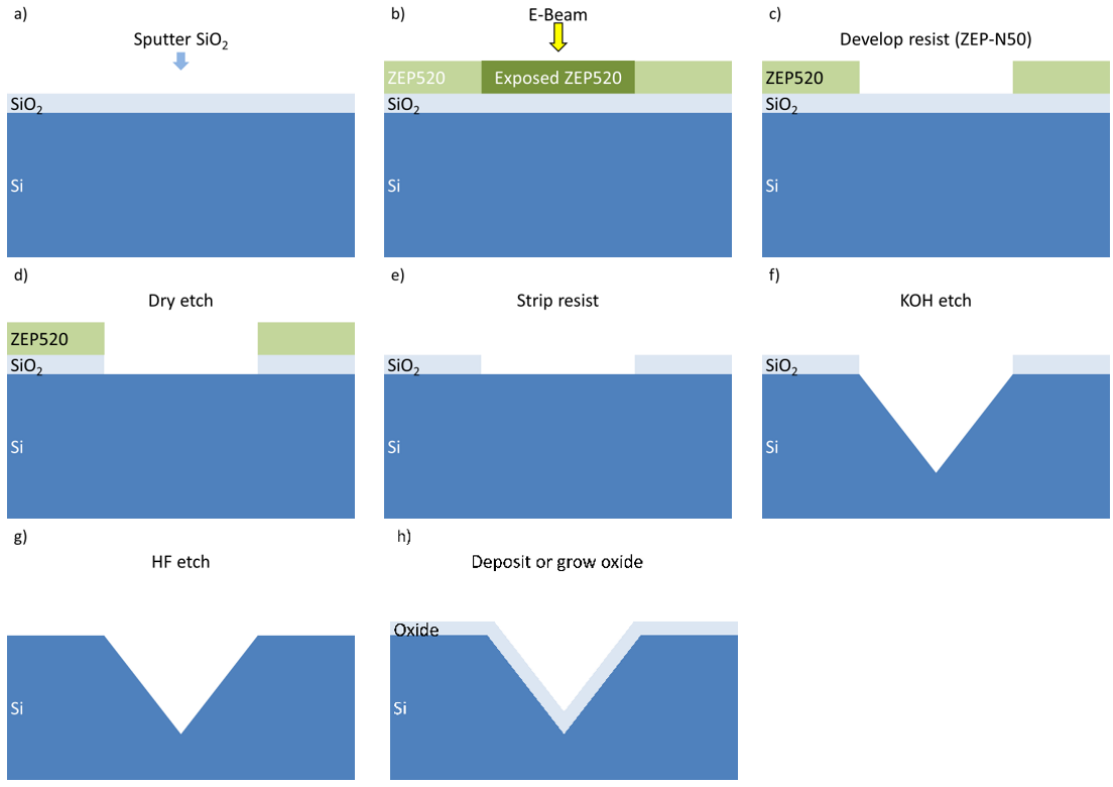

Figure 5.1 Process used for fabricating inverted pyramid grating structures on Silicon substrates.

A six-inch silicon wafer is first cleaned by immersion in fuming nitric acid for fifteen minutes to remove any organic or metallic contaminants followed by DI water rinsing. After being dried, the

wafer is immersed in hydrofluoric acid solution to remove any native oxide from the surface. Consequently, the wafer is washed in DI water and then dehydrated in an oven for at least thirty minutes in order to avoid any moisture from affecting the quality of the following process steps.

After the initial preparation steps, a 100nm layer of SiO_2 is sputtered on the top surface of the wafer in order to form a hard mask for the patterning process. ZEP520 photoresist is then spin coated on top the oxide layer at a speed of 3370 rpm for a time frame of 3 minutes. The wafer is then baked for two minutes at 180°C and an e-spacer layer is coated on top at 3500 rpm for a duration of 2 minutes to prevent charge trapping during E-beam (electron beam) lithography. The pattern is then transferred to the resist with the use of E-beam lithography using a beam current of 25nA. After the completion of the patterning process, the ESPACER is removed by placing the wafer in DI water for 30 seconds. The resist is developed by immersing the wafer in a ZED-N50 solution for 90 seconds followed by immersion in IPA (isopropyl alcohol) for 30 seconds forming a soft mask of the desired pattern. The unprotected oxide is then removed through reactive ion etching at a radio-frequency power of 200W and a pressure of 30mTorr in presence of argon and trifluromethane gases at a flow rate of 25 sccm and 25 sccm respectively. The remaining resist is then stripped away, leaving behind a hard mask of the desired pattern.

KOH etching of <100> silicon is known to produce inverted pyramid structures due to anisotropic etching along the relevant crystal planes [204]. The exposed silicon substrate is etched anisotropically with 40% concentrated KOH at 70°C for 9 minutes, resulting in the inverted pyramid structures. Subsequently, the wafer is cleaned with DI water and dried. The hard mask is removed by immersing the wafer in HF for one minute followed by another DI water cleaning step. Finally, as an optional step, a thin uniform oxide layer (for example 10nm of sputtered TiO_2 or 295nm SiO_2) is grown/deposited following the pyramid topology as seen in Figure 5.1.h.

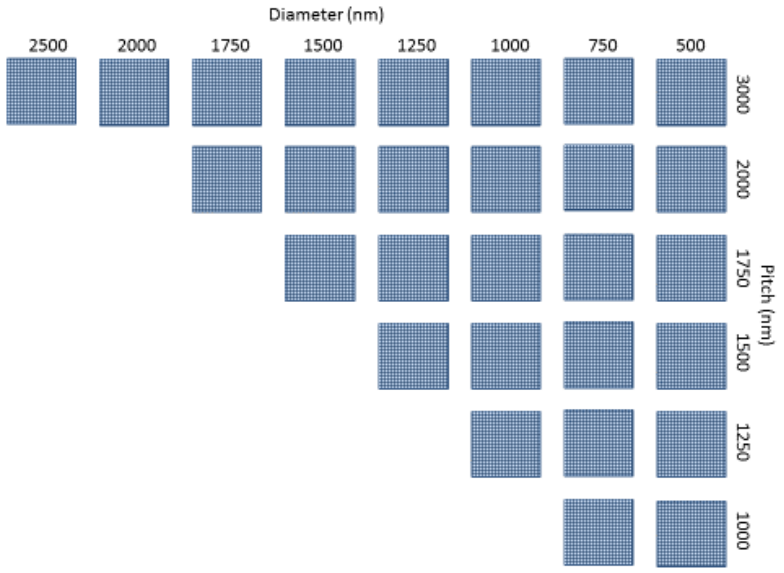

Figure 5.2 Top view of fabricated test sample with areas that have different size of pyramids and inter structure distances.

Figure 5.2 presents the top view and morphology of a test device with several areas of different pit diameters and pitches fabricated on the same chip with the purpose of investigating the geometric effect on diffraction efficiency. Samples with different aspect ratios of the pyramid structure are

also tested. In Figure 5.3 a Helium Ion microscopy image of one of the areas of the fabricated structures with an aspect ratio of 1-1 can be seen.

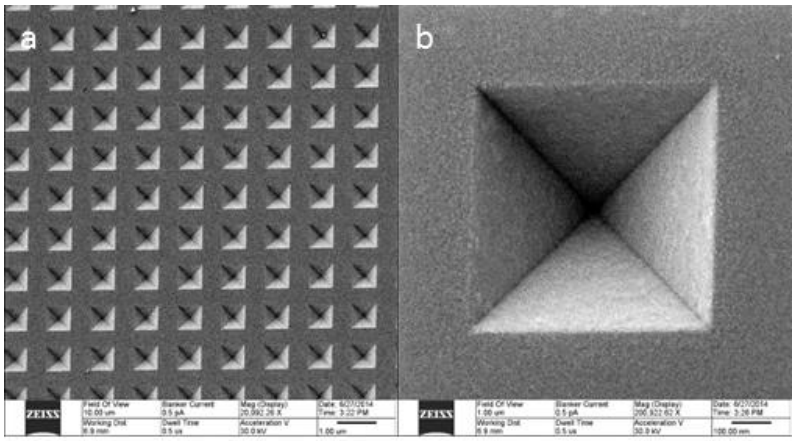

Figure 5.3 Helium Ion Microscopy images of inverted pyramid structures (aspect ratio 1-1) etched on a Silicon substrate. **a.** scale bar 1µm, **b.** scale bar 100 nm.

5.1.2. Reflectometry

In this section, the angle-dependant dispersion of the diffraction features appearing for arrays of inverted pyramid structures is discussed. The measurement system used for irradiating light and capturing the reflected spectrum is the reflectometry setup depicted in Figure 5.4.a. This setup can produce broadband spectroscopic reflectometry measurements for different angles of incidence (θ) and azimuth angles (ϕ) for both TE and TM polarizations (as seen in Figure 5.4.b). The setup consists of a white laser source, precision motorized stages, two polarizers, a focusing lens and a spectrometer, all connected to a console that can receive commands from a computer using a LabVIEW software (produced by National Instruments) graphical user interface.

The white laser source used in this setup has an unpolarised spectral range from 450nm to 1800nm and a maximum steady power output of 289mW. The power output is controlled through the use of two polarizers out of which one can be rotated. A focusing achromatic double lens with constant focal position and minimum beam distortion across a wide range of wavelengths is used to obtain a spot size of 745µm x 895µm when the sample is correctly positioned and in focus. High precision positioning motors can be used to carefully adjust the position of the sample in the X, Y, and Z axis while a camera is used to observe the position of the stage. Two rotary stages allow dynamic control over incident angle (θ) and azimuth angle (ϕ).

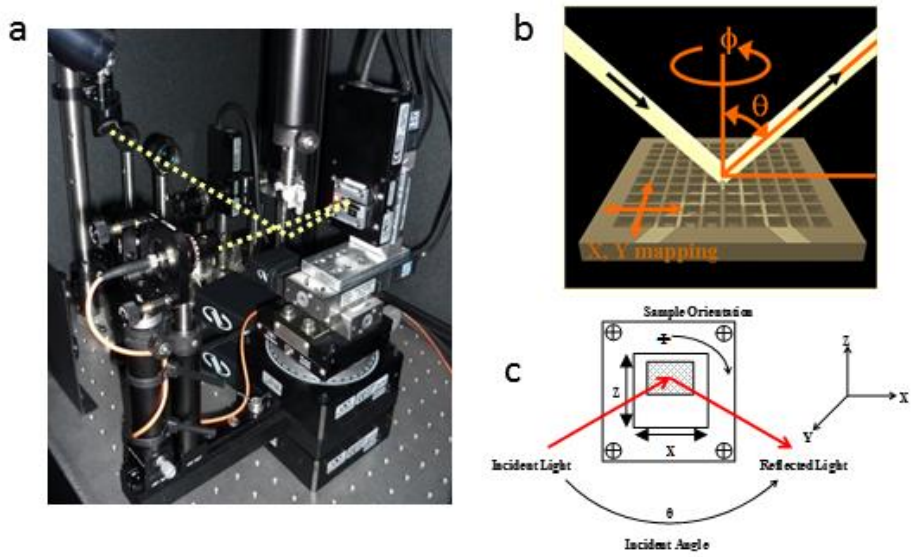

Figure 5.4 a. Reflectometry setup, light irradiates the sample and is then reflected back to the spectrometer through an optic fibre **b**. Schematic of the sample stage, thanks to the precision mechanical motors full control over the position in all X, Y and Z axis can be achieved. Two rotary motors allow for dynamic control over the incident (θ) and azimuth (ϕ) angles.

The sample is positioned on the stage of the reflectometer and the area of interest must be carefully adjusted in the X, Y, and Z directions in order to bring it in focus and keep it in constant alignment during all angular measurements. During measurement the white laser source is constantly irradiating the sample area with photons of a wavelength spectrum ranging from 450nm to 1800nm. The light reflects from the sample surface and captured through an optic fibre which in turn transfers the optical information to a spectrometer with a detection range within 450nm and 1050nm. The spectrometer is connected to a computer allowing for direct data observation, extraction and manipulation.

The measurement parameters used to collect reflection spectra from the grating are set for incident angle ranging from 0° to 60° and azimuth angle between 0° and 100° for both TM and TE polarizations (Azimuthal rotation results can be found in appendix section 12.1). Power output of the laser needs to be individually adjusted for different samples to avoid saturation or weak signal to noise ratio. For clear observation of diffraction features obtained data is normalized, and the background signal is subtracted.

Figure 5.5 demonstrates the test sample setup with different pyramid sizes and inter-structure distances available. It is useful to have an initial analysis of how different pitch/pyramid size combinations affect diffraction features. Measurements were taken for different combinations of pyramid size, inter structure distance, and periodicity. The results can provide information regarding diffraction efficiency, and diffraction dispersion over a large range of angles of incidence.

Figure 5.5 Different combinations of pyramid size and inter-structure distances available on the sample. The effect of pyramid size, inter-structure distances, and periodicity on diffraction features can be studied.

Before talking about the diffraction features in the measured spectra, it is important to clarify that broad vertical features that appear in most of the graphs in this chapter correspond to artefacts originating from the imperfect removal of the background source laser spectra from the obtained data and thus provide no real physical meaning. These peaks can be ignored and have thus not been labelled in the graphs. All features with real physical meaning have been labelled and are discussed in detail.

The experimental data in Figure 5.6.a-c have been plotted as a function of wavelength versus detection angle (2 times the angle of incidence) for stable pitch length and different pyramid sizes. Areas of high reflectivity appear in the bright spectrum of the colourmap while areas of low reflectivity are represented through the darker range. In the data presented on Figure 5.6, the areas with a. 1000nm pyramid side/ 1250nm pitch length, b. 750nm pyramid side/ 1250nm inter pyramid distance, and c. 500nm pyramid side/ 1250nm inter pyramid distance are compared. Change in pyramid size or inter-structure distance do not result in changes in the wavelength of the diffraction features/lines (sharp low-reflection peaks marked by dashed lines). These sharp peaks correspond to points where light is diffracted in a way that it propagates in parallel to the grating surface and thus is not reflected back to the sensor (Wood-Rayleigh anomalies, chapter 3.1.2) [79,81]. Frequency of diffraction lines is insensitive to a variation of pyramid size or inter-structure distance. On the other hand, diffraction efficiency for larger pyramids and thus (due to constant periodicity) smaller inter structure distance is higher providing sharper and clearer diffraction features. In Figure 5.6.d solutions of equation (3-4), showing the dispersion of the Wood-Rayleigh anomalies for up to the fourth diffraction order, are plotted having excellent agreement with the red dashed lines in Figure 5.6.a-c. The extra purple dashed lines that appear in the measured spectra, but not in the theoretical calculations, correspond to higher order modes and possibly to split bands originating from the more complex structure of the 2D inverted pyramid grating.

Figure 5.7.a-c compares measured spectra for a set pyramid size, and variation in pitch length and inter-structure distance. Change in pitch seems to have a significant effect in the wavelength of the

diffraction features. Shorter pitch lengths result in a blue-shift of the diffraction features. The effect of inter-structure distance on diffraction feature wavelength can be dismissed as in the previous measurement it was proven to be insignificant. These results agree with the theoretical predictions for the Wood-Rayleigh anomalies that can be seen in Figure 5.7.d. Once again the extra features that appear in the measurement can be attributed to higher order modes. When moving to higher inter-structure distances there is also an observable decrease of diffraction efficiency (features become weaker) which can be attributed to the lower density of diffraction structures per mm^2.

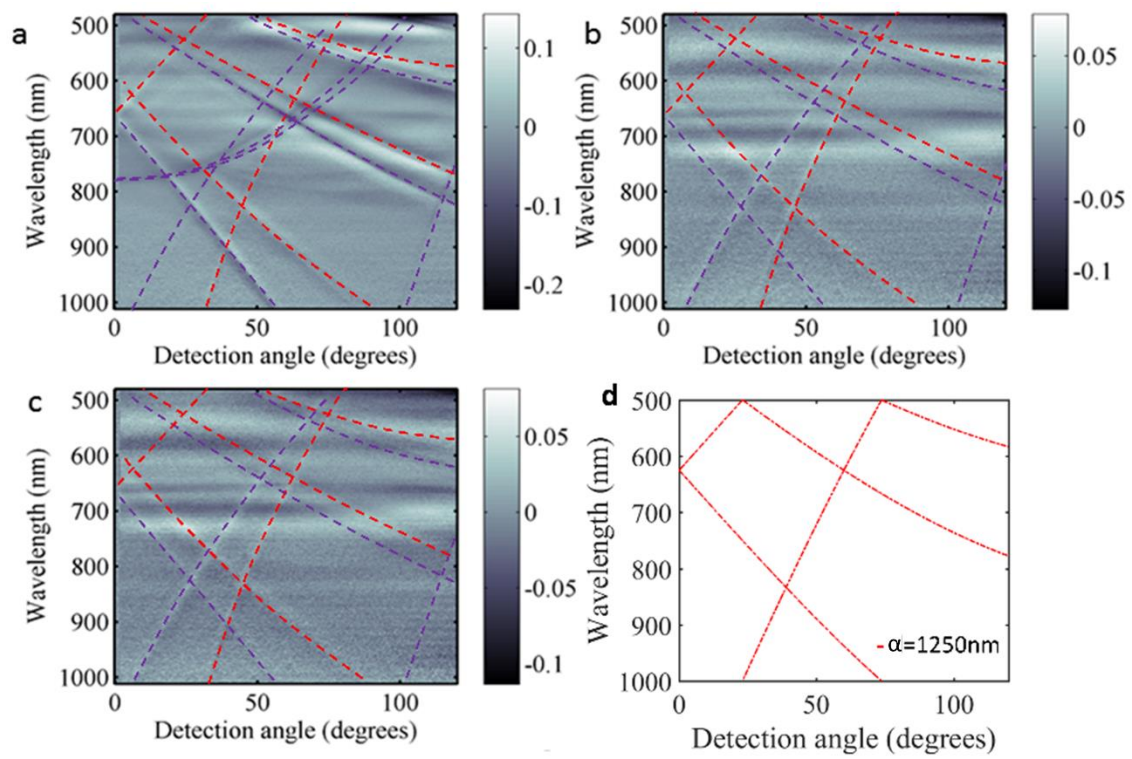

Figure 5.6 Reflectivity plot showing the intensity (arbitrary units) for measurement of the detection angle versus wavelength for structures with different pyramid sizes and stable pitch **a**. 1000nm pyramid side/ 1250nm pitch **b**. 750nm pyramid side/ 1250nm pitch **c.** 500nm pyramid side/ 1250nm pitch. **d.** Theoretical calculations. Red dashed lines in a-c match theoretical predictions and purple lines are higher order modes.

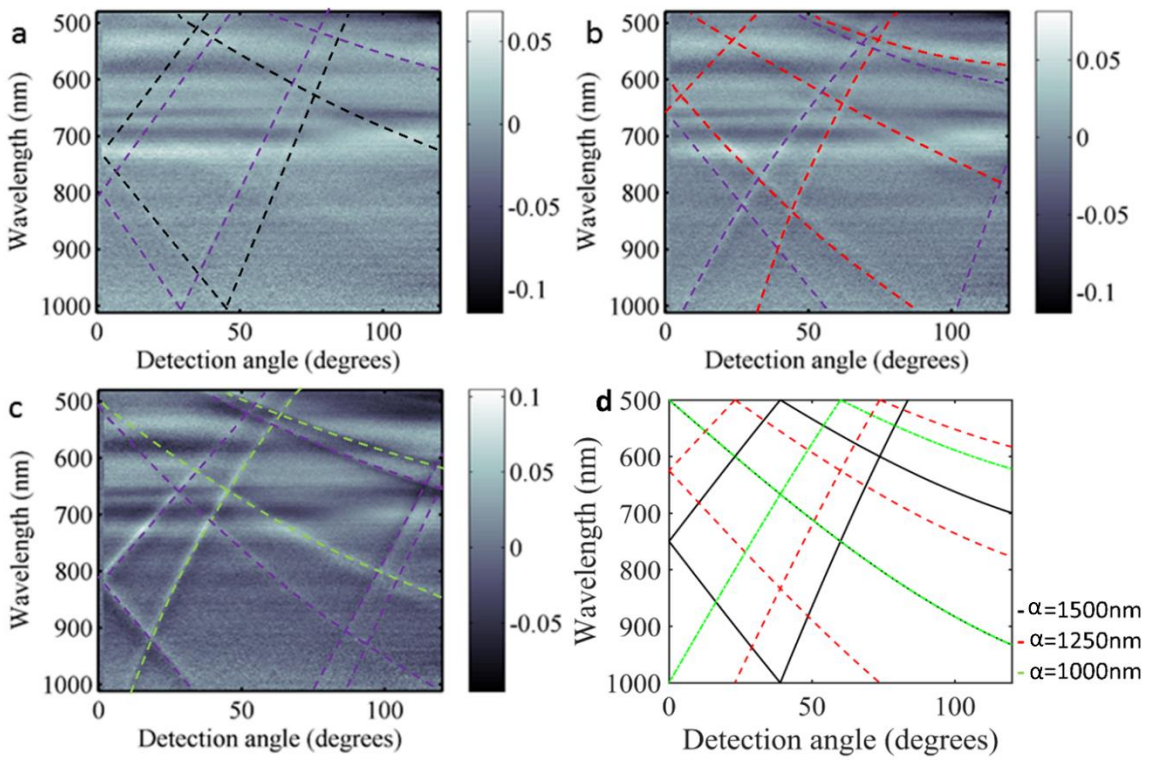

Figure 5.7 Reflectivity plot showing the intensity (arbitrary units) for measurement of the detection angle versus the wavelength for stable pyramid width and varying pitch lengths. **a**. 500nm pyramid side/ 1500nm pitch **b**. 500nm pyramid side/1250nm pitch **c.** 500nm pyramid side/ 1000nm pitch. **d.** Theoretical calculations. Black, red, green dashed lines in a-c match theoretical calculations in d, purple lines are higher order modes.

Figure 5.8.a-c compares the measured spectrum of structures with stable inter-structure distance but varying pyramid size and pitch length. Once again, change in pitch has a significant effect on diffraction feature wavelength as theoretically predicted in Figure 5.8.d. The effect of pyramid size on wavelength can be dismissed due to previous observations from Figure 5.6 and Figure 5.7. Maintaining a stable inter-structure distance seems to provide stable diffraction efficiency regardless of the change in pyramid size. Thus inter-structure distance can be assumed to be the most significant factor for defining diffraction efficiency.

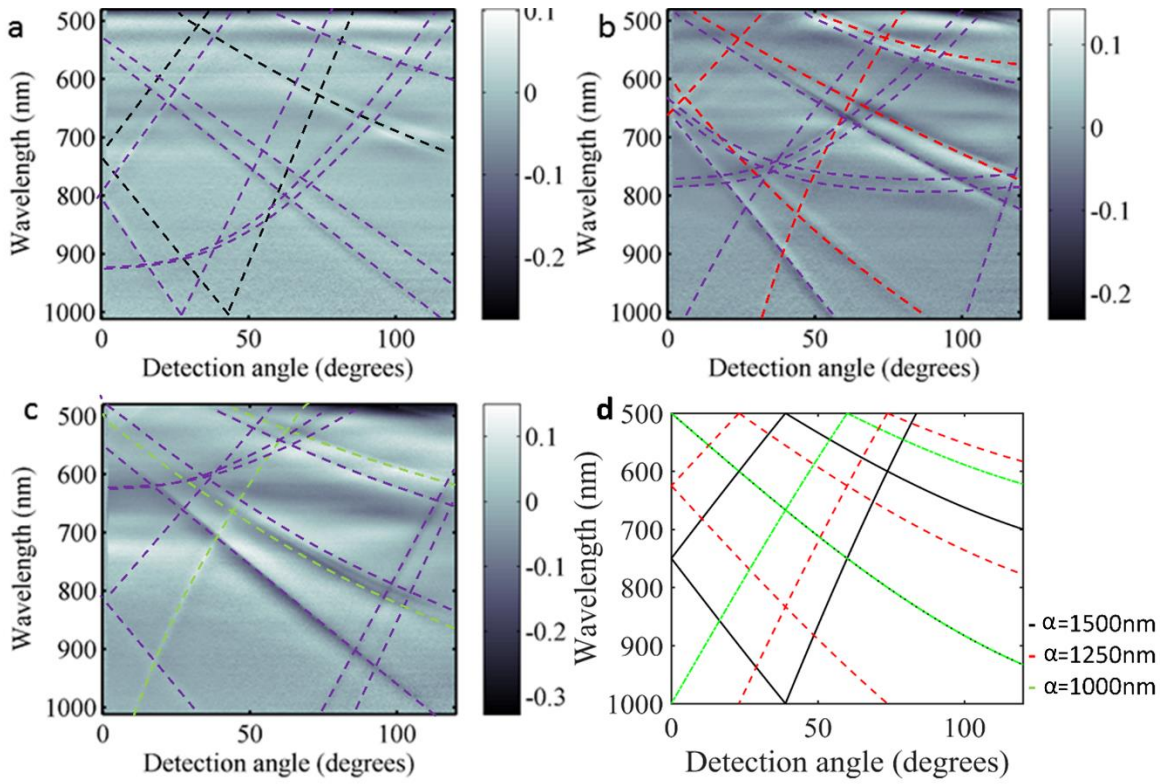

Figure 5.8 Reflectivity plot showing the intensity (arbitrary units) for measurement of the detection angle versus the wavelength for varying pyramid size and pitch lengths (constant inter structure distances). **a.** 1250nm pyramid side/ 1500nm pitch **b**. 1000nm pyramid side/ 1250nm pitch **c.** 750nm pyramid side/ 1000nm pitch. **d.** Theoretical calculations. Black, red, green dashed lines in a-c match theoretical calculations in d, purple lines are higher order modes.

Figure 5.9 shows spectra measured from diffraction gratings with a 750nm pyramid side/ 1000nm pitch length but varying aspect ratios for both pitch and pyramid size. The results correspond to P polarization and the electric field is parallel to the direction that the pitch and pyramid width is varied. As the pyramid width is shortened in one direction, the pitch length is also reduced. Since the electric field is set parallel to the direction of the shortened features, changing aspect ratio affects the shape and location of the Wood-Rayleigh anomalies due to the corresponding change in pitch length. This can be seen by observing the changes in the diffraction features (black dashed lines) for larger aspect rations.

Figure 5.10 presents spectra for a 750nm pyramid side/ 1000nm pitch length grating under a. TE polarization and b. TM polarization for square pyramid structures (1-1 aspect ratio). Because of the symmetry of the pyramid structures there is no difference between the two measurements.

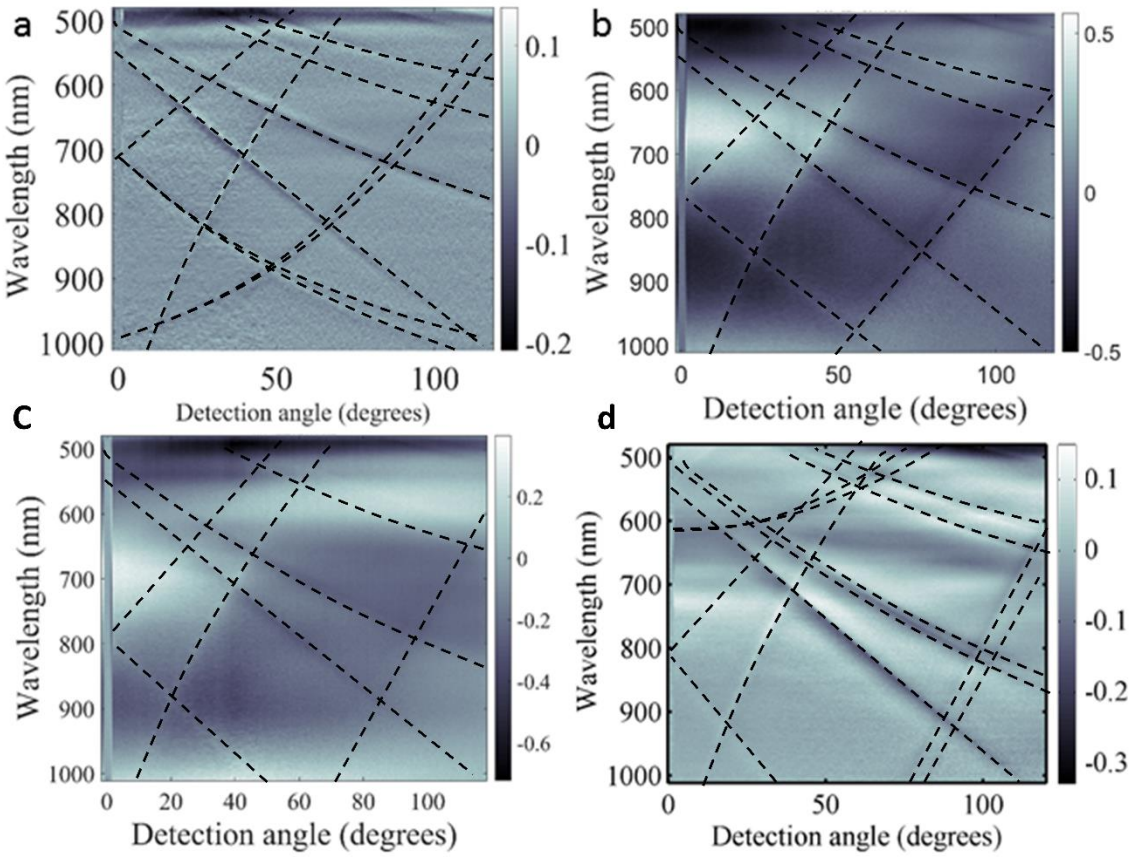

Figure 5.9 Reflectivity plot showing the intensity (arbitrary units) for measurement of the detection angle versus the wavelength for varying aspect ratios of a 750nm pyramid side/ 1000nm grating, **a**. 1-1.3 aspect ratio **b**. 1-1.2 aspect ratio **c**. 1-1.1 aspect ratio **d**. 1-1 aspect ratio.

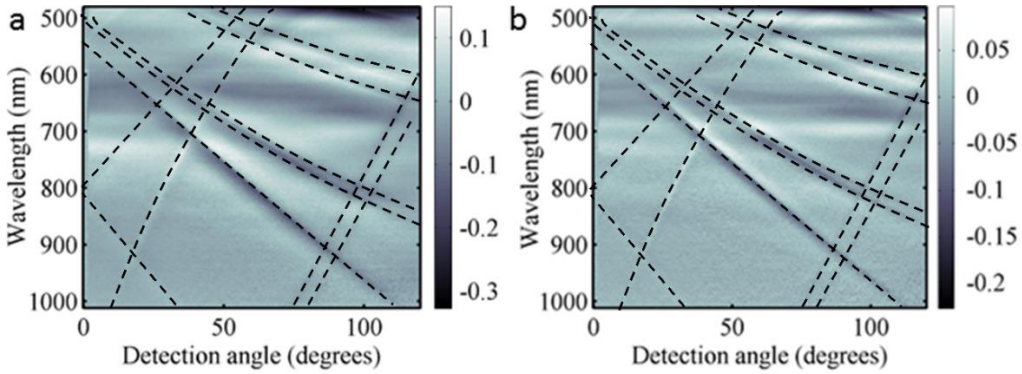

Figure 5.10 Reflection plots for S and P polarization. Because of the close symmetry of the pyramid structures (in this case 1-1 pitch aspect ratio) no variation was observed for the reflected spectra of the two different polarizations **a**. Reflected light for TM (P) polarization **b**. Reflected light for TE (S) polarization

The diffraction grating presents very strong and clear diffraction features agreeing with expectations from grating theory. Characterization of diffraction features is useful and necessary for understanding how phase matching occurs when exciting plasmons in graphene and also for demonstrating the diffraction efficiency of the grating. Diffraction is necessary for exciting propagating plasmons in graphene as the phase of the photon beam needs to match that of the plasmons. Diffraction at certain wavelengths can allow for the necessary phase relations to form and thus excite plasmons on the conducting layer.

5.2. Graphene Transfer Process

In this section an optimised graphene transfer method, utilized to place graphene on top the diffraction grating, is described in detail. The process is described step-by-step, and Raman spectroscopy, SEM, and HIM imaging techniques are used to demonstrate the quality of the transferred monolayer (other transfer methods can be seen in appendix sections 12.2.1, 12.2.2 and 12.2.3). The graphene used in this thesis has been obtained from Graphene Supermarket.

5.2.1. Optimised Transfer Process

The process steps of the optimised transfer method can be seen in Figure 5.11. Alternative efforts for transfers can be seen in the appendix. The method presented here provides the best results for transferring graphene on both flat Si wafers and on the inverted pyramid diffraction gratings while maintaining a minimum amount of steps.

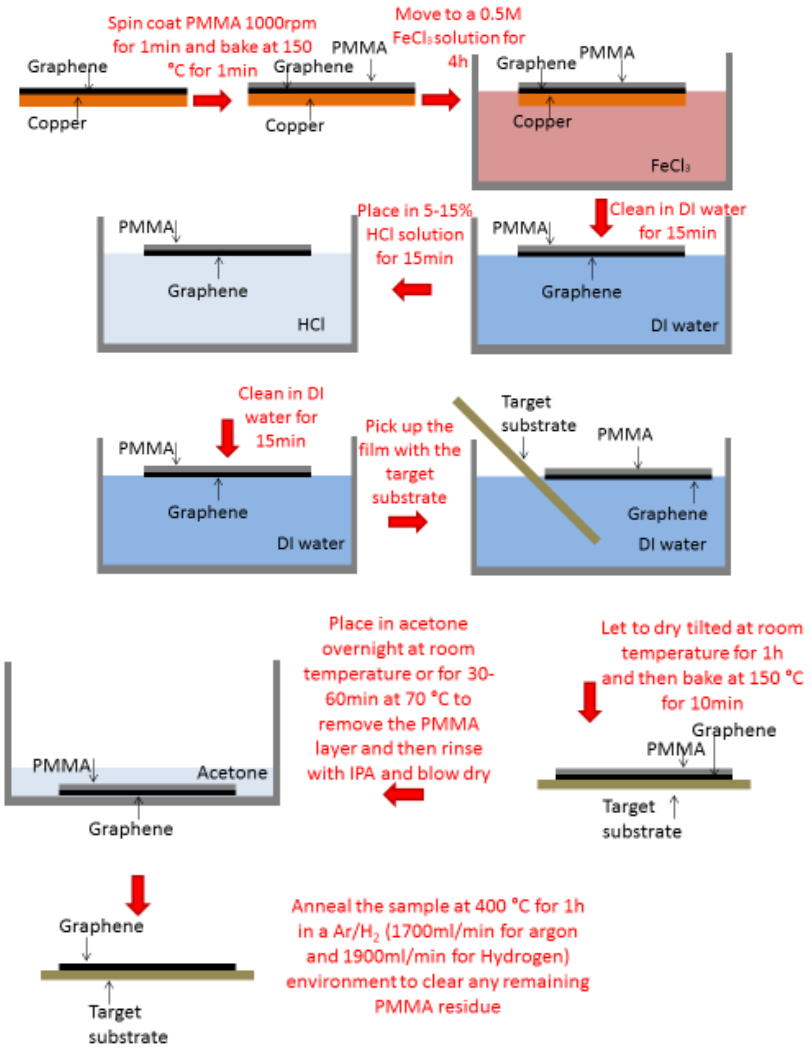

Figure 5.11 Transfer process used for placing the graphene monolayer on top of the patterned Silicon substrate.

The graphene monolayer used in the transfer process is typically grown on 25μm thick copper foils. Initially a thin PMMA layer is spin coated on top of the graphene monolayer at a speed of 1000rpm for a duration of one minute. A soft bake is performed at 150°C for one minute in order to remove any residual solvent. A 0.5 M ferric chloride solution is then prepared and used to etch away the copper foil. The etching process takes approximately 4 hours. The graphene/PMMA bilayer is then placed in DI water for 15 minutes in order to remove residual ferric chloride contamination. Consequently, the bilayer is carefully transferred to a beaker with a 5-15% HCl solution in order to remove metal contamination originating from the etching process, followed by another DI water clean step.

The graphene/PMMA bilayer can then be lifted off the DI water surface using the desired substrate. The sample is left to dry at a tilted position overnight at room temperature (alternatively it can be left to dry for one hour and then be baked at 150°C for 10min). Finally, the sample is placed in acetone bath overnight at room temperature in order to remove the PMMA layer. An acetic acid bath can be used to remove any remaining PMMA residue. As an extra step to further reduce PMMA residue and avoid unwanted doping originating from the transfer process, the sample is annealed at 400°C for one hour in an Ar/H_2 environment (1700ml/min argon flow and 1900ml/min for hydrogen flow). Ammonium persulfate can be used instead of ferric chloride with no noticeable difference in the result of the transfer. Additionally, PVB (polyvinyl butyral) polymer can be used instead of PMMA. PVB can be dissolved in methanol solution followed by ethanol rinse.

5.2.2. Raman Spectroscopy and SEM of Graphene on Copper

The success of the transfer, as well as the quality of the transferred graphene layer, is analysed with the use of Raman spectroscopy (with a 532nm laser excitation source). Initially the quality of graphene grown on a copper foil was measured by Raman spectroscopy. The Raman spectrum of a copper foil without graphene was first measured in order to then be subtracted from the graphene/copper foil measured data. The resulting spectrum can be seen in Figure 5.12 where the characteristic G and 2D peaks of graphene appear. The strong noise in the spectrum originates from the highly reflective surface of the copper foil. The peak positions for the G (1589.06 cm^{-1}) and 2D (2682.7 cm^{-1}) peaks are identified. The 2D peak position is very close to the one mentioned in the literature (~2680 cm^{-1}) but the G (~1580 cm^{-1}) peak position seems to be slightly upshifted by 9 cm^{-1}. This possibly originates from the underlying copper foil resulting in a doping effect on the monolayer. Both G and 2D peaks are sensitive to doping but the 2D peak is very weakly affected [165]. This could explain why only the G peak is upshifted. FWHM of the 2D peak (which can be fitted by a single Lorentzian peak) was found to be ~28 cm^{-1} which is within the commonly obtained values for single layer graphene (22-33 cm^{-1}) [179,184]. The FWHM of the G band was found to be 15 cm^{-1} and the I_G/I_D ratio was calculated giving an intensity ratio of 0.55 which is a characteristic value for single layer graphene [152,165]. Unfortunately, (even though a small peak can be observed around 1365 cm^{-1}, which is in the common range for the D peak) the signal was too noisy to accurately obtain the peak position and the FWHM of the D peak and as a result the I_D/I_G intensity ratio could not be identified.

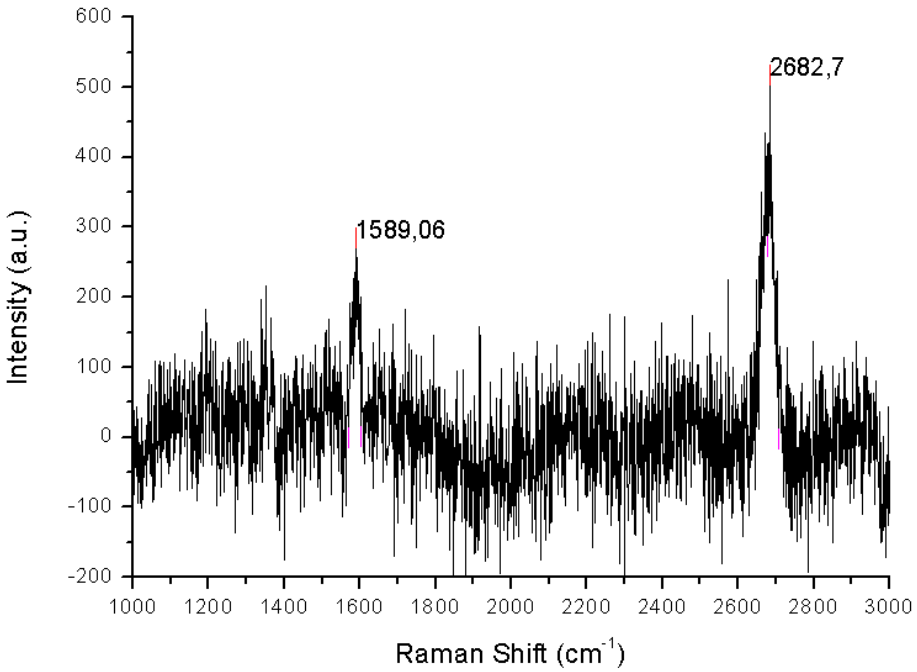

Figure 5.12 a. Raman spectrum of a copper foil with graphene grown on top. By subtracting the copper spectrum from the graphene/copper spectrum the typical graphene Raman peaks can be observed.

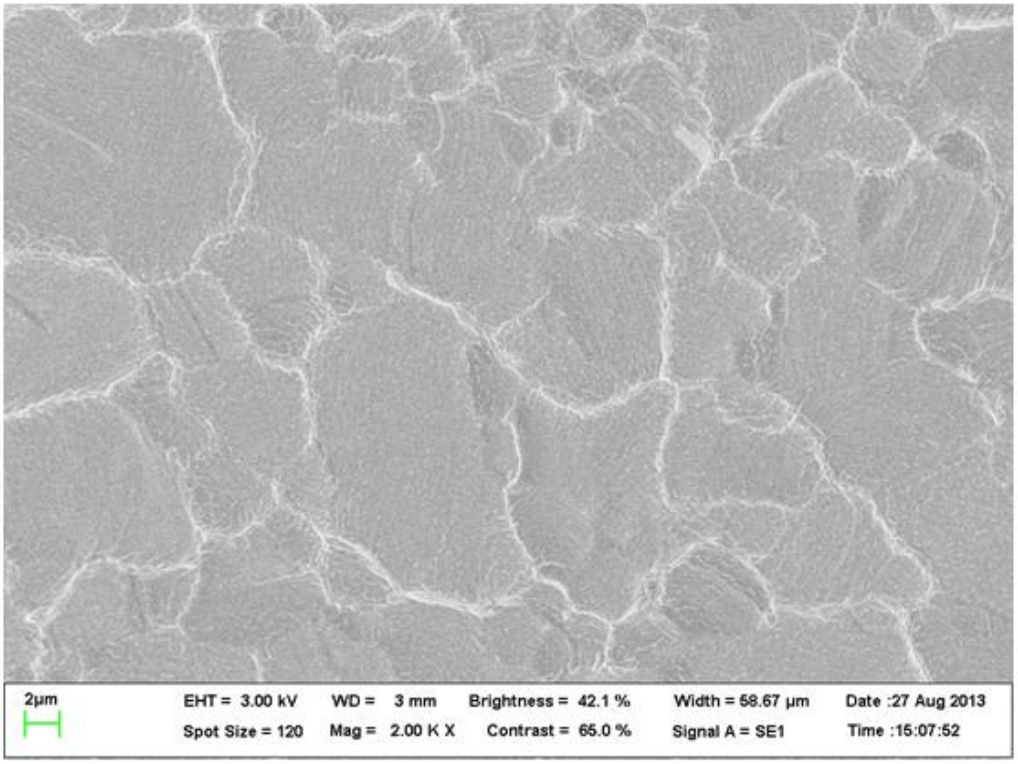

Figure 5.13 SEM image of the as grown graphene on the copper substrate. The graphene wrinkles that originate from the growth process can be clearly seen.

SEM imaging was used as complementary tool in order to investigate the morphology of the graphene layer grown on the copper substrate. Low primary electron energy (~3kV) was used since

the graphene layer is very thin and transparent to higher energy electrons. The graphene layer covers the entire region and is mostly visible at the locations where wrinkles are formed and mostly around the copper grain boundaries (Figure 5.13). These wrinkles originate from the thermal expansion mismatch of graphene with copper [180]. The graphene layer is uniform and no cracks are visible.

5.2.3. Raman Spectroscopy and SEM of Graphene on Flat Si Wafers

Raman spectroscopy data measured from a transferred graphene layer on a hydrophilic Si/SiO_2 substrate can be seen in Figure 5.14. The 2D, G peaks are very clear and a small D peak is easily observable meaning that there is some disorder in the atomic structure of graphene. Raman spectroscopy over various areas of the transferred graphene layer showed excellent uniformity with very small variations in the measured spectra. In some areas the Raman spectrum had intensity fluctuations due to the existence of wrinkled areas which are known to cause height variations in the G and 2D bands [152]. Not much variation was observed in terms of peak positions, peak intensity and FWHM for different areas of the sample. The transferred graphene was found to be monolayer over large areas and without a significant amount of defects.

In more detail, the 2D peak position (single Lorentzian fit) was found to vary between 2674 and 2670 cm^{-1} with a FWHM between 29 and 33 cm^{-1} while the G peak position was almost always stable at 1585 cm^{-1} with a FWHM of 12-18 cm^{-1}. The I_G/I_{2D} was also almost always stable for different areas varying around 0.24 and 0.27 meaning that the peak intensity ratio was maintained. All these values are common for single layer graphene. A D peak was also observed meaning that there were defects on the transferred graphene layer. The D peak's position was found to be at 1341 cm^{-1} and the I_D/I_G intensity ratio was found to be 0.38.

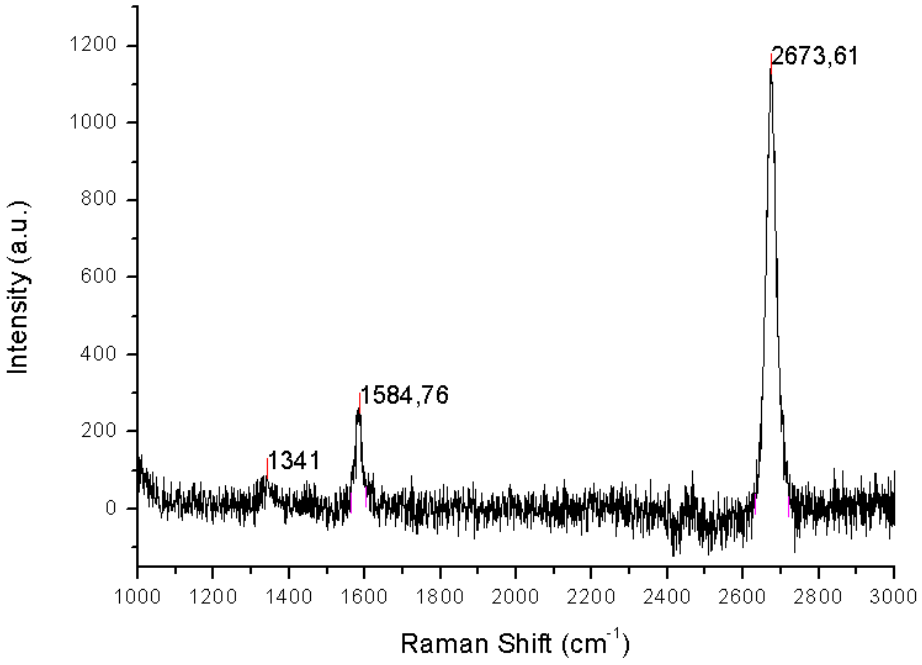

Figure 5.14 Raman spectrum of transferred graphene on a flat Si wafer.

By using the empirical relations suggested by Carnado et al (equation 3-7). [191] the I_D/I_G intensity ratio can be used to quantify point like defects in the transferred graphene layer as

$$L_D{}^2\left(nm^2\right)=\left(1.8\pm0.5\right)\times10^{-9}\lambda_L{}^4\left(\frac{I_D}{I_G}\right)^{-1}=1.8\times10^{-9}\times532^4\left(0.38\right)^{-1}=379.4\,\mathrm{nm}^2,$$

$$L_D\left(\mathrm{nm}\right)=\sqrt{L_D{}^2\left(\mathrm{nm}^2\right)}=19.5\mathrm{nm}\ .$$

Inserting the laser excitation wavelength in nanometers (which was 532nm) and the intensity ratio (0.38 for this measurement) the inter-defect distance of the point defects was found to be 19.5nm or in terms of defect density n_D (equation 3-8) as

$$n_D\left(\mathrm{cm}^{-2}\right)=\frac{\left(1.8\pm0.5\right)\times10^{22}}{\lambda_L{}^4}\left(\frac{I_D}{I_G}\right)=\frac{1.8\times10^{22}}{532^4}0.38=8.54\times10^{10}\,\mathrm{cm}^{-2}$$

meaning that the inter-defect distance of the graphene layer is 19.5nm and the defect density is $8.54\text{x}10^{10}$ per cm^2.

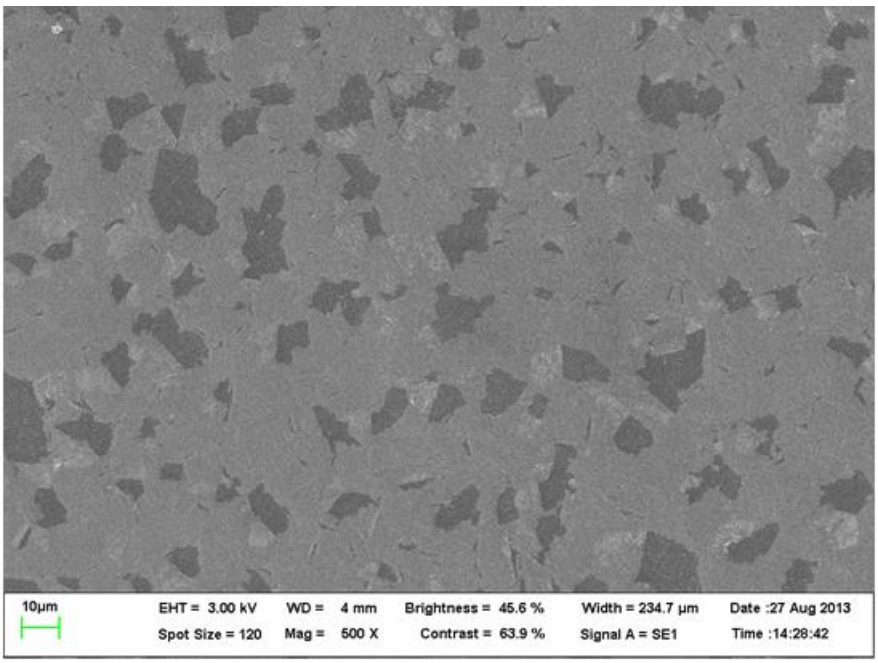

Figure 5.15 SEM image of a transferred graphene on the Si/SiO_2 wafer showing cracks induced during transfer process.

SEM imaging was used to observe the quality of the transferred graphene layer on Si/SiO_2 substrates. Low primary electron voltage was used (3kV) to observe the extremely thin graphene layer. Figure 5.15 shows the transferred graphene layer on a Si/SiO_2 substrate. Only a low amount of wrinkles can be observed in the image but there is a large amount of cracks throughout the whole graphene layer which resulted in many areas of folded graphene (also known as Grafold). The mean area and density of the cracks were obtained with the use of the Imagej software (Figure 5.16). The mean area of cracks was found to be 42.5µm^2, with bigger cracks having areas of even 280.6µm^2. The density of the cracks was found to be $3\text{x}10^5$ cracks per cm^2. The origin of the cracks can be

attributed to the drying process and is due to damage from evaporation of water that is trapped between graphene and the substrate. Careful temperature control should be used while drying the sample to avoid this issue. Poor contact with the substrate can also result to cracks during the PMMA removal step [162,180]. Gaps between the graphene/PMMA film and the target substrate originate from morphology of the PMMA film which still follows the source substrate's (copper) rough surface topology. A crucial step to overcome this problem is to have good temperature control during the bake of the sample after the drying process has been completed. This helps any remaining water escape from between the PMMA/graphene layer and substrate while relaxing the PMMA layer and allowing it to follow the topology of the new substrate. By following these two suggested steps the problem was resolved as will be demonstrated in the next section.

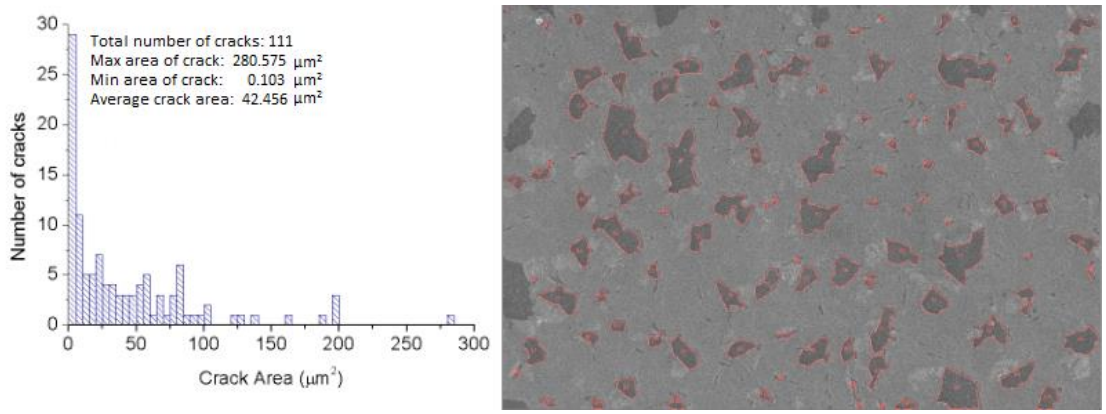

Figure 5.16 Histogram of the area of the cracks that were found on the graphene layer after the PMMA assisted transfer process. By analysing the SEM image with the use of the imagej software 111 large defects (areas>0.1µm^2) were observed on a graphene area of 3.64x10^{-4} cm^2 giving a crack density of 3x10^5 cracks per cm^2.

5.2.4. Raman Spectroscopy of Graphene on Inverted Pyramid Structures

This chapter shows successful graphene transfers on top of Si wafers with inverted pyramid structures etched on the surface. Figure 5.17 presents Raman spectroscopy data obtained from the transferred graphene layer. Great uniformity was achieved with very small variations over the area of the transferred graphene monolayer. The 2D and G peaks can be observed very clearly and the D peak is absent or very small, indicating a small amount of damage and good uniformity of the monolayer. The 2D peak position was typically found to be at 2675 cm^{-1} and always symmetric (single Lorentzian peak) with a FWHM of 31cm^{-1}, indicating a graphene monolayer. The G peak was measured at 1588cm^{-1} with a FWHM of 13cm^{-1}. The peak ratio I_G/I_{2D} had a stable value of ~0.22 following demonstrating characteristics of a high quality transfer of monolayer graphene [179].

Helium ion microscopy demonstrated a high quality transfer with minimum amount of cracks and wrinkles even on top the diffraction grating as seen from Figure 5.18. Even though the surface of the structure has deformations due to the pyramid structures the graphene monolayer maintains good uniformity with a minimum amount of wrinkles, folds, and cracks. For this to be achieved it is crucial to maintain perfect control of temperature during the entire transfer process. Thicker PMMA layers also help avoid cracking of the graphene layer due to the inverted pyramid structures

by providing more efficient support. This way suspended graphene can be obtained above the pyramid structures.

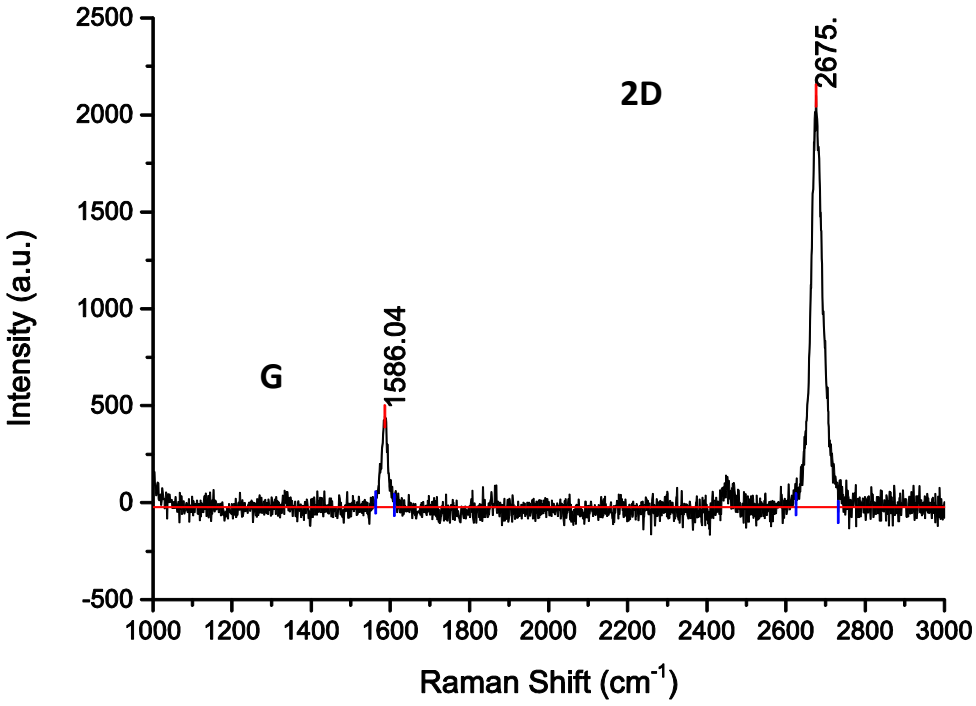

Figure 5.17 Raman signal of the transferred graphene monolayer on top of the inverted pyramid structures. The 2D and G peaks as seen in this figure are typical for a graphene monolayer. The intensity ratio between the two peaks and the lack of a D peak indicate a high quality graphene transfer.

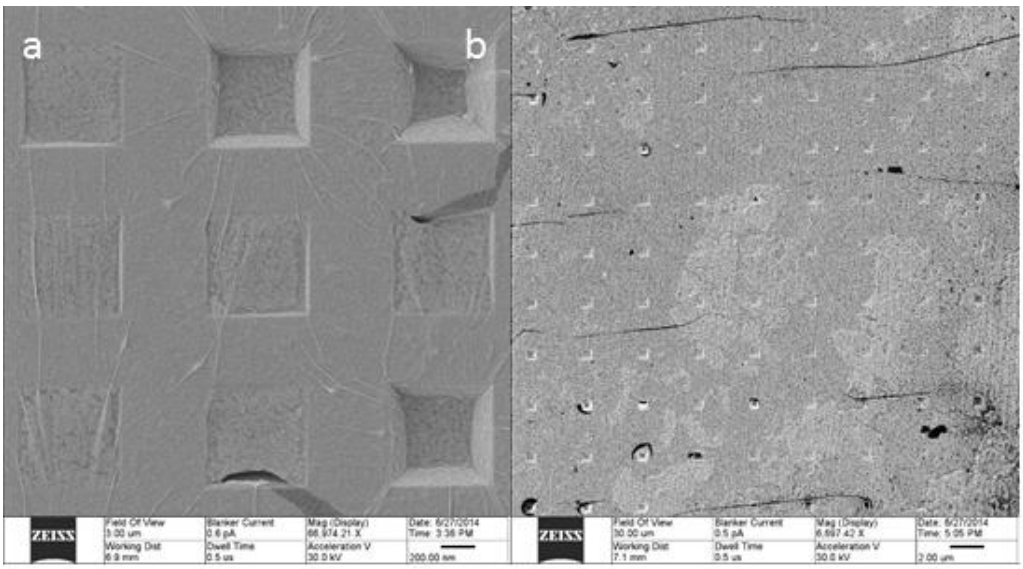

Figure 5.18 Helium Ion Microscopy images of the transferred graphene monolayer above the inverted pyramid structures. **a.** 200nm scale bar, **b.** 2µm scale bar,

5.2.5. Helium Ion Microscopy of Transferred Graphene

Helium ion microscopy is a very powerful imaging technique as it allows for much higher resolution to be obtained when compared with a SEM. The heavy He ions have a lower amount of scattering in the material in comparison with electrons which are used for SEM imaging and thus much smaller areas can be probed. HIM can be used to observe the quality of the transferred graphene layer on top of the diffraction grating, providing information on uniformity, structural integrity, and PMMA residuals on the graphene monolayer. Low current (typically 0.5pA) is used in order to avoid damaging the graphene monolayer from He-Ion bombardment that occurs during the imaging process. In this section graphene transfers on different substrates with different pyramid size and inter-structure distances are characterized through HIM. A discussion is made to explain the effect of pyramid size and inter-structure distance to the quality of the transferred graphene layer.

Figure 5.19 demonstrates a graphene monolayer transferred on a Si wafer with inverted pyramid structures etched on the surface. The pyramid structures are of very high quality with very smooth sidewalls and the graphene layer outside the grating region has excellent uniformity with few wrinkles and very few cracks. Graphene at the region of the pyramid grating structures seems to have an extensive amount of cracking resulting in the graphene following the surface topology of the structures. This is a crucial issue for graphene transfers when substrates with unusual surface topologies are used. After picking graphene from DI water with the substrate, trapped water remains in the holes. When the water begins to evaporate the graphene layer is pulled downwards due to induced capillary forces from the slowly residing water [165]. Similar issues have been observed when releasing graphene with HF on SiO_2 in order to obtain suspended ribbons [171]. Dry transfer methods or careful control of the drying process is necessary to overcome this issue. Critical point drying can possibly provide a solution for obtaining uniform suspended graphene above the grating region.

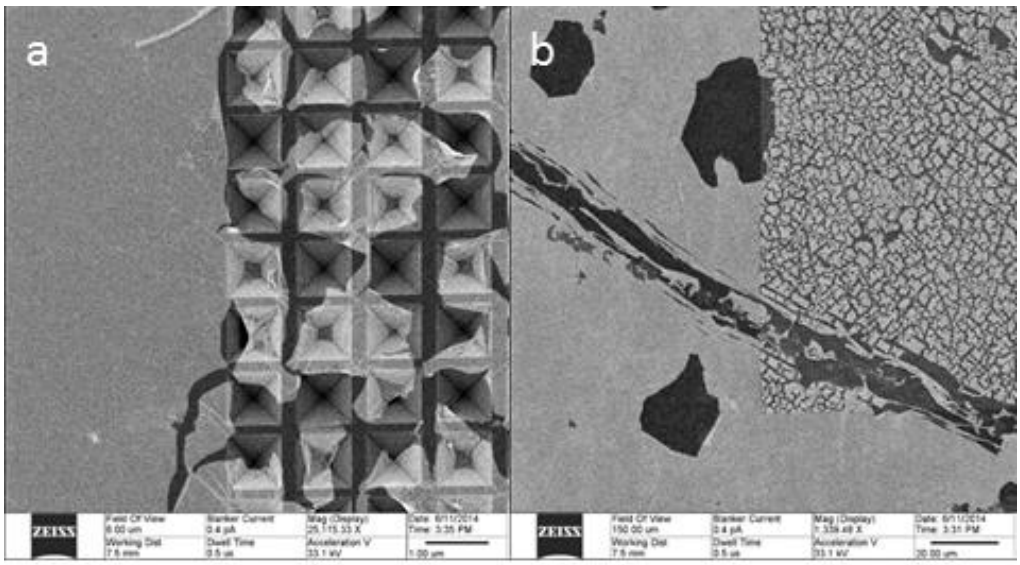

Figure 5.19 a. Boundary between the patterned area and un-patterned Si substrate, scale bar of 1µm **b**. Lower magnification image showing the same area of the sample with a higher field of view, 20µm scale bar.

The size and density of the pyramid structures also plays an important role on the conditions that lead to the formation of cracks. Test structures have been fabricated with areas that have different

pyramid sizes and inter structure distances as seen in Figure 5.20 in order to investigate the effect of topological features on the quality of graphene under identical transfer conditions.

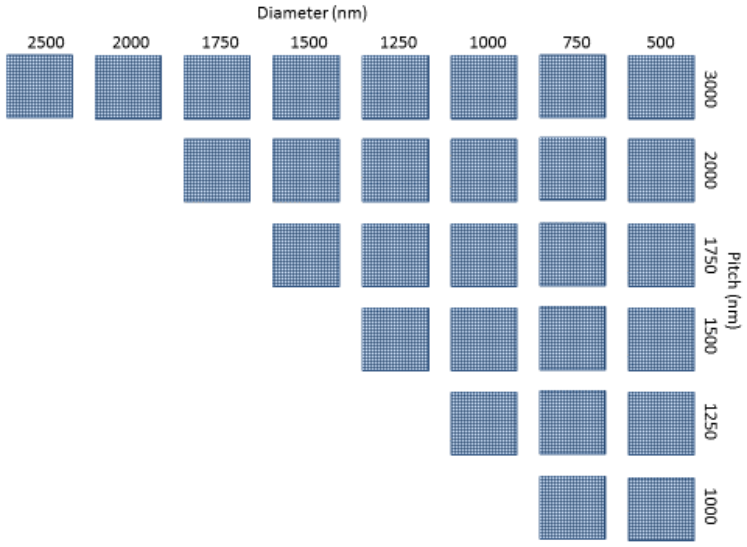

Figure 5.20 Top view of the fabricated sample with areas that have different size of pyramids and inter structure distances.

It was observed that areas with shorter inter-structure distances (gaps between pyramids) result in a higher amount of cracks as seen in Figure 5.21. This can be explained by taking into account the distribution of force experienced by graphene due to capillary forces originating from water evaporating from the inverted pyramid structures. Smaller pitch lengths translate to a higher density of inverted-pyramid structures. Each pyramid can be assumed to apply a certain force, pulling down the graphene layer towards the sidewalls of the structure. Thus having a higher density of pyramids results in a higher net applied force per μm^2 experienced by the monolayer leading to higher stress on the material and eventually fracturing of the layer.

Changing the size of pyramid structures while maintaining pitch length has a similar effect on the quality of the transferred layer (Figure 5.22). As pyramid structures increase in size cracks increase in number. Having a larger pyramid means that graphene needs to be suspended over larger distances. When capillary forces pull the suspended monolayer towards the sidewalls of the pyramid structure, graphene suspended over larger areas experiences a larger amount of stress on the anchor points resulting in fracturing of the layer. This happens because a larger suspended area translates to a larger contact area with water, thus resulting to a much higher overall force experienced due to capillary forces.

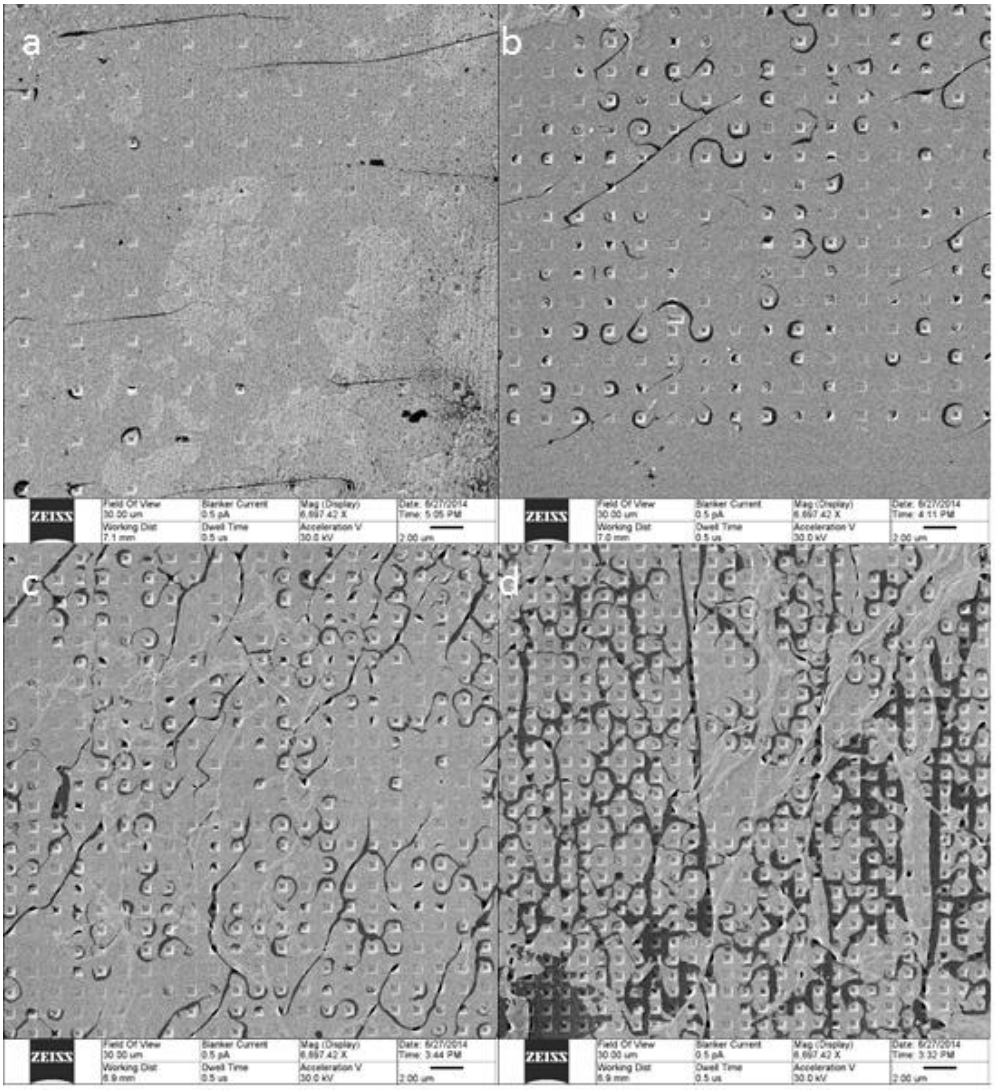

Figure 5.21 Helium Ion Microscopy images for areas with pyramid width of 500nm and different inter structure distances. **a**. Area with pitch of 3000nm. **b**. Area with pitch of 1750nm. **c**. Area with pitch of 1250nm. **d**. Area with pitch of 1000nm.

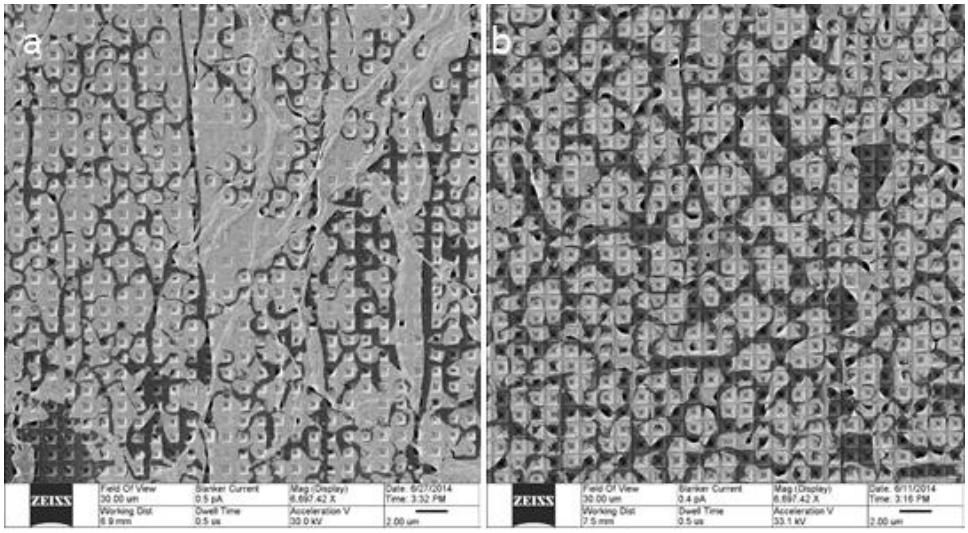

Figure 5.22 By maintaining stable pitch length (1000nm) the effect of the pyramid structures size can be observed **a**. Area with pyramid side length of 500nm. **b**. Area with pyramid side length of 750nm.

This means that depending on structural parameters graphene can be either suspended of conformal to the underlying structures. For example in Figure 5.23.a and Figure 5.23.b graphene is perfectly suspended above the pyramid structures. In Figure 5.23.c graphene has been pulled to the sidewalls of the pyramid structures while in Figure 5.23.d only a small part of graphene is suspended at the lower part of the structure. Such deformities of the graphene layer can have very interesting effects on plasmonic properties as they might allow the excitation of localized plasmons in combination with propagating plasmons. Helium Ion Microscopy can also be used as a milling tool. Figure 5.24 shows an area of suspended graphene on which a small square has been milled on. With this method suspended graphene beams or crosses as well as other more complicated structures can be obtained with possibly interesting properties in terms of plasmon oscillations.

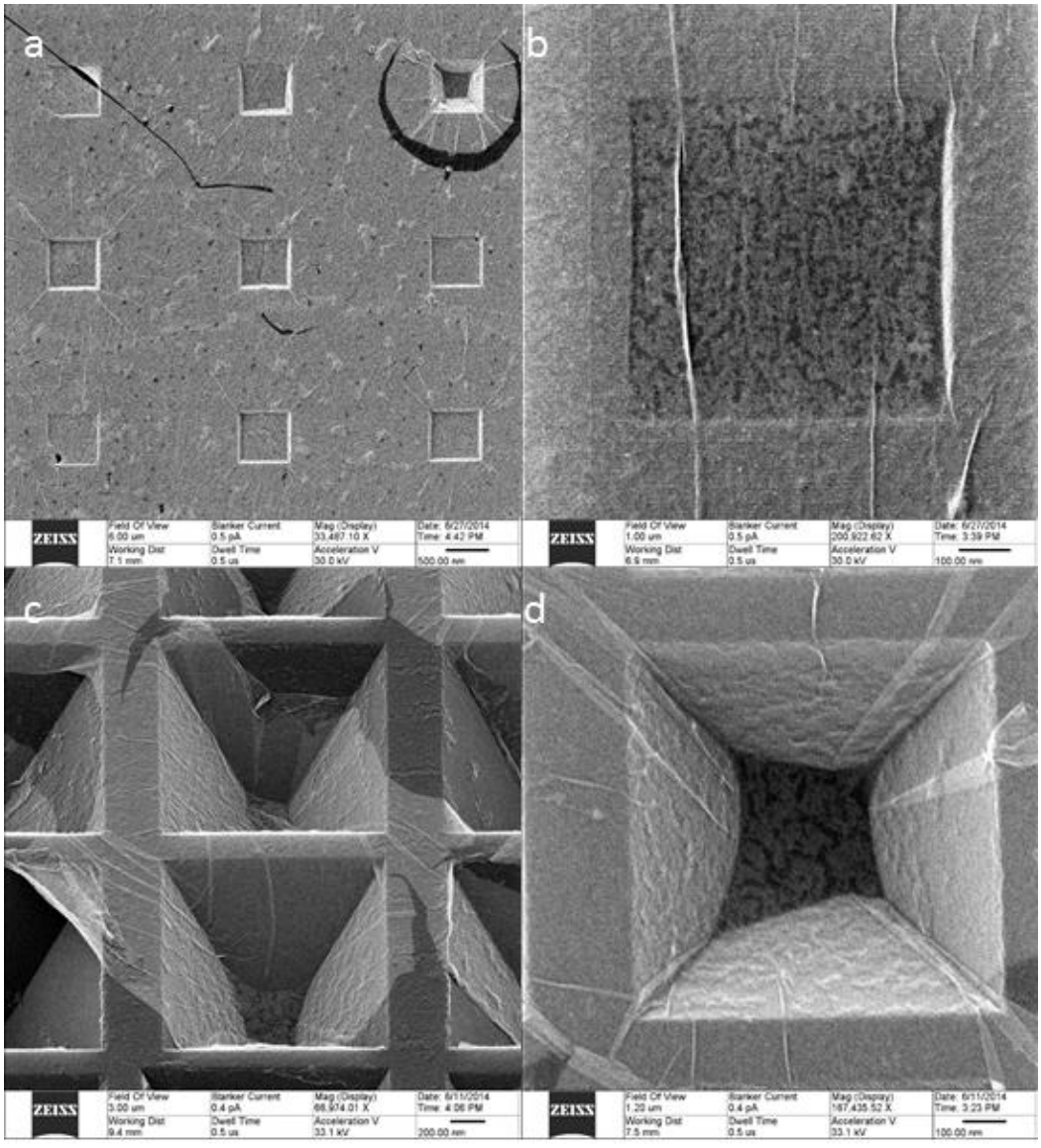

Figure 5.23 a. Suspended graphene over several pyramid structures (scale bar 500nm) **b**. Closer view of a suspended graphene over a pyramid structure (scale bar 100nm). **c**. Tilted view of cracked graphene over several pyramid structures (scale bar 200nm) **d**. Top view of a cracked graphene that follows the surface topology of a pyramid structure (scale bar 100nm).

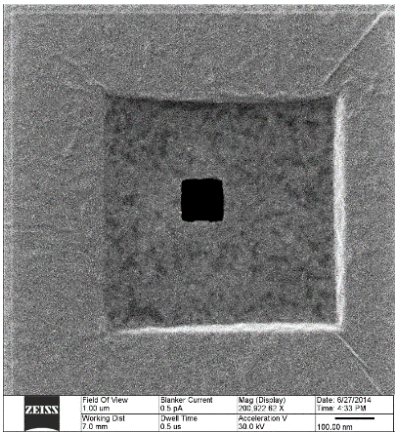

Figure 5.24 Square milled on a suspended area of graphene with the use of a Helium Ion Microscope.

In order to obtain continuous graphene with minimum amount of cracks that would allow electrostatic modulation through the introduction of contacts important care needs to be taken when choosing the dimensions and inter-structure distances between the pyramids. Suspended graphene can be obtained more easily for small pyramid sizes and large pitch lengths. Careful optimisation of the transfer process (or by utilizing dry transfer methods) could allow continuous suspended graphene layers for larger pyramids and shorter pitch lengths. Nevertheless, fractures and semi-suspended parts of graphene could lead to excitation of localized plasmons which would also provide some potentially interesting results.

5.3. Gate Modulation of Carrier Concentration in Graphene

The results presented in this chapter were possible thanks to the valuable transfer of technical knowledge as well as provision of experimental equipment from the Mizuta and Murata labs in JAIST, Japan. Professor Hiroshi Mizuta, Dr. Marek Schmidt, Mr. Jothiramalingam Kulothungan, and Mr. Ahmed Hammam provided valuable information and assistance for the preparation and measurement of the graphene FET device. Prof. Hideyuki Murata, Prof. Heisuke Sakai provided technical knowledge and facilities for the preparation of the ionic gel.

Achieving a very large shift in the chemical potential of graphene (several hundreds of meV) requires a very high gate capacitance. Ionic liquids provide high performance gating in FET devices but due to their liquid state they are neither durable nor do they provide the ability to form a permanent layer that can be part of a device [236]. On the other hand Ionic gel gates have recently attracted a lot of attention from the scientific community due to their transparency, mechanical flexibility, and very high capacitance (30μF cm^{-2} at 10Hz [192,237]) up to MHz frequencies when compared with conventional gate dielectrics [192,238]. Photo patternable ionic gels that can further provide the role of a mask for patterning graphene have also been reported [237–239], the photo-patterning is achieved by replacing the basic polymeric binder with a UV-cross-linkable binder. Performance improvements and better thermal stability has been reported for this type of ionic gels [237].

Ionic gels consist of a mixture of an ionic liquid with a block copolymer [192]. The block copolymers in the mixture provide mechanical strength while causing little reduction in the ionic mobility of the ionic liquid. The operating mechanism of the ionic gel gate is as follows. As a gate voltage is applied, anions and cations in the gel form electrical double layers at the gate/electrolyte and electrolyte/graphene or semiconductor interface. The graphene/electrolyte electrical double layer consists of accumulated carriers in the graphene and oppositely charge ions in the electrolyte thus providing electrostatic doping.

There are many different approaches for making ionic gels. Different anions and cations can be combined as well as different binders [192]. Depending on the molecular weight of the ionic liquid, the gate leakage and position of the Dirac point voltage of graphene varies [193]. For example, ionic liquids of higher molecular weights result in the Dirac point shifting to higher voltages. Furthermore, higher molecular weights lead to higher leakage currents. Care must also be taken for the electrochemical window of the liquid by avoiding using high voltage since, for voltages above a certain threshold, the liquid becomes ineffective for gate modulation due to the high leakage through the gate. The high capacitance of the ionic gel allows the generation of more than 10^{13} charges per cm^2 in graphene with the application of a few volts (<3V) [238]. graphene devices implementing Ionic gel gates with tuneable Fermi energy up to 0.6eV with the application of a gate voltage of just 1.73V have been reported [44,240].

By using equations $n_c = V_g C$ for the carrier density and $\mu = \hbar v_f \sqrt{\pi n_c}$ for the chemical potential (where V_g the gate voltage, C the gate capacitance, and v_f Fermi velocity), the efficiency of the ionic gel for modulating the chemical potential in graphene can be compared to that of conventional dielectrics (see section 4.1.1). Figure 5.25 compares the modulation efficiency a 20nm thick SiO_2 gate dielectric, a 20nm HfO_2 gate dielectric, and that of an ionic gel with a capacitance value of 10.7

µF/cm^2 as obtained from literature (even higher capacitances up to 30 F/cm^2 have been reported). Thin SiO_2 dielectrics suffer from high leakage currents thus high-K dielectrics like HfO_2 are typically used for achieving high capacitance and low voltage operation (an HfO_2 gate was studied in appendix section 12.2.4). Despite the leakage currents at high applied voltages, ionic gel easily outperforms conventional dielectrics, providing, much higher chemical potential shifts at a very low voltage. This strong modulation efficiency, transparency, and ability to fully modulate isolated or broken graphene areas over the entire sample area make ionic gel an ideal candidate for a gate material for this project. Nevertheless it should be noted that ionic gels are currently not suitable for high frequency operation as the moving ions have a relatively slow response to applied fields.

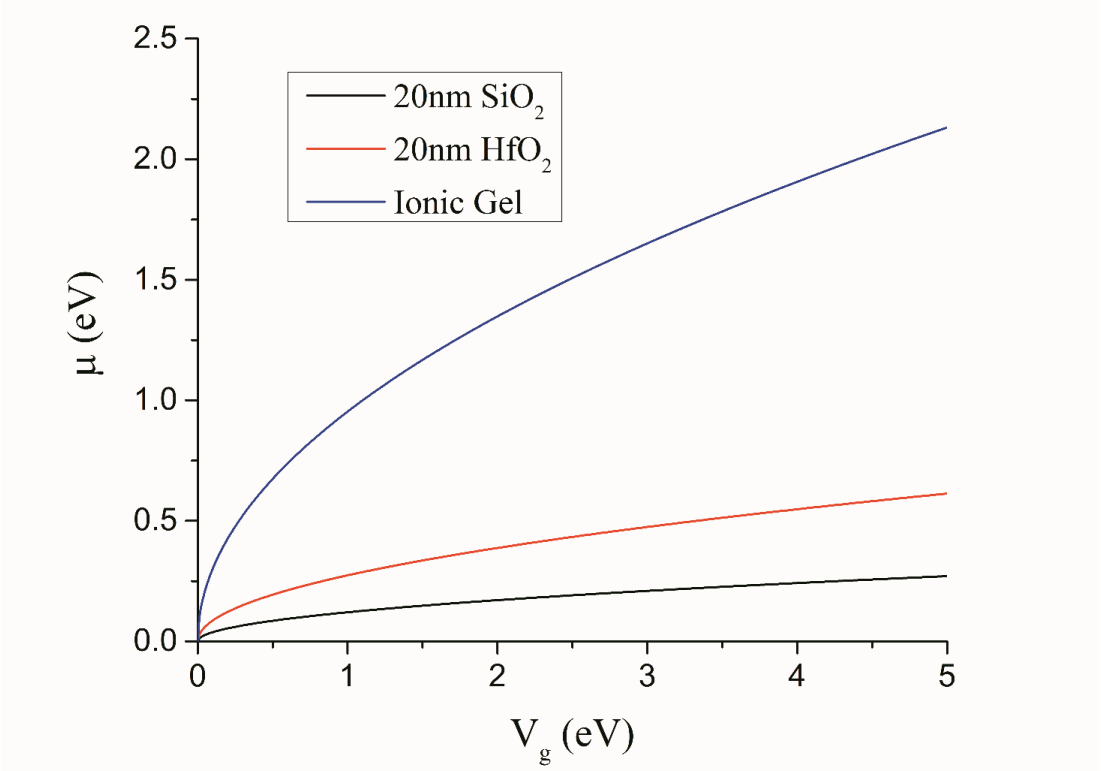

Figure 5.25 Graph of applied gate voltage versus chemical potential comparing 20nm thick conventional gate dielectrics (SiO_2 and HfO_2) and an ionic gel with a realistic capacitance value of 10.7µF/cm^2 (from reference [241])

5.3.1. Preparation and Deposition of Ionic Gel

In this work the method of preparing the ionic gel is similar to that of Chen et al.[240]. The ionic liquid of choice is 1-ethyl-3-methylimidazolium bis(trifluoromethylsulphonyl)imide ([EMIM][TFSI]) and the binder is polystyrene-b-poly(ethylene oxide)-b-polystyrene (PS-PEO-PS) triblock copolymer. Molecular weights of the block copolymer moiety are 10-44-10 kgmol^{-1} for the PS-PEO-PS blocks, respectively (PEO volume fraction=0.67). Dry dichloromethane is used as the mixing initiator. Finally Poly(3,4-ethylenedioxythiophene)-poly(styrenesulfonate) which is referred to as 'PEDOT:PSS', and is also transparent, can be used as the gate contact above the ionic gel. 3.0-4.0% high-conductivity grade PEDOT:PSS in water was used. If photo-patterning of the ionic gel is required, poly(ethyleneglycol) diacrylate (PEG-DA) (molecular weight = 575) can be used as the binder polymer while

at the same time acting as a negative photoresist. In this case, 2-hydroxy-2-methylpropiophenone (HOMPP) is used as an initiator for the mixing.

In more detail, the ionic liquid [EMIM][TFSI] is dried at 100°C under a vacuum of 200mtorr for three days and then transferred into an inert gas supplied glove box (the ionic gel is moisture sensitive). In the glove box, 0.55g of the ionic liquid is dissolved with 21mg of PS-PEO-PS in 2ml of dry dichloro-methane and is left to stir overnight at room temperature. The ionic gel is then spin coated on the sample at 1000rpm while still in the glove box. The refractive index of this ionic gel is approximately 1.42 in the visible spectrum [242,243]. The transparent conductive polymer contact can then be placed above the ionic gel by using the following method (as described in reference [237]). The substrate with the ionic gel is placed flipped over on top of a PEDOT:PSS thin film. A PEDOT:PSS layer is then transferred on top of the ionic gel by annealing the sample at 50°C for 5min. Alternatively, a gate contact can be fabricated at the desired area by evaporating gold through a stencil mask or by simply placing an Au foil on top. Figure 5.26.a shows the schematic of the fabrication process of the ionic gel gate and Figure 5.26.b the ion distribution in the gel under positive gate bias.

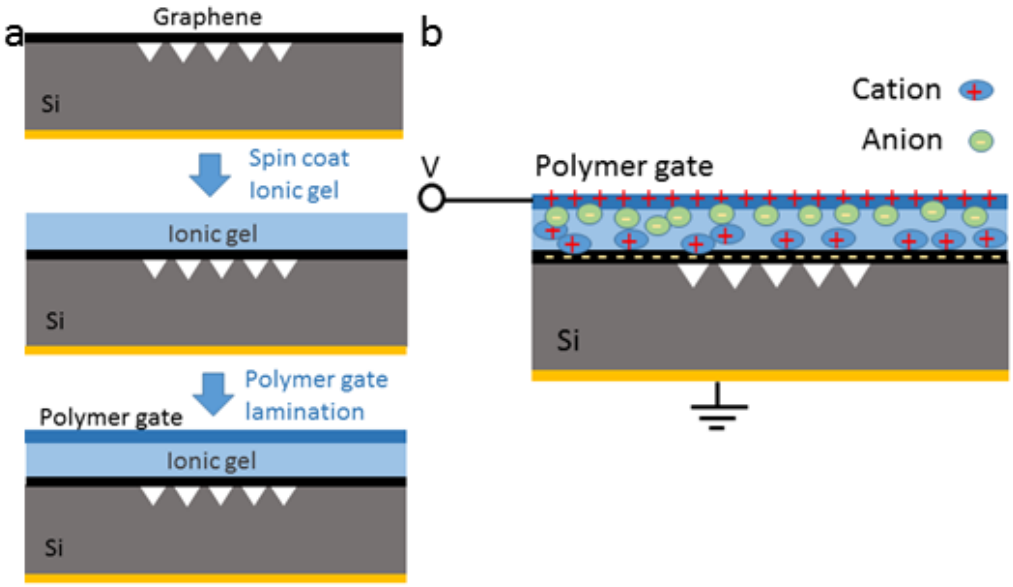

Figure 5.26 a. Schematic of the Ionic gel gate fabrication for unpatterned gel. **b**. Ion distribution for unpatterned gel under positive gate bias.

5.3.2. CV and IV Measurements of a Graphene Nanoribbon Ion Gel Gate FET

As discussed, good capacitance-gate voltage (CV) properties and good current-gate voltage (IV) properties are important for evidencing efficient modulation over the carrier concentration of the graphene layer. In this section, measurements of these properties are presented.

For test measurements a set of graphene micro-ribbons (length of 1µm and width of 1µm) were fabricated on a Si/SiO_2 wafer with an oxide thickness of 295nm as seen in Figure 5.27. The ion gel was then prepared and spin coated above the chip following the previously mentioned method.

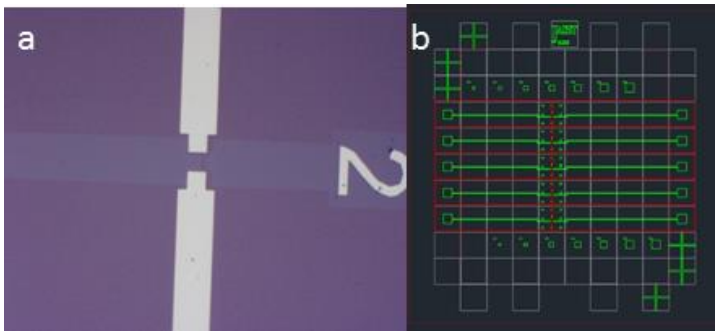

Figure 5.27 a. Optical microscopy image of graphene micro-ribbon. **b**. Mask file for contacts and graphene ribbons.

Since the ion gel works by utilizing mobile ions forming an electrical double layer at the interface of the channel and the gate contact, the entire ion gel is conductive and therefore there is no need to place the gate at a specific location on the gel. As seen from Figure 5.28 a top gate setup utilizing an Au foil contact or a side gate from evaporated gold on the SiO_2 layer can effectively be used as a gate for the device. Capacitance measured between either of the metal gate contacts (e.g. Gate 1 and gate 2) and either of the source/drain contacts is expected to result in the same value. This is because the capacitance is dominated by the capacitance originating from the electrical double layer in the ion gel, which is expected to be very high. As the electrical double layer is expected to be on the order of less than a nanometre for high ionic strength materials (the calculated Debye length is approximately less than 0.7 nm for approximately greater than 200 mM ionic strength), if the gate is greater than a nanometre distance from the source contact, the distance between the gate and contact is expected to be irrelevant. Experiments in which either Gate 1 or Gate 2 were used to measure the capacitance to the source or drain contact showed the same capacitance, proving this hypothesis. All measurements were performed under vacuum conditions and the drain source voltage was kept at V_{ds} = 5mV for the I_D-V_g measurements.

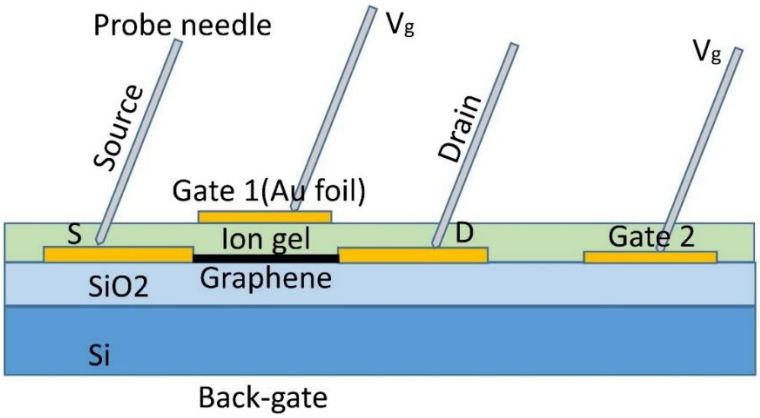

Figure 5.28 Schematic of the measurement setup with a top Au foil gate and a side gate of evaporated gold on the SiO_2 layer.

Figure 5.29.a demonstrates capacitance measurements of the ion gel device. The gate voltage can be applied as an AC voltage with a certain defined DC component. The capacitance has a strong

dependence on the level of the DC component around which the AC voltage fluctuates. This happens due to the force experienced by the positive and negative ions when DC voltage is applied. At 0V for the DC component the ions do not experience any constant force and thus they only follow the field resulting from the applied AC voltage. As the DC component value increases the constant field cancels out with the AC field in one direction thus resulting on periodically weaker force experienced by the ions depending on the polarity of the applied DC voltage and thus providing weaker charge separation, reducing the capacitance value. Stronger DC component can lead to strong accumulation of ions on the contact surface and thus constant strong separation between positive and negative ions. In this case the AC voltage could lead in a fluctuation of the accumulated ions on the contact surface resulting in stronger capacitance values. In Figure 5.29.b the frequency dependence of the ionic gel capacitance is shown. Since the ion gel capacitance works by the separation of positive and negative ions and the formation of electrical double layers on the surface of the two contacts, the capacitance has a high dependence on the time that the ions are allowed to accumulate on the surfaces. As the frequency becomes higher the ions have less time to travel and thus cannot reach the contact surface (less charge accumulating on the surface) and the capacitance becomes lower.

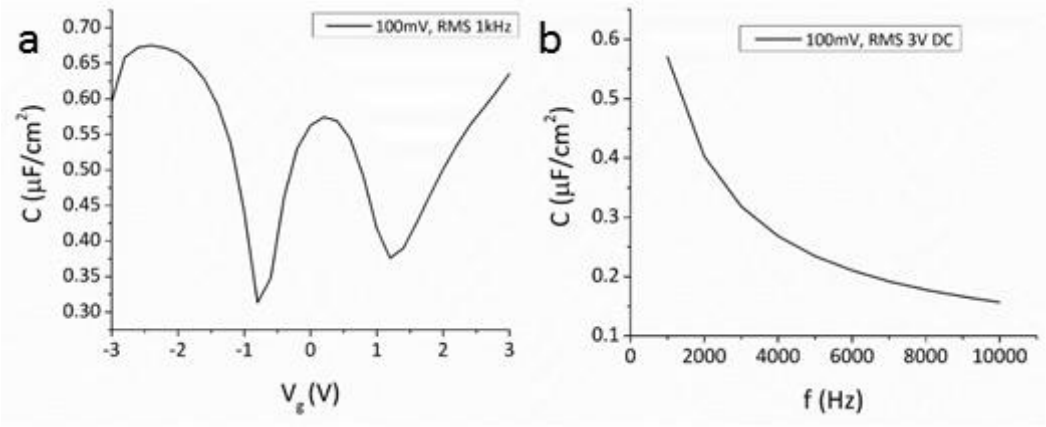

Figure 5.29 Capacitance measurements of ion gel gate **a.** Gate voltage versus capacitance measurement. **b.** Frequency of AC voltage bias versus capacitance measurement.

Having a very high capacitance, the ionic gel can provide very strong modulation over the carrier concentration of the graphene layer. Figure 5.30.a shows a comparison of I_D-V_g Characteristics between the same graphene ribbon with gate modulation from the ion gel (black line) and from a 295nm SiO_2 back gate (red line, voltage range scaled by 1/20). Applying a gate voltage modulated the current passing through the graphene layer as measured via the change in drain current (I_D), showing the device is operating as a transistor. The ion gel provides much higher modulation efficiency with a much sharper increase in current over a very small voltage range. Since the ion gel results in a much larger chemical potential shift in the graphene layer, due to the large gate capacitance achieved, moving from hole to electron conduction can occur under a very short voltage window. The ion gel gate also achieved a much higher max current when compared with the SiO_2 gate since it has a much higher modulation efficiency of the chemical potential of graphene thus achieving much higher carrier concentration while still requiring very low applied voltage.

In Figure 5.30.b the measurement of the same device took place under different scanning rates (longer time of applied voltage per voltage step) and a clear dependence was found on the I_D-V_g results. Since the ion gel depends on mobile ions for the modulation of the channel, when the voltage is applied for a longer time, ions have more time to travel and accumulate on the surface of the channel thus providing a stronger modulation effect. It is important to mention that within the first four days of when the gel is prepared the modulation efficiency is lower than in normal operation. This is due to the mixing agent that assisted on the preparation of the gel requiring some time to evaporate thus allowing the gel to settle. When the ion gel becomes stable the modulation efficiency increases as seen in Figure 5.30.c. The asymmetry in the I_D-V_g curves originates from the different properties between the positive and negative ions of the ionic liquid and depends of the choice of ions that are used in the ionic gel [192]. The sudden drop of current for higher positive voltages in the black curve of Figure 5.30.c can be attributed to reaching the electrochemical window of the ionic liquid thus making it conductive and allowing leakage current to pass. The fact that this is no longer apparent in the red line could be due to the gel chemical properties being slightly different when left to settle. Finally, the ion gel was found to be stable over long periods of time thus making it a suitable choice for devices that require strong modulation without high frequency operation.

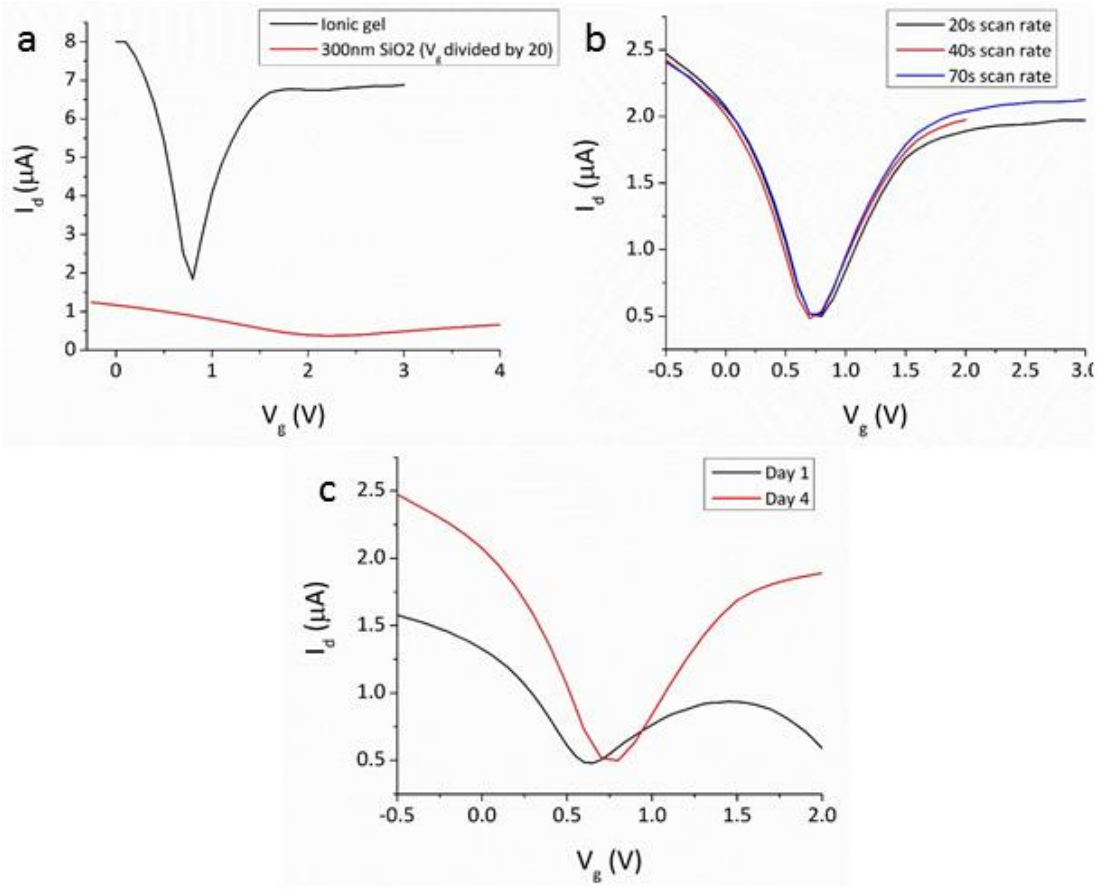

Figure 5.30 a. I_D-V_g comparison between ion gel gate (black line) and SiO_2 back-gate (red line, voltage range scaled by 20). **b.** I_D-V_g measurements of the same ribbon under ion gel gating for different scan rates. **c.** Comparison of the ion gel efficiency right after preparation of the device (black) and after four days that it has been allowed to settle (Red).

From the results of this section it is clear that the modulation of carrier concentration in graphene with the use of an ion gel gate is highly efficient and much more effective than that of conventional dielectric gates. Ion gel gates were found to provide significantly higher max current (and thus higher amount of available free carriers) and the results can be obtained within a very short voltage range. For the device fabrication of this work, strong modulation efficiency of carriers is necessary but high frequency operation is not required and thus an ion gel gate is ideal for providing dynamic electrostatic control of plasmons in graphene.

5.4. Tuneable Total Optical Absorption Plasmonic Device

In this the section, the final steps for fabricating a dynamically tuneable total optical absorption device based on graphene are presented. In previous chapters a theoretical model and simulations have been provided demonstrating the operation of the device. Having also provided the design and analysis of an efficient diffraction grating, a successful method for transferring graphene, and a way to dynamically modulate the carrier concentration in graphene, the final device concept as presented in chapter 4.2 can be realised experimentally.

5.4.1. Deposition of Gold Back Reflector and Spacer

First a diffraction grating is fabricated following the process presented in chapter 5.1.1. In this case the grating pitch for the structure is set at 1.165μm and the pyramid base width at 0.65μm to match the theoretical and simulation results presented in chapter 4.2. A 74nm thick Au film is then evaporated on top the diffraction grating at a deposition rate of 0.5Å/s in order to achieve a smooth uniform layer. A transparent spacer of 120nm thickness (SiO_2 or ITO) is then sputtered above the gold layer. The two-step process can be seen in Figure 5.31.a and the complete wafer in Figure 5.31.b. SEM microscopy of the structure can be seen in Figure 5.31.c. These two new steps are expected to create a novel device capable of significant enhancement of plasmon excitations on the graphene layer as theoretically predicted in chapter 4.2.c due to collective interference of electromagnetic waves in the grating structures and the Salisbury screen cavity that is formed.

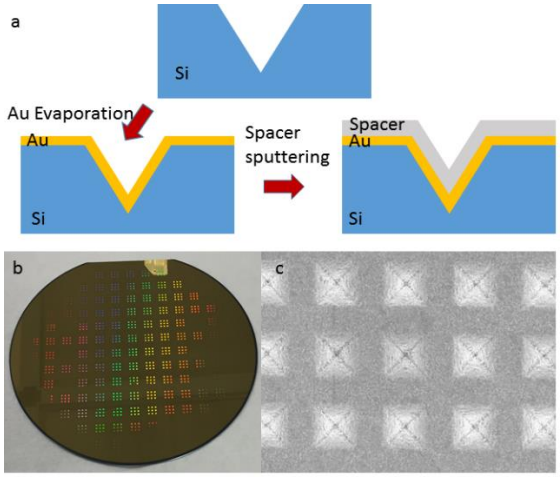

Figure 5.31 a. Process steps for fabrication of the back reflector and transparent spacer. **b.** Fabricated wafer including the diffraction grating and Au back reflector and SiO_2 spacer. **c.** SEM image of the grating after fabrication of Au back reflector and SiO_2 spacer.

5.4.2. Transfer of Graphene Monolayer and Fabrication of Ion Gel Gate

After the preparation of the diffraction grating and Salisbury screen optical cavity a graphene monolayer can be transferred using the method presented in chapter 5.2. SEM of successful graphene transfer on the diffraction grating with the Salisbury screen cavity can be seen in Figure 5.32. Successfully transferred graphene over a large area can be seen with few wrinkles and cracks. When moving to higher magnification (Figure 5.32.b-c) it can be seen that graphene is suspended above the majority of pyramid structures. Figure 5.32.d shows an area above an inverted pyramid when graphene is only partly suspended. Small particle formations in the pyramid can be seen originating from the deposition of the gold back reflector.

When the graphene layer has been successfully transferred, a gold contact can be fabricated through shadow mask evaporation. In order to ensure efficient contact with the graphene layer, first a titanium layer (10nm) is evaporated followed by a thick layer of gold (150nm). An ion gel film can then be prepared and spin coated using the method described in chapter 5.3.1. Finally a contact can be placed on top the ion gel through shadow mask evaporation or simply by gold foil lamination. The process steps required are presented in Figure 5.33. After the completion of the final step the device is ready for testing. For optical characterization an FTIR setup attached to a near-infrared microscope can be used since it can efficiently cover a spectral range from approximately 2µm to 25 µm.

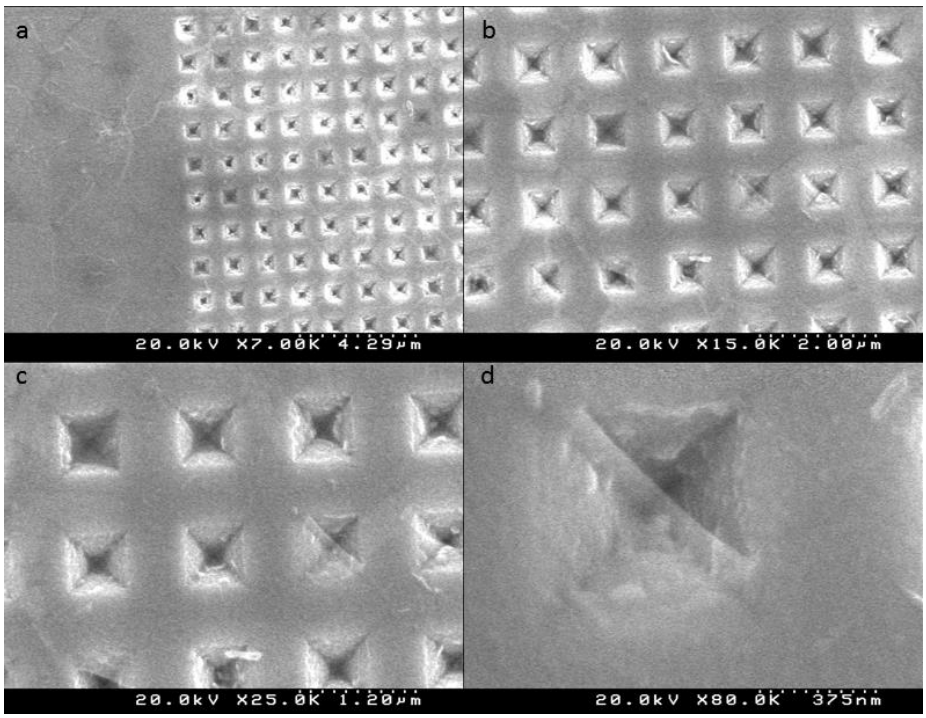

Figure 5.32 SEM images of graphene transferred on the diffraction grating with a gold back reflector and an 120nm thick ITO spacer. **a. G**raphene successfully transferred on a large area above the diffraction grating structures. **b-c** show close up view of the same region. **d.** semi suspended graphene above an inverted pyramid structure.

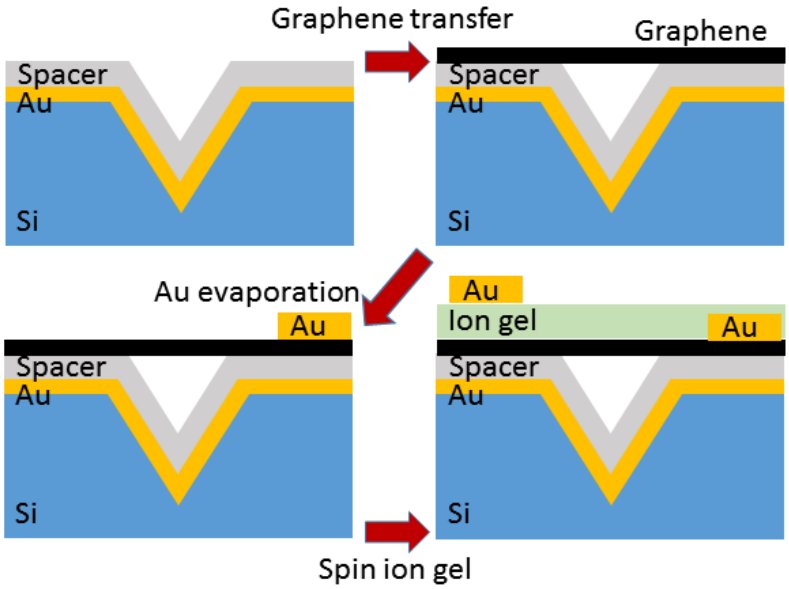

Figure 5.33 Process flow showing the transfer of a graphene layer on the diffraction grating and the fabrication of the gate structure.

5.4.3. Final Device and Measurements

The final step for fabricating the device is yet to be completed due to time constraints. This was because there was no available ionic gel process in the University of Southampton Nano-Group labs and transport of the ionic gel is very sensitive to atmospheric conditions when in liquid form and thus transferring it from Japan to the UK is difficult. Fabrication and characterisation of a complete practical device has to be postponed for after the completion of this thesis.

The device fabrication is currently at an almost functional stage only requiring a new ionic gel process to be established at the Nano group labs. For future work a dry transfer method could also be used to obtain improved quality fully suspended graphene, since the currently used method sometimes results in cracked layers. After the completion of the device fabrication, a measuring setup needs to be prepared allowing for electrostatic tuning and broad wavelength reflection spectroscopy in the near-infrared electromagnetic frequency range in order to experimentally verify the results of chapter 4. The setup should include a power supply, a sample stage allowing for electrical contact to be made with the device, a visible/near infrared light source (1µm to 10µm would be an ideal range), and a spectrometer covering the same spectral range. As mentioned earlier in the previous section, this can be satisfied by utilizing and FTIR setup with an infrared-microscope attached.

6. Conclusion

Graphene is an excellent candidate for allowing the fabrication of broadband and dynamically tuneable plasmonic devices. Obtaining strong coupling of light with monolayer graphene has been a long anticipated goal for both the graphene and nanophotonics communities. Achieving this goal while maintaining broadband tuneability is expected to open the way for different fields of novel commercial applications based on graphene. Nevertheless, achieving these goals has proved an extremely difficult task even though the graphene plasmonics community is large and constantly increasing in size. Graphene, being atomically thin, has a very weak interaction with light, hence methods to enhance this interaction are crucial for photonic applications. Furthermore obtaining a large operational frequency range is difficult since it requires efficient gating methods.

This project focuses on overcoming these issues by presenting a novel device that should allow for highly tuneable total optical absorption in a graphene monolayer. A diffraction grating structure consisting of an array of inverted pyramid structures etched on silicon is used to couple plasmons in graphene by acting as a phase matching component. By designing a hybrid gold-insulator-graphene plasmonic structure (by including a gold layer and a transparent spacer) significant enhancement in diffraction efficiency and plasmon excitations in graphene is predicted. The properties of the diffraction grating were studied experimentally and graphene was successfully transferred on the structure. An ion gel gate was implemented to provide efficient and dynamic control of the carrier concentration in the graphene monolayer. The efficiency of the ion gel in modulating the carrier density of graphene was experimentally tested on a graphene micro-ribbon FET showing excellent results (the gradient of the IV curve was found to be 0.17V/μA in comparison with the SiO_2 backgate which had a gradient of 80V/μA).

A theoretical model in combination with RCWA simulations was used to characterize the efficiency of the suggested device demonstrating total optical absorption with more than 60% of the absorption attributed to plasmons in the monolayer. By including an ion gel gate, efficient modulation of plasmon excitation frequency was achieved with a tuning range from the mid infrared to almost visible frequencies. The proposed device was predicted to provide significant enhancement of plasmon absorption in graphene (1650% over a simple 2D grating based device) while providing a wide wavelength tuning range (mid-infrared-to near-infrared range shifting by 2μm/V) for plasmon excitations thus achieving the previously mentioned goals. Furthermore this setup allows for dynamic switching of plasmon excitations in graphene through electrostatic gating thus opening the way for photonic logic applications in the nanoscale. ITO ENZ devices were also investigated in order provide alternative solutions for electrostatic tuning of plasmons that are easier to fabricate when compared to graphene based devices.

The novel devices as well as theoretical models presented in this thesis provide an excellent approach for fabricating highly tuneable total optical absorption devices while also providing the possibility of achieving on-chip photonic switching. Utilizing the properties of the suggested devices has great promise in improving technologies in the fields of health care (sensing applications), telecommunications (on-chip modulators, polarizers, photonic switches, waveguides), and computing (small scale optical interconnect and photonic logic).

7. Future Work

7.1. Finalising and Measuring the Total Optical Absorption Device

As part of future work finalizing the device presented in chapter 4.2 by using the fabrication methods of chapter 5 is of highest priority. As all the methods for preparing the device have been described in detail, combining them to provide a functional device is the only missing step. As currently there is no ionic gel process available in the University of Southampton Nanogroup labs, which is currently the missing link for completing the fabrication of the device, establishing the process would be the first step for finalizing the device. For this to be achieved, the guidelines presented in chapter 5.3 should be followed. Testing how different concentrations of the ionic liquid and binding polymer affect the efficiency of carrier modulation in graphene could investigated as this would potentially provide more efficient modulation of carrier concentration in graphene.

Whilst the ion gel gate makes it possible to operate the device over very large spectral ranges, if the device is not required to operate over such large spectral ranges, then a simple dielectric backgate can be used, also playing the role of the spacer structure. Not using an ion gel gate would severely limit the tuning range of the device and also limit operation to the mid-infrared spectral range but would allow for much easier fabrication. Since the graphene in this case would be suspended and the majority of the graphene would not be in contact with any other materials, it is expected that the monolayer could operate under much higher mobility values thus improving the absorption efficiency of the device. Chemically doping graphene would enable the device to operate at higher frequencies but the mobility of the carriers in graphene would not be as high as for a pristine layer.

For the device to be operational, it is also of crucial importance for the graphene layer to be of high quality, otherwise dissipative losses can lead to significant reduction of plasmon generation and thus reduced absorption efficiency. The current method of transferring graphene, which can be seen in chapter 5.2, even though effective, does not provide a high enough yield of successful devices for academic/commercial applications. Investigating a dry transfer method in order to avoid graphene being pulled into the pyramid structures due to capillary forces could possibly provide much better results. Otherwise critical point drying during the removal of the floating PMMA/graphene bilayer from water by the target substrate, could reduce the damage induced on the layer due to the evaporation of water and the resulting capillary forces that pull graphene inside the pyramid structures. It would be interesting and also useful to examine if transfer of graphene can be successful by utilizing the ionic gel layer itself as the transfer polymer as it would simplify the fabrication by reducing the process steps. In spite of these practical considerations for obtaining high graphene transfer yield, it is of high importance firstly to verify how the ionic gel reacts with the other chemicals involved in the process since safety issues could arise. Furthermore, even if there are no safety issues for performing the transfer this way it should be taken into account the ionic gel could be severely damaged in the process or that its properties could be strongly diminished. The advantage of this method would be that there is no need to remove the polymer layer

used during transfer and thus damage induced to the graphene layer during this step can be minimized. If the ionic gel is found to be sensitive to this process then a PDMS layer could be used to cover and protect the ionic gel layer. This could also allow for a stamp based dry transfer.

For fabricating the top contact, the method described in 5.4.2 should be used but different methods might be necessary depending on the measuring setup that is available. If Au foils or evaporated Au on top of the ion gel is used, wire bonding is extremely difficult and thus the measuring system would need to support probes that can softly be positioned on the top contacts of the device. Since ionic gels are conductive it is not necessary to create a sandwich structure in which the gate dielectric (ionic gel in this case) is vertically aligned with the semiconductor (graphene) in order to apply a gate voltage to the graphene. The gate contact could be deposited below the ionic gel layer and alongside (but not in contact with) the graphene layer. Since certain binding polymers used for the preparation of ionic gels allow photo patterning, this gate contact could be left partially uncovered from the ion gel and thus wire bonding becomes possible. Regarding the back gate contact of the device, a conductive ITO layer can be used as the spacer thus allowing for voltage application through the back surface of the wafer. If the spacer material used is not conductive then contacts need to be fabricated on top of the graphene layer but below the ionic gel structure.

Finally, a measuring system capable of covering a broad spectral region between the mid-Infrared and up to near-infrared wavelengths should be used in order to observe the ultra-broad range tuning of the device. Furthermore this measurement system should allow for voltage to be applied to the device in a controlled way in order to modulate the plasmon excitation wavelength. If such a broad range measuring system is not available then a target region should be chosen suitable for the available tools and the device parameters should be optimised to operate at this specific spectral region by using the theory and simulation methods presented in this project. Nevertheless Fourier-transform infrared spectroscopy systems can typically cover a big part of the near-infrared to mid-infrared region so they could offer an ideal solution for performing measurements on the suggested device.

7.2. Hexagonal Boron Nitride Gate

Monolayer hexagonal boron nitride is a two-dimensional material with alternating sp^2-bonded boron and nitrogen atoms arranged in a honeycomb lattice. This material provides excellent dielectric properties due to having a wide direct bandgap [244,245]. Similarly to graphene, hexagonal boron nitride is optically transparent, has high mechanical strength [246], chemical stability [244], and high thermal conductivity [247,248]. Hexagonal boron nitride has been used in a wide variety of applications as a transparent membrane [249], tunnelling barrier [250,251], encapsulation layer [252], and dielectric layer [253].

Excellent dielectric properties, with low leakage current, high breakdown field, high interface quality (low interface state densities), and an equivalent oxide thickness to that of high-k dielectrics, have been observed In devices where hexagonal boron nitride was used as a gate dielectric [245]. Unlike other dielectrics, hexagonal boron nitride does not form dangling bonds when interfacing with 2D materials, and also does not suffer from trap charging [245]. Since two dimensional materials (like graphene) are highly sensitive to the surrounding environment (see section 3.2.4), the lack of

dangling bonds and trapped charges can result in significant increase of carrier mobility in the monolayer [244,245,254]. Graphene devices implementing hexagonal boron nitride substrates thus have significantly higher mobility than devices implementing Si/SiO_2 substrates, while at the same time providing a gate capacitance approaching that of high-k dielectrics [244]. Record mobility values for graphene [215,254] have been demonstrated by utilizing hexagonal boron nitride back-gates with carrier mobility reaching values up to 145 000$cm^2V^{-1}s^{-1}$ at room temperature and 350 000$cm^2V^{-1}s^{-1}$ for low temperature measurements [215].

Losses are a significant limiting factor from which the field of plasmonics is suffering. Methods to optimise plasmonic structures have become of significant interest in order to lift this strongly limiting bottleneck [255]. The effect of losses was found to significantly degrade the efficiency of the device studied in this thesis as seen from section 4.2.10. More losses in graphene resulted in the plasmon excitations becoming significantly weakened, and thus the light absorption was poor. Hexagonal boron nitride encapsulation could be a way to overcome these issues for graphene based plasmonic devices.

7.2.1. Hexagonal Boron Nitride Back-Gate

Since hexagonal boron nitride is an efficient dielectric material and can also strongly improve the mobility of graphene layers, it would be ideal to modify the device presented in chapter 4.2 to include a hexagonal boron nitride back-gate as seen in Figure 7.1. This way the graphene layer is isolated from the spacer material (typically SiO_2) and thus dangling bonds between graphene and the substrate, or effects from trapped charges in the spacer layer, can be avoided resulting in higher mobility for graphene carriers. Furthermore, the inclusion of the hexagonal boron nitride layer can assist in more easily achieving regions of suspended graphene above the pyramid structures thus further improving the carrier mobility of the graphene layer.

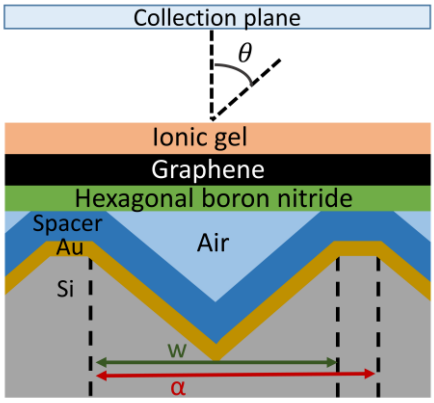

Figure 7.1 Schematic of the proposed device with a hexagonal boron nitride back gate and an ionic gel top gate.

7.2.2. Hexagonal Boron Nitride/ Graphene Sensing Platform

Even though the ionic gel is the most efficient method of modulating the chemical potential of graphene, it can introduce a high amount of losses in the monolayer as explained in section 4.1.6. If very broadband modulation of plasmon wavelength is not required, and if the required operation

of the device is within the mid-infrared spectral range, then the ionic gel can be excluded from the device and the hexagonal boron nitride layer previously used to isolate graphene from the spacer can also be used as a gate dielectric as seen in Figure 7.2.a. Since for this structure graphene is only in contact with the hexagonal boron nitride layer, very high mobility values can be achieved. As a result, the light absorption efficiency due to plasmon excitations is expected to be significantly higher as predicted in section 4.2.10.

As in this setup the top layer is not covered, the device could be used as a bio-sensor (Figure 7.2.b). Since graphene is extremely sensitive to interfacial conditions (it is known that adsorption of molecules on the surface of graphene can degrade the carrier mobility in the monolayer [256]), when analytes are placed on the surface of graphene the carrier mobility of the monolayer is expected to be reduced. This reduction in mobility translates to a direct drop in the plasmon excitation efficiency and thus to a reduction in optical absorption by excited plasmons as predicted in section 4.2.10. The amount or type of analytes used can be recognized by the observed drop in optical absorption since the reduction in mobility is directly dependent on the chemical properties of the analytes adsorbed to the graphene layer [256]. Gas sensing, as well as solution, or dry substance sensing could potentially be achieved with this device.

As graphene is also susceptible to surface transfer doping (section 3.2.4), it is expected that analytes adsorbed to the graphene layer can also introduce doping and thus change the amount of free carriers in the monolayer. In terms of plasmon excitations this translates to either a red-shift or a blue-shift of plasmon wavelength depending or the density of states of the analytes [256]. This means that there can be two methods of analyte identification in a single device.

Specific receptors can be used in both cases in order to have high sensing selectivity. Since the hexagonal boron nitride layer can also be used as a back gate, this device can have a flexible spectral range of operation thus opening the way for dynamically tuneable plasmonic bio-sensing devices.

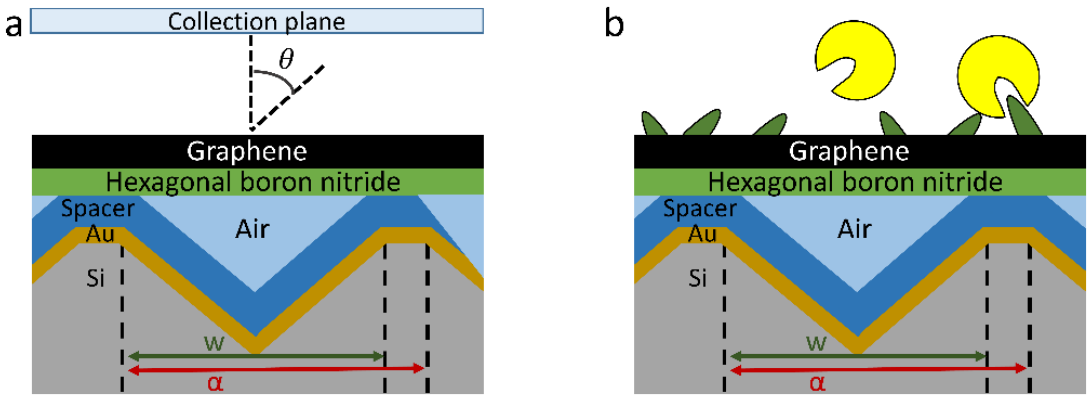

Figure 7.2 a. Schematic of the proposed device with a hexagonal boron nitride back gate. **b.** Sensor based on the proposed structure. Receptors in green and analytes in yellow.

7.2.3. High Mobility Platform for Modulation and Wave-Guiding

Encapsulating graphene between two hexagonal boron nitride layers can completely isolate graphene from the surrounding environment, thus allowing for extremely high carrier mobility in the

monolayer (mobility values exceeding 100 000$cm^2V^{-1}s^{-1}$ at room temperature). This can allow for very high efficiency plasmon excitations with minimum losses, long propagation distances, and thus strong coupling to incident light as expected from the theory presented in section 4.2.10. Such heterostructures have recently been utilized to produce exotic plasmonic effects that can only be observed in very high quality graphene layers [257]. It is thus very interesting to observe the efficiency of such a hetero-structure in combination with the device proposed in chapter 4.2 (Figure 7.3 and Figure 7.4).

Due to the high efficiency of plasmon excitations, and the possibility of tuneable total optical absorption in the graphene monolayer possible with this structure, highly efficient atomically thin modulators can be fabricated. Furthermore, as very large plasmon propagation distances are expected, long range plasmonic wave-guiding becomes possible, allowing for high density and high frequency data transfer in the nanoscale [258]. Finally given the very high mobility and low losses carriers experience, by providing sufficient gain, the fabrication of nanoscale plasmonic lasers could potentially be achieved [259].

Utilization of low loss plasmonic structures for fabrication of wave-guides, modulators, and plasmonic lasers are crucial for achieving nanophotonic logic applications. Thus there is a huge academic and commercial market that could benefit from successful fabrication of such devices.

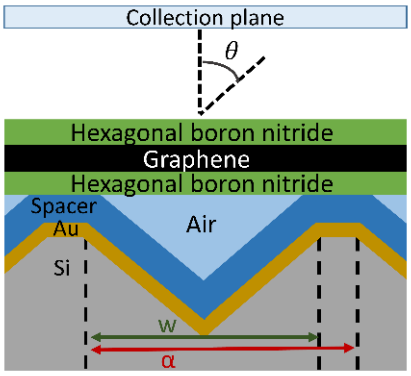

Figure 7.3 Schematic of the proposed device with a hexagonal boron nitride back gate and top hexagonal nitride layer that protects graphene from exposure to the surrounding environment.

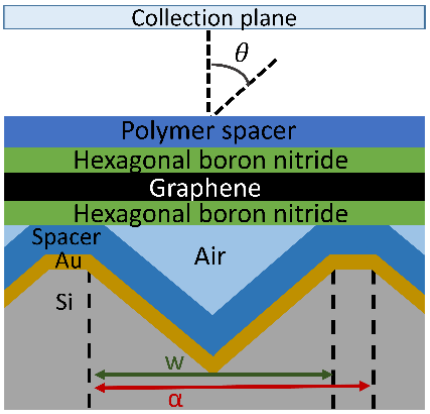

Figure 7.4 Schematic of the proposed device with a hexagonal boron nitride back gate and top hexagonal nitride layer that protects graphene from exposure to the surrounding environment. In this case an extra polymer based spacer is span on top in order to extend the optical micro-cavity.

7.3. Exploring Different 2D materials

Since the discovery of graphene the way for unveiling other two dimensional materials has opened. Recently an increasing amount of such materials has been proven to exist in stable condition [260–263]. The list includes a 2D layer of carbon atoms known as graphyne (with a lattice formation that differs from that of graphene) [264], as well as other atomic layers such as borophene [265–267], germanene [268], silicene [269–276], and phosphorene [261,277–287].

Since each of these monolayers consists of different type of atoms, or are the result of different lattice formations, the resulting band structures vary and allow for different fundamental properties for each individual of the newly discovered materials. It is thus very interesting to explore if 2D materials alternative to graphene are suitable candidates for plasmonic applications or fundamental plasmonic research. Currently the most promising of these materials, with numerous publications in the field of plasmonics, are silicene [269–271,274], and phosphorene [261,277,280,283,285,287]. Nevertheless investigating the properties of the other less explored two dimensional materials could prove to provide interesting results.

Putting this information into perspective with the proposed methods presented in this thesis, it would be interesting to investigate how the structure presented in chapter 4.2 would perform if the graphene layer was replaced with any of the newly discovered two dimensional materials.

7.4. Fabrication and Measurement of the ENZ-based device

The device that was theoretically studied in chapter 4.3 also demonstrates efficient modulation of reflectance. Further theoretical study could help to better understand the physical mechanisms behind the operation of the device. In particular, a model that takes into account the charge distribution in the accumulation (or depletion) region that is formed in the ITO layer, and the effect it has on refractive index, could provide more accurate predictions of the device behaviour.

Since this device does not require as delicate processing as the device presented in chapter 4.2 much easier fabrication is possible following standard lithography and deposition techniques thus allowing for mass production.

The fabrication steps required to make this device are almost identical to the ones presented in chapter 5. First, a diffraction grating needs to be fabricated following the guidelines that can be found in chapter 5.1.1 and then an optically thick Au layer needs to be deposited following the guidelines of chapter 5.4.1. The main difference is that instead of depositing a single transparent dielectric spacer, an ITO layer needs to be evaporated or sputtered followed by an HfO_2 layer which can be deposited with the use of atomic-layer-deposition. Finally, an optically thin Au layer needs to be deposited as the top layer to complete the structure. Applying voltage to the device in order to modulate the carrier concentration in the ITO accumulation region is very easy since it can be applied through the top metal layer and the back of the (highly doped) Si layer. Wire bonding is also possible. The most crucial factor to be taken into account for the device to operate effectively is the carrier concentration of the as deposited bulk ITO layer. Since the properties of the bulk ITO

layer define the ENZ wavelength, care should be taken in order to match it with the plasmon excitation wavelength of the device otherwise modulation is not possible. This can be controlled by adjusting the deposition parameters of the ITO layer. Fabricating chips that include areas with different grating pitch allow for easier matching of the ENZ wavelength of ITO with that of the plasmon excitations as there are more options for measurement.

A similar measuring system to the one suggested for measuring the device of chapter 4.2 can be used. In contrast however, the light source and detector do not need to cover such a broad range of wavelengths since reflection modulation for this device occurs only at regions where diffraction lines or Au plasmon excitations already exist.

7.5. Further Research Ideas

There are numerous ways the structure presented in chapter 4.2 could be altered to accommodate for different applications or that the proposed device could be further optimised. With the aim of enhancing the excitations of tuneable plasmon modes within the device, it would be interesting to investigate patterning the individual structures to alter their properties. For example, this could be achieved by patterning the gold back reflector with the use of lithography methods to only cover the pyramid structure and not the surrounding flat region thus not allowing propagating plasmon modes and potentially resulting in enhanced excitations of localized modes at the borders of the gold structure. Another interesting idea would be to investigate what happens when nano-patterned graphene (disk, ring, cross, etc. shaped) is used instead of a large 2D layer covering the entire structure as it could potentially enhance plasmon excitations within the graphene structures due to the excitation of localized modes. In this case the pattern dimensions should be defined to support localized plasmon excitations in graphene at the wavelength that overlaps with the vertical cavity and *Au* plasmon modes. Using different materials alternative to graphene or ITO, or a multilayer structure instead of a single graphene layer would also be an interesting approach to continuing this research in order to achieve easier fabrication or more efficient modulation respectively.

Effort should be made towards commercialization if the fabricated prototype device shows plasmonic properties which are as promising as the results predicted by modelling within this work. It can be seen that there is a range of potential future work which can be used to extend upon the tuneable-graphene devices presented within this thesis which would provide opportunities for improving fundamental understanding of the plasmonic properties of graphene whilst providing devices with enhanced properties in areas such as modulators, tuneable sensors, waveguides, and possibly photonic switches.

8. List of Publications

Journal Publications:

[1] N. Matthaiakakis, H. Mizuta, M. D. B. Charlton. Strong modulation of plasmons in graphene with the use of an Inverted pyramid array diffraction grating. *Sci. Rep.* **6,** 1–11 (2016).

[2] Matthaiakakis, N., Y. Xingzhao, Mizuta, H. & Charlton, M. D. B. Tuneable strong optical absorption in a graphene-insulator-metal hybrid plasmonic device. *Sci. Rep. (2017).*

Conferences:

[3] N. Matthaiakakis, H. Mizuta, M. D. B. Charlton. (2016). Excitation and strong electrical modulation of plasmons in graphene with the use of a 2-dimensional inverted pyramid array diffraction grating. In 63rd JSAP spring meeting. Tokyo Institute of technology, Ookayama campus.

[4] N. Matthaiakakis, H. Mizuta, M. D. B. Charlton. (2017). Excitation and dynamic control of plasmons in graphene by utilizing a 2-dimensional inverted pyramid array diffraction grating. In CLEO®/Europe-EQEC 2017. Munich (ICM), Germany.

[5] N. Matthaiakakis, H. Mizuta, M. D. B. Charlton. (2017). Tuneable Total Optical Absorption in a Triply Resonant Metal-Insulator-Graphene Hetero-Structure Plasmonic Device. In Graphene Week 2017. Athens, Greece.

9. References

1. Barnes, W. L., Dereux, A. & Ebbesen, T. W. Surface plasmon subwavelength optics. *Nature* **424,** 824–830 (2003).
2. Anker, J. N. *et al.* Biosensing with plasmonic nanosensors. *Nat. Mater.* **7,** 442–453 (2008).
3. Zia, R., Schuller, J. A., Chandran, A. & Brongersma, M. L. Plasmonics : the next chip-scale technology The development of chip-scale electronics and photonics has led to. *Mater. Today* **9,** 20–27 (2006).
4. Geim, a K. & Novoselov, K. S. The rise of graphene. *Nat. Mater.* **6,** 183–91 (2007).
5. Geim, a K. Graphene: status and prospects. *Science* **324,** 1530–4 (2009).
6. Novoselov, K. S. *et al.* Electric field effect in atomically thin carbon films. *Science* **306,** 666–669 (2004).
7. Novoselov, K. S. *et al.* Two-dimensional atomic crystals. *Proc. Natl. Acad. Sci. U. S. A.* **102,** 10451–10453 (2005).
8. Novoselov, K. S. *et al.* Two-dimensional gas of massless Dirac fermions in graphene. *Nature* **438,** 197–200 (2005).
9. Novoselov, K. S. *et al.* A roadmap for graphene. *Nature* **490,** 192–200 (2012).
10. Kinaret, J., Ferrari, A. C., Fal'ko, V. & Kivioja, J. Graphene-Driven Revolutions in ICT and Beyond. *Procedia Comput. Sci.* **7,** 30–33 (2011).
11. Mak, K. F., Ju, L., Wang, F. & Heinz, T. F. Optical spectroscopy of graphene: From the far infrared to the ultraviolet. *Solid State Commun.* **152,** 1341–1349 (2012).
12. Avouris, P. & Dimitrakopoulos, C. Graphene: synthesis and applications. *Mater. Today* **15,** 86–97 (2012).
13. Grigorenko, A. N., Polini, M. & Novoselov, K. S. Graphene plasmonics. *Nat. Photonics* **6,** 749–758 (2012).
14. Bonaccorso, F., Sun, Z., Hasan, T. & Ferrari, a. C. Graphene photonics and optoelectronics. *Nat. Photonics* **4,** 611–622 (2010).
15. Bao, Q. & Loh, K. P. Graphene photonics, plasmonics, and broadband optoelectronic devices. *ACS Nano* **6,** 3677–94 (2012).
16. Sun, Z. *et al.* Graphene mode-locked ultrafast laser. *ACS Nano* **4,** 803–10 (2010).
17. Otsuji, T. *et al.* Terahertz-Wave Generation Using Graphene : Toward New Types of Terahertz Lasers. *IEEE J. Sel. Top. Quantum Electron.* **19,** (2013).
18. Bao, Q. *et al.* Graphene-Polymer Nanofiber Membrane for Ultrafast Photonics. *Adv. Funct. Mater.* **20,** 782–791 (2010).
19. Xia, F., Mueller, T., Lin, Y.-M., Valdes-Garcia, A. & Avouris, P. Ultrafast graphene photodetector. *Nat. Nanotechnol.* **4,** 839–43 (2009).
20. Mueller, T., Xia, F. & Avouris, P. Graphene photodetectors for high-speed optical communications. *Nat. Photonics* **4,** 297–301 (2010).
21. Hwang, G. *et al.* Graphene as Thin Film Infrared Optoelectronic Sensor. *ISOT 2009 Int. Symp. Optomechatronic Technol.* 169–174 (2009).
22. Lai, K. W. C. *et al.* Fabrication of graphene devices for infrared detection. *2010 IEEE Nanotechnol. Mater. Devices Conf.* 14–17 (2010). doi:10.1109/NMDC.2010.5652175
23. Christensen, J., Manjavacas, A., Thongrattanasiri, S., Koppens, F. H. L. & de Abajo, F. J. G.

Graphene plasmon waveguiding and hybridization in individual and paired nanoribbons. *ACS Nano* **6,** 431–40 (2012).

24. Kim, J. T. & Choi, S.-Y. Graphene-based plasmonic waveguides for photonic integrated circuits. *Opt. Express* **19,** 24557–62 (2011).
25. Liu, M. *et al.* A graphene-based broadband optical modulator. *Nature* **474,** 64–7 (2011).
26. Bao, Q. *et al.* Broadband graphene polarizer. *Nat. Photonics* **5,** 411–415 (2011).
27. Gu, T. *et al.* Regenerative oscillation and four-wave mixing in graphene optoelectronics. *Nat. Photonics* **6,** 554–559 (2012).
28. Liu, Z. *et al.* Organic Photovoltaic Devices Based on a Novel Acceptor Material: Graphene. *Adv. Mater.* **20,** 3924–3930 (2008).
29. Llatser, I. *et al.* Graphene-based nano-patch antenna for terahertz radiation. *Photonics Nanostructures - Fundam. Appl.* **10,** 353–358 (2012).
30. Rana, F., Strait, J. H., George, P. A., Wang, H. & Besant, J. D. Graphene Plasmonics for Subwavelength Terahertz Oscillators. *LEOS Annu. Meet. Conf. Proc.* **3,** 650–651 (2009).
31. Rangel, N. L. & Seminario, J. M. Vibronics and plasmonics based graphene sensors. *J. Chem. Phys.* **132,** 125102 (2010).
32. Kim, J. A. *et al.* Graphene based fiber optic surface plasmon resonance for bio-chemical sensor applications. *Sensors Actuators B Chem.* **187,** 426–433 (2013).
33. Ju, L. *et al.* Graphene plasmonics for tunable terahertz metamaterials. *Nat. Nanotechnol.* **6,** 630–634 (2011).
34. Vakil, A. & Engheta, N. Transformation optics using graphene. *Science* **332,** 1291–1294 (2011).
35. Jiang, Y., Lu, W. B., Xu, H. J., Dong, Z. G. & Cui, T. J. A planar electromagnetic 'black hole' based on graphene. *Phys. Lett. A* **376,** 1468–1471 (2012).
36. N. Matthaiakakis, H. Mizuta, M. D. B. C. Strong modulation of plasmons in Graphene with the use of an Inverted pyramid array diffraction grating. *Sci. Rep.* **6,** 1–11 (2016).
37. Gao, W. *et al.* Excitation and active control of propagating surface plasmon polaritons in graphene. *Nano Lett.* **13,** 3698–702 (2013).
38. Gao, W., Shu, J., Qiu, C. & Xu, Q. Excitation of plasmonic waves in graphene by guided-mode resonances. *ACS Nano* **6,** 7806–13 (2012).
39. Ju, L. *et al.* Graphene plasmonics for tunable terahertz metamaterials. *Nat. Nanotechnol.* **6,** 630–4 (2011).
40. Freitag, M. *et al.* Photocurrent in graphene harnessed by tunable intrinsic plasmons. *Nat. Commun.* **4,** 1951; DOI:10.1038/ncomms2951 (2013).
41. Fang, Z. *et al.* Active tunable absorption enhancement with graphene nanodisk arrays. *Nano Lett.* **14,** 299–304 (2014).
42. Yan, H. *et al.* Tunable infrared plasmonic devices using graphene/insulator stacks. *Nat. Nanotechnol.* **7,** 330–4 (2012).
43. Yan, H., Xia, F., Li, Z. & Avouris, P. Plasmonics of coupled graphene micro-structures. *New J. Phys.* **14,** 125001; DOI:10.1088/1367-2630/14/12/125001 (2012).
44. Fang, Z. *et al.* Gated tunability and hybridization of localized plasmons in nanostructured graphene. *ACS Nano* **7,** 2388–2395 (2013).
45. Liu, P., Cai, W., Wang, L., Zhang, X. & Xu, J. Tunable terahertz optical antennas based on graphene ring structures. *Appl. Phys. Lett.* **100,** 153111; DOI:10.1063/1.3702819 (2012).

46. Papasimakis, N. *et al.* Graphene in a photonic metamaterial. *Opt. Express* **18,** 8353–9 (2010).

47. Zou, Y., Tassin, P., Koschny, T. & Soukoulis, C. M. Interaction between graphene and metamaterials: split rings vs wire pairs. *Opt. Express* **20,** 12198–12204 (2012).

48. Yao, Y. *et al.* Broad electrical tuning of graphene-loaded plasmonic antennas. *Nano Lett.* **13,** 1257–1264 (2013).

49. Alonso-González, P. *et al.* Controlling graphene plasmons with resonant metal antennas and spatial conductivity patterns. *Science* **344,** 1369–73 (2014).

50. Kim, J. *et al.* Electrical control of optical plasmon resonance with graphene. *Nano Lett.* **12,** 5598–602 (2012).

51. Emani, N. K. *et al.* Electrically tunable damping of plasmonic resonances with graphene. *Nano Lett.* **12,** 5202–6 (2012).

52. Thongrattanasiri, S., Koppens, F. H. L. & Garcı, F. J. Complete Optical Absorption in Periodically Patterned Graphene. **47401,** 1–5 (2012).

53. Alaee, R., Farhat, M., Rockstuhl, C. & Lederer, F. A perfect absorber made of a graphene micro-ribbon metamaterial. *Opt. Express* **20,** 28017–24 (2012).

54. Zhang, J., Zhu, Z., Liu, W., Yuan, X. & Qin, S. Towards photodetection with high efficiency and tunable spectral selectivity: Graphene plasmonics for light trapping and arXiv absorption engineering. *Nanoscale* **7,** 13530–13536 (2015).

55. Pirruccio, G., Martín Moreno, L., Lozano, G. & Gómez Rivas, J. Coherent and broadband enhanced optical absorption in graphene. *ACS Nano* **7,** 4810–4817 (2013).

56. Deng, X.-H., Liu, J.-T., Yuan, J., Wang, T.-B. & Liu, N.-H. Tunable THz absorption in graphene-based heterostructures. *Opt. Express* **22,** 30177 (2014).

57. Su, Z., Yin, J. & Zhao, X. Terahertz dual-band metamaterial absorber based on graphene/MgF_2 multilayer structures. *Opt. Express* **23,** 1679–90 (2015).

58. Fante, R. L. & McCormack, M. T. Reflection properties of the Salisbury screen. *IEEE Trans. Antennas Propag.* **36,** 1443–1454 (1988).

59. Thareja, V. *et al.* Electrically Tunable Coherent Optical Absorption in Graphene with Ion Gel. *Nano Lett.* 150211144205005 (2015). doi:10.1021/nl503431d

60. Ying, X., Pu, Y., Li, Z., Liu, Z. & Jiang, Y. Absorption enhancement of graphene Salisbury screen in the mid-infrared regime. *J. Opt.* **44,** 59–67 (2014).

61. Jang, M. S. *et al.* Tunable large resonant absorption in a midinfrared graphene Salisbury screen. *Phys. Rev. B* **90,** 165409 (2014).

62. Lee, S. *et al.* Angle- and position-insensitive electrically tunable absorption in graphene by epsilon-near-zero effect. *Opt. Express* **23,** 33350 (2015).

63. Zhang, Y. *et al.* Independently tunable dual-band perfect absorber based on graphene at mid-infrared frequencies. *Sci. Rep.* **5,** 18463 (2015).

64. Xiong, F., Zhang, J., Zhu, Z., Yuan, X. & Qin, S. Ultrabroadband, More than One Order Absorption Enhancement in Graphene with Plasmonic Light Trapping. *Sci. Rep.* **5,** 16998 (2015).

65. Zhang, Y., Feng, Y., Zhu, B., Zhao, J. & Jiang, T. Graphene based tunable metamaterial absorber and polarization modulation in terahertz frequency. *Opt. Express* **22,** 22743–52 (2014).

66. Liu, P. Q. *et al.* Highly tunable hybrid metamaterials employing split-ring resonators strongly coupled to graphene surface plasmons. 24–28 (2015). doi:10.1038/ncomms9969

67. Song, S., Chen, Q., Jin, L. & Sun, F. Great light absorption enhancement in a graphene photodetector integrated with a metamaterial perfect absorber. *Nanoscale* **5,** 9615–9 (2013).

68. Cai, Y. *et al.* Enhanced spatial near-infrared modulation of graphene-loaded perfect absorbers using plasmonic nanoslits. *Opt. Express* **23,** 32318 (2015).

69. Jadidi, M. M. *et al.* Tunable Terahertz Hybrid Metal − Graphene Plasmons. (2015). doi:10.1021/acs.nanolett.5b03191

70. Piper, J. R. & Fan, S. Total Absorption in a Graphene Monolayer in the Optical Regime by Critical Coupling with a Photonic Crystal Guided Resonance. (2014).

71. Matthaiakakis, N., Xingzhao, Y., Mizuta, H. & Charlton, M. D. B. Tuneable strong optical absorption in a graphene-insulator-metal hybrid plasmonic device. *Sci. Rep.* (2017).

72. Maier, S. A. *Plasmonics: Fundamentals and applications*. *Plasmonics: Fundamentals and Applications* (2007). doi:10.1007/0-387-37825-1

73. Fei, Z. *et al.* Gate-tuning of graphene plasmons revealed by infrared nano-imaging. *Nature* **487,** 82–5 (2012).

74. Zourob, M. *Recognition receptors in biosensors*. *Recognition Receptors in Biosensors* (2010). doi:10.1007/978-1-4419-0919-0

75. Gramotnev, D. K. & Bozhevolnyi, S. I. Plasmonics beyond the diffraction limit. *Nat. Photonics* **4,** 83–91 (2010).

76. Schuller, J. a *et al.* Plasmonics for extreme light concentration and manipulation. *Nat. Mater.* **9,** 193–204 (2010).

77. Gjerding, M. N., Pandey, M. & Thygesen, K. S. Band structure engineered layered metals for low-loss plasmonics. *Nat. Commun.* **8,** 1–8 (2017).

78. Koppens, F. H. L., Chang, D. E. & García de Abajo, F. J. Graphene plasmonics: a platform for strong light-matter interactions. *Nano Lett.* **11,** 3370–7 (2011).

79. Wood, R. W. On a Remarkable Case of Uneven Distribution of Light in a Diffraction Grating Spectrum. *Proc. Phys. Soc. London* **18,** 269–275 (1902).

80. Wood, R. W. Anomalous diffraction gratings. *Phys. Rev.* **48,** 928–936 (1935).

81. Lord Rayleigh. On the Dynamical Theory of Gratings. *Proc. R. Soc.* **A 79,** 399–416 (1907).

82. Lin, I. Optical Properties of Graphene from the THz to the Visible Spectral Region. *Thesis* Date of access:12/04/2016 (2012).

83. Wright, a. R., Xu, X. G., Cao, J. C. & Zhang, C. Strong nonlinear optical response of graphene in the terahertz regime. *Appl. Phys. Lett.* **95,** 72101 (2009).

84. Dawlaty, J. M. *et al.* Measurement of the optical absorption spectra of epitaxial graphene from terahertz to visible. *Appl. Phys. Lett.* **93,** 2013–2016 (2008).

85. Mak, K. F. *et al.* Measurement of the opptical conductivity of graphene. *Phys. Rev. Lett.* **101,** 2–5 (2008).

86. Xu, F. *et al.* Complex refractive index tunability of graphene at 1550 nm wavelength. *Appl. Phys. Lett.* **31109,** 2–5 (2015).

87. Cheon, S. *et al.* How to Reliably Determine the Complex Refractive Index (RI) of Graphene by Using Two Independent Measurement Constraints. *Sci. Rep.* **4,** 6364 (2014).

88. Nelson, F. J. *et al.* Optical properties of large-area polycrystalline chemical vapor deposited graphene by spectroscopic ellipsometry. *Appl. Phys. Lett.* **97,** 253110; DOI:10.1063/1.3525940 (2010).

89. Ochoa-Martínez, E. *et al.* Determination of a refractive index and an extinction coefficient of standard production of CVD-graphene. *Nanoscale* **7,** 1491–1500 (2015).

90. Matković, A. & Gajić, R. Spectroscopic imaging ellipsometry of graphene. *SPIE Newsroom* 2–5 (2013). doi:10.1117/2.1201311.005227

91. Gogoi, P. K. *et al.* Optical conductivity study of screening of many-body effects in graphene interfaces. *EPL (Europhysics Lett.* **99,** 67009; DOI:10.1209/0295-5075/99/67009 (2012).

92. Santoso, I. *et al.* Observation of room-temperature high-energy resonant excitonic effects in graphene. *Phys. Rev. B - Condens. Matter Mater. Phys.* **84,** 1–4 (2011).

93. Nelson, F. *et al.* Spectroscopic Ellipsometry of CVD Graphene. in *ECS Transactions* **35,** 173–183 (2011).

94. Stauber, T., Peres, N. M. R. & Geim, a. K. Optical conductivity of graphene in the visible region of the spectrum. *Phys. Rev. B - Condens. Matter Mater. Phys.* **78,** 1–8 (2008).

95. Gusynin, V. P., Sharapov, S. G. & Carbotte, J. P. Sum rules for the optical and Hall conductivity in graphene. *Phys. Rev. B - Condens. Matter Mater. Phys.* **75,** 1–12 (2007).

96. Falkovsky, L. a. Optical properties of graphene. *J. Phys. Conf. Ser.* **129,** 12004 (2008).

97. Margulis, V. a, Muryumin, E. E. & Gaiduk, E. a. Theoretical calculations of nonlinear refraction and absorption coefficients of doped graphene. *J. Opt.* **16,** 125203 (2014).

98. Gusynin, V. P., Sharapov, S. G. & Carbotte, J. P. Magneto-optical conductivity in Graphene. *J. Phys. Condens. Matter* **26222,** 28 (2007).

99. Nelson, F. J. *et al.* Optical properties of large-area polycrystalline chemical vapor deposited graphene by spectroscopic ellipsometry. *Appl. Phys. Lett.* **97,** 253110 (2010).

100. Kravets, V. G. *et al.* Spectroscopic ellipsometry of graphene and an exciton-shifted van Hove peak in absorption. *Phys. Rev. B* **81,** 155413 (2010).

101. Weber, J. W., Calado, V. E. & van de Sanden, M. C. M. Optical constants of graphene measured by spectroscopic ellipsometry. *Appl. Phys. Lett.* **97,** 91904-91904–3 (2010).

102. Wang, F. *et al.* Gate-variable optical transitions in graphene. *Science* **320,** 206–209 (2008).

103. Otsuji, T., Popov, V. & Ryzhii, V. Active graphene plasmonics for terahertz device applications. *J. Phys. D. Appl. Phys.* **47,** 94006 (2014).

104. Li, T. *et al.* Femtosecond population inversion and stimulated emission of dense dirac fermions in graphene. *Phys. Rev. Lett.* **108,** (2012).

105. Boubanga-Tombet, S. *et al.* Ultrafast carrier dynamics and terahertz emission in optically pumped graphene at room temperature. *Physical Review B* **85,** (2012).

106. Bostwick, A., Ohta, T., Seyller, T., Horn, K. & Rotenberg, E. Quasiparticle dynamics in graphene. *Nature Physics* **3,** 36–40 (2007).

107. Prechtel, L. *et al.* Time-resolved ultrafast photocurrents and terahertz generation in freely suspended graphene. *Nature Communications* **3,** (2012).

108. An, X., Liu, F., Jung, Y. J. & Kar, S. Tunable graphene-silicon heterojunctions for ultrasensitive photodetection. *Nano Lett.* **13,** 909–16 (2013).

109. Gangadharaiah, S., Farid, A. M. & Mishchenko, E. G. Charge response function and a novel plasmon mode in graphene. *Phys. Rev. Lett.* **100,** 166802 (2008).

110. Ju Xu, H., Bing Lu, W., Zhu, W., Gao Dong, Z. & Jun Cui, T. Efficient manipulation of surface plasmon polariton waves in graphene. *Appl. Phys. Lett.* **100,** 243110 (2012).

111. Chen, J. *et al.* Optical nano-imaging of gate-tunable graphene plasmons. *Nature* **487,** 77–81 (2012).

112. Avouris, P. & Freitag, M. Graphene Photonics, Plasmonics, and Optoelectronics. *IEEE J. Sel. Top. Quantum Electron.* **20,** 6000112–6000112 (2014).

113. Freitag, M. *et al.* Photocurrent in graphene harnessed by tunable intrinsic plasmons. *Nat. Commun.* **4,** 1951 (2013).

114. Fischetti, M. V., Neumayer, D. A. & Cartier, E. A. Effective electron mobility in Si inversion layers in metal-oxide-semiconductor systems with a high-?? insulator: The role of remote phonon scattering. *J. Appl. Phys.* **90,** 4587–4608 (2001).

115. Emani, N. K. *et al.* Electrically Tunable Plasmonic Resonances with Graphene. *Conf. Lasers Electro-Optics 2012* JTu1M.2 (2012). doi:10.1364/CLEO_AT.2012.JTu1M.2

116. Yan, H., Xia, F., Li, Z. & Avouris, P. Plasmonics of coupled graphene micro-structures. *New J. Phys.* **14,** 125001 (2012).

117. Liu, P., Cai, W., Wang, L., Zhang, X. & Xu, J. Tunable terahertz optical antennas based on graphene ring structures. *Appl. Phys. Lett.* **100,** 153111 (2012).

118. Bludov, Y. V., Vasilevskiy, M. I. & Peres, N. M. R. Tunable graphene-based polarizer. *J. Appl. Phys.* **112,** 84320 (2012).

119. Lee, S. H. *et al.* Switching terahertz waves with gate-controlled active graphene metamaterials. *Nature Materials* **11,** 936–941 (2012).

120. Danaeifar, M., Granpayeh, N., Mohammadi, A. & Setayesh, A. Graphene-based tunable terahertz and infrared band-pass filter. *Appl. Opt.* **52,** E68-72 (2013).

121. Fang, Z. *et al.* Gated tunability and hybridization of localized plasmons in nanostructured graphene. *{ACS} nano* **7,** 2388–2395 (2013).

122. Low, T. & Avouris, P. Graphene plasmonics for terahertz to mid-infrared applications. *ACS Nano* **8,** 1086–101 (2014).

123. Jornet, J. M., Akyildiz, I. F. & York, N. Graphene-based Plasmonic Nano-transceiver for Terahertz Band Communication. 492–496 (2014).

124. Otsuji, T. *et al.* Graphene plasmonic heterostructures for new types of terahertz lasers. **9199,** 91990F (2014).

125. Dubinov, a. a., Aleshkin, V. Y., Ryzhii, V., Shur, M. S. & Otsuji, T. Surface-plasmons lasing in double-graphene-layer structures. *J. Appl. Phys.* **115,** 44511 (2014).

126. Zhu, Z. H. *et al.* Electrically controlling the polarizing direction of a graphene polarizer. *J. Appl. Phys.* **116,** 104304 (2014).

127. Yan, H. *et al.* Damping pathways of mid-infrared plasmons in graphene nanostructures. *Nat. Photonics* **7,** 394–399 (2013).

128. Li, H.-J. *et al.* Graphene-based mid-infrared, tunable, electrically controlled plasmonic filter. *Appl. Phys. Express* **7,** 24301 (2014).

129. Chen, F., Yao, D. & Liu, Y. Graphene–metal hybrid plasmonic switch. **82202,** (1882).

130. Yang, L. *et al.* Ultracompact plasmonic switch based on graphene-silica metamaterial. *Appl. Phys. Lett.* **104,** 211104 (2014).

131. Ooi, K. J. a, Chu, H. S., Bai, P. & Ang, L. K. Electro-optical graphene plasmonic logic gates. *Opt. Lett.* **39,** 1629–32 (2014).

132. Kim, J. T., Yu, Y.-J., Choi, H. & Choi, C.-G. Graphene-based plasmonic photodetector for photonic integrated circuits. *Opt. Express* **22,** 803–8 (2014).

133. Andryieuski, A. & Lavrinenko, A. Graphene metamaterials based tunable terahertz absorber: effective surface conductivity approach. *Opt. Express* **21,** 9144–9155 (2013).

134. Xu, B., Gu, C., Li, Z. & Niu, Z. A novel structure for tunable terahertz absorber based on graphene. *Opt. Express* **21,** 23803 (2013).

135. Hao, Q. *et al.* Surface-Enhanced Raman Scattering Study on Graphene-Coated Metallic Nanostructure Substrates. *J. Phys. Chem. C* **116,** 7249–7254 (2012).

136. Xu, W. *et al.* Surface enhanced Raman spectroscopy on a flat graphene surface. *Proceedings of the National Academy of Sciences* **109,** 9281–9286 (2012).

137. Zhao, Y. *et al.* Enhanced SERS Stability of R6G Molecules with Monolayer Graphene. *J. Phys. Chem. C* **118,** 11827–11832 (2014).

138. Wang, P., Liang, O., Zhang, W., Schroeder, T. & Xie, Y.-H. Ultra-Sensitive Graphene-Plasmonic Hybrid Platform for Label-Free Detection. *Adv Mat* 4918–4924 (2013). doi:10.1002/adma.201300635

139. Tite, T. *et al.* Graphene-based textured surface by pulsed laser deposition as a robust platform for surface enhanced Raman scattering applications. *Appl. Phys. Lett.* **104,** 41912 (2014).

140. Choi, S. H., Kim, Y. L. & Byun, K. M. Graphene-on-silver substrates for sensitive surface plasmon resonance imaging biosensors. *Opt. Express* **19,** 458–466 (2011).

141. Verma, R., Gupta, B. D. & Jha, R. Sensitivity enhancement of a surface plasmon resonance based biomolecules sensor using graphene and silicon layers. *Sensors Actuators B Chem.* **160,** 623–631 (2011).

142. Wu, J. *et al.* Design of infrared surface plasmon resonance sensors based on graphene ribbon arrays. *Opt. Laser Technol.* **59,** 99–103 (2014).

143. Zhao, Y. *et al.* Infrared biosensors based on graphene plasmonics: modeling. *Phys. Chem. Chem. Phys.* **15,** 17118–25 (2013).

144. Reckinger, N., Vlad, A., Melinte, S., Colomer, J.-F. & Sarrazin, M. Graphene-coated holey metal films: Tunable molecular sensing by surface plasmon resonance. *Appl. Phys. Lett.* **102,** 211108 (2013).

145. Szunerits, S., Maalouli, N., Wijaya, E., Vilcot, J.-P. & Boukherroub, R. Recent advances in the development of graphene-based surface plasmon resonance {(SPR)} interfaces. *Anal. Bioanal. Chem.* **405,** 1435–1443 (2013).

146. Liu, Y. *et al.* Plasmon resonance enhanced multicolour photodetection by graphene. *Nat. Commun.* **2,** 579 (2011).

147. Tao, J., Yu, X., Hu, B., Dubrovkin, A. & Wang, Q. J. Graphene-based tunable plasmonic Bragg reflector with a broad bandwidth. *Opt. Lett.* **39,** 271–4 (2014).

148. Pumera, M. Graphene in biosensing. *Materials Today* **14,** 308–315 (2011).

149. Li, P. & Taubner, T. Broadband subwavelength imaging using a tunable graphene-lens. *ACS Nano* **6,** 10107–14 (2012).

150. Blake, P. *et al.* Graphene-based liquid crystal device. *Nano Lett.* **8,** 1704–1708 (2008).

151. Hernandez, Y. *et al.* High-yield production of graphene by liquid-phase exfoliation of graphite. *Nat. Nanotechnol.* **3,** 563–568 (2008).

152. Li, X. *et al.* Large-area synthesis of high-quality and uniform graphene films on copper foils. *Science* **324,** 1312–4 (2009).

153. Forbeaux, I., Themlin, J.-M. & Debever, J.-M. Heteroepitaxial graphite on 6H-SiC(0001): Interface formation through conduction-band electronic structure. *Phys. Rev. B* **58,** 16396–16406 (1998).

154. Mattevi, C., Kim, H. & Chhowalla, M. A review of chemical vapour deposition of graphene

on copper. *J. Mater. Chem.* **21,** 3324 (2011).

155. Ismach, A. *et al.* Direct chemical vapor deposition of graphene on dielectric surfaces. *Nano Lett.* **10,** 1542–1548 (2010).

156. Wang, G. *et al.* Direct growth of graphene film on germanium substrate. *Sci. Rep.* **3,** 2465 (2013).

157. Chau, R., Doyle, B., Datta, S., Kavalieros, J. & Zhang, K. Integrated nanoelectronics for the future. *Nat. Mater.* **6,** 810–2 (2007).

158. Su, C.-Y. *et al.* Transfer printing of graphene strip from the graphene grown on copper wires. *Nanotechnology* **22,** 185309 (2011).

159. Gautam, M., Jayatissa, A. H. & Sumanasekera, G. U. Synthesis and characterization of transferable graphene by CVD method. *Nanotechnol. Mater. Devices Conf. (NMDC), 2010 IEEE* 1–5 (2010). doi:10.1109/NMDC.2010.5652416

160. Lin, Y.-C. *et al.* Clean transfer of graphene for isolation and suspension. *ACS Nano* **5,** 2362–8 (2011).

161. Li, X. *et al.* Transfer of large-area graphene films for high-performance transparent conductive electrodes. *Nano Lett.* **9,** 4359–63 (2009).

162. Liang, X. *et al.* Toward clean and crackless transfer of graphene. *ACS Nano* **5,** 9144–53 (2011).

163. Kang, S. J. *et al.* Inking elastomeric stamps with micro-patterned, single layer graphene to create high-performance OFETs. *Adv. Mater.* **23,** 3531–5 (2011).

164. Ko, P. J. *et al.* Simple method to transfer graphene from metallic catalytic substrates to flexible surfaces without chemical etching. *J. Phys. Conf. Ser.* **433,** 12002 (2013).

165. Suk, J. W. *et al.* Transfer of CVD-grown monolayer graphene onto arbitrary substrates. *ACS Nano* **5,** 6916–24 (2011).

166. Song, J. *et al.* A general method for transferring graphene onto soft surfaces. *Nat. Nanotechnol.* **8,** 356–62 (2013).

167. Verma, V. P., Das, S., Lahiri, I. & Choi, W. Large-area graphene on polymer film for flexible and transparent anode in field emission device. *Appl. Phys. Lett.* **96,** 203108 (2010).

168. Bae, S. *et al.* Roll-to-roll production of 30-inch graphene films for transparent electrodes. *Nat. Nanotechnol.* **5,** 574–578 (2010).

169. Ishigami, M., Chen, J. H., Cullen, W. G., Fuhrer, M. S. & Williams, E. D. Atomic structure of graphene on SiO2. *Nano Lett.* **7,** 1643–1648 (2007).

170. Her, M., Beams, R. & Novotny, L. Graphene Transfer with Reduced Residue. 1–3 (2013).

171. Aydin, O. I., Hallam, T., Thomassin, J. L., Mouis, M. & Duesberg, G. Challenges in suspending CVD graphene: More than capillary effects. *2014 15th Int. Conf. Ultim. Integr. Silicon* 33–36 (2014). doi:10.1109/ULIS.2014.6813899

172. Gao, L. *et al.* Face-to-face transfer of wafer-scale graphene films. *Nature* **505,** 190–4 (2014).

173. Zhang, Y. *et al.* Direct observation of a widely tunable bandgap in bilayer graphene. *Nature* **459,** 820–823 (2009).

174. Liu, H., Liu, Y. & Zhu, D. Chemical doping of graphene. *J. Mater. Chem.* **21,** 3335 (2011).

175. Iwasaki, T. *et al.* Hydrogen intercalation: An approach to eliminate silicon dioxide substrate doping to graphene. **15101,** (1882).

176. Wang, H., Maiyalagan, T. & Wang, X. Review on recent progress in nitrogen-doped graphene: Synthesis, characterization, and its potential applications. *ACS Catal.* **2,** 781–794 (2012).

177. Guo, B. *et al.* Controllable N-doping of graphene. *Nano Lett.* **10,** 4975–4980 (2010).

178. Ferrari, A. C. & Basko, D. M. Raman spectroscopy as a versatile tool for studying the properties of graphene. *Nat. Nanotechnol.* **8,** 235–46 (2013).

179. Ferrari, a. C. *et al.* Raman Spectrum of Graphene and Graphene Layers. *Phys. Rev. Lett.* **97,** 187401 (2006).

180. Spallas, J. X. and J. P. Imaging Graphene via Low Voltage Field Emission Scanning Electron Microscopy Application Note. *Agil. Technol.* (2012).

181. Spallas, J. X. and J. P. Different Contrast Mechanisms in SEM Imaging of Graphene. *Agil. Technol.* (2012).

182. Park, M.-H., Kim, T.-H. & Yang, C.-W. Thickness contrast of few-layered graphene in SEM. *Surf. Interface Anal.* **44,** 1538–1541 (2012).

183. Kochat, V. *et al.* High contrast imaging and thickness determination of graphene with in-column secondary electron microscopy. *J. Appl. Phys.* **110,** 14315 (2011).

184. Giannazzo, F. *et al.* Optical, morphological and spectro- scopic characterization of graphene on SiO 2. *Phys. Status Solidi* **7,** 1251–1255 (2010).

185. Filleter, T. & Bennewitz, R. Structural and frictional properties of graphene films on SiC(0001) studied by atomic force microscopy. *Phys. Rev. B* **81,** 155412 (2010).

186. Boneschanscher, M. P. *et al.* Quantitative atomic resolution force imaging on epitaxial graphene with reactive and nonreactive AFM probes. *ACS Nano* **6,** 10216–21 (2012).

187. Nemes-Incze, P., Osváth, Z., Kamarás, K. & Biró, L. P. Anomalies in thickness measurements of graphene and few layer graphite crystals by tapping mode atomic force microscopy. *Carbon N. Y.* **46,** 1435–1442 (2008).

188. Kim, J., Kim, F. & Huang, J. Seeing graphene-based sheets. *Mater. Today* **13,** 28–38 (2010).

189. Duong, D. L. *et al.* Probing graphene grain boundaries with optical microscopy. *Nature* **490,** 235–9 (2012).

190. Xu, M., Fujita, D., Gao, J. & Hanagata, N. Auger electron spectroscopy: a rational method for determining thickness of graphene films. *ACS Nano* **4,** 2937–2945 (2010).

191. Cançado, L. G. *et al.* Quantifying defects in graphene via Raman spectroscopy at different excitation energies. *Nano Lett.* **11,** 3190–6 (2011).

192. Lee, J. *et al.* Ion gel-gated polymer thin-film transistors: Operating mechanism and characterization of gate dielectric capacitance, switching speed, and stability. *J. Phys. Chem. C* **113,** 8972–8981 (2009).

193. Kim, U. J. *et al.* Modulation of the Dirac Point Voltage of Graphene by Ion-Gel Dielectrics and Its Application to Soft Electronic Devices. *ACS Nano* **9,** 602–611 (2015).

194. Lindquist, N. C. *et al.* Plasmonic tooth-multilayer structure with high enhancement fi eld for surface enhanced Raman spectroscopy. *Nanotechnology* **28,** (2017).

195. Steuwe, C., Kaminski, C. F., Baumberg, J. J. & Mahajan, S. Surface enhanced coherent anti-stokes Raman scattering on nanostructured gold surfaces. *Nano Lett* **11,** 5339–5343 (2011).

196. Yan, Y., Zhang, J., Xu, P. & Miao, P. Fabrication of arrayed triangular micro-cavities for SERS substrates using the force modulated indention process. *RSC Adv.* **7,** 11969–11978 (2017).

197. Correia-Ledo, D. *et al.* Assessing the location of surface plasmons over nanotriangle and nanohole arrays of different size and periodicity. *J. Phys. Chem. C* **116,** 6884–6892 (2012).

198. Sannomiya, T., Saito, H., Junesch, J. & Yamamoto, N. Coupling of plasmonic nanopore pairs: facing dipoles attract each other. *Light Sci. Appl.* **5,** e16146 (2016).

199. Oo, S. Z. & Charlton, M. D. B. Effect of non-conformal gold deposition on SERS related plasmonic effects. *Opt. Express* **24,** 27425–27432 (2016).

200. Oo, S. Z., Siitonen, S., Kontturi, V., Eustace, D. A. & Charlton, M. D. B. Disposable gold coated pyramidal SERS sensor on the plastic platform. *Opt. Express* **24,** 724–731 (2016).

201. Cheng, H.-H. *et al.* Effects of the tip shape on the localized field enhancement and far field radiation pattern of the plasmonic inverted pyramidal nanostructures with the tips for surface-enhanced Raman scattering. *Opt. Express* **19,** 22125–22141 (2011).

202. Jeon, T. Y., Kim, D. J., Park, S.-G., Kim, S.-H. & Kim, D.-H. Nanostructured plasmonic substrates for use as SERS sensors. *Nano Converg.* **3,** 18 (2016).

203. Kumar, G. V. P. Plasmonic nano-architectures for surface enhanced Raman scattering: a review. *J. Nanophotonics* **6,** 64503 (2012).

204. Bean, K. E. & Bean, K. E. Anisotropic etching of silicon. *IEEE Trans. Electron Devices* **25,** 1185–1193 (1978).

205. Oo, S. Z. *et al.* Disposable plasmonic plastic SERS sensor. *Opt. Express* **21,** 18484–91 (2013).

206. Avouris, P. & Freitag, M. Graphene Photonics, Plasmonics, and Optoelectronics. *IEEE J. Sel. Top. Quantum Electron.* **20,** 6000112; DOI:10.1109/JSTQE.2013.2272315 (2014).

207. Klintenberg, M. *et al.* Evolving properties of two-dimensional materials: from graphene to graphite. *J. Phys. Condens. Matter* **21,** 335502; DOI:10.1088/0953-8984/21/33/335502 (2009).

208. Taft, E. & Philipp, H. Optical Properties of Graphite. *Phys. Rev.* **138,** A197–A202 (1965).

209. Johnson, L. G. & Dresselhaus, G. Optical Properties of Graphite. *Phys. Rev. B* **7,** 2275–2285 (1973).

210. Boriskina, S. *et al.* Enhancement and Tunability of Near-Field Radiative Heat Transfer Mediated by Surface Plasmon Polaritons in Thin Plasmonic Films. *Photonics* **2,** 659–683 (2015).

211. Allen, S. J., Tsui, D. C. & Logan, R. a. Observation of the two-dimensional plasmon in silicon inversion layers. *Phys. Rev. Lett.* **38,** 980–983 (1977).

212. Tassin, P., Koschny, T. & Soukoulis, C. M. Graphene for terahertz applications. *Science (80-.).* **341,** 620–621 (2013).

213. Tassin, P., Koschny, T., Kafesaki, M. & Soukoulis, C. M. A comparison of graphene, superconductors and metals as conductors for metamaterials and plasmonics. **6,** 259–264 (2012).

214. Bolotin, K. I. *et al.* Ultrahigh electron mobility in suspended graphene. *Solid State Commun.* **146,** 351–355 (2008).

215. Banszerus, L. *et al.* Ultrahigh-mobility graphene devices from chemical vapor deposition on reusable copper. *Sci. Adv.* **1,** 1–6 (2015).

216. Liu, J. *et al.* Enhanced performance of graphene transistor with ion-gel top gate. *Carbon N. Y.* **68,** 480–486 (2014).

217. Lee, S.-K. *et al.* Photo-patternable ion gel-gated graphene transistors and inverters on plastic. *Nanotechnology* **25,** 014002; DOI:10.1088/0957-4484/25/1/014002 (2014).

218. Hanson, G. W. Dyadic Green's Functions and Guided Surface Waves for a Surface Conductivity Model of Graphene. *J. Appl. Phys.* **103,** 064302; DOI:10.1063/1.2891452 (2007).

219. Jun, Y. C. *et al.* Epsilon-near-zero strong coupling in metamaterial-semiconductor hybrid structures. *Nano Lett.* **13,** 5391–5396 (2013).

220. Olivieri, A. *et al.* Plasmonic Nanostructured Metal − Oxide − Semiconductor Re fl ection Modulators. *Nano Lett.* **15,** 2304–2311 (2015).

221. Soref, R., Hendrickson, J. & Cleary, J. W. Mid- to long-wavelength infrared plasmonic-photonics using heavily doped n-Ge/Ge and n-GeSn/GeSn heterostructures. *Opt. Express* **20,** 3814 (2012).

222. Thomas, R., Ikonic, Z. & Kelsall, R. W. Plasmonic modulators for near-infrared photonics on a silicon-on-insulator platform. *IEEE J. Sel. Top. Quantum Electron.* **19,** (2013).

223. Wu, K., Zhan, Y., Zhang, C., Wu, S. & Li, X. Strong and highly asymmetrical optical absorption in conformal grating system for plasmonic hot-electron photodetection application. *Nat. Publ. Gr.* 1–7 (2015). doi:10.1038/srep14304

224. Adams, D. C. *et al.* Funneling light through a subwavelength aperture with epsilon-near-zero materials. *Phys. Rev. Lett.* **107,** 1090–1099 (2011).

225. Babicheva, V. E. *et al.* Towards CMOS-compatible nanophotonics: Ultra-compact modulators using alternative plasmonic materials. *Opt. Express* **21,** 27326 (2013).

226. Naik, G. V., Kim, J. & Boltasseva, A. Oxides and nitrides as alternative plasmonic materials in the optical range. *Opt. Mater. Express* **1,** 1090–1099 (2011).

227. Abb, M., Albella, P., Aizpurua, J. & Muskens, O. L. All-optical control of a single plasmonic nanoantenna-ITO hybrid. *Nano Lett.* **11,** 2457–2463 (2011).

228. Feigenbaum, E., Diest, K. & Atwater, H. A. Unity-order index change in transparent conducting oxides at visible frequencies. *Nano Lett.* **10,** 2111–2116 (2010).

229. Krasavin, A. V. & Zayats, A. V. Photonic signal processing on electronic scales: Electro-optical field-effect nanoplasmonic modulator. *Phys. Rev. Lett.* **109,** 1–5 (2012).

230. Kuo, W.-K. & Chen, M.-T. Simulation study of surface-plasmon-resonance electro-optic light modulator based on a polymer grating coupler. *Opt. Lett.* **34,** 3812–3814 (2009).

231. Leuthold, J., Freude, W., Koos, C., Melikyan, a & Lindenmann, N. A Surface Plasmon Polariton Absorption Modulator 1. **19,** 4–6 (2011).

232. Liu, X. *et al.* Quantification and impact of nonparabolicity of the conduction band of indium tin oxide on its plasmonic properties. *Appl. Phys. Lett.* **105,** (2014).

233. Park, J., Kang, J., Liu, X. & Brongersma, M. L. Electrically Tunable Epsilon-Near- Zero (ENZ) Metafilm Absorbers. *Sci. Rep.* 1–9 (2015). doi:10.1038/srep15754

234. Vasudev, A. P., Kang, J.-H., Park, J., Liu, X. & Brongersma, M. L. Electro-optical modulation of a silicon waveguide with an 'epsilon-near-zero' material. *Opt. Express* **21,** 26387–26397 (2013).

235. Yi, F. *et al.* Voltage tuning of plasmonic absorbers by indium tin oxide Voltage tuning of plasmonic absorbers by indium tin oxide. *Appl. Phys. Lett.* **102,** (2013).

236. Fujimoto, T. & Awaga, K. Electric-double-layer field-effect transistors with ionic liquids. *Phys. Chem. Chem. Phys.* **15,** 8983–9006 (2013).

237. Lee, S. W. *et al.* Periodic array of polyelectrolyte-gated organic transistors from electrospun poly(3-hexylthiophene) nanofibers. *Nano Lett.* **10,** 347–351 (2010).

238. Lee, S.-K. *et al.* Photo-patternable ion gel-gated graphene transistors and inverters on plastic. *Nanotechnology* **25,** 014002; DOI:10.1088/0957-4484/25/1/014002 (2014).

239. Lee, S. W. *et al.* High performance foldable polymer thin film transistors with a side gate architecture. *J. Mater. Chem.* **21,** 18804 (2011).

240. Chen, C.-F. *et al.* Controlling inelastic light scattering quantum pathways in graphene. *Nature* **471,** 617–620 (2011).

241. Pu, J. *et al.* Highly flexible MoS2 thin-film transistors with ion gel dielectrics. *Nano Lett.* **12,** 4013–7 (2012).

242. Buffeteau, T., Grondin, J., Danten, Y. & Lassègues, J. C. Imidazolium-based ionic liquids: Quantitative aspects in the far-infrared region. *J. Phys. Chem. B* **114,** 7587–7592 (2010).

243. Seki, S. *et al.* Comprehensive refractive index property for room-temperature ionic liquids. *J. Chem. Eng. Data* **57,** 2211–2216 (2012).

244. Kim, K. K. K. K. K. *et al.* Synthesis and Characterization of Hexagonal Boron Nitride Film as a Dielectric Layer for Graphene Devices. *ACS Nano* **6,** 8583–8590 (2012).

245. Sung Kyu Jang, Jiyoun Youn, Young Jae Song, S. L. Synthesis and Characterization of Hexagonal Boron Nitride as a Gate Dielectric. *Sci. Rep.* (2016). doi:10.1021/nn301675f

246. Li, C., Bando, Y., Zhi, C., Huang, Y. & Golberg, D. Thickness-dependent bending modulus of hexagonal boron nitride nanosheets. *Nanotechnology* **20,** 385707 (2009).

247. Jo, I. *et al.* Thermal conductivity and phonon transport in suspended few-layer hexagonal boron nitride. *Nano Lett.* **13,** 550–554 (2013).

248. Ouyang, T. *et al.* Thermal transport in hexagonal boron nitride nanoribbons. *Nanotechnology* **21,** 245701 (2010).

249. Jin-Xiang, D. *et al.* Optical properties of hexagonal boron nitride thin films deposited by radio frequency bias magnetron sputtering. *Chinese Phys. B* **18,** 4013–4018 (2009).

250. Britnell, L. *et al.* Electron tunneling through ultrathin boron nitride crystalline barriers. *Nano Lett.* **12,** 1707–1710 (2012).

251. Britnell, L. *et al.* Field-Effect Tunneling Transistor Based on Vertical Graphene Heterostructures. *Science (80-.).* **335,** 947–950 (2012).

252. Masubuchi, S. *et al.* Fabrication and characterization of high-mobility graphene p-n-p junctions encapsulated by hexagonal boron nitride. *Jpn. J. Appl. Phys.* **52,** (2013).

253. Dean, C. R. *et al.* Boron nitride substrates for high-quality graphene electronics. *Nat. Nanotechnol.* **5,** 722–726 (2010).

254. Zomer, P. J., Dash, S. P., Tombros, N. & Van Wees, B. J. A transfer technique for high mobility graphene devices on commercially available hexagonal boron nitride. *Appl. Phys. Lett.* **99,** 96–99 (2011).

255. Khurgin, J. B. How to deal with the loss in plasmonics and metamaterials. *Nat. Nanotechnol.* **10,** 2–6 (2015).

256. Pinto, H. & Markevich, A. Electronic and electrochemical doping of graphene by surface adsorbates. *Beilstein J. Nanotechnol.* **5,** 1842–1848 (2014).

257. Ni, G. X. *et al.* Ultrafast optical switching of infrared plasmon polaritons in high-mobility graphene. *Nat. Photonics* **10,** 1–13 (2016).

258. Fang, Y. & Sun, M. Nanoplasmonic waveguides: towards applications in integrated nanophotonic circuits. *Light Sci. Appl.* **4,** e294 (2015).

259. Oulton, R. F. *et al.* Plasmon lasers at deep subwavelength scale. *Nature* **461,** 629–632 (2009).

260. Matthes, L., Pulci, O. & Bechstedt, F. Optical properties of two-dimensional honeycomb crystals graphene, silicene, germanene, and tinene from first principles. *New J. Phys.* **16,** (2014).

261. Gangaraj, S. A. H., Low, T., Nemilentsau, A. & Hanson, G. Directive Surface Plasmons on Tunable Two-Dimensional Hyperbolic Metasurfaces and Black Phosphorus: Green's Function and Complex Plane Analysis. *IEEE Trans. Antennas Propag.* **PP,** 1 (2016).

262. Politano, A., Chiarello, G. & Spinella, C. Plasmon spectroscopy of graphene and other two-dimensional materials with transmission electron microscopy. *Mater. Sci. Semicond. Process.* (2016). doi:10.1016/j.mssp.2016.05.002

263. Bablich, A., Kataria, S. & Lemme, M. Graphene and Two-Dimensional Materials for Optoelectronic Applications. *Electronics* **5,** 13 (2016).

264. Nulakani, N. V. R. & Subramanian, V. A Theoretical Study on the Design, Structure, and Electronic Properties of Novel Forms of Graphynes. *J. Phys. Chem. C* **120,** 15153–15161 (2016).

265. Charlier, A. L. and A. R. B.-M. and J.-C. Electronic and optical properties of pristine and oxidized borophene. *2D Mater.* **3,** 45006 (2016).

266. Peng, B. *et al.* First-principles calculations of electronic, optical, and thermodynamic properties of borophene. *J. Mater. Chem. C* **4,** 1–15 (2016).

267. Zhang, Z., Yang, Y., Penev, E. S. & Yakobson, B. I. Elasticity, Flexibility and Ideal Strength of Borophenes. *Adv. Funct. Mater.* **27,** 1–7 (2017).

268. D??vila, M. E., Xian, L., Cahangirov, S., Rubio, A. & Le Lay, G. Germanene: A novel two-dimensional germanium allotrope akin to graphene and silicene. *New J. Phys.* **16,** (2014).

269. Tabert, C. J. & Nicol, E. J. Dynamical polarization function, plasmons, and screening in silicene and other buckled honeycomb lattices. *Phys. Rev. B - Condens. Matter Mater. Phys.* **89,** 1–9 (2014).

270. Van Duppen, B., Vasilopoulos, P. & Peeters, F. M. Spin and valley polarization of plasmons in silicene due to external fields. *Phys. Rev. B - Condens. Matter Mater. Phys.* **90,** 1–10 (2014).

271. Wu, J., Lin, C., Gumbs, G. & Lin, M. The effect of perpendicular electric field on Temperature-induced plasmon excitations for intrinsic silicene. 1–19 (2015). doi:10.1039/c5ra07721d

272. Chowdhury, S., Nath, P. & Jana, D. Shape dependent magnetic and optical properties in silicene nanodisks: A first principles study. *J. Phys. Chem. Solids* **83,** 32–39 (2015).

273. Wu, J. Y., Chen, S. C., Gumbs, G. & Lin, M. F. Feature-rich electronic excitations of silicene in external fields. *Phys. Rev. B - Condens. Matter Mater. Phys.* **94,** 1–29 (2016).

274. Gomez, C. V., Pisarra, M., Gravina, M., Riccardi, P. & Sindona, A. Plasmon properties and hybridization effects in Silicene. 1–13 (2016). doi:10.1103/PhysRevB.95.085419

275. Zhao, J. *et al.* Rise of silicene: A competitive 2D material. *Prog. Mater. Sci.* **83,** 24–151 (2016).

276. Mokkath, J. H. Tunable optical absorption in silicene molecules. *J. Mater. Chem. C* **966,** 1–10 (2016).

277. Low, T. *et al.* Plasmons and screening in monolayer and multilayer black phosphorus. *Phys. Rev. Lett.* **113,** 5–9 (2014).

278. Ling, X. *et al.* The renaissance of black phosphorus. *Pnas* **112,** 4523 (2015).

279. Kou, L., Chen, C. & Smith, S. C. Phosphorene: Fabrication, Properties, and Applications. *J. Phys. Chem. Lett.* **6,** 2794–2805 (2015).

280. Jin, F., Rold??n, R., Katsnelson, M. I. & Yuan, S. Screening and plasmons in pure and disordered single- and bilayer black phosphorus. *Phys. Rev. B - Condens. Matter Mater. Phys.* **92,** 1–12 (2015).

281. Mehboudi, M. *et al.* Strain and the optoelectronic properties of nonplanar phosphorene monolayers. *Proc. Natl. Acad. Sci. U. S. A.* **112,** 5888–5892 (2015).

282. Lin, J. H., Zhang, H. & Cheng, X. L. First-principle study on the optical response of phosphorene. *Front. Phys.* **10,** 1–9 (2015).

283. Bao, Z.-W., Wu, H.-W. & Zhou, Y. Edge plasmons in monolayer black phosphorus. *Appl. Phys. Lett.* **109,** 241902 (2016).

284. Lu, J. *et al.* Light-Matter Interactions in Phosphorene. *Acc. Chem. Res.* **49,** 1806–1815 (2016).

285. Liu, Z. & Aydin, K. Localized Surface Plasmons in Nanostructured Monolayer Black Phosphorus. *Nano Lett.* **16,** 3457–3462 (2016).

286. Mogulkoc, Y., Modarresi, M., Mogulkoc, A. & Ciftci, Y. O. Electronic and optical properties of bilayer blue phosphorus. *Comput. Mater. Sci.* **124,** 23–29 (2016).

287. Lu, H., Gong, Y., Mao, D., Gan, X. & Zhao, J. Strong plasmonic confinement and optical force in phosphorene pairs. *Opt. Express* **25,** 5255 (2017).

10. Nomenclature

2DEG (2-Dimentional Electron Gas), 22
AFM (Atomic Force Microscopy), 44
APCVD (Atmospheric Pressure Chemical Vapour Deposition), 36
CVD (Chemical Vapour Deposition), 20
DI (deionized), 38
E-beam (electron beam), 92
ENZ (Epsilon-Near-Zero), 81
FDTD (Finite-Difference Time-Domain), 60
FEM (Finite Element Methods), 60
FET (field effect transistor), 43
FWHM (full width at half maximum), 44
HIM (Helium Ion Microscopy), 13
IPA (isopropyl alcohol), 92
M-ENZ-IM (Metal-Epsilon-Near-Zero-Insulator-Metal), 90
MIM (Metal-Insulator-Metal), 81
ITO (Indium Tin Oxide), 70
PET (Polyethylene terephthalate), 42
PMMA (polymethylmethacrylate), 38
PVB (polyvinyl butyral), 100
RCA (Radio Corporation of America), 40
RCWA (Rigorous Coupled Wave Analysis), 13
RCWA (Rigorous coupled wave-analysis), 60
SEM (Scanning Electron Microscopy), 13
SERS (Surface Enhanced Raman Spectroscopy), 32
SPPs (surface plasmon polaritons), 15
SPR (Surface Plasmon Resonance), 17
STM (Scanning Tunnelling Microscopy), 44
TE (Transverse electric), 23
TEM (Transmission Electron microscopy), 44
TM (Transverse magnetic), 23
TO (transverse optical), 45

11. List of Variables

A: Absorption
C: Capacitance
c: Speed of light
D: Drude weight
d: Thickness
d_{Au}: Gold thickness
d_g: Graphene thickness
d_s: Spacer thickness
E: Electric Field
e: Electron charge
E_D: Energy dispersion
H: Magnetic field
h: Planck constant
ħ: Reduced Planck constant
I_{2D}: 2D peak intensity
I_D: D peak intensity
I_D: Drain current
I_G: G peak intensity
k: Imaginary part of refractive index
k: Wave-vector
k_0: Free space photon wave-vector
k_B: Boltzman constant
k_{sp}: Plasmon wave-vector
L_D: Interdefect distance
m: Cavity mode integer
m_e: Free space electron mass
m_{eff}: Effective electron mass
n: Real part of refractive index
n_c: Charge carrier density
n_D: Defect density
n_{gr}: Complex refractive index of graphene
n_{or}: Diffraction order
n_s: Spacer refractive index
q: Momentum
R: Reflectance
r_0: Reflectivity of substrate
t: Hoping parameter
T: Temperature
T_r: Transmittance
v: Grating order
V_{ds}: Drain-Source voltage
v_f: Fermi velocity
V_g: Gate voltage
w: Width
α: Grating lattice constant
α_g: Fine structure constant
Γ: Carrier scattering rate
δ_d: Decay length in dielectric
δ_m: Decay length in metal
δ_{sp}: Plasmon propagation length
ε: Permittivity
ε_0: Permittivity of vacuum
ε_∞: Background permittivity
ε_d: Permittivity of dielectric
ε_g: Permittivity of graphene
ε_I: Permittivity of ITO
ε_{ITO}: Dielectric constant of ITO
ε_m: Permittivity of metal
θ: Angle of incidence
θ_n: Diffraction angle
λ: Wavelength
λ_L: Source laser wavelength
μ: Chemical potential
μ_g: Graphene mobillity
σ: Conductivity
σ_0: Universal conductivity
τ: Relaxation time
ω: Angular frequency
ω_p: Plasma frequency
ω_{pl}: Plasmon frequency

12. Appendices

12.1. Matlab codes

12.1.1. Matlab Code: Electrostatically Tuneable Refractive index of Graphene

Matlab code used for theoretically calculating and plotting the tuneable optical properties and plasmon dispersion of graphene:

```
% ********************************************************
%Testing now:
% ********************************************************
%improve dispersion plot
%make modes for more Ef
%make peaks optional
% ********************************************************
% graphene optical model
% ********************************************************
clc
clear all;
% ********************************************************
% Code options
% ********************************************************
Ef_val=0; % for 0 it runs only for chosen Ef values, for 1 it calculates
Ef through voltage
carrier=1; % for 0 calculates carrier concentration from dielectric con-
stant, for 1 from capacitance
spectra=1; %0 defines range from frequency, 1 from wavelength, 2 from
photon energy
print=0; %1 prints txt files
plot_val=0; % 0 plots all results, 1 plots only the refractive index,
plasmon dispersion, and voltage vs Ef
keep_dat=0; % if set to 0 clears data after done calculating
lorentz=0; %1 includes Lorenz oscillator model for exciton peak (Warn-
ing!model becomes semi-analytical, Fermi level effect not taen into ac-
count)
multi=1; %1 enables multilayer dispersion
peakm=0; %1 enables e-e excitation peaks
Drude=0;% 1 calculates from drude model with given mobillity
Skin=0;% 1 Skin depth enabled
% ********************************************************
% Output file names
% ********************************************************
filename_r=('n_test.txt');%file name for n
filename_i=('k_test.txt');%file name for k
rsoft_name_r=('graphene_n_0_630000.txt');%file name for n
rsoft_name_i=('graphene_k_0_630000.txt');%file name for k
% ********************************************************
% Input values
% ********************************************************
Ef_1=abs(-0.3:0.6:0.3); %Fermi level in eV -1.5:0.01:1.5 High frequency
mode only for length(Ef)<3
Vg=(0:0.01:5); %Voltage in V
mobil=30000;%cm^2/V.s
mass=1.6*10^-20;
mpset=1; %relative permeabillity of graphene
%-----------------------------------
T=300; %Temperature in K
```

```
%----------------------------------
la=1.1:0.02:3; %wavelength range in um
om=100:1:194; %Frequency range in THz
eVl=(0.7:0.002:2);%(0.61992:0.0001:0.85506);%0.619:0.0005:0.855;%0.6:0.00
1:3; %photon energy in eV
%----------------------------------
d=1*10^-9;% thickness for plasmon mode calculation
d_oxide=11*10^-7;%11*10^-7; %cm oxide thickness
A_r=1;%contact area, leave at 1 for capacitance in F/cm^2. otherwise use
value in cm^2
epsilon_oxide=20; %permittivity of substrate dielectric (3.9 SiO2, 20
HfO2, 10 Al2O3, 50 TiO2)
voltage_ef=('Ionic gel');%title for voltage vs Ef level plot
C_gate=10.7*10^-6;% gate capacitance in Farad/cm^2
%----------------------------------
a_g=(1000:500:2500)*10^-9; % gratting latice constant in m (Warning! only
use 1 or 2 steps if double length(v_f)>1 only give more than one value
when length(theta=1))
theta=(60); %incident photon angle degree, 0 is perpendicular to layer
(Warning! only give more than one value when length(a_g=1))
v_f=(2); % gratting factor (Warning! only use multiple values when a_g
has a length of 3)
epsilon_sur=1^2; % dielectric constant of surrounding medium
%-----------------------------------------------------------
%Main program*********************************************
%-----------------------------------------------------------

% ********************************************************
% Constants and variables
% ********************************************************
h_plank=6.582*10^-16; %eV.s
epsilon_0=8.85*10^-14; %F/cm permittivity of vacuum
e=1.6*10^-19; %C electron charge
k=8.6*10^-5; %eVK^-1 Boltzmann constant
c = 2.99792458*10^8; %m/s speed of light
uf=10^8; %cm/s fermi velocity
t=2.7; %eV hopping parameter
dgr=0.34*10^-9; %m thickness of the graphene layer
epsilon_air=1; % relative permittivity of air
mv=4*pi*10^-7; %megnetic permeabillity of vacuum
%Lorentz parameters----
FL=2.234; %oscillation strength f /5
EL=4.61; %position E0
GL=0.6*2; %width gama *1.4
%mass=1.1*10^-30;%kg
%Lorentz parameters end
if spectra==0
    omega=2*pi*om*10^12; %hz
    lambda=2*pi*c./omega; %m
    eVl=((4.136*10^-15)*3*10^8)./lambda; %eV
elseif spectra==1
    lambda=la*10^-6; %m
    omega=2*pi*c./lambda; %hz
    eVl=((4.136*10^-15)*3*10^8)./lambda; %eV;
else
    lambda=((4.136*10^-15)*3*10^8)./eVl; %m
    omega=2*pi*c./lambda; %hz
end
%plasmon variables
thetarad=theta*pi/180; %angle in rads
K0=(omega/c); %incident photon wavevector
K0_g=zeros(length(a_g),length(K0),length(v_f));
```

```
if length(theta)==1
    Kx=K0*sin(thetarad)*sqrt(epsilon_sur); %inplane momentum of inpinging
photons
    for i=1:1:length(a_g)
        for j=1:1:length(v_f)
            K0_g(i,:,j)=Kx+2*pi*v_f(j)/a_g(i); %wave vector of incident
light with gratting
        end
    end
else
    Kx=zeros(length(theta),length(K0));
    for i=1:1:length(theta)
        for j=1:1:length(v_f)
            Kx(i,:)=K0*sin(thetarad(i))*sqrt(epsilon_sur); %inplane mo-
mentum of inpinging photons
            K0_g(i,:,j)=Kx(i,:)+2*pi*v_f(j)/a_g; %wave vector of incident
light with gratting
        end
    end
end
% ********************************************************
% Carrier concentration in graphene
% ********************************************************
if carrier==0
    C_gate=epsilon_0*epsilon_oxide*A_r/d_oxide; %Farad/cm^2
    n=Vg*C_gate*6.24*10^18; %1/cm^2 carrier concentration
    %n=Vg*epsilon_0*epsilon_oxide/(e*d_oxide); %1/cm^2 carrier concentra-
tion
else
    n=Vg*C_gate*6.24*10^18; %1/cm^2 carrier concentration
end
% ********************************************************
% Fermi Level in graphene
% ********************************************************
Ef=sqrt(pi*n)*uf*h_plank; %eV Fermi level
Ef_calc=Ef';
n_calc=n';
Vg_calc=Vg';
if Ef_val==0 % if chosen provides the user provided Ef range
    Ef=Ef_1; %eV
end
Ef1(length(Ef),length(lambda))=0;
for i=1:1:length(lambda)
    Ef1(:,i)=Ef';
end
tmob=mobil*Ef/(e*uf^2)*(1.602177*10^-19); % plasmon lifetime s
Gama=e/(mobil*mass); %1*10^-3;% eV damping rate
if length(Ef)==1
    ngama=(Ef/(h_plank*uf))^2/pi;
    Gama=uf/(mobil*sqrt(pi*ngama));%*e eV damping rate
end
% ********************************************************
% Refractive index of graphene
% ********************************************************
cond_gr=zeros(length(Ef),length(omega)); %pre-allocation of matrices
cond_gi=cond_gr;
cond_g=cond_gr;
perm=cond_gr;
ng=cond_gr;
permlorenrz=cond_gr;
Ksp=cond_gr;
Tr=cond_gr;
```

```
ab=cond_gr;
kz=cond_gr;
Lsp=cond_gr;
peak=Ksp;
s_peak=peak;
for ji=1:1:max(length(Ef)) % calculation of the optical conductivity,
permitivvity and refractive index
    if Drude==0;

cond_gr(ji,:)=((e^2/(4*h_plank)*(1+(h_plank*omega).^2./(36*t^2))/2.*
(tanh((h_plank*omega+2*Ef(ji))/(4*k*T))+tanh((h_plank*omega-
2*Ef(ji))/(4*k*T)))))/(e^2/h_plank); % real part of conductivity
        cond_gi(ji,:)=((4*Ef(ji))*
(e^2/(4*h_plank))./(h_plank*omega*pi)*(1-2*Ef(ji)^2/(9*t^2))-
(1+(h_plank*omega).^2/(36*t^2))*
e^2/(4*h_plank)/pi.*log(abs(h_plank*omega+2*Ef(ji))./abs(h_plank*omega-
2*Ef(ji))))/(e^2/h_plank); % imaginary part of conductivity
        cond_g(ji,:)=cond_gr(ji,:)+cond_gi(ji,:)*1i; %e^2/h_plank
        perm(ji,:)=(5.5/(dgr/(0.34*10^-
9))+(1i*cond_g(ji,:)*(e^2/h_plank)./(dgr*omega))*7.05*10^29); % permit-
tivity, 7.05*10^29 is the convertion number from e^2/h_plank to S over
the permittivity of vacuum
    else
        cond_gi(ji,:)=( 1i*e^2/(4*pi*h_plank)  *  log(  (2*abs(Ef(ji))-
h_plank*omega-1i*Gama)  ./  (2*abs(Ef(ji))+h_plank*omega+1i*Gama)
))/(e^2/h_plank);
        cond_gr(ji,:)=( 1i*e^2./(pi*h_plank*(h_plank*omega+1i*Gama))  .*
(Ef(ji)+2*k*T*log(exp(-Ef(ji)/(k*T))+1)))/(e^2/h_plank);
        cond_g(ji,:)=(cond_gr(ji,:)+cond_gi(ji,:));  %e^2/h_plank
        perm(ji,:)=(5.5/(dgr/(0.34*10^-
9))+(1i*cond_g(ji,:)*(e^2/h_plank)./(dgr*omega))*7.05*10^29); % permit-
tivity, 7.05*10^29 is the convertion number from e^2/h_plank to S over
the permittivity of vacuum
    end

%perm(ji,:)=(5.5+(1i*cond_g(ji,:)*(e^2/h_plank)./(dgr*omega))*7.05*10^29)
; % permittivity, 7.05*10^29 is the convertion number from e^2/h_plank to
S over the permittivity of vacuum
    permlorenrz(ji,:)=FL*EL^2./((EL^2-
(h_plank*omega).^2).^2+GL^2.*(h_plank*omega).^2).*((EL^2-
(h_plank*omega).^2)+1i*GL.*h_plank*omega); % Lorentz term
    ng(ji,:)=sqrt(perm(ji,:)); % refractive index
    Ksp(ji,:)=K0.*sqrt(epsilon_sur.*perm(ji,:)./(epsi-
lon_sur+perm(ji,:))); %surface plasmon wave vector m^-1

peak(ji,:)=imag(perm(ji,:)./(real(perm(ji,:)).^2+imag(perm(ji,:)).^2);
    s_peak(ji,:)=imag(perm(ji,:)./((epsi-
lon_sur+real(perm(ji,:))).^2+imag(perm(ji,:)).^2);
    Tr(ji,:)=(1+cond_gr(ji,:)*(e^2/h_plank)*7.05*10^29/(2*c)).^-2;
%Transmittance
    ab(ji,:)=-log(Tr(ji,:)); %Absorption
    kz(ji,:) = sqrt(Ksp(ji,:).^2 - epsilon_sur*(K0).^2); %wave vector
perpendiclar to interface
    Lsp(ji,:)=(2*imag(Ksp(ji,:))).^-1; %plasmon propagation lenght
end
%multilayer-----------
%Kspodd=zeros(length(Ef),length())
%Kspeven=zeros(length(Ef),length())
if length(Ef)<3
if multi==1
for ji=1:1:length(Ef)
%odd------------------
```

```
    %perm= @ (x,y) real(1-omegap^2./(x.^2+1i*gama.*x))
    perm_both= @
(x,y)real((5.5+(1i*((((e^2/(4*h_plank)*(1+(h_plank*x).^2./(36*t^2))/2.*
(tanh((h_plank*x+2*Ef(ji))/(4*k*T))+tanh((h_plank*x-
2*Ef(ji))/(4*k*T)))))/(e^2/h_plank))+(((4*Ef(ji))*
(e^2/(4*h_plank)).*(h_plank*x*pi)*(1-2*Ef(ji)^2/(9*t^2))-
(1+(h_plank*x).^2/(36*t^2))*
e^2/(4*h_plank)/pi.*log(abs(h_plank*x+2*Ef(ji)).*abs(h_plank*x-
2*Ef(ji))))/(e^2/h_plank))*1i)*(e^2/h_plank).*(dgr*x))*7.05*10^29)); %
permittivity, 7.05*10^29 is the convertion number from e^2/h_plank to S
over the permittivity of vacuum
    k1= @ (x,y) sqrt(y^2-(x/c)^2*perm_both(x,y));
    k2= @ (x,y) sqrt(y^2-(x/c)^2*epsilon_sur);
    k3= @ (x,y) sqrt(y^2-(x/c)^2*epsilon_sur2);
    odd_F=@(x,y) (tanh(k1(x,y)*d/2)+(k2(x,y)*perm_both(x,y))/(k1(x,y)*ep-
silon_sur));
    %ezplot--------------
        figure

odd=ezplot(@(y,x)odd_F(x,y),[2*10^6,6*10^7,omega(1),omega(length(omega))]
);
        tmp1 = get(odd,'contourMatrix');
        omegatmp1=tmp1(2,:);
        if ji==1
            Kspodd(1,:)=tmp1(1,:);
            omegaodd=omegatmp1/(2*pi); %hz
            eVlodd=omegatmp1*h_plank; %eV
        else
            Kspodd2(2,:)=tmp1(1,:);
            omegaodd2=omegatmp1/(2*pi); %hz
            eVlodd2=omegatmp1*h_plank; %eV
        end
        close figure 1
%even-----------------
    %perm= @ (x,y) real(1-omegap^2./(x.^2+1i*gama.*x))
    even_F=@(x,y) (tanh(k1(x,y)*d/2)+(k1(x,y)*epsi-
lon_sur)/(k2(x,y)*perm_both(x,y)));
    %ezplot--------------
        figure

even=ezplot(@(y,x)even_F(x,y),[2*10^6,6*10^7,omega(1),omega(length(omega)
)]);
        tmp2 = get(even,'contourMatrix');
        omegatmp2=tmp2(2,:);
        if ji==1
            Kspeven(1,:)=tmp2(1,:);
            omegaeven=omegatmp2/(2*pi); %hz
            eVleven=omegatmp2*h_plank; %eV
        else
            Kspeven2(2,:)=tmp2(1,:);
            omegaeven2=omegatmp2/(2*pi); %hz
            eVleven2=omegatmp2*h_plank; %eV
        end
        close figure 1
end
end
end
%Lorentz-------------
if lorentz==1 % if selected incldues a lorentz oscillator term to fit the
exciton peak
    perm=perm-4.5+permlorenrz;
    ng=sqrt(perm);
```

```
end
%--------------------
nr=real(ng);
ni=imag(ng);
permr=real(perm);
permi=imag(perm);
condr=real(cond_g);
condi=imag(cond_g);
z_a=1./abs(kz); %decay length of plasmon in dielectric
% ********************************************************
% Skin depth in graphene
% ********************************************************
if length(Ef)<2
    if Skin==1;
    mp=mpset*mv;%permeabillity of graphene
    cond2=cond_g(ji,:)*0.2428;%mS

%Ds=sqrt(2./(omega.*mp.*cond2/1000))%.*sqrt(sqrt(1+(1./(cond2/1000).*omeg
a.*perm*epsilon_0).^2)+1./(cond2/1000).*omega.*perm*epsilon_0);
    Ds2=1./(omega./c.*ng);
    %Skin depth
        figure;
        GraphTitle = ('Skin layer');
        plot(eVl,real(Ds2))%,eVl,imag(Ds),'--')
        xlabel ('Photon energy (eV)','FontSize',20);
        ylabel ('Skin layer (m)','FontSize',20);
        title(GraphTitle,'FontSize',20);
        saveas (gcf,GraphTitle,'jpg');
        % figure;
        %GraphTitle = ('Skin effect');
        %plot(eVl,real(Ds2),eVl,imag(Ds2),'--')
        %xlabel ('Photon energy (eV)','FontSize',20);
        %ylabel ('Skin effect(m)','FontSize',20);
        %title(GraphTitle,'FontSize',20);
        %saveas (gcf,GraphTitle,'jpg');
        %Condactivity
        figure;
        GraphTitle = ('graphene refractive index skin');
        plot(eVl,nr,eVl,ni,'--')
        xlabel ('Photon energy (eV)','FontSize',20);
        ylabel ('Refractive index','FontSize',20);
        title(GraphTitle,'FontSize',20);
        saveas (gcf,GraphTitle,'jpg');
        %GraphTitle = ('graphene Conductivity skin');
        %plot(eVl,real(cond2),eVl,imag(cond2),'--')
        %plot(eVl,real(cond_g),eVl,imag(cond_g),'--')
        %xlabel ('Photon energy (eV)','FontSize',20);
        %ylabel ('mS','FontSize',20);
        %ylabel ('Conductivity (e^2/h_p)','FontSize',20);
        %title(GraphTitle,'FontSize',20);
        %saveas (gcf,GraphTitle,'jpg');
    end
end
% ********************************************************
%Plot results
% ********************************************************
cd('figures')
figure;
GraphTitle = voltage_ef;
[ax,p1,p2]=plotyy(Vg,Ef_calc,Vg,n);%(Ef_calc,n,Ef_calc,Vg);
xlabel (ax(1),'Voltage (V)','FontSize',20);
ylabel (ax(1),'Chemical potential (eV)','FontSize',20);
```

```
ylabel (ax(2),'Carrier concentration (1/cm^2)','FontSize',20);
title(GraphTitle,'FontSize',20);
saveas (gcf,GraphTitle,'jpg');
if length(Ef)<10
    if plot_val==0
    %Condactivity
        figure;
        GraphTitle = ('graphene Conductivity');
        plot(omega/(2*pi*10^12),condr,omega/(2*pi*10^12),condi,'--')
        xlabel ('Frequency (THz)','FontSize',20);
        ylabel ('Conductivity (e^2/h_p)','FontSize',20);
        title(GraphTitle,'FontSize',20);
        saveas (gcf,GraphTitle,'jpg');
    %Permittivity
        figure;
        GraphTitle = ('graphene permittivity');
        plot(lambda*10^9,real(perm),lambda*10^9,imag(perm),'--')
        xlabel ('Wavelength (nm)','FontSize',20);
        ylabel ('permittivity','FontSize',20);
        title(GraphTitle,'FontSize',20);
        saveas (gcf,GraphTitle,'jpg');
    %Transmission
        figure;
        GraphTitle = ('Transmission %');
        plot(lambda*10^9,Tr*100)
        xlabel ('Wavelength (nm)','FontSize',20);
        ylabel ('Transmission %','FontSize',20);
        title(GraphTitle,'FontSize',20);
        saveas (gcf,GraphTitle,'jpg');
     %Absorption
        figure;
        GraphTitle = ('Absorption %');
        plot(lambda*10^9,ab*100)
        xlabel ('Wavelength (nm)','FontSize',20);
        ylabel ('Absorption %','FontSize',20);
        title(GraphTitle,'FontSize',20);
        saveas (gcf,GraphTitle,'jpg');
     %Plasmon Lsp and confinment
        figure;
        GraphTitle = ('Plasmon Lsp and Decay length');
        plot(real(z_a),omega/(2*pi*10^12),Lsp,omega/(2*pi*10^12),'--')
        set(gca,'xscale','log');
        xlabel ('Length (m)','FontSize',20);
        ylabel ('Frequency (THz)','FontSize',20);
        title(GraphTitle,'FontSize',20);
        saveas (gcf,GraphTitle,'jpg');
    end
%Refractive index
    figure;
    GraphTitle = ('graphene refractive index');
    plot(lambda*10^9,nr,lambda*10^9,ni,'--')
    xlabel ('Wavelength (nm)','FontSize',20);
    ylabel ('Refractive index','FontSize',20);
    title(GraphTitle,'FontSize',20);
    saveas (gcf,GraphTitle,'jpg');
if peakm==1;
%Plasmon Peak
        figure;
        GraphTitle = ('Bulk plasmon peak');
        plot(lambda*10^9,peak(:,:))
        xlabel ('Wavelength (nm)','FontSize',20);
        ylabel ('Im\{-1/?_g\}','FontSize',20);
```

```
        title(GraphTitle,'FontSize',20);
        saveas (gcf,GraphTitle,'jpg');

        figure;
        GraphTitle = ('Surface plasmon peak');
        plot(lambda*10^9,s_peak(:,:))
        xlabel ('Wavelength (nm)','FontSize',20);
        ylabel ('Im\{-1/[1+?_g]\}','FontSize',20);
        title(GraphTitle,'FontSize',20);
        saveas (gcf,GraphTitle,'jpg');
end
%Plasmon dispersion curve
    if multi==1
    if length(Ef)==1
        figure
        GraphTitle = ('graphene plasmon modes');
        plot(Kspodd,eVlodd,'.',Kspeven,eVleven,'.',Ksp,eVl,K0*sqrt(epsi-
lon_sur),eVl,'k--',K0_g,eVl,'-.','markers',2)
        ylabel ('Photon energy (eV)','FontSize',20);
        xlabel ('Wave vector','FontSize',20);
        title(GraphTitle,'FontSize',20);
        saveas (gcf,GraphTitle,'jpg');
    elseif length(Ef)==2
        figure
        GraphTitle = ('graphene plasmon modes');

plot(Kspodd,eVlodd,'.',Kspeven,eVleven,'.',Kspodd2,eVlodd2,'.',Kspeven2,e
Vleven2,'.',Ksp,eVl,K0*sqrt(epsilon_sur),eVl,'k--',K0_g,eVl,'markers',2)
        ylabel ('Photon energy (eV)','FontSize',20);
        xlabel ('Wave vector','FontSize',20);
        title(GraphTitle,'FontSize',20);
        saveas (gcf,GraphTitle,'jpg');
    end
    end
    if length(v_f)>1
        if length(Ef_1)==3
            figure;
            GraphTitle = ('SP mode dispersion eV');
            if length(a_g)<2
                plot(real(Ksp(1,:)),eVl,'K',-
real(Ksp(1,:)),eVl,'K',real(Ksp(2,:)),eVl,'b',-
real(Ksp(2,:)),eVl,'b',real(Ksp(3,:)),eVl,'r',-
real(Ksp(3,:)),eVl,'r',K0_g(1,:,1),eVl,'b-.',K0_g(1,:,2),eVl,'b-
.',K0_g(1,:,3),eVl,'b-.',K0_g(1,:,4),eVl,'b-.',K0_g(1,:,5),eVl,'b-
.',K0_g(1,:,6),eVl,'b-.',K0_g(1,:,7),eVl,'b-.')
            else
                plot(real(Ksp(1,:)),eVl,'K',-
real(Ksp(1,:)),eVl,'K',real(Ksp(2,:)),eVl,'b',-
real(Ksp(2,:)),eVl,'b',real(Ksp(3,:)),eVl,'r',-
real(Ksp(3,:)),eVl,'r',K0_g(1,:,1),eVl,'b-.',K0_g(1,:,2),eVl,'b-
.',K0_g(1,:,3),eVl,'b-.',K0_g(1,:,4),eVl,'b-.',K0_g(1,:,5),eVl,'b-
.',K0_g(1,:,6),eVl,'b-.',K0_g(1,:,7),eVl,'b-.',K0_g(2,:,1),eVl,'r--
',K0_g(2,:,2),eVl,'r--',K0_g(2,:,3),eVl,'r--',K0_g(2,:,4),eVl,'r--
',K0_g(2,:,5),eVl,'r--',K0_g(2,:,6),eVl,'r--',K0_g(2,:,7),eVl,'r--')
            end
            xlabel ('K_x (m^-^1)','FontSize',20);
            ylabel ('Photon energy (eV)','FontSize',20);
            title(GraphTitle,'FontSize',20);
            saveas (gcf,GraphTitle,'jpg');
        else
            figure;
            GraphTitle = ('SP mode dispersion eV');
```

```
            if length(a_g)<2
                plot(real(Ksp),eVl,'K',-
real(Ksp),eVl,'K',K0_g(1,:,1),eVl,'b-.',K0_g(1,:,1),eVl,'b-
.',K0_g(1,:,2),eVl,'b-.',K0_g(1,:,3),eVl,'b-.',K0_g(1,:,4),eVl,'b-
.',K0_g(1,:,5),eVl,'b-.',K0_g(1,:,6),eVl,'b-.',K0_g(1,:,7),eVl,'b-.')
            else
                plot(real(Ksp),eVl,'K',-
real(Ksp),eVl,'K',K0_g(1,:,1),eVl,'b-.',K0_g(1,:,1),eVl,'b-
.',K0_g(1,:,2),eVl,'b-.',K0_g(1,:,3),eVl,'b-.',K0_g(1,:,4),eVl,'b-
.',K0_g(1,:,5),eVl,'b-.',K0_g(1,:,6),eVl,'b-.',K0_g(1,:,7),eVl,'b-
.',K0_g(2,:,1),eVl,'r--',K0_g(2,:,2),eVl,'r--',K0_g(2,:,3),eVl,'r--
',K0_g(2,:,4),eVl,'r--',K0_g(2,:,5),eVl,'r--',K0_g(2,:,6),eVl,'r--
',K0_g(2,:,7),eVl,'r--')
            end
            xlabel ('K_x (m^-^1)','FontSize',20);
            ylabel ('Photon energy (eV)','FontSize',20);
            title(GraphTitle,'FontSize',20);
            saveas (gcf,GraphTitle,'jpg');
        end
    else
        figure;
        GraphTitle = ('SP mode dispersion');
        plot(real(Ksp),omega/(2*pi*10^12),K0*sqrt(epsi-
lon_sur),omega/(2*pi*10^12),'k--',K0_g,omega/(2*pi*10^12),'-
.',imag(Ksp),omega/(2*pi*10^12),':')
        xlabel ('K_x (m^-^1)','FontSize',20);
        ylabel ('Frequency (THz)','FontSize',20);
        title(GraphTitle,'FontSize',20);
        saveas (gcf,GraphTitle,'jpg');
    end
else
    if plot_val==0
    %Condactivity 3D
        figure;
        GraphTitle = ('Conductivity vs Ef 3D');
        surf(lambda*10^9,Ef1,cond_gr,'EdgeColor','none')
        xlabel ('Wavelength (nm)','FontSize',20);
        ylabel ('Fermi level','FontSize',20);
        zlabel ('Conductivity (e^2/h_p)','FontSize',20);
        title(GraphTitle,'FontSize',20);
        saveas (gcf,GraphTitle,'fig');

        figure;
        GraphTitle = ('Conductivity im vs Ef 3D');
        surf(lambda*10^9,Ef1,cond_gi,'EdgeColor','none')
        xlabel ('Wavelength (nm)','FontSize',20);
        ylabel ('Fermi level','FontSize',20);
        zlabel ('Conductivity (e^2/h_p)','FontSize',20);
        title(GraphTitle,'FontSize',20);
        saveas (gcf,GraphTitle,'fig');
    %Permittivity 3D
        figure;
        GraphTitle = ('permittivity vs Ef 3D');
        surf(lambda*10^9,Ef1,real(perm),'EdgeColor','none')
        xlabel ('Wavelength (nm)','FontSize',20);
        ylabel ('Fermi level','FontSize',20);
        zlabel ('permittivity','FontSize',20);
        title(GraphTitle,'FontSize',20);
        saveas (gcf,GraphTitle,'fig');

        figure;
        GraphTitle = ('permittivity im vs Ef 3D');
```

```
        surf(lambda*10^9,Ef1,imag(perm),'EdgeColor','none')
        xlabel ('Wavelength (nm)','FontSize',20);
        ylabel ('Fermi level','FontSize',20);
        zlabel ('permittivity','FontSize',20);
        title(GraphTitle,'FontSize',20);
        saveas (gcf,GraphTitle,'fig');
    %Transmission 3D
        figure;
        GraphTitle = ('Transmission %');
        surf(lambda*10^9,Ef1,Tr*100,'EdgeColor','none')
        xlabel ('Wavelength (nm)','FontSize',20);
        ylabel ('Fermi level (eV)','FontSize',20);
        zlabel ('Transmission %','FontSize',20);
        title(GraphTitle,'FontSize',20);
        saveas (gcf,GraphTitle,'fig');
    %Absorption 3D
        figure;
        GraphTitle = ('Absorption %');
        surf(lambda*10^9,Ef1,ab*100,'EdgeColor','none')
        xlabel ('Wavelength (nm)','FontSize',20);
        ylabel ('Fermi level (eV)','FontSize',20);
        zlabel ('Absorption %','FontSize',20);
        title(GraphTitle,'FontSize',20);
        saveas (gcf,GraphTitle,'fig');
    end
%Refractive index 3D
    figure;
    GraphTitle = ('n vs Ef 3D');
    surf(lambda*10^9,Ef1,nr,'EdgeColor','none')
    xlabel ('Wavelength (nm)','FontSize',20);
    ylabel ('Fermi level','FontSize',20);
    zlabel ('Refractive index','FontSize',20);
    title(GraphTitle,'FontSize',20);
    saveas (gcf,GraphTitle,'fig');

    figure;
    GraphTitle = ('k vs Ef 3D');
    surf(lambda*10^9,Ef1,ni,'EdgeColor','none')
    xlabel ('Wavelength (nm)','FontSize',20);
    ylabel ('Fermi level','FontSize',20);
    zlabel ('Refractive index','FontSize',20);
    title(GraphTitle,'FontSize',20);
    saveas (gcf,GraphTitle,'fig');
%3D Plasmon Peak
        figure;
        GraphTitle = ('3D Bulk plasmon peak');
        surf(lambda*10^9,Ef1,peak,'EdgeColor','none')
        xlabel ('Wavelength (nm)','FontSize',20);
        ylabel ('Fermi level','FontSize',20);
        zlabel ('Im\{-1/?_g\}','FontSize',20);
        title(GraphTitle,'FontSize',20);
        saveas (gcf,GraphTitle,'jpg');

        figure;
        GraphTitle = ('Surface plasmon peak');
        surf(lambda*10^9,Ef1,s_peak,'EdgeColor','none')
        xlabel ('Wavelength (nm)','FontSize',20);
        ylabel ('Fermi level','FontSize',20);
        zlabel ('Im\{-1/[1+?_g]\}','FontSize',20);
        title(GraphTitle,'FontSize',20);
        saveas (gcf,GraphTitle,'jpg');
```

```
        figure;
        GraphTitle = ('3D Bulk and surface plasmon peak with interband');
        surf(lambda*10^9,Ef1,peak./20+ab*50+s_peak./20,'EdgeCol-
or','none')
        xlabel ('Wavelength (nm)','FontSize',20);
        ylabel ('Fermi level','FontSize',20);
        zlabel ('Im(-1/epsilon)','FontSize',20);
        title(GraphTitle,'FontSize',20);
        saveas (gcf,GraphTitle,'jpg');
end

% ********************************************************
%Export data to text
% ********************************************************
if print==1
    cd('../')
    cd('data')
    voltage_vs_Ef=table(Vg_calc,n_calc,Ef_calc);
    writetable(voltage_vs_Ef)% save data
    lambda1(2:length(lambda)+1,:)=lambda';
    length_p=length(lambda);
    %permittivity
    perm_r(1,:)=Ef;
    perm_r(2:length_p+1,:)=permr';
    perm_i=Ef;
    perm_i(2:length_p+1,:)=permi';
    permittivity_real=table(lambda1,perm_r);
    permittivity_imag=table(lambda1,perm_i);
    writetable(permittivity_real)
    writetable(permittivity_imag)
    permittivity_real_eV=table(((4.136*10^-15)*3*10^8)./lambda1,perm_r);
    permittivity_imag_ev=table(((4.136*10^-15)*3*10^8)./lambda1,perm_i);
    writetable(permittivity_real_eV)
    writetable(permittivity_imag_ev)
    %conductivity
    cond_r=Ef;
    cond_r(2:length_p+1,:)=condr';
    cond_i=Ef;
    cond_i(2:length_p+1,:)=condi';
    conductivity_real=table(lambda1,cond_r);
    conductivity_imag=table(lambda1,cond_i);
    writetable(conductivity_real)
    writetable(conductivity_imag)
    %refractive index
    n__r=Ef;
    n__r(2:length_p+1,:)=nr';
    n__i=Ef;
    n__i(2:length_p+1,:)=ni';
    N=table(lambda1,n__r);
    K=table(lambda1,n__i);
    writetable(N)
    writetable(K)
    %for specific software------
    %plasmon mode dispersion
    Ksp__r=Ef;
    Ksp__r(2:length_p+1,:)=real(Ksp)';
    Ksp=table(lambda1,Ksp__r);
    writetable(Ksp)
    %for specific software------
    if length(abs(Ef))<2
        ngwa(:,1)=lambda;
        ngwa(:,2)=nr;
```

```
        ngwa1(:,1)=lambda;
        ngwa1(:,2)=ni;
        ngwaboth(:,1)=lambda*10^9;
        ngwaboth(:,2)=nr;
        ngwaboth(:,3)=ni;
        dlmwrite(filename_r,ngwa,'delimiter','\t','newline','PC')
        dlmwrite(filename_i,ngwa1,'delimiter','\t','newline','PC')
        dlmwrite('nk_model.mat',ngwaboth,'delimiter','\t','newline','PC')
        dlmwrite(rsoft_name_r,nr','newline','PC')
        dlmwrite(rsoft_name_i,ni','newline','PC')
    end
    %for specific software end---
end
%output messages-------------
sprintf('The file names are \n %s \n %s \n %s \n %s \n',filename_r,file-
name_i,rsoft_name_r,rsoft_name_i)
sprintf('The Fermi level is %0.2f \n',Ef)
sprintf('The temperature is %0.2f \n',T)
sprintf('The minimum wavelength is %0.2f \n',min(lambda*10^9))
sprintf('The maximum wavelength is %0.2f \n',max(lambda*10^9))
sprintf('The number of wavelength steps is %0.1f \n',length(nr))
if keep_dat==0
    clear all
end
```

12.1.2. Matlab Code: Voltage Dependent Drude Model of ITO

Matlab code that calculates the voltage depended permittivity of ITO:

```
% ********************************************************
% Drude model
% ********************************************************
clc
clear all
% ********************************************************
% Constants
% ********************************************************
h_bar=1.05*10^-34; %J.s
h_plank=6.626*10^-34; %J.s
epsilon_0=8.85*10^-12; %F/m permittivity of vacuum
e=1.6*10^-19; %C electron charge
c = 2.99792458*10^8; %m/s speed of light
me_s=9.109*10^-31; %electron mass in free space kg
me=0.45*me_s; %electron mass in ITO kg
% ********************************************************
% Input values
% ********************************************************
set_=1;%calculates from voltage, 2 from carrier conc, other from omega_p
d_oxide=10*10^-9; %m thickness of diel
epsilon_oxide=25; %permittivity of dielectric
epsilon_ITO=3.34; %permittivity of dITO
A_r=1; %contact area, leave at 1 for capacitance in F/cm^2. otherwise use
value in cm^2
T=300; % Temperature K
epsilon_inf=3.9; %infinate frequency permittivity
omega_p=0; %wavelength range in um
gama_=20; %wavelength range in um
la=0.6:0.005:1.2; %wavelength range in um
V=0:0.005:5; % Voltage V
n_cr=0.5;%:1:5; %carrier density *10^20 cm^3
% ********************************************************
% Carrier concentration in ITO
% ********************************************************
n_ct=n_cr*10^20*(2*pi)^2;%1/cm^3
n_c=(n_ct/10^-6);%convert to 1/m^3
n_c2=(n_c/(2*pi)^2+(epsilon_0*epsilon_oxide*V/(e*d_oxide^2)))*(2*pi)^2;
% ********************************************************
% Layer thickness
% ********************************************************
tTF=((pi^4./(3*n_c)).^(1/6)).*(epsilon_0*epsi-
lon_ITO*h_plank^2/(4*me*e^2*pi^2))^(1/2);
% ********************************************************
% Permittivity and Refractive index
% ********************************************************
if set_==1
    omegap=sqrt(n_c2*e^2/((me*epsilon_0)));
elseif set_==2
    omegap=sqrt(n_c*e^2/((me*epsilon_0)));
else
    lambda_op=omega_p*10^-6; %m
    omegap=2*pi*c./lambda_op;
end
lambda=la*10^-6; %m
omega_=2*pi*c./lambda;
lambda_G=gama_*10^-6; %m
gama=2*pi*c./lambda_G;
```

```
for i=1:1:length(V)
    perm(i,:)=epsilon_inf-omegap(i).^2./(omega_.^2+1i.*gama.*omega_);
end
n=sqrt(perm);
% ********************************************************
% Plot
% ********************************************************
for i=1:length(n_cr)
    sprintf('Thomas-Fermi length= %f nm for n_c= %f
*10^21/cm^3',tTF*10^9,n_ct/10^21)
    sprintf('Nc= %f *10^27 m^-3 ',n_c/10^27)
    sprintf('Nc= %f *10^21 cm^-3 ',n_ct/10^21)

end
    n_take=n_c2*10^-6;

if length(V)<3

    figure
    GraphTitle = ('Permittivity of ITO');
    plot(lambda*10^6,real(perm),lambda*10^6,imag(perm))
    ylabel(['Epsilon'],'FontSize',22,'FontName','Calibri');
    xlabel(['wavelength(',char(181),'m)'],'FontSize',22,'FontName','Cali-
bri');
    title(GraphTitle,'FontSize',20);
    saveas (gcf,GraphTitle,'jpg');

    figure
    GraphTitle = ('Refractive index of ITO');
    plot(lambda*10^6,real(n),lambda*10^6,imag(n))
    ylabel ('n,k','FontSize',20);
    xlabel ('wavelength (um)','FontSize',20);
    title(GraphTitle,'FontSize',20);
    saveas (gcf,GraphTitle,'jpg');
else
    figure
    GraphTitle ='n';
    imagesc ( lambda*10^6,n_c2/10^6,real(n));
    colormap();
    caxis();
    set(gca,'YDir','normal','FontSize',22,'FontName','Calibri');
    ylabel(['N_i (1/cm^3)'],'FontSize',22,'FontName','Calibri');
    xlabel(['wavelength(',char(181),'m)'],'FontSize',22,'FontName','Cali-
bri');
    title(GraphTitle,'FontSize',20);
    imac=colorbar('FontSize',14,'FontName','Calibri','Font-
Weight','bold');
    %set(imac,'YTick',[0,1,2,3,4,5]);
    saveas (gcf,'fig_ref');
    print('n','-dtiff','-r500');

    figure
    GraphTitle ='k';
    %fFigHandle = figure('Position', [100, 100, 700, 700]);
    ima=imagesc ( lambda*10^6,n_c2/10^6,imag(n));
    colormap();
    caxis();
    set(gca,'YDir','normal','FontSize',22,'FontName','Calibri');
    %axis ([-0.35,0.35,0.12,0.64])
    %set(gca,'XTick',[-0.3,-0.15,0,0.15,0.3],'YDir','normal','Font-
Size',20,'FontName','Calibri')
```

```
    ylabel(['N_i (1/cm^3)'],'FontSize',22,'FontName','Calibri');
    xlabel(['wavelength(',char(181),'m)'],'FontSize',22,'FontName','Cali-
bri');
    title(GraphTitle,'FontSize',20);
    imac=colorbar('FontSize',14,'FontName','Calibri','Font-
Weight','bold');
    %set(imac,'YTick',[0,1,2,3,4,5]);
    saveas (gcf,'fig_ref');
    print('k','-dtiff','-r500');

        figure
    GraphTitle ='?r';
    imagesc ( lambda*10^6,n_c2/10^6,real(perm));
    colormap();
    caxis();
    set(gca,'YDir','normal','FontSize',22,'FontName','Calibri');
    ylabel(['N_i (1/cm^3)'],'FontSize',22,'FontName','Calibri');
    xlabel(['wavelength(',char(181),'m)'],'FontSize',22,'FontName','Cali-
bri');
    %title(GraphTitle,'FontSize',20);
    imac=colorbar('FontSize',14,'FontName','Calibri','Font-
Weight','bold');
    %set(imac,'YTick',[0,1,2,3,4,5]);
    saveas (gcf,'er');
    print('n','-dtiff','-r500');

    figure
    GraphTitle ='?i';
    %fFigHandle = figure('Position', [100, 100, 700, 700]);
    ima=imagesc ( lambda*10^6,n_c2/10^6,imag(perm));
    colormap();
    caxis();
    set(gca,'YDir','normal','FontSize',22,'FontName','Calibri');
    %axis ([-0.35,0.35,0.12,0.64])
    %set(gca,'XTick',[-0.3,-0.15,0,0.15,0.3],'YDir','normal','Font-
Size',20,'FontName','Calibri')
    ylabel(['N_i (1/cm^3)'],'FontSize',22,'FontName','Calibri');
    xlabel(['wavelength(',char(181),'m)'],'FontSize',22,'FontName','Cali-
bri');
    %title(GraphTitle,'FontSize',20);
    imac=colorbar('FontSize',14,'FontName','Calibri','Font-
Weight','bold');
    %set(imac,'YTick',[0,1,2,3,4,5]);
    saveas (gcf,'ei');
    print('k','-dtiff','-r500');
end
if set_==1
    figure
    GraphTitle = ('Carrier concentration');
    set(gca,'FontSize',28,'FontName','Calibri');
    plot(V,n_c2/10^6)
    ylabel ('n_c (1/cm^3)','FontSize',28);
    xlabel ('V_G (V)','FontSize',28);
    title(GraphTitle,'FontSize',24);
    saveas (gcf,GraphTitle,'jpg');
end
%clear all
```

12.1.3. Matlab Code: Wood-Rayleigh Anomalies

Matlab code that calculates the angular dependence of Rayleigh anomalies in diffraction gratings:

```
%Diffraciton grating
clc
clear all
%input
a_g=(700)*10^-9; % gratting latice constant in m (Warning! only use 1 or
2 steps if double length(v_f)>1 only give more than one value when
length(theta=1))
n=1;%refractive index
la=0.4:0.001:1; %wavelength range in um
%thetag2=45*pi/180;
%wavelength convert
lambda=la*10^-6; %m
%Rayleigh 2D
i=0;
for int=-1:2:1
    for v_g=-4:1:4
            i=i+1;
            thetar(i,:)=asin(int-lambda/a_g*v_g)/pi*180;
    end
end
%for int=-1:2:1
    %for v_g=-3:1:3
            %i=i+1;
            %thetar(i,:)=asin(int-lambda/(sqrt(a_g^2+a_g^2))*v_g/cos(the-
tag2))/pi*180;
    %end
%end
        figure;
        GraphTitle = ('diffraction dispersion');
        plot(lambda*10^6,thetar)
        xlabel ('Wavelength (um)','FontSize',20);
        ylabel ('angle (degrees)','FontSize',20);
        title(GraphTitle,'FontSize',20);
        saveas (gcf,GraphTitle,'jpg');
k=0;
 for i=1:2:2*length(thetar(:,1)')
    j=i+1;
    k=k+1;
    print(:,i)=lambda';
    print(:,j)=real(thetar(k,:)');
end
```

12.1.4. Matlab code: Salisbury screen

Matlab code that calculates the wavelength of destructive interference in a Salisbury screen for a given spacer width:

```
% ********************************************************
%Testing now:
% ********************************************************
%write
% ********************************************************
% Salisbury screen
% ********************************************************
clc
clear all;

% ********************************************************
% Code options
% ********************************************************
test=1;
set=1;% 1 change ds, 2 change dig, 3 ns
datac=1;%1 enables data save
nig=0;%refractive index of ion gel
ns=1.8;%refractive index of spacer
dig=0;%thickness of ion gel in um
ds=0:0.01:0.462;%thickness of ion gel in um
nn=1:2:6;%order
lrange=1:0.1:2;%wavelength range in um
% ********************************************************
% Output file names
% ********************************************************

if set==1
    nig=0;%refractive index of ion gel
    ns=1.8;%refractive index of spacer
    dig=0;%thickness of ion gel in um
    l=zeros(length(ds),length(nn));
    for i=1:length(ds)
        for j=1:length(nn)
         l(i,j)=((4*ns*ds(i)+4*nig*dig)/nn(j));
        end
    end
        figure;
        GraphTitle = ('Salisbury screen central wavelength 1');
        plot(l,ds)
        xlabel ('Wavelength (um)','FontSize',20);
        ylabel ('Spacer thickness (um)','FontSize',20);
        title(GraphTitle,'FontSize',20);
        saveas (gcf,GraphTitle,'fig');
        %cd('data')
    if datac==1
        data=table(l,ds');
        writetable(data)% save data
    end
elseif set==2
    nig=1.42;%refractive index of ion gel
    ns=1.42;%refractive index of spacer
    ds=0.12;
    l=zeros(length(dig),length(nn));
    for i=1:length(dig)
        for j=1:length(nn)
         l(i,j)=((4*ns*ds+4*nig*dig(i)))/nn(j);
```

```
        end
    end
        figure;
        GraphTitle = ('Salisbury screen central wavelength 2');
        plot(l,dig)
        xlabel ('Wavelength (um)','FontSize',20);
        ylabel ('Ion gel thickness (um)','FontSize',20);
        title(GraphTitle,'FontSize',20);
        saveas (gcf,GraphTitle,'fig');
    if datac==1
        data=table(l,dig');
        writetable(data)% save data
    end
else
        nig=1.42;%refractive index of ion gel
        dig=0.15;%thickness of ion gel in um
        ds=0.12;
        l=zeros(length(ns),length(nn));
    for i=1:length(ns)
        for j=1:length(nn)
         l(i,j)=((4*ns(i)*ds+4*nig*dig))/nn(j);
        end
    end
        figure;
        GraphTitle = ('Salisbury screen central wavelength 3');
        plot(l,ns)
        xlabel ('Wavelength (um)','FontSize',20);
        ylabel ('Spacer refractive index (um)','FontSize',20);
        title(GraphTitle,'FontSize',20);
        saveas (gcf,GraphTitle,'fig');
    if datac==1
        data=table(l,ns');
        writetable(data)% save data
    end
end

if test==5
clear all
nSiO2=1/1.42;
nITO=1/1.8;
thickness_SiO2=0.015;

Thickness_ITO=nITO.*thickness_SiO2/nSiO2;

plot_range=0:0.00625:0.45;
plot_range2=plot_range+Thickness_ITO
end
```

12.1.5. Matlab Code: Data Plotting of Rsoft RCWA Simulation Results

Matlab code used for data plotting of Rsoft simulation results:

```
clc
clear all
%input
variable=-3.5:0.5:6;
wavelength=0.6:0.005:0.9;
toggle_r=2; % for 0 r(0.0), for 1 total reflection, for 2 absorption
cell_number=4; %how naby cells in file
data_01='Voltage_';
data_02='Voltage_';

if toggle_r==0;
    tr=1;
elseif toggle_r==1;
    tr=2;
else
    tr=3;
end

%load
cd('data1')
fid=fopen([data_01 num2str(0) '.dat'],'r');
delete_header =fgetl(fid);
x=fscanf(fid,'%f');
fclose(fid);
absorbance=zeros(max(length(x)/cell_number),1);
wavelength01=zeros(max(length(x)/cell_number),1);
j=1;
for i=1:cell_number:max(length(x))
    wavelength01(j,1)=x(i);
    absorbance(j,1)=x(i+tr);
    j=j+1;
end
for i=1:length(variable)-1;
    fid=fopen([data_01 num2str(i) '.dat'],'r');
    delete_header =fgetl(fid);
    x=fscanf(fid,'%f');
    fclose(fid);
    j=1;
    for k=1:cell_number:max(length(x))
        absorbance(j,i+1)=x(k+tr);
        j=j+1;
    end
end

cd('../')
cd('data_r')
fid2=fopen([data_02 num2str(0) '.dat'],'r');
delete_header2 =fgetl(fid2);
x2=fscanf(fid2,'%f');
fclose(fid2);
absorbance2=zeros(max(length(x2)/cell_number),1);
wavelength02=zeros(max(length(x2)/cell_number),1);
j=1;
for i=1:cell_number:max(length(x2))
    wavelength02(j,1)=x2(i);
    absorbance2(j,1)=x2(i+tr);
    j=j+1;
```

```
end
for i=1:length(variable)-1;
    fid2=fopen([data_02 num2str(i) '.dat'],'r');
    delete_header2 =fgetl(fid2);
    x2=fscanf(fid2,'%f');
    fclose(fid2);
    j=1;
    for k=1:cell_number:max(length(x2))
        absorbance2(j,i+1)=x2(k+tr);
        j=j+1;
    end
end

%calculations
absorbancef=(absorbance)*100;%-absorbance2)*100;
%result
cd('../')
cd('results')
            GraphTitle ='eV-ref';
            fFigHandle = figure('Position', [100, 100, 900, 700]);
            hold on
            imagesc ( wavelength, variable, absorbancef')
            colormap(hot(200))
            caxis([0 100])
            set(gca,'YDir','normal','FontSize',20,'FontName','Calibri');
            ylabel ('variable','FontSize',28,'FontName','Calibri');
            xlabel ('Wavelength (um)','FontSize',28,'FontName','Cali-
bri');
            axis tight
            imac=colorbar('FontSize',14,'FontName','Calibri','Font-
Weight','bold');
            colorbar;
            saveas (gcf,'fig_ref');
            print('ScreenSizeFigure','-dtiff','-r500')


    length_p=length(wavelength);
    wavelength1(2:length_p+1,:)=wavelength';
    ref=zeros(length_p+1,length(variable));
    abs=zeros(length_p+1,length(variable));
    abs(1,:)=variable;
    abs(2:length_p+1,:)=absorbancef;
    abs_eV=table(wavelength1,abs);
    writetable(abs_eV)

    %figure
    %plot(wavelength,absorbancef(:,1),'k',wavelength,absorb-
ancef(:,41),'r',wavelength,absorbancef(:,105),'b',wavelength,absorb-
ancef(:,201),'g')
```

12.1.6. Matlab Code: Data Plotting of Rsoft FDTD Simulation Results

```
clc
clear all
%input
x=-0.35:0.00199:0.35;
y=0:0.001:0.64;
wavelength=1.4:0.0003:2;
data_01='Top_Au_20nm_m2_t442_eden';

%load
cd('data1')
a=load('a6_23_l0_777_m2_t442_eden.dat');
a_f=flip(a');

%result
cd('../')
cd('results')

            GraphTitle ='E - Energy Density';
            %fFigHandle = figure('Position', [100, 100, 700, 700]);
            hold on
            ima=imagesc ( x, y, a_f);
            colormap(hot)
            caxis([0 5])
            axis ([-0.35,0.35,0.12,0.64])
            set(gca,'XTick',[-0.3,-0.15,0,0.15,0.3],'YDir','nor-
mal','FontSize',20,'FontName','Calibri')
            ylabel(['Z(',char(181),'m)'],'FontSize',28,'FontName','Cali-
bri');
            xlabel(['X(',char(181),'m)'],'FontSize',28,'FontName','Cali-
bri');

            imac=colorbar('FontSize',14,'FontName','Calibri','Font-
Weight','bold');
            set(imac,'YTick',[0,1,2,3,4,5]);
            saveas (gcf,'fig_ref');
            print('ScreenSizeFigure','-dtiff','-r500')
            clear all
    %length_p=length(x);
    %x1(2:length_p+1,:)=x';
    %abs=zeros(length_p+1,length(y));
    %abs(1,:)=y;
    %abs(2:length_p+1,:)=a_f';
    %abs_fdtd=table(x1,abs);
    %writetable(abs_fdtd)
```

12.2. Rsoft codes

12.2.1. Rsoft Simulation File: RCWA

```
Angle = 0
Ef = 0.6
ITO = 0
ITO_V = 3
ITO_dox = w_L4
ITO_gama = 1*10^14
ITO_nc = 1.47*10^20
ITO_ncm = ITO_nc/(10^-6)
ITOep_inf = 3.9
ITOep_ox = 25
ITOme = 0.45*9.109*10^-31
ITOnc2 = ITO_ncm+(epsilon_space*ITOep_ox*ITO_V/(e_*(ITO_dox*10^-6)^2))
ITOop = sqrt(ITOnc2*e_^2/((ITOme*epsilon_space)))
ITOopst = sqrt(ITO_ncm*e_^2/((ITOme*epsilon_space)))
N_Air = 1
N_DIEL = 2
N_act = 1
N_diel2 = 0
T = 300
W_AR = 1
W_Pitch = 0.7
Wx1 = 0.6
Wy1 = Wx1*W_AR
Wz1 = Wx1*sin(54.7)^2/sin(70.6)
adder = 0.001
alpha = 0
background_index = 1
boundary_max = W_Pitch/2
boundary_max_y = W_Pitch/2
boundary_min = -W_Pitch/2
boundary_min_y = -W_Pitch/2
c_ = 2.99792458*10^8
cad_aspectratio = 1
cad_aspectratio_x = 1
cad_aspectratio_y = 1
cad_yselect_pos = 0.3
cond_gi = (cond_gia+cond_gib)/(e_^2/h)
cond_gia = (4*Ef)*(e_^2/(4*h))/(h*om*pi)*(1-2*Ef^2/(9*t^2))
cond_gib = -
(1+(h*om)^2/(36*t^2))*e_^2/(4*h)/pi*log(abs(h*om+2*Ef)/abs(h*om-2*Ef))
cond_gr = cond_gra*cond_grb/(e_^2/h)
cond_gra = e_^2/(4*h)*(1+(h*om)^2/(36*t^2))/2
cond_grb = tanh((h*om+2*Ef)/(4*k*T))+tanh((h*om-2*Ef)/(4*k*T))
datapath = ..\..\
delta = index-background_index
dgr = 0.34*10^-9
dimension = 3
domain_max = Wz1+0.39789+w_L1+w_L2+w_L4
domain_min = 0.05
e_ = 1.6*10^-19
eim = 0
epsilon_i = ((cond_gr*(e_^2/h)/(dgr*om))*7.05*10^29)
epsilon_r = (5.5+(-cond_gi*(e_^2/h)/(dgr*om))*7.05*10^29)
epsilon_space = 8.85*10^-12
fdtd_overlap_extend_warning = 0
free_space_wavelength = 0.785
```

```
grid_size = 0.001
grid_size_y = 0.001
h = 6.582*10^-16
height = W_Pitch
iITOperm = ITO_gama*ITOop^2/(om*(om^2+ITO_gama^2))
iITOpermst = ITO_gama*ITOopst^2/(om*(om^2+ITO_gama^2))
index = 3.882
index_display_mode = DISPLAY_CONTOURMAPXZ
index_min = 0.15
k = 8.6*10^-5
k0 = (2*pi)/free_space_wavelength
launch_angle = 0
launch_theta = Angle
material_display_prefix = 0_2
material_display_wmax = 2
material_display_wmin = 0.2
mode_set_setting = 0
om = 2*pi*c_/(free_space_wavelength*10^-6)
rITOperm = ITOep_inf-ITOop^2/(om^2+ITO_gama^2)
rITOpermst = ITOep_inf-ITOopst^2/(om^2+ITO_gama^2)
rcwa_dynamic_plot = 0
rcwa_harmonics_x = 7
rcwa_harmonics_y = 7
rcwa_harmonics_z = 3
rcwa_index_res_x = 0.005
rcwa_index_res_y = 0.005
rcwa_index_res_z = 0.005
rcwa_launch_delta_phase = 0
rcwa_launch_pol = 90
rcwa_material_dispersion = 1
rcwa_output_absorption = 1
rcwa_output_diff_refl = 1
rcwa_output_option = 2
rcwa_output_total_refl = 1
rcwa_reference_plane_dm = 1
rcwa_variation_max = 0.9
rcwa_variation_min = 0.6
rcwa_variation_step = 0.005
sim_area = W_Pitch/10
sim_tool = ST_DIFFRACTMOD
slice_grid_size = 0.001
slice_grid_size_y = 0.001
slice_step_size = 0.001
step_size = 0.0001
structure = STRUCT_CHANNEL
t = 2.7
w_Gr = 0.00034
w_L1 = 0.074
w_L2 = 0.009+0.001-adder
w_L3act = adder
w_L4 = 0.01
w_L5 = 0.02
w_hl_env = (w_L1+w_L2+w_L3act+w_L4+w_L5)*sin(90)*sin(35.3)/sin(54.7)
w_hl_l2 = w_L1*sin(90)*sin(35.3)/sin(54.7)
w_hl_l3 = (w_L2+w_L1)*sin(90)*sin(35.3)/sin(54.7)
w_hl_l4 = (w_L2+w_L1+w_L3act)*sin(90)*sin(35.3)/sin(54.7)
w_hl_l5 = (w_L1+w_L2+w_L3act+w_L4)*sin(90)*sin(35.3)/sin(54.7)
w_xl_env = sqrt((w_L1+w_L2+w_L3act+w_L4+w_L5)^2+w_hl_env^2)
w_xl_l2 = sqrt(w_L1^2+w_hl_l2^2)
w_xl_l3 = sqrt((w_L1+w_L2)^2+w_hl_l3^2)
w_xl_l4 = sqrt((w_L1+w_L2+w_L3act)^2+w_hl_l4^2)
w_xl_l5 = sqrt((w_L1+w_L2+w_L3act+w_L4)^2+w_hl_l5^2)
```

```
w_xr_env = Wx1-2*w_xl_env
w_xr_l2 = Wx1-2*w_xl_l2
w_xr_l3 = Wx1-2*w_xl_l3
w_xr_l4 = Wx1-2*w_xl_l4
w_xr_l5 = Wx1-2*w_xl_l5
wh_env = w_xr_env*sin(54.7)^2/sin(70.6)
wh_env2 = wh_env+w_L2+w_L1+w_L3act+w_L4+w_L5
wh_l2 = w_xr_l2*sin(54.7)^2/sin(70.6)
wh_l22 = wh_l2+w_L1
wh_l3 = w_xr_l3*sin(54.7)^2/sin(70.6)
wh_l3_2 = wh_l3+w_L2+w_L1
wh_l4 = w_xr_l4*sin(54.7)^2/sin(70.6)
wh_l42 = wh_l4+w_L3act+w_L2+w_L1
wh_l5 = w_xr_l5*sin(54.7)^2/sin(70.6)
wh_l52 = wh_l5+w_L2+w_L1+w_L3act+w_L4
width = 1.05
wp_env2 = wh_env2*sin(70.6)/sin(54.7)^2
wp_l22 = wh_l22*sin(70.6)/sin(54.7)^2
wp_l3_2 = wh_l3_2*sin(70.6)/sin(54.7)^2
wp_l42 = wh_l42*sin(70.6)/sin(54.7)^2
wp_l52 = wh_l52*sin(70.6)/sin(54.7)^2


material 1
    name = Active_ITO
    optical
        inputmode = 1
        ni = iITOperm
        nr = rITOperm
    end optical
end material

material 2
    name = Ag
    epsinf = 1
    num_dsp = 6
    delta_1 = 1759.471
    a_1 = 1
    b_1 = 0.243097
    c_1 = 0
    delta_2 = 135.344
    a_2 = 1
    b_2 = 19.68071
    c_2 = 17.07876
    delta_3 = 258.1946
    a_3 = 1
    b_3 = 2.289161
    c_3 = 515.022
    delta_4 = 22.90436
    a_4 = 1
    b_4 = 0.329194
    c_4 = 1718.357
    delta_5 = 1749.06
    a_5 = 1
    b_5 = 4.639097
    c_5 = 2116.092
    delta_6 = 11756.18
    a_6 = 1
    b_6 = 12.25
    c_6 = 10559.42
end material
```

```
material 3
    name = Al
    epsinf = 1
    num_dsp = 5
    delta_1 = 3010.241
    a_1 = 1
    b_1 = 0.238032
    c_1 = 0
    delta_2 = 1306.548
    a_2 = 1
    b_2 = 1.686484
    c_2 = 0.673141
    delta_3 = 287.7859
    a_3 = 1
    b_3 = 1.580129
    c_3 = 61.14635
    delta_4 = 955.4493
    a_4 = 1
    b_4 = 6.842161
    c_4 = 83.84415
    delta_5 = 172.6716
    a_5 = 1
    b_5 = 17.12819
    c_5 = 309.3752
end material

material 4
    name = Au
    epsinf = 1
    num_dsp = 6
    delta_1 = 1589.516
    a_1 = 1
    b_1 = 0.268419
    c_1 = 0
    delta_2 = 50.19525
    a_2 = 1
    b_2 = 1.220548
    c_2 = 4.417455
    delta_3 = 20.91469
    a_3 = 1
    b_3 = 1.747258
    c_3 = 17.66982
    delta_4 = 148.4943
    a_4 = 1
    b_4 = 4.406129
    c_4 = 226.0978
    delta_5 = 1256.973
    a_5 = 1
    b_5 = 12.63
    c_5 = 475.1387
    delta_6 = 9169
    a_6 = 1
    b_6 = 11.21284
    c_6 = 4550.765
end material

material 5
    name = Be
    epsinf = 1
    num_dsp = 5
    delta_1 = 738.1898
    a_1 = 1
```

```
    b_1 = 0.177258
    c_1 = 0
    delta_2 = 272.4272
    a_2 = 1
    b_2 = 8.427355
    c_2 = 0.256493
    delta_3 = 1230.316
    a_3 = 1
    b_3 = 17.19403
    c_3 = 27.31715
    delta_4 = 4657.626
    a_4 = 1
    b_4 = 22.55735
    c_4 = 259.8658
    delta_5 = 1142.437
    a_5 = 1
    b_5 = 9.126258
    c_5 = 543.684
end material

material 6
    name = Cr
    epsinf = 1
    num_dsp = 5
    delta_1 = 497.9688
    a_1 = 1
    b_1 = 0.238032
    c_1 = 0
    delta_2 = 447.5791
    a_2 = 1
    b_2 = 16.07984
    c_2 = 0.375532
    delta_3 = 444.615
    a_3 = 1
    b_3 = 6.609194
    c_3 = 7.562677
    delta_4 = 3405.751
    a_4 = 1
    b_4 = 13.55265
    c_4 = 99.54246
    delta_5 = 2445.382
    a_5 = 1
    b_5 = 6.761129
    c_5 = 1975.014
end material

material 7
    name = Cu
    epsinf = 1
    num_dsp = 5
    delta_1 = 1729.819
    a_1 = 1
    b_1 = 0.15193
    c_1 = 0
    delta_2 = 183.51123
    a_2 = 1
    b_2 = 1.91438
    c_2 = 2.17201
    delta_3 = 312.87161
    a_3 = 1
    b_3 = 5.348129
    c_3 = 224.27381
```

```
    delta_4 = 2175.059429
    a_4 = 1
    b_4 = 16.27229
    c_4 = 720.4895
    delta_5 = 1919.34
    a_5 = 1
    b_5 = 21.8027
    c_5 = 3205.97
end material

material 8
    name = Graphene
    optical
        inputmode = 1
        ni = epsilon_i
        nr = epsilon_r
    end optical
end material

material 9
    name = ITOst
    optical
        inputmode = 1
        ni = iITOpermst
        nr = rITOpermst
    end optical
end material

material 10
    name = Ni
    epsinf = 1
    num_dsp = 5
    delta_1 = 624.07
    a_1 = 1
    b_1 = 0.243097
    c_1 = 0
    delta_2 = 650.72
    a_2 = 1
    b_2 = 22.84603
    c_2 = 0.776559
    delta_3 = 877.598
    a_3 = 1
    b_3 = 6.756065
    c_3 = 8.688041
    delta_4 = 689.077
    a_4 = 1
    b_4 = 11.03052
    c_4 = 65.41627
    delta_5 = 4739.031
    a_5 = 1
    b_5 = 31.86594
    c_5 = 950.9723
end material

material 11
    name = Pd
    epsinf = 1
    num_dsp = 5
    delta_1 = 799.6913
    a_1 = 1
    b_1 = 0.040516
    c_1 = 0
```

```
    delta_2 = 1572.726
    a_2 = 1
    b_2 = 14.94032
    c_2 = 2.895706
    delta_3 = 293.2202
    a_3 = 1
    b_3 = 2.810806
    c_3 = 6.438006
    delta_4 = 1546.07
    a_4 = 1
    b_4 = 23.40313
    c_4 = 70.59415
    delta_5 = 1097.758
    a_5 = 1
    b_5 = 16.38877
    c_5 = 837.7383
end material

material 12
    name = Pt
    epsinf = 1
    num_dsp = 5
    delta_1 = 785.5202
    a_1 = 1
    b_1 = 0.405161
    c_1 = 0
    delta_2 = 450.5536
    a_2 = 1
    b_2 = 2.618355
    c_2 = 15.60505
    delta_3 = 1554.528
    a_3 = 1
    b_3 = 9.308581
    c_3 = 44.28602
    delta_4 = 1290.329
    a_4 = 1
    b_4 = 18.57665
    c_4 = 253.0532
    delta_5 = 8435.496
    a_5 = 1
    b_5 = 43.13448
    c_5 = 2194.146
end material

material 13
    name = Silicon
    epsinf = 1
    num_dsp = 3
    delta_1 = 1396.848
    a_1 = 1
    b_1 = 0
    c_1 = 130.9329
    delta_2 = 0.105884
    a_2 = 1
    b_2 = 0
    c_2 = 34.79037
    delta_3 = 0.055117
    a_3 = 1
    b_3 = 0
    c_3 = 0.035759
end material
```

```
material 14
    name = Ti
    epsinf = 1
    num_dsp = 5
    delta_1 = 201.7403
    a_1 = 1
    b_1 = 0.41529
    c_1 = 0
    delta_2 = 1225.436
    a_2 = 1
    b_2 = 11.52684
    c_2 = 15.48524
    delta_3 = 535.7023
    a_3 = 1
    b_3 = 12.75245
    c_3 = 61.22558
    delta_4 = 254.9016
    a_4 = 1
    b_4 = 8.42229
    c_4 = 161.4646
    delta_5 = 1.36311
    a_5 = 1
    b_5 = 8.923677
    c_5 = 9683.258
end material

material 15
    name = W
    epsinf = 1
    num_dsp = 5
    delta_1 = 923.4344
    a_1 = 1
    b_1 = 0.324129
    c_1 = 0
    delta_2 = 242.0653
    a_2 = 1
    b_2 = 2.684194
    c_2 = 25.85493
    delta_3 = 744.1267
    a_3 = 1
    b_3 = 6.487645
    c_3 = 94.25842
    delta_4 = 3164.78
    a_4 = 1
    b_4 = 16.87497
    c_4 = 328.732
    delta_5 = 11610.17
    a_5 = 1
    b_5 = 29.55652
    c_5 = 1442.005
end material


user_taper 1
    type = UF_EXPRESSION
    expression = Au-thickness*sin(35.3)
    xmin = 1
    xmax = 2
end user_taper

user_taper 2
    type = UF_EXPRESSION
```

```
    expression = w_L1hickness*sin(35.3)
end user_taper

user_taper 16
    type = UF_EXPRESSION
    expression =
end user_taper


segment 1
    priority = 1
    color = 14
    position_taper = TAPER_LINEAR
    begin.x = 0
    begin.z = 0 rel end segment 4
    begin.height = W_Pitch+sim_area
    begin.width = W_Pitch+sim_area
    begin.delta = 1.42-background_index
    begin.alpha = 0
    end.x = 0 rel begin segment 1
    end.y = 0 rel begin segment 1
    end.z = w_L1 rel begin segment 1
    end.height = W_Pitch+sim_area
    end.width = W_Pitch+sim_area
    end.delta = 1.42-background_index
    end.alpha = 0
    mat_name = Au
end segment

segment 2
    priority = 2
    color = 10
    position_taper = TAPER_LINEAR
    begin.x = 0
    begin.z = 0 rel end segment 10
    begin.height = W_Pitch+sim_area
    begin.width = W_Pitch+sim_area
    begin.delta = N_DIEL-background_index
    begin.alpha = 0
    end.x = 0
    end.z = w_L4 rel begin segment 2
    end.height = W_Pitch+sim_area
    end.width = W_Pitch+sim_area
    end.delta = N_DIEL-background_index
    end.alpha = 0
end segment

segment 3
    color = 7
    position_taper = TAPER_LINEAR
    begin.x = 0
    begin.z = 0 rel end segment 1
    begin.height = W_Pitch+sim_area
    begin.width = W_Pitch+sim_area
    begin.delta = 3.5-background_index
    begin.alpha = 0.004
    end.x = 0
    end.z = Wz1+0.74755 rel begin segment 3
    end.height = W_Pitch+sim_area
    end.width = W_Pitch+sim_area
    end.delta = 3.5-background_index
    end.alpha = 0.004
```

```
end segment

segment 4
    priority = 2
    color = 2
    position_taper = TAPER_LINEAR
    begin.x = 0
    begin.z = 0 rel end segment 5
    begin.height = W_Pitch+sim_area
    begin.width = W_Pitch+sim_area
    begin.delta = N_DIEL-background_index
    begin.alpha = 0
    end.x = 0 rel begin segment 4
    end.y = 0 rel begin segment 4
    end.z = w_L2 rel begin segment 4
    end.height = W_Pitch+sim_area
    end.width = W_Pitch+sim_area
    end.delta = N_DIEL-background_index
    end.alpha = 0
    mat_name = ITOst
end segment

segment 5
    priority = 5
    color = 12
    position_taper = TAPER_LINEAR
    begin.x = 0
    begin.z = 0 rel end segment 2
    begin.height = W_Pitch+sim_area
    begin.width = W_Pitch+sim_area
    begin.delta = N_act-background_index
    begin.alpha = 0
    end.x = 0
    end.z = w_L3act rel begin segment 5
    end.height = W_Pitch+sim_area
    end.width = W_Pitch+sim_area
    end.delta = N_act-background_index
    end.alpha = 0
    mat_name = Active_ITO
end segment

segment 6
    priority = 1
    color = 14
    width_taper = TAPER_LINEAR
    height_taper = TAPER_LINEAR
    arc_type = ARC_SBEND
    begin.x = 0
    begin.z = 0 rel end segment 1
    begin.height = Wy1
    begin.width = Wx1
    begin.delta = N_Air-background_index
    end.x = 0
    end.z = Wz1 rel begin segment 6
    end.height = Wy1-Wx1
    end.width = 0
    end.delta = N_Air-background_index
    mat_name = Au
end segment

segment 7
    priority = 2
```

```
    color = 2
    width_taper = TAPER_LINEAR
    height_taper = TAPER_LINEAR
    arc_type = ARC_SBEND
    begin.x = 0
    begin.z = 0 rel end segment 4
    begin.height = wp_l22*W_AR
    begin.width = wp_l22
    begin.delta = N_DIEL-background_index
    begin.alpha = 0
    end.x = 0
    end.z = wh_l22 rel begin segment 7
    end.height = wp_l22*W_AR-wp_l22
    end.width = 0
    end.delta = N_DIEL-background_index
    end.alpha = 0
    mat_name = ITOst
end segment

segment 8
    priority = 3
    color = 12
    width_taper = TAPER_LINEAR
    height_taper = TAPER_LINEAR
    arc_type = ARC_SBEND
    begin.x = 0
    begin.z = 0 rel end segment 5
    begin.height = wp_l3_2*W_AR
    begin.width = wp_l3_2
    begin.delta = N_act-background_index
    begin.alpha = 0
    end.x = 0
    end.z = wh_l3_2 rel begin segment 8
    end.height = wp_l3_2*W_AR-wp_l3_2
    end.width = 0
    end.delta = N_act-background_index
    end.alpha = 0
    mat_name = Active_ITO
end segment

segment 9
    priority = 6
    color = 10
    width_taper = TAPER_LINEAR
    height_taper = TAPER_LINEAR
    arc_type = ARC_SBEND
    begin.x = 0
    begin.z = 0 rel end segment 2
    begin.height = wp_l42*W_AR
    begin.width = wp_l42
    begin.delta = N_DIEL-background_index
    begin.alpha = 0
    end.x = 0
    end.z = wh_l42 rel begin segment 9
    end.height = wp_l42*W_AR-wp_l42
    end.width = 0
    end.delta = N_DIEL-background_index
    end.alpha = 0
end segment

segment 10
    priority = 2
```

```
    color = 14
    position_taper = TAPER_LINEAR
    begin.x = 0
    begin.z = 0.1
    begin.height = W_Pitch+sim_area
    begin.width = W_Pitch+sim_area
    begin.delta = N_diel2-background_index
    begin.alpha = 0
    end.x = 0
    end.z = w_L5 rel begin segment 10
    end.height = W_Pitch+sim_area
    end.width = W_Pitch+sim_area
    end.delta = N_diel2-background_index
    end.alpha = 0
    mat_name = Au
end segment

segment 11
    priority = 7
    color = 14
    width_taper = TAPER_LINEAR
    height_taper = TAPER_LINEAR
    arc_type = ARC_SBEND
    begin.x = 0
    begin.z = 0 rel end segment 10
    begin.height = wp_l52*W_AR
    begin.width = wp_l52
    begin.delta = N_Air-background_index
    end.x = 0
    end.z = wh_l52 rel begin segment 11
    end.height = wp_l52*W_AR-wp_l52
    end.width = 0
    end.delta = N_Air-background_index
    mat_name = Au
end segment

segment 12
    priority = 8
    color = 9
    width_taper = TAPER_LINEAR
    height_taper = TAPER_LINEAR
    arc_type = ARC_SBEND
    begin.x = 0
    begin.z = 0 rel begin segment 10
    begin.height = wp_env2*W_AR
    begin.width = wp_env2
    begin.delta = N_Air-background_index
    end.x = 0
    end.z = wh_env2 rel begin segment 12
    end.height = wp_env2*W_AR-wp_env2
    end.width = 0
    end.delta = N_Air-background_index
end segment




text_block 1
    name = MOST
    text =
RSScanOptFormat1
```

```
[MODE]
SCAN

PREFIX active_w
PREFIX_STYLE 0
CLUSTER 0 0 0 0 1 ""
USERSIM_CALLSTYLE 0 0

[SIMULATION]
SIMTOOL ST_DIFFRACTMOD
WINDOW_SIZE 2
VERBOSITY 0
PRE_WHOLE_CMD
POST_WHOLE_CMD
PRE_CMD
POST_CMD
PREPOST_ACTIVE 0
PREPOST_ERRCODES 0
EXTRA_DATAINDEX_CMDS

[ALGORITHM]
NAME root_1d_brent
MAXSTEPS DEFAULT  1000
CONVERGENCE DEFAULT  1.0e-7

[INDEPENDENT_VARIABLES_SCAN]
IV_Declarations
SYMTAB_SCALAR Ef N :  IV_LINEAR_STEPS : 0.3 : 0.65 : 0.00175 : 201 :  :
:
SYMTAB_SCALAR Angle N :  IV_LINEAR_STEPS : 0 : 60 : 1 : 61 :  :  :
SYMTAB_SCALAR W_AR N :  IV_LINEAR_STEPS : 1 : 2 : 0.005 : 201 :  :  :
SYMTAB_SCALAR W_Pitch N :  IV_LINEAR_STEPS : 0.65 : 2 : 0.025 : 55 :  :
:
SYMTAB_SCALAR Wx1 N :  IV_LINEAR_STEPS : 0.2 : 0.7 : 0.01 : 51 :  :  :
SYMTAB_SCALAR w_L1 N :  IV_LINEAR_STEPS : 0 : 0.4 : 0.002 : 201 :  :  :
SYMTAB_SCALAR w_L4 N :  IV_LINEAR_STEPS : 0 : 3.5 : 0.0175 : 201 :  :  :
SYMTAB_SCALAR w_L2 N :  IV_LINEAR_STEPS : 0.005 : 0.3 : 0.005 : 60 :  :
:
SYMTAB_SCALAR ITO N :  IV_LINEAR_STEPS : 1 : 2 : 0.005 : 201 :  :  :
SYMTAB_SCALAR ITO_V N :  IV_LINEAR_STEPS : -3.5 : 3.5 : 0.5 : 15 :  :  :
SYMTAB_SCALAR adder Y :  IV_LINEAR_STEPS : 0 : 0.0015 : 5e-005 : 31 :  :
:

[INDEPENDENT_VARIABLES_OPT]
IV_Declarations

IV_InitialValues

[MEASUREMENTS:ST_DIFFRACTMOD]
STANDARD dm_de_r_0_0_vs_wavelength Y
STANDARD dm_de_r_total_vs_wavelength Y

[METRICS]

    end text
end text_block
```

12.2.2. Rsoft Simulation File: FDTD

```
Angle = 0
Ef = 0.6
ITO = 0
ITO_V = 3
ITO_dox = w_L4
ITO_gama = 1*10^14
ITO_nc = 1.47*10^20
ITO_ncm = ITO_nc/(10^-6)
ITOep_inf = 3.9
ITOep_ox = 25
ITOme = 0.45*9.109*10^-31
ITOnc2 = ITO_ncm+(epsilon_space*ITOep_ox*ITO_V/(e_*(ITO_dox*10^-6)^2))
ITOop = sqrt(ITOnc2*e_^2/((ITOme*epsilon_space)))
ITOopst = sqrt(ITO_ncm*e_^2/((ITOme*epsilon_space)))
N_Air = 1
N_DIEL = 2
N_act = 1
N_diel2 = 0
T = 300
W_AR = 1
W_Pitch = 0.7
Wx1 = 0.6
Wy1 = Wx1*W_AR
Wz1 = Wx1*sin(54.7)^2/sin(70.6)
alpha = 0
background_index = 1
boundary_max = W_Pitch/2
boundary_max_y = W_Pitch/2
boundary_min = -W_Pitch/2
boundary_min_y = -W_Pitch/2
c_ = 2.99792458*10^8
cad_aspectratio = 1
cad_aspectratio_x = 1
cad_aspectratio_y = 1
cad_ind_file = v1745_l0775.ind
cad_yselect_pos = 0.3
color_shades = 128
cond_gi = (cond_gia+cond_gib)/(e_^2/h)
cond_gia = (4*Ef)*(e_^2/(4*h))/(h*om*pi)*(1-2*Ef^2/(9*t^2))
cond_gib = -
(1+(h*om)^2/(36*t^2))*e_^2/(4*h)/pi*log(abs(h*om+2*Ef)/abs(h*om-2*Ef))
cond_gr = cond_gra*cond_grb/(e_^2/h)
cond_gra = e_^2/(4*h)*(1+(h*om)^2/(36*t^2))/2
cond_grb = tanh((h*om+2*Ef)/(4*k*T))+tanh((h*om-2*Ef)/(4*k*T))
datapath = ..\..\
delta = index-background_index
dgr = 0.34*10^-9
dimension = 2
domain_max = 5
domain_min = 0
e_ = 1.6*10^-19
eim = 0
epsilon_i = ((cond_gr*(e_^2/h)/(dgr*om))*7.05*10^29)
epsilon_r = (5.5+(-cond_gi*(e_^2/h)/(dgr*om))*7.05*10^29)
epsilon_space = 8.85*10^-12
fdtd_bc_x = FDTD_BC_PERIODIC
fdtd_bc_y = FDTD_BC_PERIODIC
fdtd_dispersion = 1
fdtd_field_output = 1
```

```
fdtd_mpi_cut_direction = 3
fdtd_overlap_extend_warning = 0
fdtd_simmemcheck_warning = 0
fdtd_slice_output = 1
fdtd_stop_time = 4.45
fdtd_time_step = 0.0007008928571
fdtd_time_step_auto = 1
free_space_wavelength = 0.785
grid_nonuniform = 1
grid_size = 0.001
grid_size_y = 0.002
h = 6.582*10^-16
height = W_Pitch
iITOperm = ITO_gama*ITOop^2/(om*(om^2+ITO_gama^2))
iITOpermst = ITO_gama*ITOopst^2/(om*(om^2+ITO_gama^2))
index = 3.882
index_display_mode = DISPLAY_CONTOURMAPXZ
index_min = 0.15
k = 8.6*10^-5
k0 = (2*pi)/free_space_wavelength
lambda = free_space_wavelength
launch_angle = 0
launch_position_z = 0.02
launch_theta = Angle
launch_type = LAUNCH_RECTANGLE
material_display_prefix = 0_2
material_display_wmax = 2
material_display_wmin = 0.2
mode_set_setting = 0
om = 2*pi*c_/(free_space_wavelength*10^-6)
polarization = 1
rITOperm = ITOep_inf-ITOop^2/(om^2+ITO_gama^2)
rITOpermst = ITOep_inf-ITOopst^2/(om^2+ITO_gama^2)
rcwa_dynamic_plot = 0
rcwa_harmonics_x = 7
rcwa_harmonics_y = 7
rcwa_harmonics_z = 3
rcwa_index_res_x = 0.005
rcwa_index_res_y = 0.005
rcwa_index_res_z = 0.005
rcwa_launch_delta_phase = 0
rcwa_launch_pol = 90
rcwa_material_dispersion = 1
rcwa_output_absorption = 1
rcwa_output_diff_refl = 1
rcwa_output_option = 2
rcwa_output_total_refl = 1
rcwa_reference_plane_dm = 1
rcwa_variation_max = 1
rcwa_variation_min = 0.5
rcwa_variation_step = 0.005
sim_area = W_Pitch/10
sim_tool = ST_FULLWAVE
slice_grid_size = 0.001
slice_grid_size_y = 0.001
slice_step_size = 0.001
step_size = 0.001
structure = STRUCT_CHANNEL
t = 2.7
w_Gr = 0.00034
w_L1 = 0.074
w_L2 = 0.009
```

```
w_L3act = 0.001
w_L4 = 0.01
w_L5 = 0.02
w_hl_env = (w_L1+w_L2+w_L3act+w_L4+w_L5)*sin(90)*sin(35.3)/sin(54.7)
w_hl_l2 = w_L1*sin(90)*sin(35.3)/sin(54.7)
w_hl_l3 = (w_L2+w_L1)*sin(90)*sin(35.3)/sin(54.7)
w_hl_l4 = (w_L2+w_L1+w_L3act)*sin(90)*sin(35.3)/sin(54.7)
w_hl_l5 = (w_L1+w_L2+w_L3act+w_L4)*sin(90)*sin(35.3)/sin(54.7)
w_xl_env = sqrt((w_L1+w_L2+w_L3act+w_L4+w_L5)^2+w_hl_env^2)
w_xl_l2 = sqrt(w_L1^2+w_hl_l2^2)
w_xl_l3 = sqrt((w_L1+w_L2)^2+w_hl_l3^2)
w_xl_l4 = sqrt((w_L1+w_L2+w_L3act)^2+w_hl_l4^2)
w_xl_l5 = sqrt((w_L1+w_L2+w_L3act+w_L4)^2+w_hl_l5^2)
w_xr_env = Wx1-2*w_xl_env
w_xr_l2 = Wx1-2*w_xl_l2
w_xr_l3 = Wx1-2*w_xl_l3
w_xr_l4 = Wx1-2*w_xl_l4
w_xr_l5 = Wx1-2*w_xl_l5
wh_env = w_xr_env*sin(54.7)^2/sin(70.6)
wh_env2 = wh_env+w_L2+w_L1+w_L3act+w_L4+w_L5
wh_l2 = w_xr_l2*sin(54.7)^2/sin(70.6)
wh_l22 = wh_l2+w_L1
wh_l3 = w_xr_l3*sin(54.7)^2/sin(70.6)
wh_l3_2 = wh_l3+w_L2+w_L1
wh_l4 = w_xr_l4*sin(54.7)^2/sin(70.6)
wh_l42 = wh_l4+w_L3act+w_L2+w_L1
wh_l5 = w_xr_l5*sin(54.7)^2/sin(70.6)
wh_l52 = wh_l5+w_L2+w_L1+w_L3act+w_L4
width = 1.05
wp_env2 = wh_env2*sin(70.6)/sin(54.7)^2
wp_l22 = wh_l22*sin(70.6)/sin(54.7)^2
wp_l3_2 = wh_l3_2*sin(70.6)/sin(54.7)^2
wp_l42 = wh_l42*sin(70.6)/sin(54.7)^2
wp_l52 = wh_l52*sin(70.6)/sin(54.7)^2


material 1
    name = Active_ITO
    optical
        inputmode = 1
        ni = iITOperm
        nr = rITOperm
    end optical
end material

material 2
    name = Ag
    epsinf = 1
    num_dsp = 6
    delta_1 = 1759.471
    a_1 = 1
    b_1 = 0.243097
    c_1 = 0
    delta_2 = 135.344
    a_2 = 1
    b_2 = 19.68071
    c_2 = 17.07876
    delta_3 = 258.1946
    a_3 = 1
    b_3 = 2.289161
    c_3 = 515.022
    delta_4 = 22.90436
```

```
    a_4 = 1
    b_4 = 0.329194
    c_4 = 1718.357
    delta_5 = 1749.06
    a_5 = 1
    b_5 = 4.639097
    c_5 = 2116.092
    delta_6 = 11756.18
    a_6 = 1
    b_6 = 12.25
    c_6 = 10559.42
end material

material 3
    name = Al
    epsinf = 1
    num_dsp = 5
    delta_1 = 3010.241
    a_1 = 1
    b_1 = 0.238032
    c_1 = 0
    delta_2 = 1306.548
    a_2 = 1
    b_2 = 1.686484
    c_2 = 0.673141
    delta_3 = 287.7859
    a_3 = 1
    b_3 = 1.580129
    c_3 = 61.14635
    delta_4 = 955.4493
    a_4 = 1
    b_4 = 6.842161
    c_4 = 83.84415
    delta_5 = 172.6716
    a_5 = 1
    b_5 = 17.12819
    c_5 = 309.3752
end material

material 4
    name = Au
    epsinf = 1
    num_dsp = 6
    delta_1 = 1589.516
    a_1 = 1
    b_1 = 0.268419
    c_1 = 0
    delta_2 = 50.19525
    a_2 = 1
    b_2 = 1.220548
    c_2 = 4.417455
    delta_3 = 20.91469
    a_3 = 1
    b_3 = 1.747258
    c_3 = 17.66982
    delta_4 = 148.4943
    a_4 = 1
    b_4 = 4.406129
    c_4 = 226.0978
    delta_5 = 1256.973
    a_5 = 1
    b_5 = 12.63
```

```
    c_5 = 475.1387
    delta_6 = 9169
    a_6 = 1
    b_6 = 11.21284
    c_6 = 4550.765
end material

material 5
    name = Be
    epsinf = 1
    num_dsp = 5
    delta_1 = 738.1898
    a_1 = 1
    b_1 = 0.177258
    c_1 = 0
    delta_2 = 272.4272
    a_2 = 1
    b_2 = 8.427355
    c_2 = 0.256493
    delta_3 = 1230.316
    a_3 = 1
    b_3 = 17.19403
    c_3 = 27.31715
    delta_4 = 4657.626
    a_4 = 1
    b_4 = 22.55735
    c_4 = 259.8658
    delta_5 = 1142.437
    a_5 = 1
    b_5 = 9.126258
    c_5 = 543.684
end material

material 6
    name = Cr
    epsinf = 1
    num_dsp = 5
    delta_1 = 497.9688
    a_1 = 1
    b_1 = 0.238032
    c_1 = 0
    delta_2 = 447.5791
    a_2 = 1
    b_2 = 16.07984
    c_2 = 0.375532
    delta_3 = 444.615
    a_3 = 1
    b_3 = 6.609194
    c_3 = 7.562677
    delta_4 = 3405.751
    a_4 = 1
    b_4 = 13.55265
    c_4 = 99.54246
    delta_5 = 2445.382
    a_5 = 1
    b_5 = 6.761129
    c_5 = 1975.014
end material

material 7
    name = Cu
    epsinf = 1
```

```
    num_dsp = 5
    delta_1 = 1729.819
    a_1 = 1
    b_1 = 0.15193
    c_1 = 0
    delta_2 = 183.51123
    a_2 = 1
    b_2 = 1.91438
    c_2 = 2.17201
    delta_3 = 312.87161
    a_3 = 1
    b_3 = 5.348129
    c_3 = 224.27381
    delta_4 = 2175.059429
    a_4 = 1
    b_4 = 16.27229
    c_4 = 720.4895
    delta_5 = 1919.34
    a_5 = 1
    b_5 = 21.8027
    c_5 = 3205.97
end material

material 8
    name = Graphene
    optical
        inputmode = 1
        ni = epsilon_i
        nr = epsilon_r
    end optical
end material

material 9
    name = ITOst
    optical
        inputmode = 1
        ni = iITOpermst
        nr = rITOpermst
    end optical
end material

material 10
    name = Ni
    epsinf = 1
    num_dsp = 5
    delta_1 = 624.07
    a_1 = 1
    b_1 = 0.243097
    c_1 = 0
    delta_2 = 650.72
    a_2 = 1
    b_2 = 22.84603
    c_2 = 0.776559
    delta_3 = 877.598
    a_3 = 1
    b_3 = 6.756065
    c_3 = 8.688041
    delta_4 = 689.077
    a_4 = 1
    b_4 = 11.03052
    c_4 = 65.41627
    delta_5 = 4739.031
```

```
    a_5 = 1
    b_5 = 31.86594
    c_5 = 950.9723
end material

material 11
    name = Pd
    epsinf = 1
    num_dsp = 5
    delta_1 = 799.6913
    a_1 = 1
    b_1 = 0.040516
    c_1 = 0
    delta_2 = 1572.726
    a_2 = 1
    b_2 = 14.94032
    c_2 = 2.895706
    delta_3 = 293.2202
    a_3 = 1
    b_3 = 2.810806
    c_3 = 6.438006
    delta_4 = 1546.07
    a_4 = 1
    b_4 = 23.40313
    c_4 = 70.59415
    delta_5 = 1097.758
    a_5 = 1
    b_5 = 16.38877
    c_5 = 837.7383
end material

material 12
    name = Pt
    epsinf = 1
    num_dsp = 5
    delta_1 = 785.5202
    a_1 = 1
    b_1 = 0.405161
    c_1 = 0
    delta_2 = 450.5536
    a_2 = 1
    b_2 = 2.618355
    c_2 = 15.60505
    delta_3 = 1554.528
    a_3 = 1
    b_3 = 9.308581
    c_3 = 44.28602
    delta_4 = 1290.329
    a_4 = 1
    b_4 = 18.57665
    c_4 = 253.0532
    delta_5 = 8435.496
    a_5 = 1
    b_5 = 43.13448
    c_5 = 2194.146
end material

material 13
    name = Silicon
    epsinf = 1
    num_dsp = 3
    delta_1 = 1396.848
```

```
    a_1 = 1
    b_1 = 0
    c_1 = 130.9329
    delta_2 = 0.105884
    a_2 = 1
    b_2 = 0
    c_2 = 34.79037
    delta_3 = 0.055117
    a_3 = 1
    b_3 = 0
    c_3 = 0.035759
end material

material 14
    name = Ti
    epsinf = 1
    num_dsp = 5
    delta_1 = 201.7403
    a_1 = 1
    b_1 = 0.41529
    c_1 = 0
    delta_2 = 1225.436
    a_2 = 1
    b_2 = 11.52684
    c_2 = 15.48524
    delta_3 = 535.7023
    a_3 = 1
    b_3 = 12.75245
    c_3 = 61.22558
    delta_4 = 254.9016
    a_4 = 1
    b_4 = 8.42229
    c_4 = 161.4646
    delta_5 = 1.36311
    a_5 = 1
    b_5 = 8.923677
    c_5 = 9683.258
end material

material 15
    name = W
    epsinf = 1
    num_dsp = 5
    delta_1 = 923.4344
    a_1 = 1
    b_1 = 0.324129
    c_1 = 0
    delta_2 = 242.0653
    a_2 = 1
    b_2 = 2.684194
    c_2 = 25.85493
    delta_3 = 744.1267
    a_3 = 1
    b_3 = 6.487645
    c_3 = 94.25842
    delta_4 = 3164.78
    a_4 = 1
    b_4 = 16.87497
    c_4 = 328.732
    delta_5 = 11610.17
    a_5 = 1
    b_5 = 29.55652
```

```
    c_5 = 1442.005
end material


user_taper 1
    type = UF_EXPRESSION
    expression = Au-thickness*sin(35.3)
    xmin = 1
    xmax = 2
end user_taper

user_taper 2
    type = UF_EXPRESSION
    expression = w_L1hickness*sin(35.3)
end user_taper

user_taper 16
    type = UF_EXPRESSION
    expression =
end user_taper


time_monitor 1
    profile_type = PROF_INACTIVE
    color = 2
    type = TIMEMON_EXTENDED
    fieldoutputmask = 8449
    length = 0.64
    begin.x = 0
    begin.z = 0.35
    begin.width = W_Pitch
end time_monitor

segment 2
    priority = 1
    color = 14
    position_taper = TAPER_LINEAR
    begin.x = 0
    begin.z = 0 rel end segment 5
    begin.height = W_Pitch+sim_area
    begin.width = W_Pitch+sim_area
    begin.delta = 1.42-background_index
    begin.alpha = 0
    end.x = 0 rel begin segment 2
    end.y = 0 rel begin segment 2
    end.z = w_L1 rel begin segment 2
    end.height = W_Pitch+sim_area
    end.width = W_Pitch+sim_area
    end.delta = 1.42-background_index
    end.alpha = 0
    mat_name = Au
end segment

segment 3
    priority = 2
    color = 10
    position_taper = TAPER_LINEAR
    begin.x = 0
    begin.z = 0 rel end segment 11
    begin.height = W_Pitch+sim_area
    begin.width = W_Pitch+sim_area
    begin.delta = N_DIEL-background_index
```

```
    begin.alpha = 0
    end.x = 0
    end.z = w_L4 rel begin segment 3
    end.height = W_Pitch+sim_area
    end.width = W_Pitch+sim_area
    end.delta = N_DIEL-background_index
    end.alpha = 0
end segment

segment 4
    color = 7
    position_taper = TAPER_LINEAR
    begin.x = 0
    begin.z = 0 rel end segment 2
    begin.height = W_Pitch+sim_area
    begin.width = W_Pitch+sim_area
    begin.delta = 3.5-background_index
    begin.alpha = 0.004
    end.x = 0
    end.z = 6 rel begin segment 4
    end.height = W_Pitch+sim_area
    end.width = W_Pitch+sim_area
    end.delta = 3.5-background_index
    end.alpha = 0.004
end segment

segment 5
    priority = 2
    color = 2
    position_taper = TAPER_LINEAR
    begin.x = 0
    begin.z = 0 rel end segment 6
    begin.height = W_Pitch+sim_area
    begin.width = W_Pitch+sim_area
    begin.delta = N_DIEL-background_index
    begin.alpha = 0
    end.x = 0 rel begin segment 5
    end.y = 0 rel begin segment 5
    end.z = w_L2 rel begin segment 5
    end.height = W_Pitch+sim_area
    end.width = W_Pitch+sim_area
    end.delta = N_DIEL-background_index
    end.alpha = 0
    mat_name = ITOst
end segment

segment 6
    priority = 5
    color = 12
    position_taper = TAPER_LINEAR
    begin.x = 0
    begin.z = 0 rel end segment 3
    begin.height = W_Pitch+sim_area
    begin.width = W_Pitch+sim_area
    begin.delta = N_act-background_index
    begin.alpha = 0
    end.x = 0
    end.z = w_L3act rel begin segment 6
    end.height = W_Pitch+sim_area
    end.width = W_Pitch+sim_area
    end.delta = N_act-background_index
    end.alpha = 0
```

```
    mat_name = Active_ITO
end segment

segment 7
    priority = 1
    color = 14
    width_taper = TAPER_LINEAR
    height_taper = TAPER_LINEAR
    arc_type = ARC_SBEND
    begin.x = 0
    begin.z = 0 rel end segment 2
    begin.height = Wy1
    begin.width = Wx1
    begin.delta = N_Air-background_index
    end.x = 0
    end.z = Wz1 rel begin segment 7
    end.height = Wy1-Wx1
    end.width = 0
    end.delta = N_Air-background_index
    mat_name = Au
end segment

segment 8
    priority = 2
    color = 2
    width_taper = TAPER_LINEAR
    height_taper = TAPER_LINEAR
    arc_type = ARC_SBEND
    begin.x = 0
    begin.z = 0 rel end segment 5
    begin.height = wp_l22*W_AR
    begin.width = wp_l22
    begin.delta = N_DIEL-background_index
    begin.alpha = 0
    end.x = 0
    end.z = wh_l22 rel begin segment 8
    end.height = wp_l22*W_AR-wp_l22
    end.width = 0
    end.delta = N_DIEL-background_index
    end.alpha = 0
    mat_name = ITOst
end segment

segment 9
    priority = 3
    color = 12
    width_taper = TAPER_LINEAR
    height_taper = TAPER_LINEAR
    arc_type = ARC_SBEND
    begin.x = 0
    begin.z = 0 rel end segment 6
    begin.height = wp_l3_2*W_AR
    begin.width = wp_l3_2
    begin.delta = N_act-background_index
    begin.alpha = 0
    end.x = 0
    end.z = wh_l3_2 rel begin segment 9
    end.height = wp_l3_2*W_AR-wp_l3_2
    end.width = 0
    end.delta = N_act-background_index
    end.alpha = 0
    mat_name = Active_ITO
```

```
end segment

segment 10
    priority = 6
    color = 10
    width_taper = TAPER_LINEAR
    height_taper = TAPER_LINEAR
    arc_type = ARC_SBEND
    begin.x = 0
    begin.z = 0 rel end segment 3
    begin.height = wp_l42*W_AR
    begin.width = wp_l42
    begin.delta = N_DIEL-background_index
    begin.alpha = 0
    end.x = 0
    end.z = wh_l42 rel begin segment 10
    end.height = wp_l42*W_AR-wp_l42
    end.width = 0
    end.delta = N_DIEL-background_index
    end.alpha = 0
end segment

segment 11
    priority = 2
    color = 14
    position_taper = TAPER_LINEAR
    begin.x = 0
    begin.z = 0.1
    begin.height = W_Pitch+sim_area
    begin.width = W_Pitch+sim_area
    begin.delta = N_diel2-background_index
    begin.alpha = 0
    end.x = 0
    end.z = w_L5 rel begin segment 11
    end.height = W_Pitch+sim_area
    end.width = W_Pitch+sim_area
    end.delta = N_diel2-background_index
    end.alpha = 0
    mat_name = Au
end segment

segment 12
    priority = 7
    color = 14
    width_taper = TAPER_LINEAR
    height_taper = TAPER_LINEAR
    arc_type = ARC_SBEND
    begin.x = 0
    begin.z = 0 rel end segment 11
    begin.height = wp_l52*W_AR
    begin.width = wp_l52
    begin.delta = N_Air-background_index
    end.x = 0
    end.z = wh_l52 rel begin segment 12
    end.height = wp_l52*W_AR-wp_l52
    end.width = 0
    end.delta = N_Air-background_index
    mat_name = Au
end segment

segment 13
    priority = 8
```

```
    color = 9
    width_taper = TAPER_LINEAR
    height_taper = TAPER_LINEAR
    arc_type = ARC_SBEND
    begin.x = 0
    begin.z = 0 rel begin segment 11
    begin.height = wp_env2*W_AR
    begin.width = wp_env2
    begin.delta = N_Air-background_index
    end.x = 0
    end.z = wh_env2 rel begin segment 13
    end.height = wp_env2*W_AR-wp_env2
    end.width = 0
    end.delta = N_Air-background_index
end segment



launch_field 1
    launch_pathway = 0
    launch_type = LAUNCH_RECTANGLE
    launch_angle = 0
    launch_theta = Angle
    launch_position_z = 0.02
    fdtd_wavelength = 0.772
    fdtd_shutoff_time = 6
end launch_field


text_block 1
    name = MOST
    text =
RSScanOptFormat1

[MODE]
SCAN

PREFIX Voltage
PREFIX_STYLE 0
CLUSTER 0 0 0 0 1 ""
USERSIM_CALLSTYLE 0 0

[SIMULATION]
SIMTOOL ST_DIFFRACTMOD
WINDOW_SIZE 2
VERBOSITY 0
PRE_WHOLE_CMD
POST_WHOLE_CMD
PRE_CMD
POST_CMD
PREPOST_ACTIVE 0
PREPOST_ERRCODES 0
EXTRA_DATAINDEX_CMDS

[ALGORITHM]
NAME root_1d_brent
MAXSTEPS DEFAULT  1000
CONVERGENCE DEFAULT  1.0e-7

[INDEPENDENT_VARIABLES_SCAN]
IV_Declarations
```

```
SYMTAB_SCALAR Ef N :  IV_LINEAR_STEPS : 0.3 : 0.65 : 0.00175 : 201 :  :
:
SYMTAB_SCALAR Angle N :  IV_LINEAR_STEPS : 0 : 60 : 0.75 : 81 :  :  :
SYMTAB_SCALAR W_AR N :  IV_LINEAR_STEPS : 1 : 2 : 0.005 : 201 :  :  :
SYMTAB_SCALAR W_Pitch N :  IV_LINEAR_STEPS : 0.65 : 0.75 : 0.005 : 21 :
:  :
SYMTAB_SCALAR Wx1 N :  IV_LINEAR_STEPS : 0.55 : 0.65 : 0.005 : 21 :  :  :
SYMTAB_SCALAR w_L1 N :  IV_LINEAR_STEPS : 0 : 0.4 : 0.002 : 201 :  :  :
SYMTAB_SCALAR w_L4 N :  IV_LINEAR_STEPS : 0 : 3.5 : 0.0175 : 201 :  :  :
SYMTAB_SCALAR w_L2 N :  IV_LINEAR_STEPS : 0 : 0.45 : 0.00625 : 73 :  :  :
SYMTAB_SCALAR ITO N :  IV_LINEAR_STEPS : 1 : 2 : 0.005 : 201 :  :  :
SYMTAB_SCALAR ITO_V Y :  IV_LINEAR_STEPS : -3.5 : 3.5 : 0.5 : 15 :  :  :

[INDEPENDENT_VARIABLES_OPT]
IV_Declarations

IV_InitialValues

[MEASUREMENTS:ST_DIFFRACTMOD]
STANDARD dm_de_r_0_0_vs_wavelength Y
STANDARD dm_de_r_total_vs_wavelength Y

[METRICS]

    end text
end text_block
```

12.3. Simulation results

12.3.1. Comparison of RCWA Simulations with Experimental Results

Rigorous coupled wave-analysis is a highly efficient semi-analytical method for simulating electromagnetic behaviour of periodic structures. In this method Fourier space calculations are used and electromagnetic fields as well as devices are represented by a sum of harmonic functions. RCWA simulations are particularly useful for graphene because they don't require very dense grids and they work by dividing devices in layers that are uniform in the z direction (staircase approximation is used for curved surfaces) where the electromagnetic modes are calculated in each layer and are analytically propagated through the z axis. The efficiency of RCWA simulations for graphene devices can easily be proven by simulating the optical behaviour of a freestanding monolayer of graphene. In Figure 12.1 the optical absorption and reflection on a graphene monolayer has been simulated for different values of chemical potential, the optical properties of graphene have been included in the form of volumetric refractive index values as calculated in chapter 4. Simulated absorption perfectly matches theoretical calculations demonstrating the tuneable optical behaviour of graphene with a simulation time shorter than 30 seconds on a personal computer. Since dense grids are not required in order to simulate the extremely thin layer of graphene not much computational power is spent on simulating the monolayer itself and the simulation time mostly depends on the complexity of the remaining structures.

Figure 12.2 shows the setup for simulating a 1000nm pitch/ 750nm size pyramid diffraction grating array. A 50nm layer of gold has been added to enhance the visibility of the diffraction features in the simulation data. Simulations are ran in order to obtain reflected spectra versus incident light wavelength and angle. Figure 12.3 shows the simulation results for the grating compared the experimental results obtained through reflectometry. The agreement between RCWA simulation and experimental data is excellent presenting the same diffraction features for the selected grating.

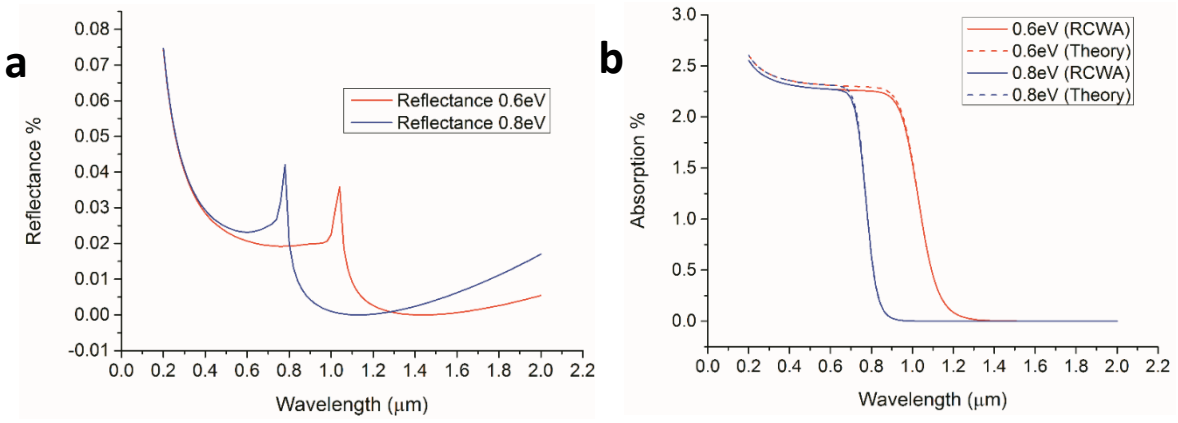

Figure 12.1 a. RCWA simulation of reflectance on a free standing graphene monolayer with a Fermi level of 0.6eV and 0.8eV **b.** RCWA simulation results for absorption through a graphene monolayer with a chemical potential of 0.6eV and 0.8eV compared with theoretical calculations.

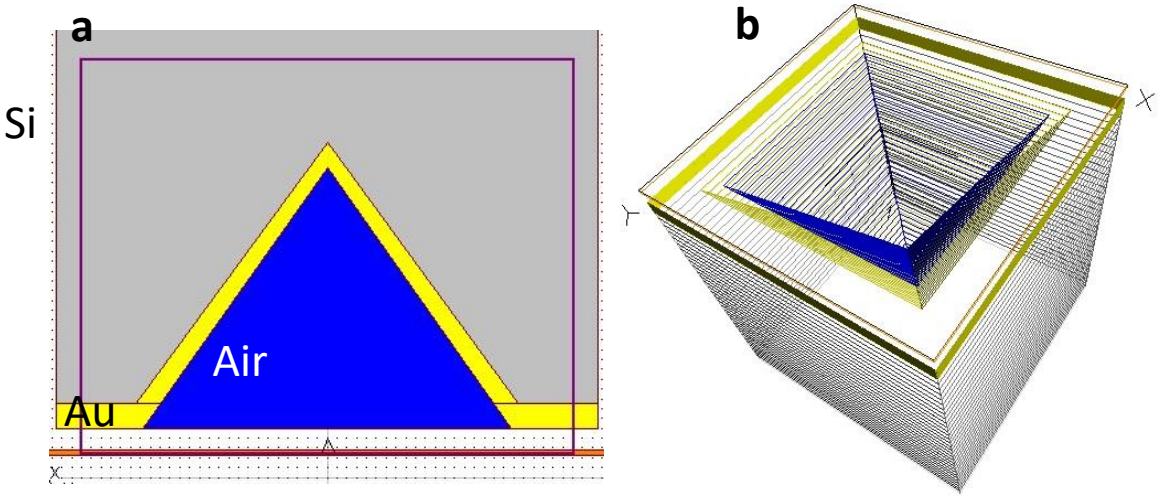

Figure 12.2 Simulated diffraction grating with 1000nm pitch and 750nm pyramid side, a 50nm thick layer of gold has been placed to enhance the visibility of the diffraction lines **a**. side view **b** 3D view.

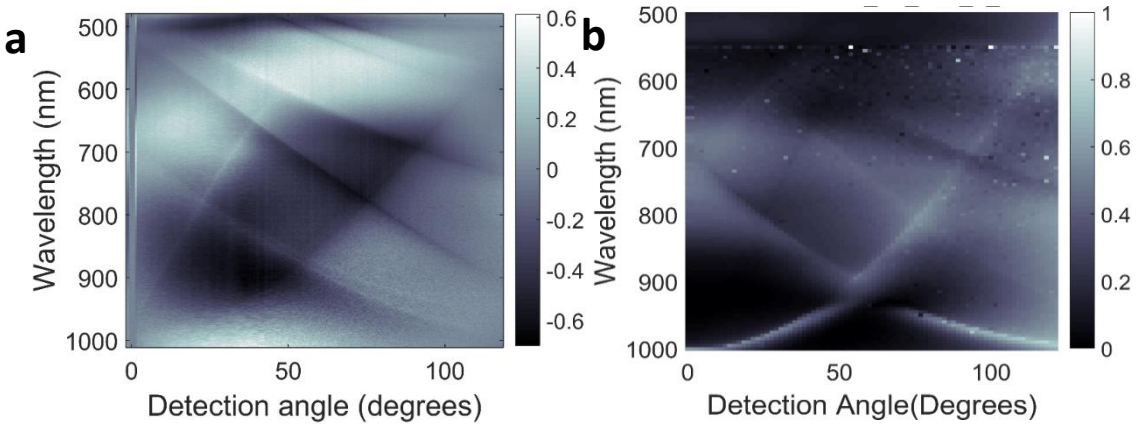

Figure 12.3 Comparison between experimental reflectometry measurement and RCWA simulation result for a 1000nm pitch/750nmnm pyramid size **a**. experimental data **b** RCWA simulation (a 50nm gold layer has been placed above the Si grating to enhance the visibility of the diffraction features in the simulation data).

12.3.2. Lumerical FDTD Simulations

Finite-difference time-domain is a numerical analysis method for simulating electromagnetic behaviour. Unlike RCWA it works in time domain instead of frequency domain and is based on a grid differential solver. Thus care is required when simulating graphene since it is very thin compared to the other device structures and it is difficult to create an accurate grid that provides quality results while not being time consuming. Lumerical FDTD solutions overcame this problem by introducing a 2D rectangle structure that acts as a 2D surface instead of a 3D structure thus overcoming the necessity of dense grids. Since the graphene layer is not treated as a 3D material the optical properties of graphene shouldn't be inserted in the form of volumetric permittivity but instead in the form of its surface conductivity. FDTD solutions includes an inbuilt model of the surface conductivity of graphene following reference [218]. Figure 12.4 compares the FDTD absorption simulation results for a freestanding graphene monolayer with theoretical calculations following the methodology of chapter 4 for a chemical potential of 0.6eV and 0.8eV. The simulation results agree well with theoretical calculations with the only exception being a small offset at the limit when approaching the ultraviolet region of the spectrum. The reason for this difference is that unlike the model described in chapter 4 the built in surface conductivity model in FDTD solutions doesn't take into account the band broadening that occurs in graphene when moving to higher photon energies at the limit within and above the optical frequencies range. Nevertheless these frequencies are not within the range of interest for this project and thus the model is acceptable for use in simulations. By treating graphene as a surface instead of a 3D material the simulation time is significantly reduced and is completed in less than one minute using a personal computer. Thus once again the computation time mainly depends on the complexity of the remaining structures in the simulation and their required grid density.

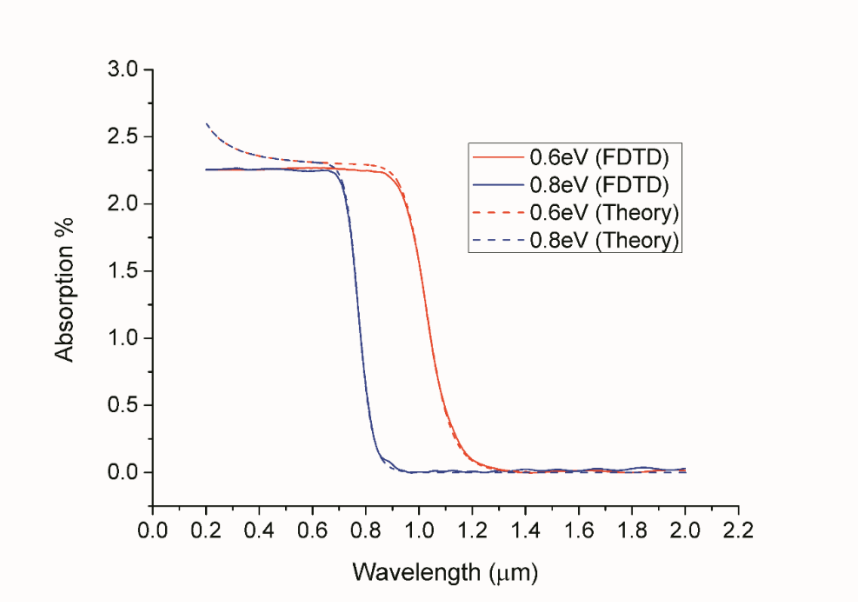

Figure 12.4 FDTD simulation results for absorption through a graphene monolayer with a chemical potential of 0.6eV and 0.8eV compared with theoretical calculations.

12.1. Optical Absorption in Graphene

Transmittance of graphene in vacuum is given by

$$T_r = \left(1+\sigma / 2c\varepsilon_0\right)^{-2}$$

where c the speed of light [82]. Transmission of light through a graphene monolayer for a combination of different incident photon wavelengths and graphene chemical potentials can be seen in Figure 12.5. In the region where interband transmission is forbidden 100% of light propagates through the layer. Transmission can easily be converted to absorption with the use of the following relation,

$$A = -\log_{10}\left(T_r\right).$$

Graphene presents a stable optical absorption of 2.3% at the interband transition region of the spectrum and no absorption outside this range as seen in Figure 12.6. At the border of the interband transition region the decrease of absorption is gradual due to the thermally excited electrons following the Fermi-Dirac distribution.

Finally, the normalized change of the power reflectivity on a sample surface with and without graphene can be calculated based on the multilayer interference theory as

$$\frac{\Delta R}{R_0} = \pi d_g . Re\left\{\frac{\left(1-n_{gr}^2\right)\left(1+r_0\right)^2}{r_0 \lambda}\right\}$$

where r_0 the optical field reflectivity of the substrate without graphene, and n_{gr} the refractive index of graphene [86].

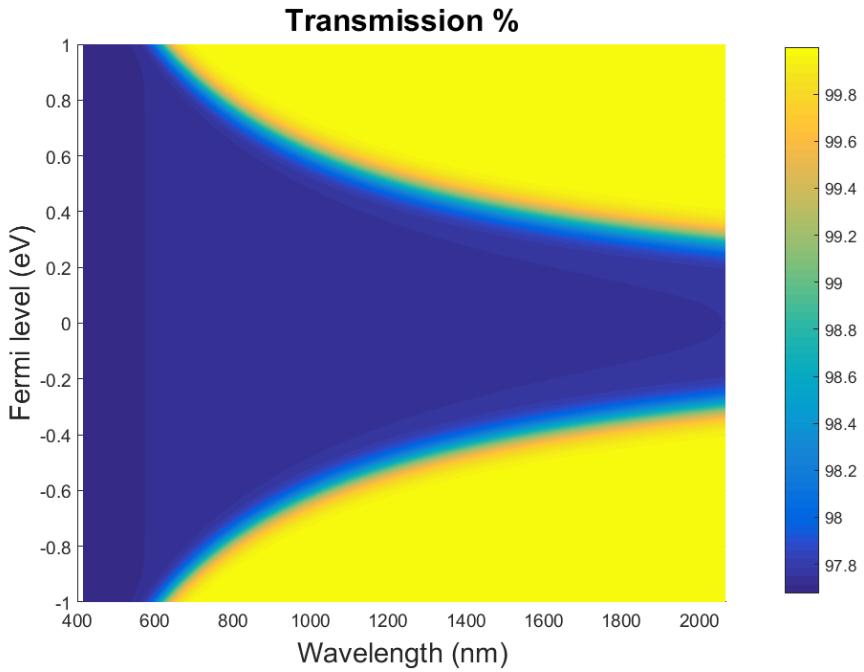

Figure 12.5 Transmission of light through a graphene monolayer for a combination of different incident photon wavelengths and chemical potential.

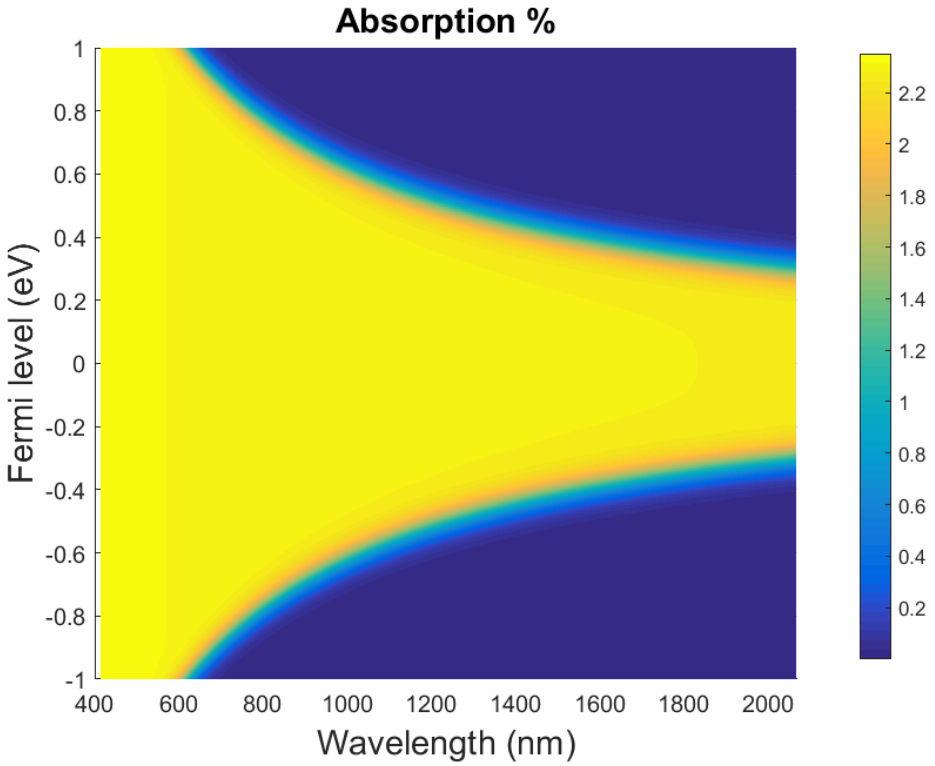

Figure 12.6 Absorption of light through a graphene monolayer for a combination of different incident photon wavelengths and chemical potential.

12.1. Azimuthal Angle Dependence of Diffraction Features

Figure 12.7 demonstrates the shift of diffraction features for different azimuthal angles at a stable angle of incidence for the grating structure presented in chapter 5.1.2.

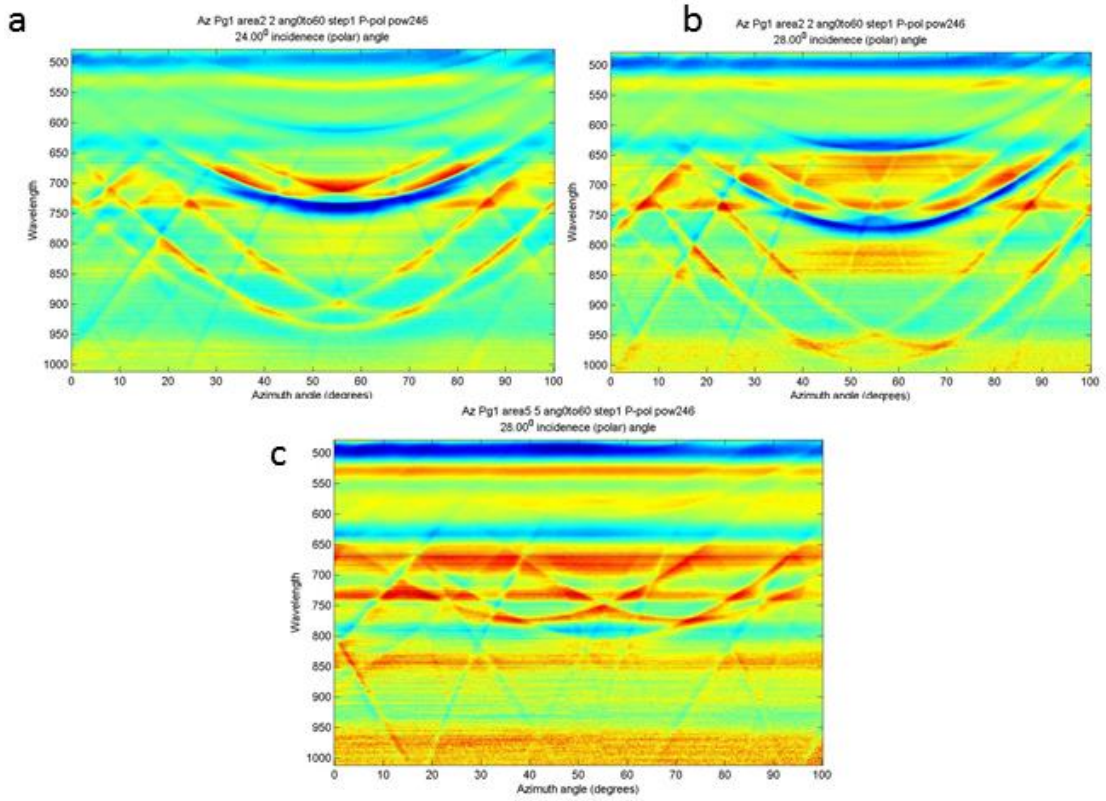

Figure 12.7 Reflectivity plot of the azimuth angle versus wavelength for different incident angles and structure geometries **a**. 1750nm pyramid side/ 250nm inter pyramid distance with a 24° incident angle **b**. 1750nm pyramid side/ 250nm inter pyramid distance with a 28° incident angle. **c**. 1000nm pyramid side/ 250nm inter pyramid distance 28° incident angle.

12.2. Fabrication

12.2.1. PMMA Assisted Wet Transfer of Graphene on Si Substrates

For the PMMA assisted wet transfer process a copper foil (or copper film on a Si substrate) is used as the graphene source. A thin PMMA layer is spin coated (1000rpm for 30-60sec) on top of the graphene layer that was grown on the copper substrate. The sample is then soft baked for several minutes at 100-150 °C or let to dry overnight in order to remove any residual PMMA solvent. The copper foil is then etched away in a Ferric Chloride solution of 0.5M. Typically the sample is left in the solution for 3-5 hours. If a Si wafer with evaporated copper on its surface is used instead of a copper foil then the $FeCl_3$ solution that is used has a 1M concentration and the etching requires more than 24 hours because the Copper film has to be under-etched since it's placed between the PMMA layer and the Si wafer.

After copper is completely etched away the sample is moved in deionized water for 10 minutes to remove some of the ferric chloride contamination (this can be repeated three times in order to further reduce the contamination but it could have a negative effect on the amount of defects like cracks or folds that form on the graphene layer). An optional cleaning step in $H2O/H_2O_2/HCl$ (20:1:1 at room temperature) is implemented in order to remove iron contamination that occurs because of the exposure to Ferric Chloride. If any organic contamination needs to be removed $H_2O/H_2O_2/NH_4OH$ (20:1:1 at room temperature) can be used since it removes any organic contamination from the sample. After each of the optional steps placing the sample in deionized water is required.

After the required deionized water cleaning step the free floating graphene/PMMA bilayer is picked up using the target substrate (using a tilted position while picking the graphene/PMMA film is suggested for better contact with the floating film). The substrate has to be very clean otherwise the graphene layer won't be able to adhere on the surface (Acetone and IPA rinsing is good enough for removing some of the organic contamination). It is also very crucial that the substrate is highly hydrophilic otherwise the transferred graphene could have a high amount of defects. A none hydrophilic surface could even cause failure of the transfer due to the poor contact of the graphene layer with the target substrate after being picked up from deionized water. Si wafers with a naturally grown oxide on their surface are already hydrophilic but an oxygen plasma treatment or a brief dip in HF could make them much more hydrophilic (HF introduces many OH groups on the surface of the wafer).

After the graphene/PMMA bilayer is picked up using the target substrate the sample is let to dry overnight or is heated gradually up to 150 °C and then let to dry for another 15 minutes. This has been suggested to reduce any defect formations that are caused during the drying process because the contact of graphene with the target substrate is highly improved [162]. The PMMA layer is then removed by placing the sample in an Acetone bath overnight at room temperature. This can be followed by an optional IPA rinse and blow drying to further remove any PMMA residue. The PMMA layer can also be removed by placing the sample in an Ar and H_2 atmosphere at 350 °C for about two hours [165]. Finally, an optional bake step at 200 °C for 10 minutes can be used to further increase the adhesion of the graphene layer to the new substrate [162]. Figure 12.8 presents all the required and optional steps of the process in the form of a flow chart, Figure 12.9 is a schematic of the process.

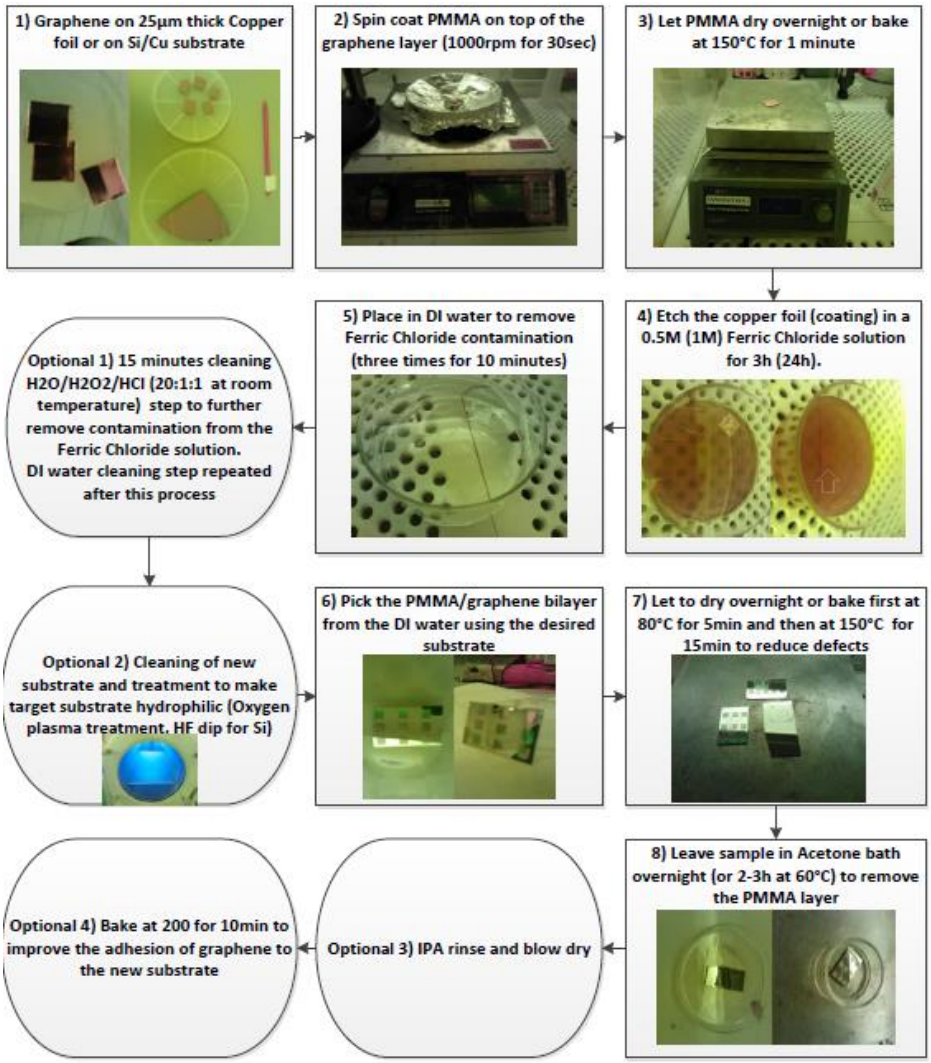

Figure 12.8 Flow chart of the required and optional steps for transferring graphene with the PMMA assisted wet transfer process.

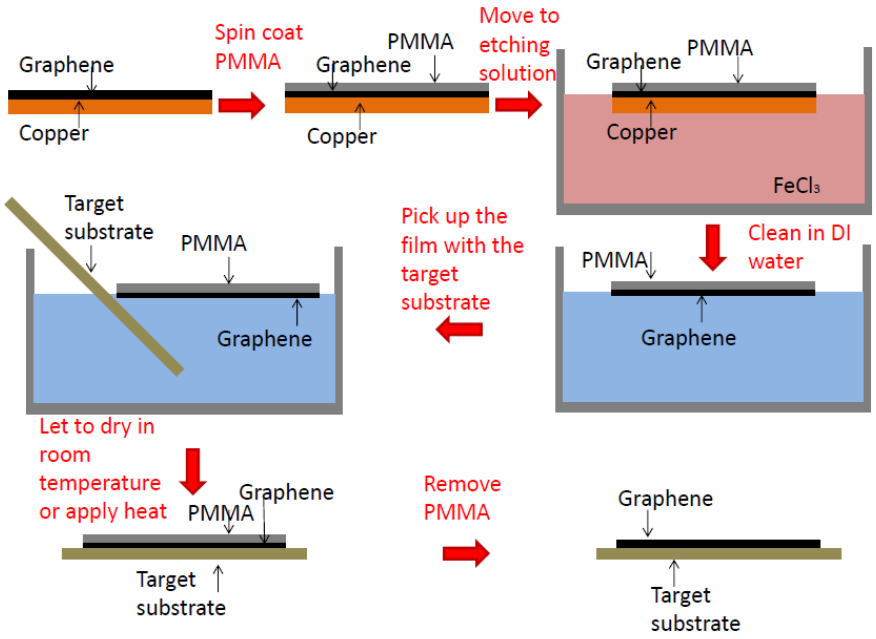

Figure 12.9 Schematic of the PMMA assisted wet transfer process.

12.2.2. PMMA Assisted Wet Transfer of Graphene on Perforated Si substrates Without Removing the PMMA Layer

This method was used in order to successfully transfer graphene on substrates that have shallow wells. Basically this process is a small alteration of the previously mentioned method that involves flipping the free floating PMMA/graphene bilayer during the deionized water cleaning step. This way when the target substrate is used to pick up the free floating film the PMMA layer will be placed between the graphene layer and the desired substrate, thus making the PMMA film part of the final device. For this method baking the sample (instead of letting it dry overnight) by gradually increasing the temperature to 150 °C and then leaving it to heat for 15 minutes provides the best results since the PMMA layer softens. As a result, the PMMA layer better follows the surface of the target substrate. Figure 12.10 presents all the required and optional steps of the process in the form of a flow chart, Figure 12.11 is a schematic of the process presenting only the required steps.

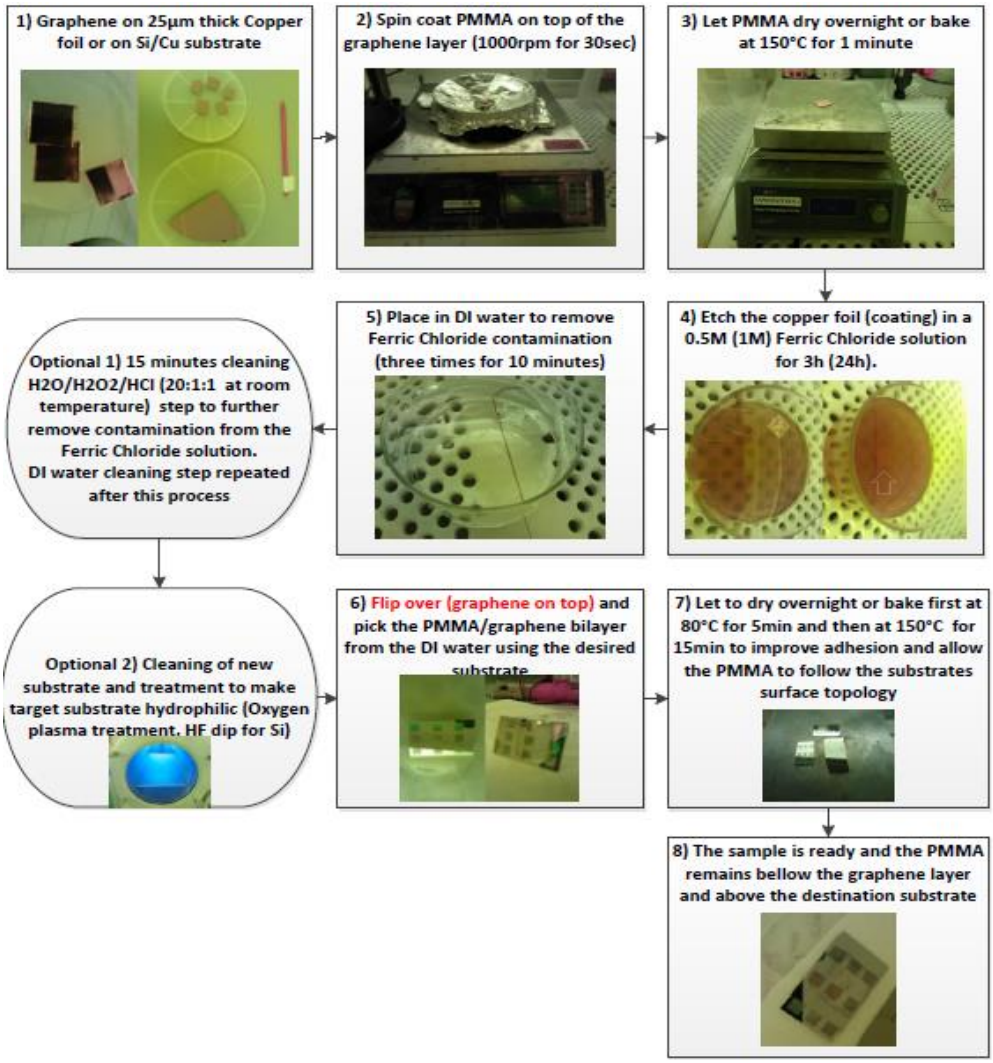

Figure 12.10 Flow chart of the required and optional steps for transferring graphene with the altered PMMA assisted wet transfer process that uses the PMMA layer as part of the final device.

Further optimization could be achieved by carefully adjusting the heat treatment temperature and time while analysing the results with the use of SEM imaging. This method was successful on transferring graphene to substrates with shallow wells like the ones shown in Figure 12.12. The PMMA may cause n-type doping of the graphene layer as well as an introduction of additional carrier scattering mechanisms [158].

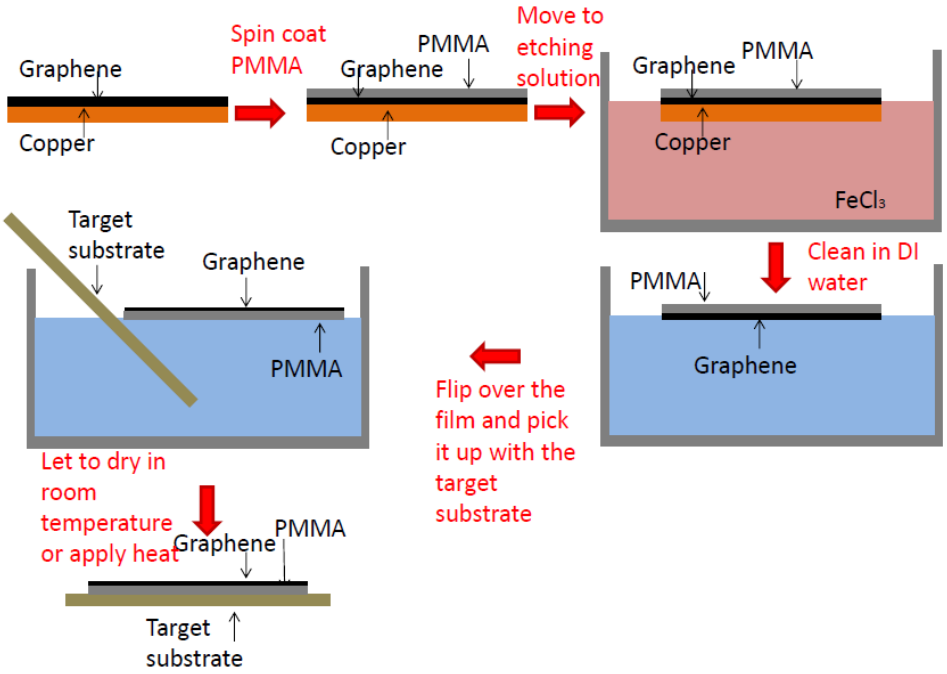

Figure 12.11 Schematic of the altered PMMA assisted wet transfer process that uses the PMMA layer as part of the final device.

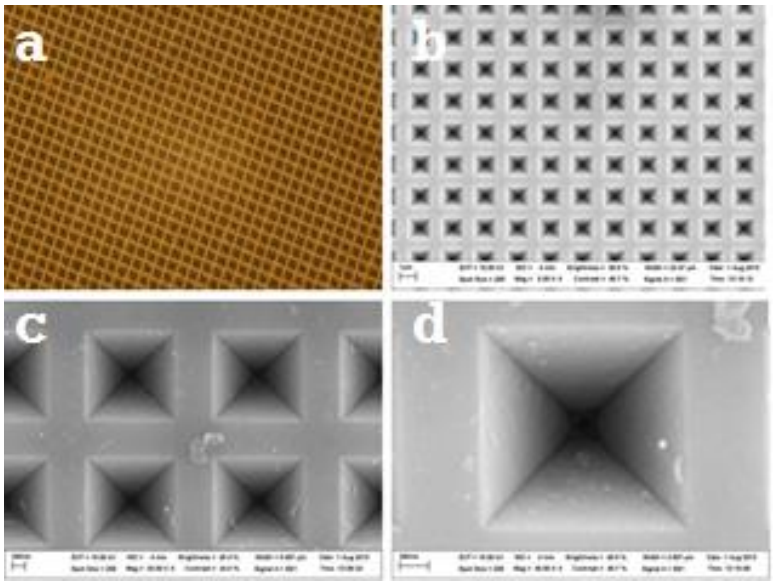

Figure 12.12 Si wafer with shallow pyramid wells patterned on its surface. **a**. Optical microscopy image of the pattern. **b-d**. SEM images of the pyramid pattern, the scale bars are 1µm, 200nm and 200nm for b to d respectively.

12.2.3. Direct Transfer of Graphene on Flexible Substrates

Direct transfer of graphene was used in order to transfer graphene on flexible polymer based substrates (in this case PMMA) with shallow wells patterned on their surface. The process steps followed for the transfer can be seen in Figure 12.13 and Figure 12.14. First the polymer substrate is laminated on the graphene surface by carefully applying heat and pressure (105-110°C) in order to avoid damaging the polymer film. After bonding is complete the sample is placed in a $FeCl_3$ solution for about 3 hours in order to etch copper. Afterwards the sample is cleaned in deionized water for ten minutes to remove contamination from the ferric chloride solution and then is let to dry overnight. An optional heat treatment step similar to the one used in the previously mentioned transfer processes was also tested but caused unwanted bending of the polymer substrate even though much lower temperatures were used.

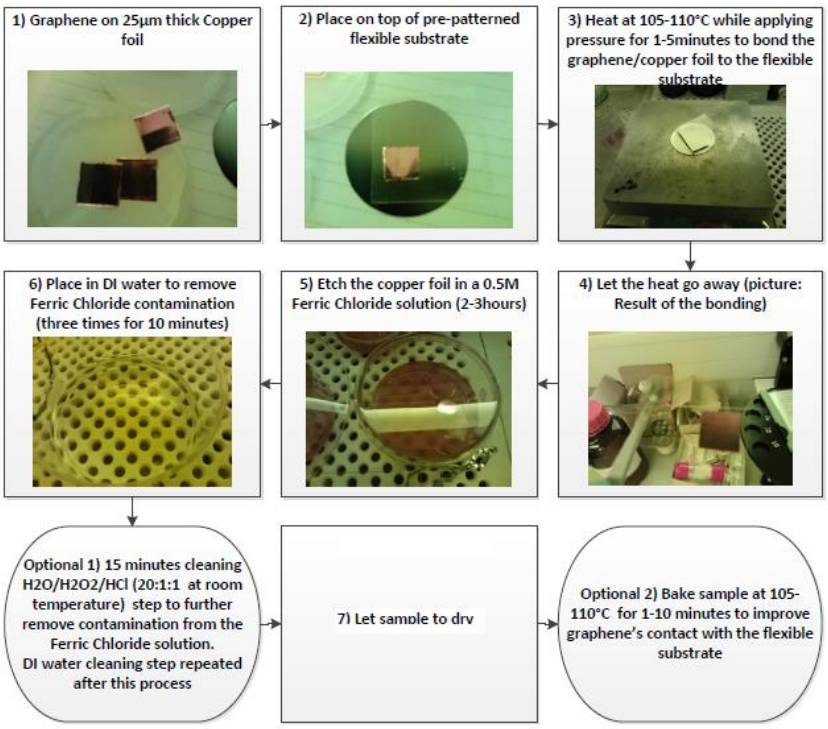

Figure 12.13 Flow chart of the required and optional steps for transferring graphene with the use of the direct transfer process.

This transfer process failed to provide any results and no graphene was observed with the use of Raman spectroscopy. The most possible reason for that is that during that laminating process the graphene layer didn't adhere well on the polymer substrate and was then detached during the copper foil etching or the deionized water cleaning steps. Careful consideration when choosing the type of flexible substrate should be taken (PET could be a much more suitable candidate than PMMA since similar transfer processes that involve lamination for direct transfer of graphene have been using it successfully [167]). Also the temperature as well as the amount of pressure that is used during the lamination process should be carefully adjusted in order to achieve good adhesion of the graphene layer without damaging the patterned structures on the substrate or causing it to melt.

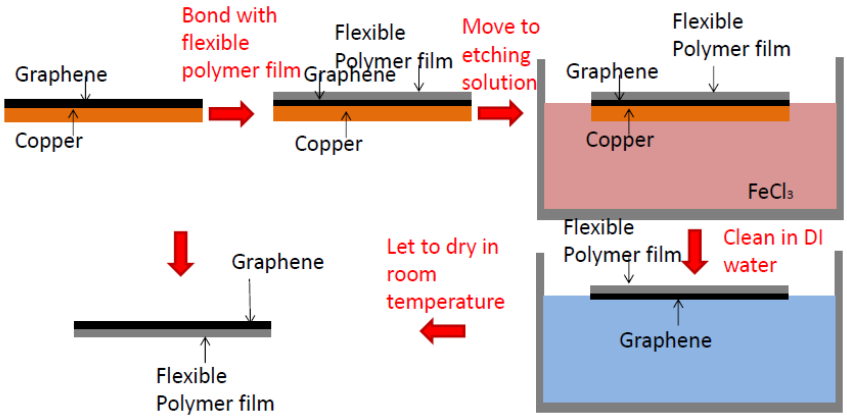

Figure 12.14 Schematic of the direct transfer process.

12.2.4. HfO_2 Gate

HfO_2 was tested as a back-gate dielectric in this project (acknowledgment to Dr. Katrina Morgan for the deposition of HfO_2) due to its high dielectric constant value (20) when compared to SiO_2 (3.9). Dielectrics with high relative permittivity allow higher control over the carrier concentration of graphene as described by the following equation,

$$n_c = \frac{V_g \varepsilon_0 \varepsilon_d}{ed}.$$

Figure 12.15 shows the corresponding chemical potential in graphene for increasing gate voltage when using 11nm HfO_2 dielectric layer as a gate dielectric.

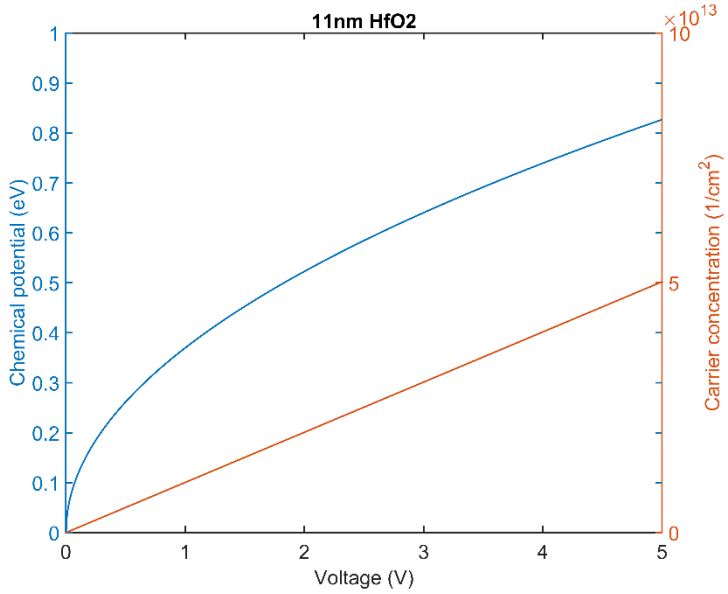

Figure 12.15 Chemical potential in graphene versus applied voltage for 11nm HfO_2 layer gate dielectric

A 11nm thick HfO_2 layer is deposited with the use of Atomic Layer Deposition in order to be used as a gate dielectric. The thickness of the dielectric was measured with the use of ellipsometry and was found to be 11.01nm (ellipsometry model seen in Figure 12.16 providing a good much with measured data).

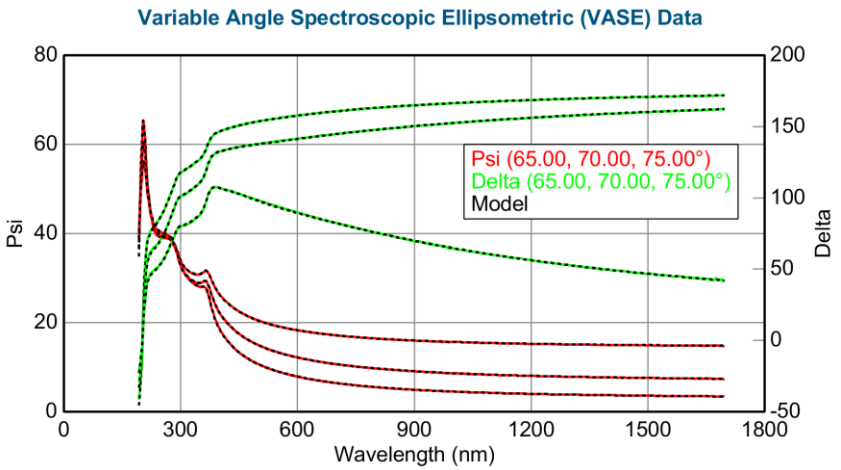

Figure 12.16 Ellipsometry data and model used to calculate the dielectric layer thickness.

The leakage current through the dielectric layer was measured with the use of electrical probing station, the results can be observed in

Figure 12.17. By observing the data it becomes clear that leakage current becomes increasingly high and above 3V it has already obtained a very high value meaning that the operation of the device could be limited between 0V and 3V thus achieving only a small chemical potential change in graphene. The leakage current could probably originate from pinholes that are created during the fabrication process or contamination. Further improvement of the process or use of different gate structures/materials should be investigated for improved performance. Due to the low quality of the ALD process and the advantages ionic gel presents over conventional dielectrics HfO_2 was proven to be inadequate for this project.

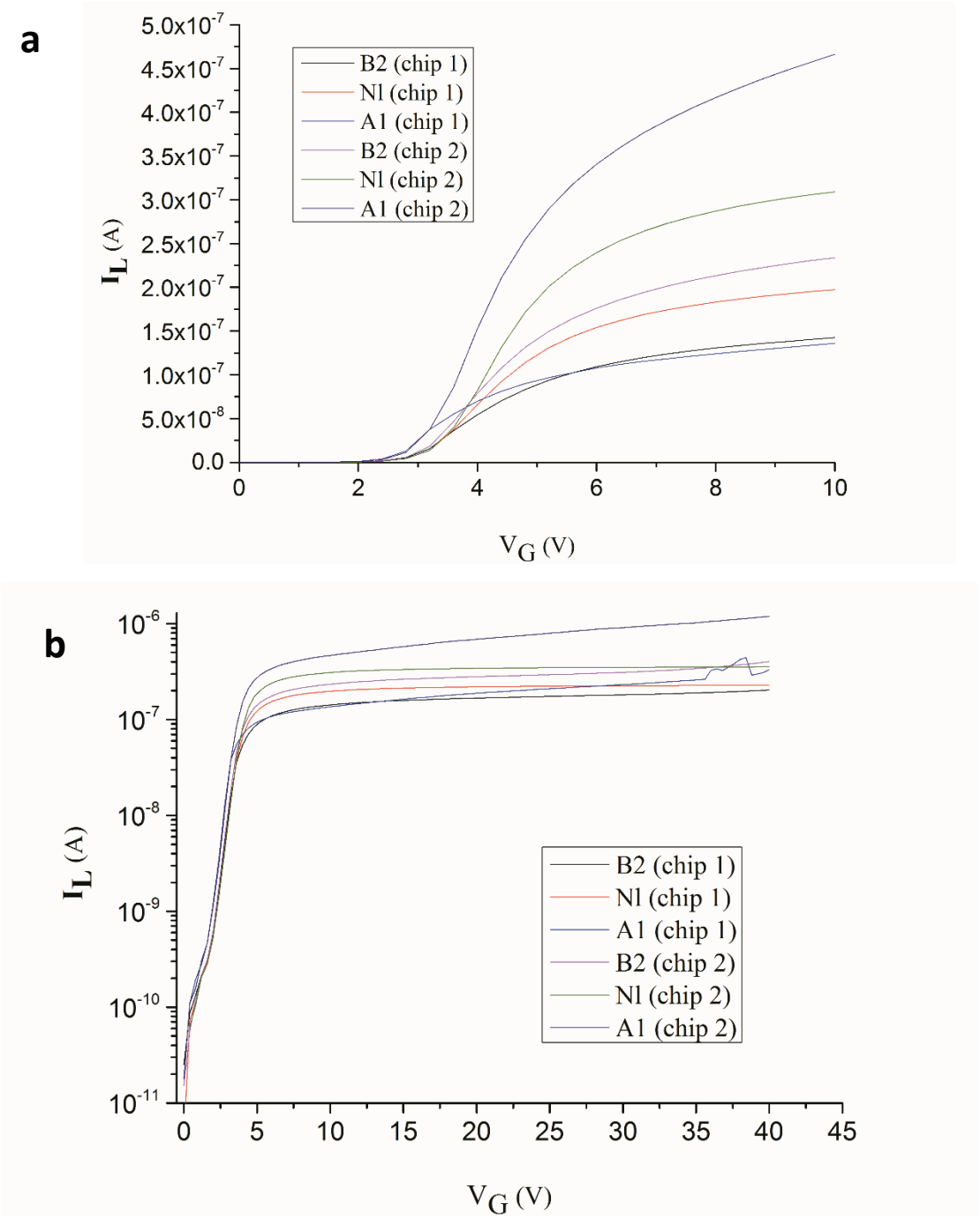

Figure 12.17 Leakage current versus voltage for 11nm thick HfO_2 layer gate dielectric for different chips in **a**. linear scale and **b**. log scale.